Dating of Ice and Ocean Samples with Atom Trap Trace Analysis of ^{39}Ar

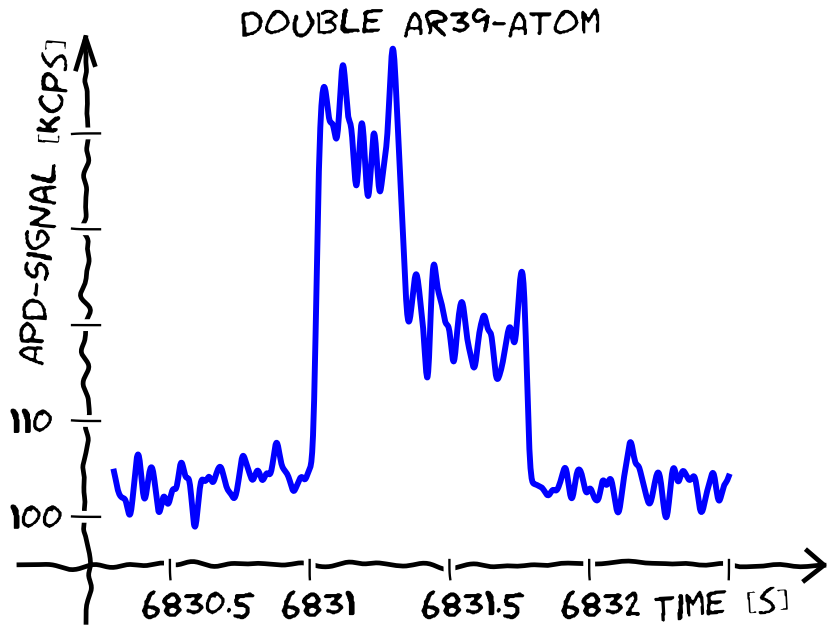

Sven C. Ebser

Issued 2018

Dissertation
submitted to the
Combined Faculties of the Natural Sciences and Mathematics
of the Ruperto-Carola University of Heidelberg, Germany
for the degree of
Doctor of Natural Sciences

Put forward by
Sven C. Ebser
born in Bad Mergentheim, Germany

Oral examination: 14 May 2018

Dating of Ice and Ocean Samples with Atom Trap Trace Analysis of ^{39}Ar

Referees: Prof. Dr. Markus K. Oberthaler
Prof. Dr. Norbert Frank

Zusammenfassung:

Das radioaktive Edelgasisotop ^{39}Ar mit einer Halbwertszeit von 269 Jahren ist ein nahezu idealer Tracer, um Eis- und Wasserproben im Zeitbereich von vor 50 bis 1000 Jahren zu datieren, für den es keine anderen verlässlichen Methoden gibt. Aufgrund der geringen relativen Häufigkeit von $^{39}\mathrm{Ar}/\mathrm{Ar} = 8.1(3) \times 10^{-16}$ konnte ^{39}Ar bisher routinemäßig nur durch Low-Level Counting gemessen werden. Hierfür sind jedoch Probenmengen in der Größenordnung von 1000 L Wasser nötig, was die Anwendung von ^{39}Ar als Tracer, abgesehen von wenigen Machbarkeitsstudien, bisher auf die Grundwasserforschung eingeschränkt hat.

In der vorliegenden experimentellen Arbeit konnte durch die Weiterentwicklung der atomoptischen Analysemethode Atom Trap Trace Analysis (ATTA) die benötigte Probengröße auf 2 mL STP Argon reduziert werden. Diese Gasmenge kann aus $\sim$5 kg Wasser oder Eis extrahiert werden. Durch eine Neugestaltung des Lasersystems sowie eine Optimierung des Vakuumsystems konnte darüber hinaus die atmosphärische Zählrate auf bis zu 7,0 Atome pro Stunde verdoppelt werden. Dies ermöglicht ^{39}Ar-Messungen mit einem typischen relativen Fehler von 10 % innerhalb eines Tages.

Das Messverfahren wurde in einer Vergleichsstudie, basierend auf leicht angereicherten Proben, mit dem etablierten Low-Level Counting Labor in Bern sowie mit einem neu geschaffenen Labor am Pacific Northwest National Laboratory validiert. Darüber hinaus konnte die neue Methode anhand der Analyse von Proben bekannter subatmosphärischer ^{39}Ar-Konzentrationen verfiziert werden. Eine definierte Probe mit 10 % der atmosphärischen Konzentration konnte dabei mit 1σ Konfidenz vom Untergrund unterschieden werden.

In einer ersten Anwendung wurden erstmals Eisproben mittels ATTA auf ^{39}Ar untersucht. Hierfür standen drei Gletschereisproben vom Gornergletscher (Monte-Rosa-Massiv, Schweiz) zur Verfügung, die teilweise eine unerwartet moderne ^{39}Ar-Konzentration aufwiesen.

Das Hauptergebnis dieser Arbeit ist jedoch die erfolgreiche Analyse dreier Tiefenprofile à acht Proben aus der Sauerstoff-Minimum-Zone des östlichen tropischen Atlantiks. Durch die um mehr als zwei Größenordnungen reduzierte Probengröße konnte die Probennahme mit 10 L-Niskin-Flaschen durchgeführt werden. Mit Hilfe der gemessenen ^{39}Ar-Konzentrationen wird in Kombination mit CFC-12 Daten gezeigt, dass die Altersverteilung des nordatlantischen Tiefenwassers deutlich jüngere Komponenten aufweist als bisher angenommen. Somit wird das bedeutende Potential von ^{39}Ar demonstriert, Altersverteilungen zu bestimmen, was essentiell für das Verständnis der Ozeanzirkulation und der Sauerstoffverteilung im Inneren des Ozeans ist und beispielsweise eine Abschätzung des gespeicherten anthropogenen Kohlenstoffs erlaubt.

Abstract:

The noble gas radioisotope ^{39}Ar with a half-life of 269 years is an almost ideal tracer for dating ice and water samples in the time range of 50 to 1000 years ago, for which no other reliable methods exist. Due to its very low relative abundance of $^{39}\mathrm{Ar}/\mathrm{Ar} = 8.1(3) \times 10^{-16}$, ^{39}Ar has only been routinely measured by Low-Level Counting so far. However, since Low-Level Counting requires samples in the order of 1000 L, the application of ^{39}Ar, besides some proof-of-principle experiments, has been limited to groundwater studies until now.

In the course of this experimental thesis, the required sample size could be reduced down to 2 mL STP of argon by further development of the atom-optical analytical method Atom Trap Trace Analysis (ATTA). This amount of gas can be extracted from ∼5 kg water or ice. Due to a redesign of the laser system together with an optimisation of the vacuum system, the atmospheric count rate could be moreover doubled up to 7.0 atoms per hour. This enables ^{39}Ar-measurements with a typical relative uncertainty of 10 % within one day.

The measuring technique was validated in an intercomparison study based on slightly enriched samples with the well established Low-Level Counting Laboratory in Bern as well as with a new laboratory at the Pacific Northwest National Laboratory. Furthermore, the new method was verified by analysing samples with a known subatmospheric ^{39}Ar concentration. A defined sample with 10 % of the modern concentration could be distinguished with 1σ confidence from the background.

In a first application, ice samples were analysed for ^{39}Ar by ATTA for the first time. Three glacial ice samples originating from the Gorner Glacier (Monte Rosa massif, Switzerland) were available for this purpose and show an unexpected modern ^{39}Ar-concentration in some cases.

The main result of this thesis, however, is the successful analysis of three depth profiles with eight samples each, taken in the eastern tropical North Atlantic oxygen minimum zone. Due to the reduction of the required sample size by more than two orders of magnitude, it was possible to conduct the sampling with 10 L-Niskin bottles. With the help of the ^{39}Ar-results it is shown, that the transit time distribution of the North Atlantic Deep Water has significantly younger water components than previously assumed. Thus, the outstanding potential of ^{39}Ar for a determination of transit time distributions is demonstrated, which is essential for the understanding of ocean circulations and oxygen supply of the interior of the ocean and which allows, for example, an estimation of the stored anthropogenic carbon.

Contents

Preface

Hardly a day goes by without a news headline about lasting droughts or water shortages, as well as discussion on the progressing anthropogenic climate change. Oceans cover about two thirds of earth's surface and contain ∼97 % of earth's water. They act as a buffer for global warming and as storage for anthropogenic CO_2 and other greenhouse gases, so that they are a fundamental part of the global climate system. Their understanding is crucial for modelling and predicting the global warming and its impacts, which is in turn essential for developing the necessary adaptation to the climate. Considering another example: Due to depletion, pollution, salination and other human influences of surface or near-surface water resources, older and deeper aquifers will be of major importance to meet the increasing needs of fresh water. A deep understanding about their recharge conditions and flow patterns is the basis for a sustainable water management.

Necessary for understanding both ocean and aquifer system is a fundamental understanding of the hydrological system, especially of the water circulations. A key parameter for this is the age of the water, which is defined as the time lapse since the last contact with the atmosphere. The standard method to determine the age is the analysis of chemical tracers with increasing or decreasing atmospheric concentrations or of radioactive isotopes, which are chronometers by their radioactive decay. Depending on the half-life and the change in atmospheric concentration, each tracer covers a particular time window.

For the time range between 50 and 1000 years ago, ^{39}Ar – with a half-life of 269 a – is practically the only existing tracer. Furthermore, the inertness of a noble gas and a homogeneous, almost exclusively cosmogenic production make ^{39}Ar an ideal environmental tracer. However, the challenge lies in the extremely low relative abundance of $^{39}\mathrm{Ar}/\mathrm{Ar} = 8.1(3) \times 10^{-16}$. Even though argon is a common gas in the atmosphere, there are only about ∼8500 ^{39}Ar-atoms in one litre of modern fresh water. Only one out of 1.2×10^{15} argon atoms in the atmosphere is an ^{39}Ar-atom. This unimaginable number can be illustrated by this comparison: The ocean samples analysed in this thesis originate from the Atlantic, which covers with a surface area of $\sim 85 \times 10^6\,\mathrm{km}^2$ about 20 % of the earth [1]. A ratio of $8.1(3) \times 10^{-16}$ corresponds to one A4-paper ($0.0625\,\mathrm{m}^2$) floating in the seemingly endless expanse of the Atlantic.

Due to this extreme rareness, ^{39}Ar has only been analysed by Low-Level Counting (LLC) in the underground laboratory in Bern so far requiring about 1000 L of water and several weeks of measurement time. ^{39}Ar-studies thus were limited to groundwater research, where degassing several tons of water is feasible in the field. Since the atom-optical detection technique Atom Trap Trace Analysis (ATTA) is not based on the activity of the desired isotopes, it allows for fast analysis of small samples in principle.

ATTA was initially developed for the rare krypton isotopes and is now available as routine analysis method for ^{85}Kr and ^{81}Kr [2]. The Heidelberg ArTTA-project (Argon Trap Trace Analysis), which is a joint effort of the atom physics group at the Kirchhoff-Institute for Physics (KIP) and the Institute of Environmental Physics (IUP), has been focussing on adapting this method to ^{39}Ar and pushing the limits further down to the required sensitivity for almost one decade.

This is the third PhD thesis addressing the atom-optical side of the ArTTA-project. The scope of the first thesis [3] was the construction of the basic ArTTA-apparatus and the first detection of single ^{39}Ar-atoms. During the second thesis [4] the count rate could be significantly increased and the system was optimised including the first groundwater study. However, the required sample size was still in the order of 1000 L of water and thus comparable with the requirements of LLC. The goal of this current thesis was the optimisation of the system to enable the first measurements with a sample size below 10 L of water, which is the magic threshold for ^{39}Ar-measurements in oceanography, since this is the volume of the standard samplers. A reduction of the sample size down to a typical argon volume of 2 mL STP, corresponding to about 5 kg of ice or water, could be achieved, which enabled the first ^{39}Ar-study in the ocean in 25 years and the first ^{39}Ar-measurements of glacier ice with ArTTA. A complementary thesis at the IUP was carried out by Arne Kersting, particularly treating sampling, purification and interpretation of the analysed samples [5].

This thesis is structured in the following way: The first chapter is a collection of some background information, starting with a short introduction of dating with radioactive and chemical tracers. A specific focus is put on the noble gas radioisotope ^{39}Ar and its applications. The degassing and purification system is briefly presented and the basic concept of transit time distribution is introduced. The second chapter describes the atom-optical apparatus focusing on the changes since the last thesis [4] and on the improvements which were necessary for an operation with small samples. Chapter three is more mathematical and deals with the statistics and the mathematical methods which were implemented to analyse the recorded photon signal and to detect single trapped atoms with a high fidelity. Moreover, the statistical model which is used to finally infer an ^{39}Ar-concentration from the number of counted atoms is discussed. All ^{39}Ar-measurements in this thesis were treated by these methods.

The ^{39}Ar-measurements were performed in three main measurement periods, which are summarised in the following three chapters. Chapter four presents the first ice samples analysed by ArTTA. Chapter five contains the intercomparison study which took place between the ArTTA-lab in Heidelberg and two LLC laboratories in Bern and at the Pacific Northwest National Laboratory, respectively. The ocean study, which is presented in chapter six, is the main result of this thesis and demonstrates the full potential of the current ArTTA-system. The second part of this chapter is a short excursion into some environmental background, and the measured ^{39}Ar-results are discussed in the context of transit time distributions.

The last chapter summarises this work and gives a short outlook on what might be the next steps on the way to a routine application of ArTTA. The appendix compiles some additional information belonging to the single chapters.

1. Fundamentals

This chapter introduces the basic concepts used in this thesis and summarises some background information about argon, the rare radioisotope ^{39}Ar, and its applications. It is not intended to give a complete overview, but to focus on the information relevant for understanding this thesis.

1.1. Dating with environmental radioisotopes

The age of an environmental sample is defined as the time between the last contact with the atmosphere and the sampling. Chemical substances and radioactive isotopes enclosed or dissolved in the sample can be employed to deduce this time information. For radioactive isotopes with a known initial concentration c_0 and no or negligible in situ production and sinks, the tracer age τ_{radio} can be derived from the radioactive decay with half-life $T_{1/2}$ by

$$c(t) = c_0 \cdot e^{-\frac{\ln(2)\cdot t}{T_{1/2}}}, \tag{1.1}$$

$$\tau_{\text{radio}} = \frac{T_{1/2}}{\ln(2)} \cdot \ln\frac{c_0}{c}, \tag{1.2}$$

where c is the measured concentration. The exact time range for which an isotope can be applied depends on many factors and the utilised detection technique. However, it can roughly be estimated by the empirical rule of thumb to be between $1/5 \cdot T_{1/2}$ and $5 \cdot T_{1/2}$ [4]. The resulting dating ranges of the commonly used tracers are depicted in figure 1.1.

The time range of the last 70 years is covered by several anthropogenic radionuclides. Tritium ($T_{1/2} = 12.32\,\text{a}$) was mainly produced during nuclear weapon tests between 1945 and 1963 and its concentration in the atmosphere has a significant maximum, known as the bomb peak, directly before the signing of the *Treaty Banning Nuclear Weapon Tests in the Atmosphere, in Outer Space and Under Water* in 1963. ^{85}Kr ($T_{1/2} = 10.739\,\text{a}$) instead mainly originates from nuclear fuel reprocessing with a steadily increasing atmospheric concentration since 1950. Both isotopes can be used to quantify young water components or as an indicator for contamination while sampling and during preparation of older water samples. However, only ^{85}Kr is sensitive to contamination with modern air since tritium can not be measured in the dissolved air but only directly in the water. Due to their high activity, these short-lived isotopes can be directly measured by counting the radioactive decays.

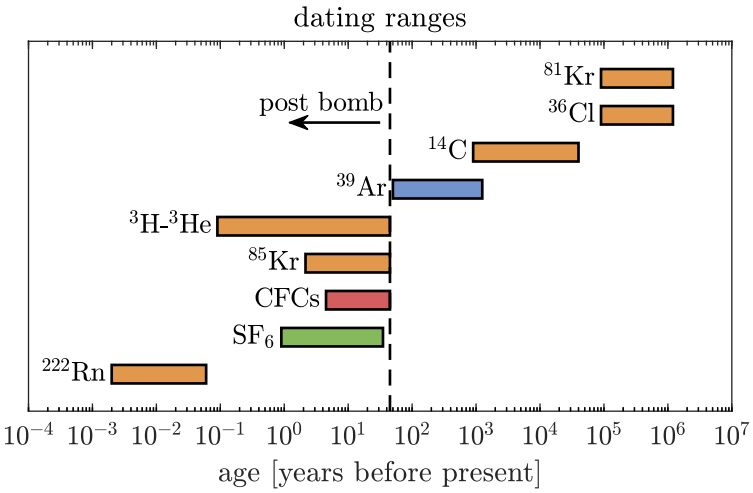

isotope	$T_{1/2}$
^{222}Rn	3.8235(3) d
^{3}H	12.32(2) a
^{85}Kr	10.739(14) a
^{39}Ar	269(3) a
^{14}C	5700(30) a
^{81}Kr	229(11) ka
^{36}Cl	301.3(15) ka

Fig. 1.1.: Dating ranges of the most important radioisotopes for dating water samples and their corresponding half-lives: For the last 70 years there exist a number of anthropogenic tracers due to the nuclear activities of humans. The anthropogenic chemical tracers CFCs (e.g. CFC-11, CFC-12) and SF_6 are included since they are used routinely in oceanography (adapted from [3, 4], half-lives taken from [6]).

Another group of tracers are conserved chemical substances with monotonically increasing or decreasing input functions $c_0(t)$. The tracer age τ_{con} of a chemical tracer is defined as the elapsed time since the input function $c_0(t)$ was equal to the concentration c, measured at time t of sampling [7]:

$$c = c_0(t - \tau_{\text{con}}) \tag{1.3}$$

Typical conserved tracers are chlorofluorocarbons (CFCs) and sulphur hexafluoride (SF_6), whose input functions are plotted in figure 1.2. The production of CFCs was phased out with the ratification of the *Montreal Protocol on Substances that Deplete the Ozone Layer* in 1989 and their concentrations in the atmosphere are decreasing since then. Thus, equation 1.3 is not unique anymore and it becomes difficult to apply most of these tracers for the time range of the past 20 years.

For the dating of very old water – sometimes also called fossil water [9] – the two radioisotopes ^{81}Kr and ^{36}Cl with a half-life of 229 ka and 301 ka, respectively can be applied. Due to their low specific activity they can only be analysed by accelerator mass spectrometry (^{36}Cl) [10] or Atom Trap Trace Analysis (^{81}Kr) [2]. Radiocarbon (^{14}C) can be measured with an extremely high precision using accelerator mass spectrometry, however its interpretation can be complex, since it is involved in many hydrogeochemical processes, which can alter the natural ^{14}C concentrations [11], and there are huge reservoir effects, so that additional corrections have to be made [12, 13]. Thus, its applicability for dating water and ice samples is limited.

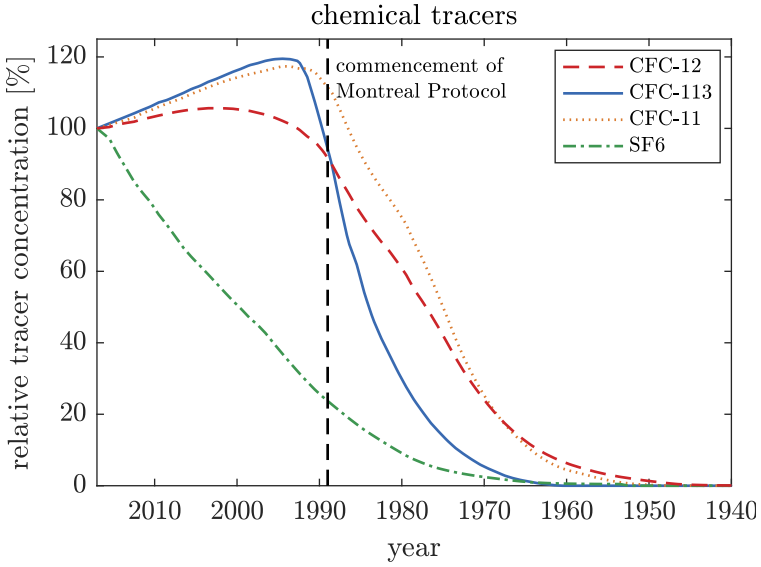

Fig. 1.2.: Time series of the concentrations of the chlorofluorocarbons CFC-12, CFC-113 and CFC-11 and of SF_6 in the atmosphere of the northern hemisphere (data taken from [8]). The vertical line indicates the commencement of the Montreal Protocol in 1989.

The dating gap between the anthropogenic tracers and ^{14}C, between 50 and 1000 years ago, is perfectly covered by the radioisotope ^{39}Ar with a half-life of 269 a. Additionally, the inertness of a noble gas and a nearly constant input function, both in time and spatially, makes ^{39}Ar a nearly ideal tracer for this time window. The challenge lies in the relatively low isotopic abundance, which is in the order of $^{39}Ar/^{40}Ar \approx 10^{-15}$. In the following section the general properties of argon and especially those of ^{39}Ar are discussed in more detail.

1.2. Argon

Argon is an inert, colour- and tasteless gas. Although it is the third-most abundant element in the earth's atmosphere (0.934 % by volume), it was not until 1894 that Lord Rayleigh and Sir William Ramsay discovered argon through weight comparisons between nitrogen (and argon) gas extracted from air and nitrogen gas formed in chemical processes [14]. They named the new element argon, derived from Greek **argos**, which means idle. Sir William Ramsay was laureated with the Nobel Price in Chemistry for his "discovery of the inert gaseous elements in air, and his determination of their place in the periodic system" in 1904 [15]. The most important properties of argon are listed in table 1.1.

Table 1.1.: Physical properties of argon [16, 17]

property	value
density at STP	$1.7835\,\mathrm{kg\,m^{-3}}$
molecular weight	$39.948\,\mathrm{g\,mol^{-1}}$
molar volume	$22.40\,\mathrm{L\,mol^{-1}}$
boiling point	87.3 K
melting point	83.8 K
atmospheric abundance	9340 ppm

1.2.1. The stable isotopes of argon

In total 24 Ar-isotopes are known (see appendix A.1). However, most of them are unstable with half-lives below 2 h and only five of them have relevance for dating with Argon Trap Trace Analyses (ArTTA). The properties of those Ar-isotopes can be found in table 1.2. ^{36}Ar and ^{38}Ar are primordial isotopes, which had existed already before the earth was formed and the ratio of ^{36}Ar/^{38}Ar did not change significantly during the earth's history. The ^{36}Ar/^{38}Ar-ratios which were measured in natural CO_2-reservoirs [18], but also the relative uniform values of ^{36}Ar/^{38}Ar = 5.3 to 5.5 found in a wide variety of solar system objects ranging from the sun to Jupiter [19] are very similar to the present atmospheric ratio of ^{36}Ar/^{38}Ar = 5.297(8) [20]. In contrast, ^{40}Ar, which is the most abundant Ar-isotope, is produced almost exclusively by the decay of ^{40}K, which is one of the most abundant elements in earth's crust. The primordial proportion of ^{36}Ar/^{40}Ar = 10^4 is extremely high [21]. Due to the production of ^{40}Ar in the lithosphere, the ratio of ^{36}Ar/^{40}Ar and equivalent of ^{38}Ar/^{40}Ar has a high variability and values of up to $1/30000$ can be found in the upper mantle [21].

Table 1.2.: Ar-isotopes relevant for dating with ArTTA (data taken from [6]). All known Ar-isotopes are listed in appendix A.1.

isotope	mass $[m_u]$	nat. abundance	nuclear spin I	$T_{1/2}$	decay
^{36}Ar	35.9675	0.3336(21) %	0	stable	-
^{37}Ar	36.9968	-	$3/2$	35.001(19) d	ec to ^{37}Cl
^{38}Ar	37.9627	0.0629(7) %	0	stable	-
^{39}Ar	38.9643	$8.1(3) \times 10^{-16}$	$7/2$	269(3) a	β^- to ^{39}K
^{40}Ar	39.9623	99.6035(25) %	0	stable	-

1.2.2. The radioisotope ^{39}Ar

^{39}Ar is the longest-lived radioactive isotope of argon and was discovered in potassium salts after neutron-bombardments in nuclear reactors [22]. There are two natural main sources of ^{39}Ar. The atmospheric ^{39}Ar is principally produced by neutron induced

spallation of ^{40}Ar in the upper atmosphere [23]:

$$^{40}\mathrm{Ar}(n, 2n)^{39}\mathrm{Ar} \tag{1.4}$$

The second source of ^{39}Ar on earth is underground production. There are two main mechanisms. Negative muon capture on ^{39}K

$$^{39}\mathrm{K}(\mu^-, \nu_\mu)^{39}\mathrm{Ar} \tag{1.5}$$

is estimated to be the dominant process in the upper 2000 m.w.e.[1] [24]. The second significant mechanism is radiogenic production in the underground

$$^{39}\mathrm{K}(n, p)^{39}Ar \tag{1.6}$$

driven by neutrons, which originate from the (α, n) reactions on light nuclei. The alpha particles, however, are provided by the decay chains of long lived natural uranium and thorium [25]. This process is particularly dominant in the earth's crust with high concentrations of uranium and thorium. A very low uranium and thorium concentration is determining for very low ^{39}Ar-concentrations in underground sources, since both, the formation of ^{40}Ar and the radiogenic production of ^{39}Ar, depend on the potassium content of the rock, but only the latter on the uranium and thorium content.

^{39}Ar has a half-life of $T_{1/2} = 269(3)$ a [26] and the only decay channel is the β^- decay to ^{39}K. ^{39}Ar is distributed homogeneously in the atmosphere, since its half-life is much longer compared to the typical time scale of mixing processes in the atmosphere.

A potential variation of the ^{39}Ar-concentration over time is depicted in figure 1.3. A fluctuation in the production rate of ^{39}Ar can be deduced indirectly from the production rate of ^{14}C, which can be measured with the help of tree rings, as both isotopes have a similar production mechanism by cosmic rays in the upper atmosphere [23]. The anthropogenic contribution generated in nuclear weapon tests until 1974 is estimated not to exceed 12 % by comparing the specific ^{39}Ar-activity of argon extracted from the atmosphere in 1940 with the one of six atmospheric samples from 1960s and early 1970s [23]. For the short time range of up to 150 a this might be – assuming the extreme case of 12 % – the dominant systematic uncertainty of the ^{39}Ar-dating method, because all measured ^{39}Ar-concentrations are referenced to the current atmospheric one. Nuclear weapon tests after 1974 are not considered, which might give an additional anthropogenic ^{39}Ar-input.

Since both, the estimation of the variation in the atmospheric ^{39}Ar-content and of the anthropogenic contribution, only give a rough upper limit, both effects are typically not included into the interpretation of the measured ^{39}Ar-concentrations and a constant input function is assumed in this thesis.

[1] mwe: **m**eter **w**ater **e**quivalent.

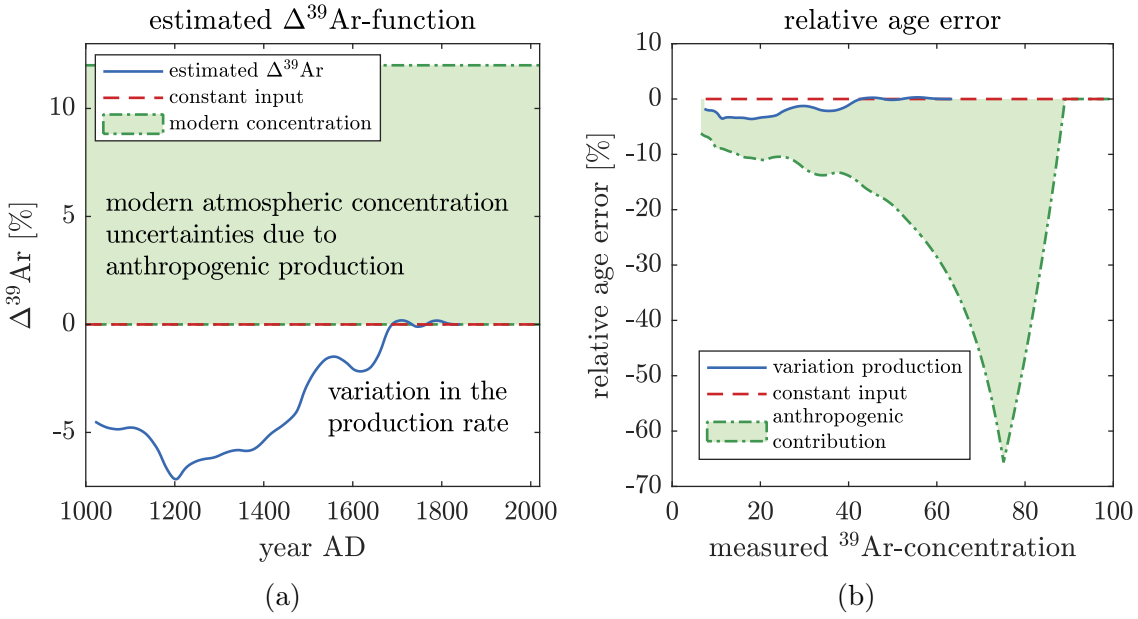

Fig. 1.3.: Potential variations of the ^{39}Ar-input function:
a) From the observed ^{14}C/C deduced variation in the ^{39}Ar-concentration (solid line) (data taken from [23]). There is an upper limit of 12 % for the anthropogenic contribution due to all nuclear weapons tests until 1974 reported in [23], which is the dominant systematic uncertainty.
b) Relative deviation of the calculated age between an ideal constant input function and considering the variable input function from a). The shaded area marks the uncertainty of an additional anthropogenic contribution of up to 12 %, which would influence the reference concentration. For this calculation a linear increase between 1950 and 1974 is assumed.

The specific activity of ^{39}Ar in atmospheric argon was initially measured with proportional counters [27]:

$$1.78(7) \times 10^{-6}\,\mathrm{Bq/cm^3_{Ar(STP)}}\ .$$

This activity corresponds to a relative isotopic abundance of

$$\frac{^{39}\mathrm{Ar}}{\mathrm{Ar}} = 8.1(3) \times 10^{-16}\ .$$

By comparing the measured activity and the measured ^{39}Ar-concentration of a slightly enriched sample used in an intercomparison study (see chapter 5) a slightly lower value was found in this thesis:

$$1.68(7) \times 10^{-6}\,\mathrm{Bq/cm^3_{Ar(STP)}}\ .$$

However, an absolute value of the specific activity of ^{39}Ar in atmospheric argon is not required for ^{39}Ar-dating of environmental samples.

The relative isotopic abundance, together with the expected argon content, gives an estimation of the number of ^{39}Ar-atoms in modern samples, which are listed in table 1.3. The gas content in natural ice depends strongly on the condition of the ice and can vary quite significantly between 10 mL STP and 100 mL STP air per kg of ice. Contrary to water samples where the argon is dissolved, in ice it is present in the form of gas trapped in air bubbles.

Table 1.3.: Expected argon content and number of ^{39}Ar-atoms in different modern samples.

sample type	Ar-volume [mL STP]	number of ^{39}Ar-atoms
1 L STP pure argon	1000	2.2×10^7
1 L STP air	9.34	2.0×10^5
1 L fresh water 10 °C, no salinity, at 1 bar	0.39	∼8500
1 L sea water 5 °C, salinity 35‰, at 1 bar	0.35	∼7600
1 kg of ice	0.5 to 1	1×10^4 to 2×10^4

1.2.3. Detection of ^{39}Ar

A detailed overview of the different detection techniques for ^{39}Ar can be found in [4, 28, 29]. Here, only a short summary is given. The following physical properties of ^{39}Ar are utilised by current detection techniques:

Radioactive decay – Low-Level Counting (LLC)

Since ^{39}Ar is the only significant radioactive Ar-isotope in the atmosphere which decays via β^--decay without γ-radiation and with a maximal energy of 0.565 MeV[22]

$$^{39}\mathrm{Ar} \rightarrow {}^{39}\mathrm{K} + e^- + \overline{\nu}_e \ ,$$

it is possible to distinguish ^{39}Ar from the other Ar-isotopes by its radioactive decay. To eliminate the background induced by present-day atmospheric ^{85}Kr activity, highly purified argon is required with a reduced Kr-content by a factor of at least 10^{-4}. The activity of the argon extracted from one litre of water is only about 0.06 decays per day. Thus, the typically required sample sizes are in the order of 500 mL STP to 2000 mL STP of pure argon corresponding to 1500 L to 5000 L of water and the typical counting times are in the range of 6 d to 60 d [28]. Due to these requirements ^{39}Ar-analyses were limited mainly to groundwater studies, where degassing huge amounts of water in the field is feasible.

So far, almost all ^{39}Ar-measurements in natural samples were conducted in the underground laboratory in Bern 35 m (70 m of water equivalent) below the surface. Furthermore, special radioactively pure construction materials, e.g. lead from a Dutch shipwreck and special selected concrete, are used and an anticoincidence arrangement

reduces the background further [30]. The achieved background level is ∼2 counts/h [31], which is similar to the activity of the argon amount extracted from 750 L of modern water.

Mass – Accelerator Mass Spectrometry (AMS)

AMS is very successfully applied for radio carbon dating. However, there are several technical challenges for ^{39}Ar [32]: The isotopic abundance of ^{39}Ar is more than one thousand-times lower than $^{14}\mathrm{C}/^{12}\mathrm{C} = 1.2 \times 10^{-12}$. Since noble gases do not form any negative ions, it is not possible to employ tandem accelerators, which is the standard technique for ^{14}C. This results in a high background of ubiquitous ^{39}K, which also can not be separated by full stripping, since the atomic number of ^{39}Ar ($Z = 18$) is not higher than that of the isobar ^{39}K ($Z = 19$) [28]. Additionally, a high over-all detection efficiency is required due to the small amount of ^{39}Ar-atoms in environmental samples.

AMS was applied at the ATLAS facility (Argonne National Laboratory) in a proof of principle experiment using an electron cyclotron resonance ion source to generate $^{39}\mathrm{Ar}^{8+}$-ions, which were then accelerated to 232 MeV and finally separated from ^{39}K in a gas-filled spectrograph [32]. The potassium contamination was reduced in the context of the search of ultra low-active argon for liquid argon scintillation detectors. The achieved sensitivity of $^{39}\mathrm{Ar}/\mathrm{Ar} = 4 \times 10^{-17}$, the required sample size of 20 L of water and typical measurement times of ∼10 h [33] are comparable to the current performance and requirements of ArTTA. However, due to the large and expensive required accelerator facility and the further needed improvements addressing the ion source, ^{39}Ar-measurements using AMS are limited to three ocean samples [32].

Atom-optical spectrum, Atom Trap Trace Analyses (ATTA)

Atoms of different elements have a highly diverse atomic energy spectrum and thus interact resonantly at different frequencies. Additionally, there is a small difference in the resonance frequencies of different isotopes of the same element. This isotopic shift is caused by the different masses, charge radii and nuclear spins. By choosing the exact resonance frequency, the desired isotope can be selectively excited, ionised or manipulated.

The selectivity S of an isotope analysis technique is defined in [28] as the ratio of the detection probabilities of the intended isotope and of the contaminant isotopes. The selectivity S_{laser} of a laser-based method scattering one photon can be approximated by assuming a Lorentzian line shape

$$S_{\mathrm{laser}} \approx 4 \cdot \left(\frac{\Delta}{\Gamma}\right)^2 \tag{1.7}$$

where Δ is the frequency difference between the isotopes and Γ is the natural linewidth of the utilised optical transition. The ArTTA utilised optical cycling transition ($1s_5 \rightarrow 2p_9$) at 812 nm has a linewidth of $\Gamma = 2\pi \cdot 5.87$ MHz [34] and the frequency difference between ^{39}Ar and ^{40}Ar is $\Delta = 492$ MHz [3] leading to $S_{\mathrm{laser}} \approx 712$.

However, compared to the atmospheric abundance of ^{39}Ar this selectivity of a single-photon process is not sufficient to distinguish the isotopes. The probability that a photon resonant with ^{39}Ar is scattered by ^{40}Ar (^{40}Ar) compared to the probability that it is scattered by ^{39}Ar (^{39}Ar) is predominant:

$$\frac{p_{^{39}\mathrm{Ar}}}{p_{^{40}\mathrm{Ar}}} = 4 \cdot \left(\frac{\Delta}{\Gamma}\right)^2 \cdot \frac{^{39}\mathrm{Ar}}{^{40}\mathrm{Ar}} \approx 6 \times 10^{-13} \,. \tag{1.8}$$

The selectivity of a multi-step process can be calculated by the product of the selectivities of the single steps. Considering a method including N scatterd photons gives:

$$\frac{p_{^{39}\mathrm{Ar}}}{p_{^{40}\mathrm{Ar}}} = S_{\mathrm{laser}}^{N} \cdot \frac{^{39}\mathrm{Ar}}{^{40}\mathrm{Ar}} = \left(4 \cdot \left(\frac{\Delta}{\Gamma}\right)^2\right)^N \cdot \frac{^{39}\mathrm{Ar}}{^{40}\mathrm{Ar}} \,. \tag{1.9}$$

The probability to detect ^{39}Ar dominates already with $N = 6$ photons. While cooling and trapping an atom in a magneto-optical trap (MOT) for 100 ms around $N = 10^6$ photons have to be scattered, so that the probability to mistake an ^{40}Ar-atom instead of an ^{39}Ar atom is vanishingly low. Utilising the repetition of resonant photon scattering while cooling and trapping the desired isotope in a MOT is the key idea of ATTA and enables an extreme isotopic selectivity.

ATTA was invented by Zheng-Tian Lu et al. and published the first time in 1999 [35], where the basic principle was proven by detecting the two rare krypton isotopes ^{85}Kr ($T_{1/2} = 10.739$ a) and ^{81}Kr ($T_{1/2} = 229$ ka). By now, ATTA has become available for routine measurements of these two isotopes [2]. The current requirements of the state of the art ATTA-system for krypton at the University of Hefei (China) are 1 μL STP (corresponding to 10 kg to 20 kg of ice or water). The atmospheric count rates are 1000 atoms/h for ^{81}Kr and 20 000 atoms/h for ^{85}Kr and typical measurement times are 1-2 h followed by 20 h of flushing with xenon, so that the sample throughput is one sample per day [36].

The first application of ATTA in the geosciences was the analysis and the detection of one-million-year-old groundwater in the Sahara [37]. Since then ATTA for krypton has been applied in several geological studies [38, 39] and also in the context of searching a permanent disposal site for nuclear waste [40]. The first ^{81}Kr-study of ice samples was conducted in Antartica where ice with an age of 120 ka could be identified [41].

ATTA for ^{39}Ar was shown in a proof of principle experiment in [42]. Analysing an atmospheric sample, 12 events were counted in 57 h resulting in a ^{39}Ar-count rate of 0.21 atoms/h, which is far too low for any application in the geoscience dealing with samples at or below the atmospheric ^{39}Ar-abundance. The first application of ATTA for ^{39}Ar was the dating of groundwater samples [43, 4, 44] with ^{39}Ar-count rates of up to 4.1(3) atoms/h. However, due to a detectable ^{39}Ar-contamination embedded in the vacuum system as a consequence of previous optimisation and characterisation of the apparatus with enriched ^{39}Ar-samples, only measurements in throughput configuration (i.e. the sample flows in continuously) were possible

resulting in a required sample size of 0.5 to 1 L STP of pure argon. A sampling of the required water amount of several tons of water was only feasible in groundwater studies. The optimisation and implementation of ^{39}Ar-analyses of a typical sampling size of ∼2 mL STP corresponding to 5 L of water or 2 kg to 5 kg of ice are the subject of this thesis. These improvements enabled the first application of ^{39}Ar in ice and ocean water analysed by ArTTA.

1.2.4. The atomic transition spectrum of argon

The isotopic selectivity of ATTA is based on small isotopic differences in the atomic energy spectra of the different Ar-isotopes. The atomic energy spectra of ^{40}Ar and ^{39}Ar are sketched in figure 1.4. All atomic states are named in this thesis with help of the Paschen notation, which is explained in [45]. Due to the noble gas configuration of argon, the energetically lowest transitions of the ground state are at 105 nm and 107 nm and thus in the XUV-range and not accessible for standard lasers and optics. Therefore, the atoms are transferred partially in a RF-discharge source into the metastable state $1s_5$ with a lifetime of 38 s [46], which is much longer than the time scale for cooling, trapping, and detecting single atoms. For laser cooling the cycling transition $1s_5 \rightarrow 2p_9$ with 812 nm is utilised. This wavelength can be easily addressed by standard diode lasers. Additionally, the quench-transition $1s_5 \rightarrow 2p_8$ at 801 nm can be used to deexcite isotope-selectively ^{40}Ar from the metastable state.

The energy levels of ^{39}Ar are shifted due to the different masses by −94.6 MHz relatively to ^{40}Ar. All stable isotopes have a vanishing nuclear spin and thus behave similarly. By contrast ^{39}Ar has a nuclear spin of $I = 7/2$ and consequently has a complex hyperfine spectrum. The transition from $F = {}^{11}/_2$ to $F = {}^{13}/_2$ is a closed transition due to the selection rule $\Delta F = 0, \pm 1$. However, due to off-resonant excitation into $2p_9(F = {}^{11}/_2)$ and a subsequent decay into $1s_5(F = {}^{9}/_2)$, ^{39}Ar-atoms can be lost from the cooling cycle. Therefore, additional sideband frequencies (repumpers) are used to bring the ^{39}Ar-atoms back into the cooling cycle. The exact energy spectrum of ^{39}Ar was measured in [47] and slightly corrected values are reported in [48].

The interactions of argon with light and magnetic fields are the basis of all atom-optical methods and thus essential for laser cooling and trapping. Since an exact knowledge thereof is not necessary to understand this thesis, it is referenced at this point to the general introduction in [34] and the specific presentation for argon in [4].

1.3. Preparation of the samples

Water and ice samples must be degassed and the argon purified in advance before they can be analysed by ATTA. For this purpose two different systems were developed at the Institute of Environmental Physics in Heidelberg. Huge samples are degassed with help of a commercial membrane conductor (maximal water flow rate 183 L min^{-1}) and the argon is separated by chromatographic columns filled with zeolite (LI-LSX).

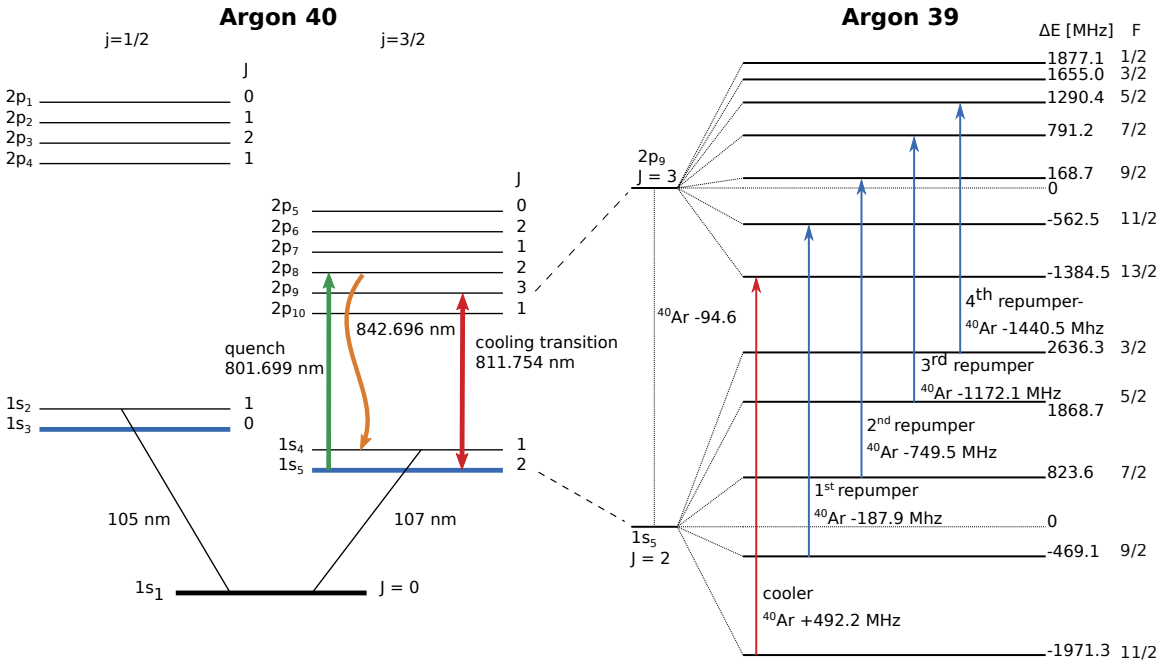

Fig. 1.4.: Atomic energy spectrum of ^{40}Ar (left) and ^{39}Ar (right) with the cooling transition at 811.754 nm and the quench transition at 801.699 nm (adapted from [4]). An overview of all wavelengths and transition strengths can be found in appendix A.3.

With this system gas samples of more than 69 L STP can be processed in one run, with a final argon purity of up to 99.6 % and a total Ar-recovery of up to 99.2 % [49].

With the reduction of the required sample size down to a few mL STP of pure argon, also a new degassing and purification system for small water and ice samples was developed in the scope of [50]. All environmental samples analysed in the context of this thesis were processed with the system sketched in figure 1.5. The ocean samples are shaken for a higher extraction yield and the ice samples are melted in an evacuated stainless steel container. Beside this difference, the preparation of ice and water samples is identical. The extracted gas is transferred to an activated charcoal trap (ACT) and water vapor is removed inside a water trap on the way. In a second step, the extracted gas is transferred to the sample container. Nitrogen and oxygen are removed by a titanium sponge getter heated to 900 °C and hydrogen is absorbed by a second getter at room temperature.

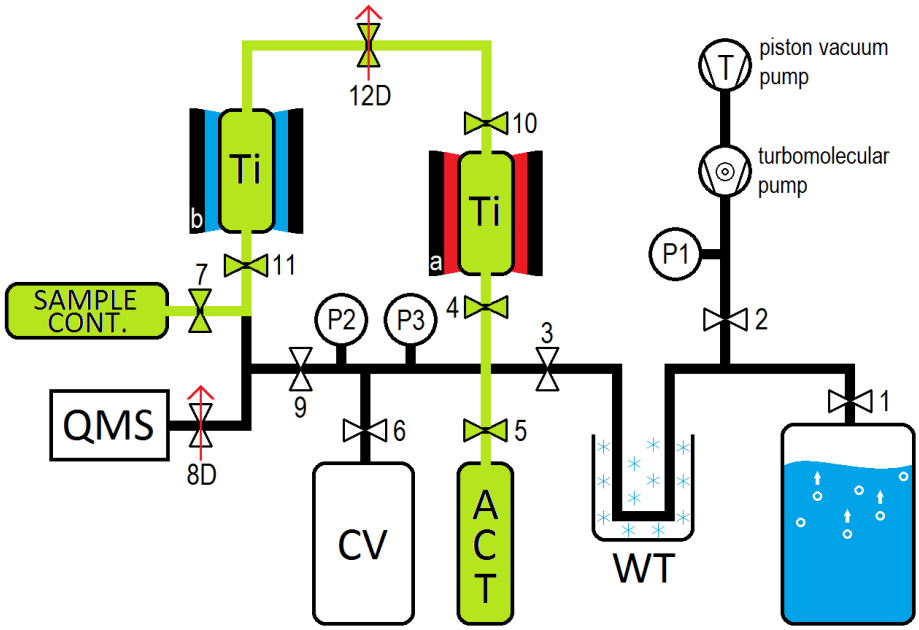

Fig. 1.5.: Sketch of the Ar-extraction and purification system used for the ice and ocean samples: The sample is purified after passing the water trap **(WT)** and two titanium sponge getters. The first getter **(a)** operates at a temperature of 900 °C to remove of nitrogen and oxygen, the second getter (b) is at room temperature to absorb hydrogen. The imaginary path of the gas during the purification step is coloured in green (graphic taken from [50]).

The achieved argon recoveries are >97 % and typical purities >99 %, which is sufficient since ArTTA is not sensitive to contaminants, particularly the time consuming separation of krypton from argon which is necessary for LLC can be let out.

1.4. ^{39}Ar-reference samples

The cosmogenic ^{39}Ar concentration in the atmosphere defines the atmospheric reference and a highly depleted ^{39}Ar-free, blank sample separated from a natural CO_2-source is used to quantify possible contaminations. Both reference samples were employed throughout the entire thesis and can be used to generate samples with well defined concentrations between 0 pmAr[2] and 100 pmAr. Thus, they are introduced in more detail.

Atmospheric reference

Commercial industrial argon 4.6 (purity ≥99.996 %), which is used for inert-gas welding, is our atmospheric standard. This argon is produced industrially by fractional distillation of liquid air and is easily available in huge amounts [51]. To ensure that there is no isotopic fractionation during the production, the ratio of the two stable isotopes ^{40}Ar and ^{36}Ar was measured with a precision noble gas mass spectrometer for noble gas temperature analyses (similar to [52]):

$$\frac{^{36}\mathrm{Ar}}{^{40}\mathrm{Ar}} = 3.337(19) \times 10^{-3} \; . \tag{1.10}$$

There is no indication for a significant discrepancy from the literature value of $^{36}\mathrm{Ar}/^{40}\mathrm{Ar} = 3.3785(60) \times 10^{-3}$ [53]. The complete noble gas composition of the atmospheric standard is listed in appendix A.2.

^{39}Ar-free sample

Huge amounts of low-radioactive argon are needed for the construction of liquid argon scintillation detectors, which are designed to detect Weakly Interacting Massive Particle (WIMP)-type dark matter directly [54]. As discussed in 1.2.1, both ^{40}Ar and ^{39}Ar can be produced in the underground. In the earth's upper mantle, where the uranium and thorium concentration can be up to thousand-times lower compared to the crust, the ^{40}Ar-production is dominant and low activity argon can be found.

The underground argon sample was provided by Henning O. Back from the DarkSide collaboration and originates from the Kinder Morgan CO_2-plant (Doe Canyon field) in Cortez, Colorado. The raw CO_2-gas is processed by a vacuum pressure swing absorption unit, which increased the Ar-concentration in the gas mixture from 400 ppm to 600 ppm up to 3 % to 5 % [54]. In a second step the argon is separated from the gas mixture through a cryogenic distillation column and purified to 99.95 % with 500 ppm remaining nitrogen [55].

An upper limit for the ^{39}Ar-concentration is given by 0.65 pmAr, based on measurements with 0.56 kg of liquid argon in a low-background single-phase liquid argon detector [25]. Due to its geologic origin the stable isotope composition also differs significantly from the one of a natural sample and the proportion $^{36}\mathrm{Ar}/_{^{40}\mathrm{Ar}} = {}^{1}/_{13300}$

[2] pmAr: percent modern argon.

is 45-times lower compared to the atmospheric one of $^1/_{295.5}$ [25]. This fact can be utilised to study contamination and cross sample contamination effects (see section 3.3.2).

Artificially mixed samples

By mixing atmospheric and ^{39}Ar-free samples, arbitrary concentrations between 0 pmAr and 100 pmAr can be generated with help of the system depicted in figure 1.6. Two identical volumes **1** (∼500 mL) are filled one after the other with the ^{39}Ar-free and the atmospheric sample to the desired pressure p_{atm} and $p_{^{39}\text{Ar-free}}$, which can be measured with the absolute pressure gauge **2**. Afterwards, the two samples are mixed. The gas inflow of the atmospheric sample is regulated with help of the dose valve **3**. The ^{39}Ar-free sample can be connected to the sample port **4**, which is also used for the sample cylinder of the resulting mixed sample. The new, mixed sample is transferred cryogenically into the sample container. The system must be pumped with a pumping stage in between the different steps. The ^{39}Ar-concentration in pmAr of the mixed sample is given by

$$c_{\text{mixed}} = \frac{p_{\text{atm}}}{p_{\text{atm}} + p_{^{39}\text{Ar-free}}} \,. \tag{1.11}$$

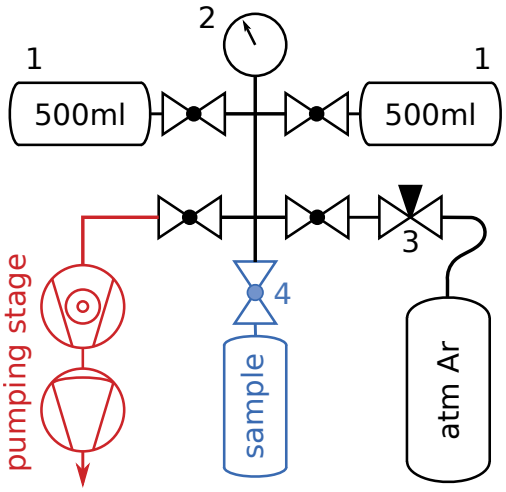

Fig. 1.6.: System for precise sample mixing: **1** two identical volumes of ∼500 mL, **2** absolute pressure gauge, **3** dose valve, and **4** sample port for ^{39}Ar-free sample and sample cylinder.

1.5. Application of ^{39}Ar

Due to the enormous sample sizes required for LLC, up to now the only routine analysis method for ^{39}Ar, the main application for ^{39}Ar-studies in the geosciences

was limited to groundwater research. Nevertheless, especially in the early days, some ^{39}Ar-measurements of ice and ocean samples exist. In addition to that there are many interesting fields of application to which ^{39}Ar-measurements can contribute. A selection of them is presented in the following.

Groundwater

The knowledge of the mean residence time of groundwater after isolation from the atmosphere (groundwater age) is fundamental in hydrological science for studying groundwater aquifers and resources. The tracer ^{39}Ar was applied in many groundwater research projects using LLC (e.g. for climate reconstruction [56]) and the first application of ArTTA was a groundwater study, too [44]. However, ^{39}Ar dating of groundwater can be complicated by subsurface production, particularly in bulk granite rich in uranium and thorium where an up to 16-times the atmospheric ^{39}Ar abundance was measured [57].

However, the production of nucleogenic ^{39}Ar can be also employed to enable a new chronometer of fluid migration in the earth's crust and allows for a much wider time range than only using the radioactive decay of cosmogenic ^{39}Ar. Since both ^{39}Ar and ^{40}Ar are produced in the underground, but ^{39}Ar reaches a production-decay equilibrium whereas ^{40}Ar accumulates, the ^{39}Ar/^{40}Ar-ratio decreases with time [58].

Ice

^{39}Ar studies on ice were limited so far due to the enormous effort for sampling to only a few measurements conducted on samples from Greenland, Antarctica and Devon Island between 1969 and 1974. For developing and cross-checking the ^{39}Ar-dating method initially, these samples were used as blank (^{39}Ar-free samples extracted from ice older than 1000 years) or as samples with known concentration obtained from ice cores, which were dated by δ^{18}O stratigraphy and ^{31}Si [27]. For sampling a melting probe system was lowered down into to a borehole to the desired depth. This section of the borehole was isolated and evacuated and finally the ice was melted and degassed. In total about 700 kWh of electrical power were needed to melt about 5×10^3 kg of ice with a rate of 90 kg h^{-1}. The complete sampling procedure for one sample took more than 5 days [59].

This thesis presents the first results of ^{39}Ar measured in ice blocks of about 5 kg sampled with a chainsaw. A further reduction in the sample size might allow for ^{39}Ar dating of ice cores. A glacier system with a well formed stratigraphy can then be used to study the historical ^{39}Ar-concentration in the atmosphere, similar to tree-rings for ^{14}C or the isolation process of the embedded gas from the atmosphere. Such an ^{39}Ar-record would reduce the uncertainties of the ^{39}Ar-input function shown in figure 1.3a significantly. But ^{39}Ar can especially be used to date Alpine glacier ice or snowfields, which can not be dated with help of stratigraphy methods since they have no clear layering.

Ocean circulation and ventilation

The time scale of ^{39}Ar and the fast equilibration at the ocean surface make ^{39}Ar to a nearly ideal tracer to investigate less ventilated water masses in the deep ocean which is essential for calibrating and benchmarking ocean circulation models. So far 125 ocean samples were analysed by LLC and the obtained ^{39}Ar-concentrations are in the range of 6 pmAr to 100 pmAr [60], whereas ^{14}C only varies from 100 % to 86 % [28]. The benefit of a globally gridded ^{39}Ar-data set was shown several times based on the spare historical data set [61, 62].

Due to the requirements for LLC (1000 L of water, 6 weeks of counting) ^{39}Ar-analyses in the ocean were discontinued for the last 25 years. The main goal of this thesis was the optimisation of the ArTTA-system to enable sampling with standard 10 L-Niskin bottles and the main result are the three ^{39}Ar-depth profiles taken in the eastern tropical North Atlantic oxygen minimum zone.

Further applications

The exposure of fast neutrons during the nuclear explosion in Hiroshima was estimated utilising argon samples separated from biotites of granite gravestone, which were activated by the production of ^{39}Ar due to the capture of fast neutrons on potassium [63]. Ultra low active, ^{39}Ar-free argon is required in huge amounts for the construction of liquid argon scintillation detectors, which are designed to detect directly Weakly Interacting Massive Particle (WIMP)-type dark matter [54].

1.6. Tracer age and transit time distribution

The tracer ages as defined in equation 1.2 and 1.3 are not the fundamental timescale of the water flow, as soon as the water parcel is a mixture of different water masses or if the transport is diffusive. In this case different tracers can yield to different inferred ages. In this section a more general concept describing the history of the sampled water with help of a transit time distribution (TTD)[3], which describes the distribution of transit times for transport from the surface to a specific point in the interior of a fluid system, is introduced. The idea was the first time introduced to describe the transport in the stratosphere [64], but is now applied to different fields (e.g. ocean [65, 66, 67], lake [68], groundwater [69]). This section directly follows the argumentation of [7].

The concentration $c(r, t_0)$ of a tracer at the interior location r at time t_0 is given by

$$c(r, t_0) = \int_0^\infty c_0(t_0 - t) e^{-\lambda t} \mathcal{G}(r, t) \mathrm{d}t \tag{1.12}$$

where $c_0(t)$ is the tracer input function at the surface and the factor $e^{-\lambda t}$ corrects the radioactive decay of radioactive tracers with a decay rate of $\lambda = -\frac{\ln 2}{T_{1/2}}$. The

[3]The TTD is sometimes also referred as age spectrum or age frequency distribution.

TTD $\mathcal{G}(r,t)$ describes the mass fraction of the fluid parcel, which was isolated from the surface at time t ago, and mathematically spoken the TTD is a type of Green's function. This approach assumes steady state conditions (a time-independent flow) and a spatially uniform input function.

Provided $c_0(t)$, λ and $\mathcal{G}(r,t)$ are known, the concentration time series can be computed from equation 1.12. A common analytical model function to describe the TTD is the Inverse Gaussian (IG) distribution

$$\mathcal{G}(r,t) = \sqrt{\frac{\Gamma^3}{4\pi\Delta^2 t^3}} \exp\left\{-\frac{\Gamma(t-\Gamma)^2}{4\Delta^2 t}\right\} \tag{1.13}$$

with two free parameters, the mean age γ and the width Δ. By varying these two parameters a wide range of distributions with different shapes can be described (see figure 1.7). The IG also describes the TTD for a one-dimensional flow model with a constant advective velocity and diffusivity (Peclet number equals to Γ^2/Δ^2) [70]. For $\Delta/\Gamma \ll 1$ the transport is dominated by advection and the TTD is more symmetric with a maximum near the mean age. With increasing Δ (diffusion becomes more dominant) the TTD broadens, has a young maximum and a long tail. The IG function is not interpreted in terms of a one-dimensional flow typically, but is used due to its simple analytical form for approximating a wide range of TTDs.

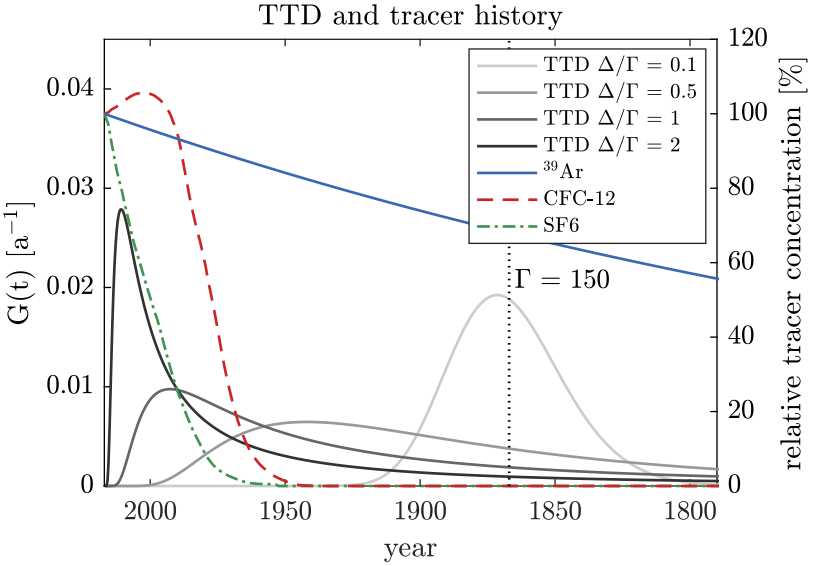

Fig. 1.7.: Different TTDs described by the Inverse Gaussian distribution (equation 1.13) with the same mean age $\Gamma = 150\,\mathrm{a}$, but different widths Δ. The radioactive decay of ^{39}Ar and the input functions of CFC-12 and SF_6 are plotted for comparison (concentration of the northern hemisphere, taken from [8]). The TTD can be constrained by utilising two tracers addressing different time windows.

Different tracers weigh different features of the TTD differently, so that they yield different tracer ages in general. Figure 1.8a shows the different tracer ages of ^{39}Ar and CFC-12 as function of the mean age Γ and width Δ of the TTD. The two tracer ages inferred from ^{39}Ar and CFC-12 can differ by several hundreds of years (figure 1.8b). If no further information about the TTD is available, the typical standard parametrisation is $\Delta/\Gamma = 1$ [71, 72]. However, by analysing two different tracers with significantly different time ranges, the two parameters of the IG can be determined and the TTD constrained.

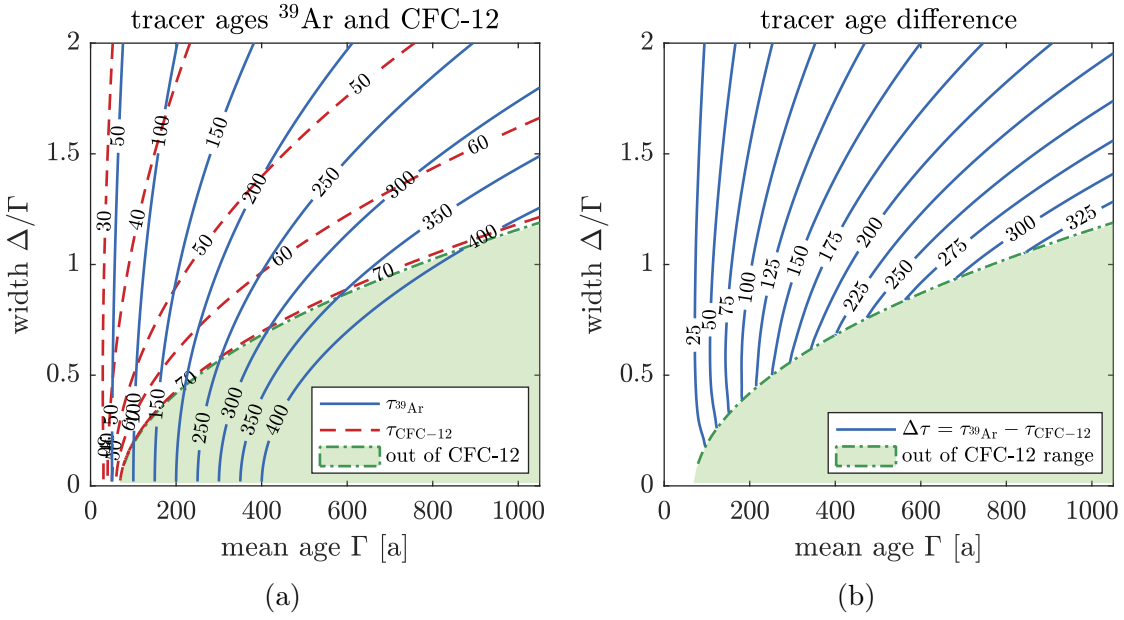

Fig. 1.8.: **a)** Tracer ages of ^{39}Ar and CFC-12 as a function of the mean age Γ and width Δ of the TTD. Especially if the lines of constant age of two tracers intersect nearly orthogonally, the mean age Γ and the width Δ/Γ can be determined by this tracer couple.
b) Difference of the tracer ages between ^{39}Ar and CFC-12.
In the shaded green area above a CFC-12 tracer age of 70 a, the CFC-12 concentrations are below the detection limit.

The mixing of to different water masses can result in a bimodal TTD, which is often described by a linear combination of two IGs

$$\mathcal{G} = \alpha \cdot \mathcal{G}(\Gamma_1, \Delta_1) + (1 - \alpha) \cdot \mathcal{G}(\Gamma_2, \Delta_2) \,, \tag{1.14}$$

whereas α parametrises the proportion of the two water masses. Since this model is not applied in the context of this thesis it is not treated in more detail.

The knowledge of the TTD is the starting point of many considerations and can be used to calibrate and benchmark ocean models or to calculate the concentration of tracers which were not measured or can not be measured directly.

2. The ArTTA-Apparatus

Most of the previous theses of the ArTTA-group focus on the characterisation of the atom beam and its manipulation by atom optics. Since there were only few updates during the last years, this thesis summarises the basic functional principle of the atom-optical ArTTA-apparatus and concentrates on the changes since the last thesis [4]. For a detailed description it is referred to the following previous theses [45, 73, 3, 43, 4], where the characterisation and simulation of all atom-optical components are exhausted. The laser system, however was rearranged completely using mainly the existing components to improve the stability and to simplify and speed up the maintenance.

In former times highly enriched samples with ^{39}Ar abundances as high as 10^{-9}, which is about one-million-times higher than the natural one, were used to characterise and optimise the whole system [3]. There is still a detectable contamination embedded in the vacuum system left and outgassing ^{39}Ar can accumulate in the sample during the measurement process. Because of this problem all vacuum parts, which might be in contact with fast ions from the source, had to be replaced by new ones. In the context of this renewal the gas throughput and the background pressure in the vacuum system were optimised, which made almost a doubling of the ^{39}Ar-count rate possible. Additionally the system was upgraded for operation with small sample sizes. Due to those major changes the vacuum system is presented in all details in the second part of this chapter.

For a reliable ^{39}Ar measurement it is indispensable to have a stable system during a long period of time. To reduce the influence of weather changes and temperature fluctuations the laboratory was insulated and a temperature stabilisation was constructed in the scope of this thesis. More details can be found in appendix B.2. To ensure the stability of the system during a measurement around 35 parameters are monitored and recorded including the locking signal of all four lasers, the two beat lock frequencies, the laser powers of the atom-optical components, a Fabry–Pérot interferometer signal for mode hop detection and the atom flux. The monitoring system of the experiment was initially developed in [43] and updated to the rearranged laser system.

2.1. Atom optics

An overview of the atom-optical apparatus is shown in figure 2.1. The atoms are excited by the RF-discharge source, which is cooled with the help of liquid nitrogen to enhance the efficiency [4] and to reduce the initial velocity spreading of the atom beam. The metastable atoms leave the source with a mean longitudinal velocity of $323\,\mathrm{m\,s^{-1}}$ and the width of the radial velocity distribution is $\sigma_r \approx 85\,\mathrm{m\,s^{-1}}$ [74]. Therefore the

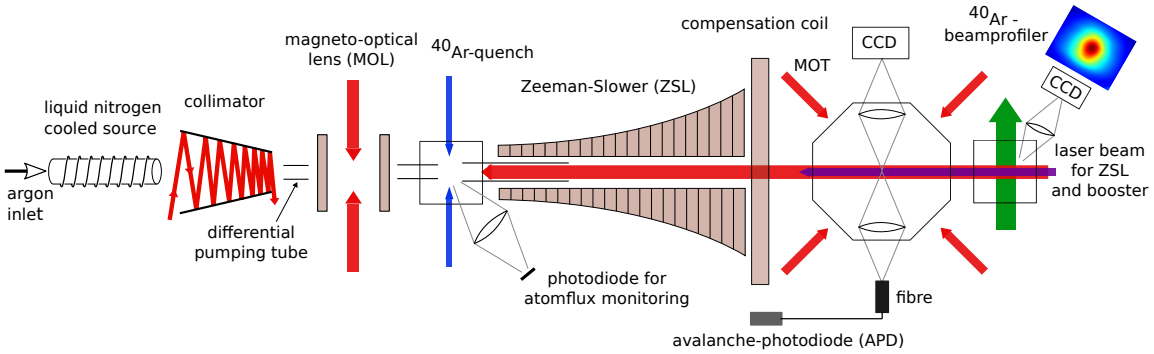

Fig. 2.1.: Overview of the atom-optical components of the ArTTA-appartus: For more details it is referred to the text (sketch adapted from [4]).

atom beam has to be collimated directly after the source. The magneto-optical lens (MOL) slows the atom further down transversally and focuses the beam inside the magneto-optical trap (MOT) chamber. The laser light of the ^{40}Ar-quench deexcites isotope-selectively almost all (98.8 %)[1] metastable ^{40}Ar-atoms via a transient state to the ground state. Without the quench off-resonant excitations of untrapped ^{40}Ar-atoms inside the MOT-chamber double the background light of the atom detection. The Zeeman slower (ZSL) can slow down atoms with a maximal longitudinal velocity up to 610 m s^{-1}. The final velocity of the Zeeman slower is $\sim$ 70 m s^{-1} and is chosen consciously above the capture velocity of the MOT (around 10 m s^{-1}) to prevent the atom beam from diverging rapidly at the end of the ZSL and to collide with the vacuum walls. An additional laser frequency, named Booster, builds a second longitudinal slowing stage together with the rising slope of the magnetic field inside the MOT chamber. There, the atoms can be already refocused by the MOT and losses due to the divergence of the atom beam are reduced significantly. The MOT is the central part of every ATTA-experiment. For trapping an atom in the order of 10^6 resonant photons have to be scattered, which is the fundamental basis of the high isotopic selectivity of ATTA. Single trapped atoms can be detected by their own fluorescence light inside the MOT either with the help of the avalanche-photodiode (APD) with a high time resolution or spatially resolved on the CCD camera from the opposite side. The ^{40}Ar-beamprofiler is a diagnostic tool behind the MOT-chamber. A thin sheet of light excites the atom beam in a small area which is monitored by a camera. A picture of the cross section of the atom beam can be made thereby, which allows a precise alignment of the collimator and MOL. Three differential pumping tubes (DPT) together with seven turbo molecular pumps build up a pressure gradient from 5.2×10^{-6} mbar in the source chamber down to 1.6×10^{-7} mbar inside the MOT.

In the following all atom-optical components are described in more detail, starting with the source and following the way of the atoms through the apparatus. Here the focus is put on changes since the last PhD-thesis at the ArTTA experiment, and not on another complete characterisation of all atom-optical components.

[1] Measured with the beam profiler.

Liquid nitrogen cooled metastable argon source

To make argon or more general noble gas atoms accessible for laser cooling with commercial lasers, they have to be excited into a metastable state (see transition scheme 1.2.4). In comparison to krypton, which can be transferred optically via a transient level into the metastable state by a vacuum-ultraviolet (VUV) lamp with 123.6 nm and a second laser beam at 819 nm [75], this is currently not possible for argon with the available technology. The particular challenge lies in the fact that the corresponding transient level $1s_4$ in argon is with 107 nm slightly more energetic, which makes it much more difficult to find a capable and persistent transparent material for the construction of the VUV lamp.[2]

Thus the common way is to use discharge sources. A compilation and comparison of different types can be found in [3]. In the ArTTA-apparatus the atoms are excited into the metastable state inside an inductively coupled plasma driven by a RF-discharge at 153 MHz. The RF-signal is generated by a 100 W-amplifier. A sketch of the current source is depicted in figure 2.2. The coil is wound from a Kapton-insulated copper wire. The effective length of the wire corresponds approximately[3] to $\lambda/2 = 0.93\,\mathrm{m}$. The last three windings are planar to enhance the plasma at the end of the source tube, where the critical area of production is. The source tube is made out of Alumina (Al_2O_3 ceramic), which has a high thermal conductivity compared to other ceramic materials. The inner and outer diameter of the source tube are 10 mm and 15 mm, respectively.

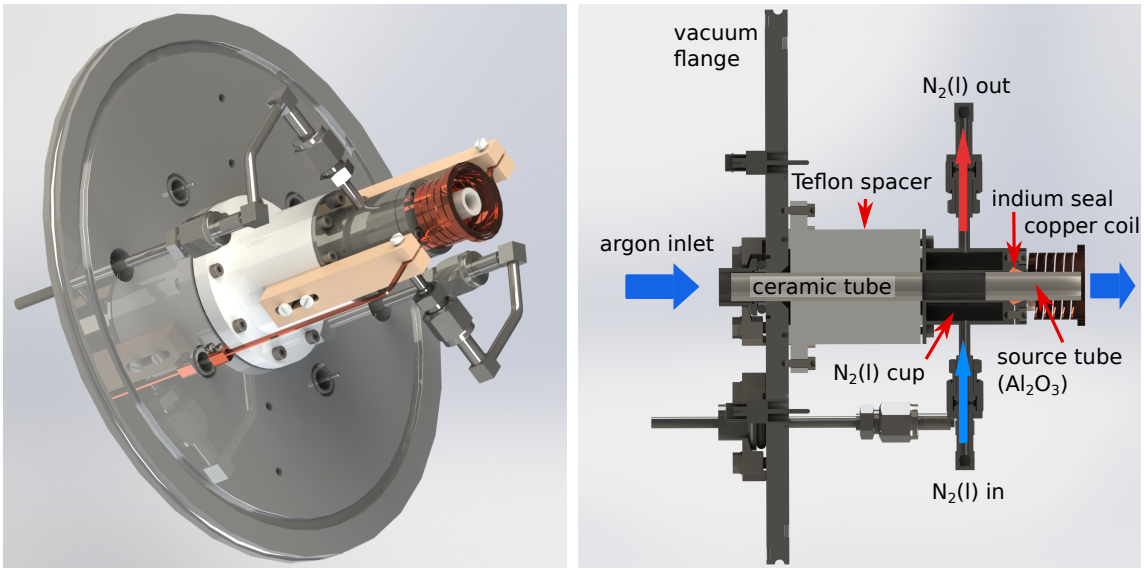

(a) Isometric representation (b) Cross section

Fig. 2.2.: Drawing of the liquid nitrogen cooled metastable argon source.

[2] Even for krypton this excitation scheme bears several technical difficulties, which is why currently all existing Kr-ATTA setups except for [75] use RF-discharges.
[3] Considering a velocity factor of 0.951.

Cooling with liquid nitrogen at 77 K enhances the efficiency of the source by a factor 2 to 3 [4]. An indium wire builds the thermal contact between the source tube and the stainless steel cup, which is flowed through by liquid nitrogen. The cup itself is insulated by a Teflon spacer from the vacuum flange. To dissipate the 100 W of the RF-discharge at least 53 L d^{-1} of liquid nitrogen are vaporised. However, the typical consumption of the current system is in the range of 120 L d^{-1} to 150 L d^{-1} due to thermal and transportation losses. For a stable operation it is essential to refill the liquid nitrogen container without any interruption of the cooling and operation of the source. For this requirement a cooling system with one storage and one transport tank, each with a capacity of 250 L, was constructed, which is sketched in figure 2.3a. A small constriction tube inside the pipe reduces the flux of liquid nitrogen. Otherwise the pressure in the storage tank, which determines the flux, would be much too low for stable regulation and variations in the filling level of the tank would influence the cooling of the source strongly. The pressure in both tanks is regulated by vaporising a small amount of liquid nitrogen. Refilling the storage tank takes about 30 min and during that time the exhaust must be open to dissipate any forming nitrogen gas. One possible improvement of the liquid nitrogen cooling might be to measure the temperature of the source and controlling the liquid nitrogen flux actively.

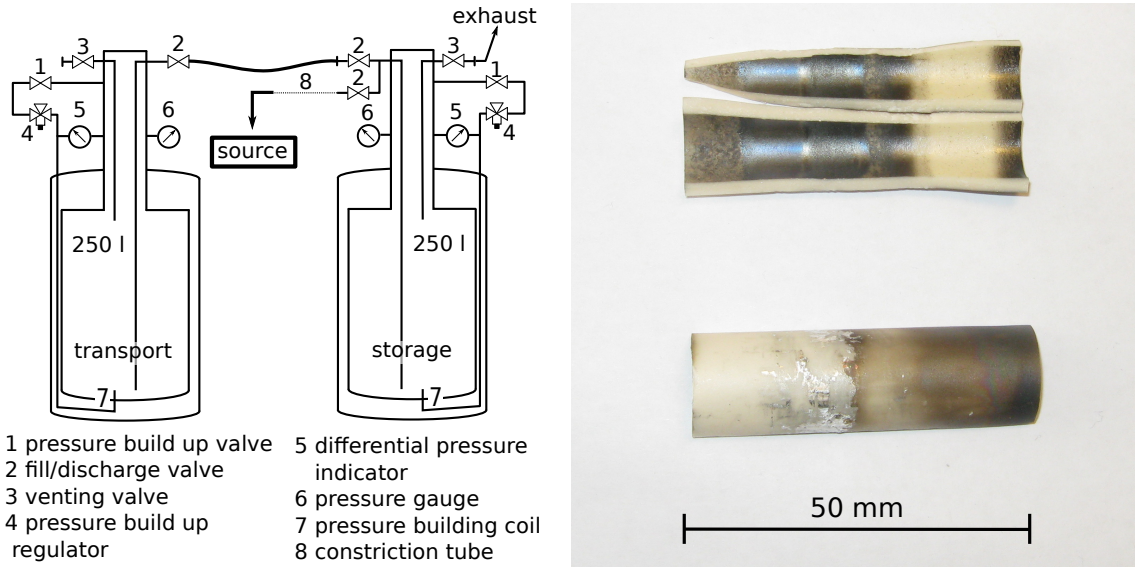

(a) (b)

Fig. 2.3.: **a)** Liquid nitrogen cooling system: For simplicity all safety components are not shown.
b) Forced open source tube: The upper two parts show the inside of the tube, the lower one the outside. The silver parts are remains of the indium seal. In this area of high thermal contact the deposition inside the tube is especially strong.

The calculated efficiency of the cooled source is only around 2×10^{-3} [4], which makes it the component of the ArTTA-apparatus with the highest potential of improvements, but its durability is of the same importance. After around 1000 h of operation the ceramic tube is covered by a thin conductive layer of a black material (picture 2.3b), which might be carbon from the stainless steel and which hinders the source to ignite. Therefore the ceramic tube has to be replaced frequently. An oxygen discharge on a regular basis might rejuvenate the discharge source, which is discussed in chapter 6.2.2. Another weak spot is the insulation of the copper wire, which degenerates at the front windings in the plasma bombardment. The exact reason has not been clarified yet, but small damages of the insulation hinder the coil from igniting the plasma. The lifetime of the coil can be extended by a layer of Kapton tape covering the wire. Any Teflon parts, which can be hit by ions from the plasma, were proven to be very problematic, since they induce a rapid damage of the reflection coating of the collimator mirrors. A possible explanation is, that the energetic ions lead to a release of extreme reactive fluorine radicals out of the Teflon (fluoropolymer), which then can react with the Ta_2O_5/SiO_2 optical high reflective coating. A damage of the coating and areas on the mirrors with a significantly reduced reflectivity are the consequence. Therefore the original Teflon mounts for the coil were replaced by Rescor 902 (machinable ceramic) and the Teflon spacer was lined by an Alumina tube.

Unfortunately most of the other attempts to improve either the efficiency or the durability of the source did not work out. For example a continuous ceramic tube, which also covers the inside of the stainless steel cup and thus prevents it from any contact with the plasma, reduced the metastable atom flux by 30 %, since the thermal contact to the argon gas was not sufficient any more. There were no further improvements possible by different diameters of the source tube. Any metal parts, which are not grounded reduce the efficiency significantly, even if they are some centimetres away from the RF-coils. For example metal thread inserts in the Teflon spacer for more robust screw connections had to be removed again.

Collimator

The collimator design implemented in the ArTTA-apparatus is treated in more detail in [45, 4]. It is realised with tilted mirrors to keep the atoms in resonance during the entire collimation. Thereby, the changing Doppler-shift is compensated by a corresponding change in angle between the atom and the laser beam. The maximum radial velocity, which can be collimated, is, for the parameter given in the experiment, around $40\,\mathrm{m\,s^{-1}}$. The orientation of the collimator defines the direction of the atom beam. Thus the complete collimator is mounted on a giant holder, which can be tilted from outside the vacuum via mechanical feedthroughs.

Since the collimator is next to the source and exposed to fast ions, it was highly contaminated by highly enriched ^{39}Ar-samples and had to be replaced by a new one. The rebuild is nearly an exact copy of the previous one. However, two major changes were made to the collimator during this process:

Simulations indicate that the entry angle of the laser beam into the collimator must be as steep as possible. This angle is constrained by the geometry of the collimator but it was especially paid attention to this angle during the adjustment of the new collimator. Thus the optimal detuning of the cooling laser decreased by 8.8 MHz to −4.2 MHz. This is consistent with the calculation in [4] and should induce an increase of the collimator gain. The current collimator gain measured with the ^{40}Ar-beam imaging is about 120 and in combination with the magneto-optical lens about 180. However, these values can differ for the ^{39}Ar-count rate.

The adjustment of the collimator is very critical and beside the Zeeman slower it is the atom-optical component with the highest impact on the ^{39}Ar-count rate. Small changes end up in a significant decrease or instabilities. Particularly, two opposite mirrors have to be perfectly parallel aligned in lateral direction, otherwise the laser beam deviates from the centre and drops off the mirrors already before its end, with the consequence of a decline of the collimator efficiency. The collimator is next to the cooled source and is exposed to high variations in temperature. One mirror of each pair is fixed and can only be adjusted when the vacuum is open. So far it was only possible to change the tilt of the mirrors from outside the vacuum with the help of two stepper motors and the second axis was fixed. To have the possibility of a complete readjustment of the mirrors in respect to each other, the collimator was updated by two additional motors, as shown in figure 2.4.

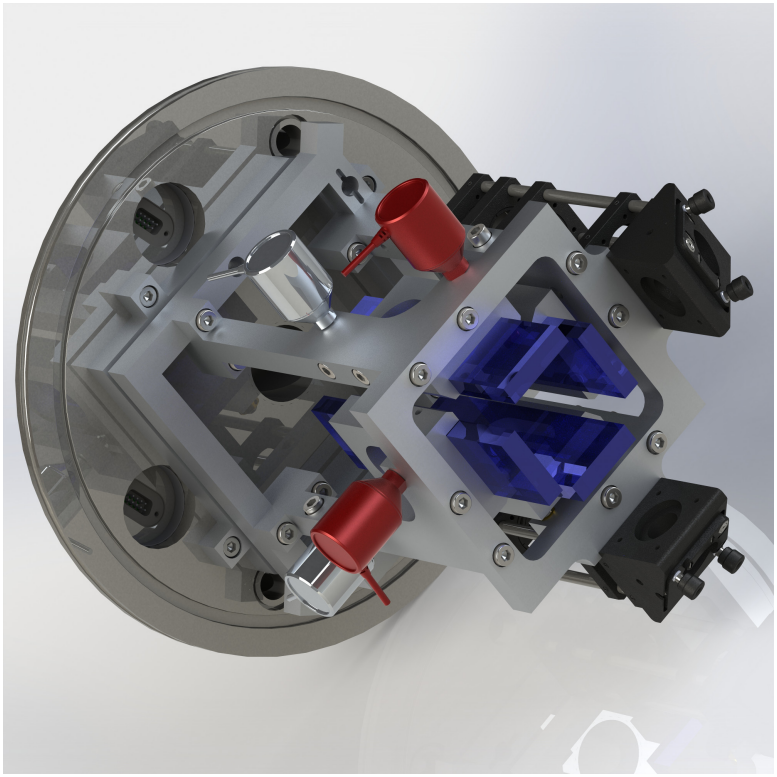

Fig. 2.4.: Sketch of the collimator: The collimator was extended by two stepper motors (red) to get two additional degrees of freedom to compensate maladjustment.

The problem of a distortion due to temperature variations can be compensated by the new degree of freedom up to a certain level, but it is still present and might be the major source of instabilities and drifts of the ^{39}Ar-count rate. The development of the ^{40}Ar-flux, measured with the beam profiler during the first 8.5 h after the cooling has been switched on, is plotted in figure 2.5. It seems that the flux saturates after 10 hours. But sometimes even after days of cooling the flux drops again and a readjustment is necessary. Since the construction does not allow to readjust all degrees of freedom, for example the fixed mirror in respect to the entry angle of the laser beam, it is not always possible to come back to the optimum and a reduction and variation in the ^{39}Ar-count rate must be accepted.

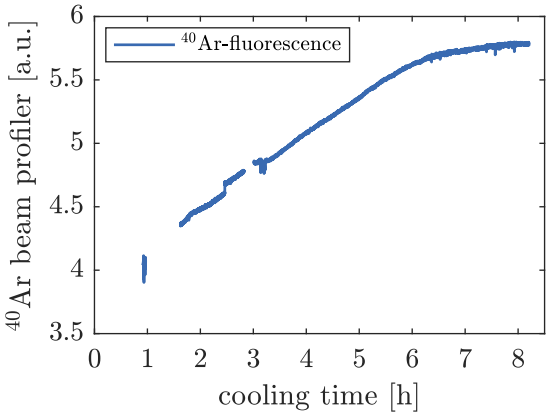

Fig. 2.5.: ^{40}Ar-fluorescence of the atom beam profile in the first 8.5 h of cooling the source: The source is switched on after 40 min. Some data points in between are missing to due adjustments of the apparatus.

For a future design it might be a good idea to eliminate the collimator mount and provide both degrees of freedoms by an actuator at each mirror. Then the collimator would be directly connected to the vacuum flange and should be less critical to thermal variations and vibrations from the big turbo pumps. The adjustment of the orientation of the atom beam would be still possible due to the additional actuators.

Magneto-optical lens (MOL)

The magneto-optical lens (MOL) is a second stage of transversal cooling. Its task is to collimate the atom beam further and to focus it into the centre of the MOT. Atoms which are off the central axis are slightly pushed towards the centre, so that it is less likely to loose them out of the beam. The MOL can be considered as a 2D-MOT and the simple realisation in the ArTTA-apparatus consists of two coils in Anti-Helmholtz configuration along the beam axes. The laser beams are retroreflected and fed by the same laser frequencies as the MOT. Thus an independent optimisation and adjustment is only possible to a limited extend. The MOL enhances the ^{39}Ar-count rate by about 25 % [43].

Zeeman slower (ZSL)

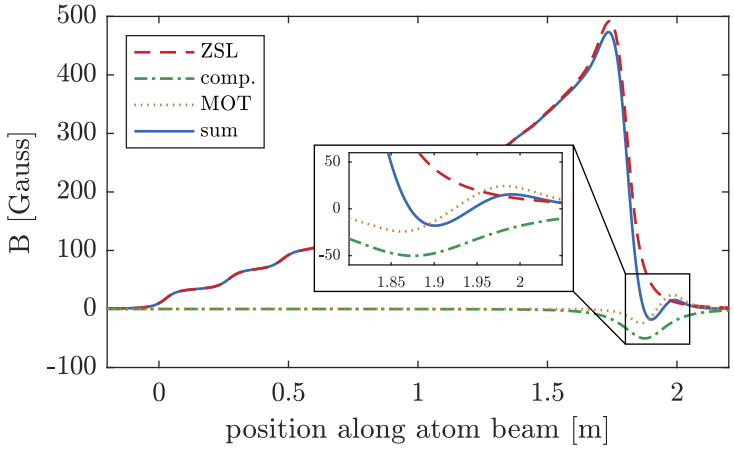

Fig. 2.6.: Calculated magnetic field of the Zeeman slower, compensation coil and MOT. The coil currents are: $I_{ZSL} = 11.35\,A$, $I_{comp.} = 4.5\,A$ and $I_{MOT} = 10.3\,A$. The inset zooms in the area of the MOT, which is used from the Booster to form a second Zeeman slowing stage with the rising slope at the end of the MOT.

The Zeeman slower is designed as an increasing field slower as shown in figure 2.6. A compensation coil is installed to generate a fast decline of the magnetic field behind the Zeeman slower and a vanishing field at the trap centre. The maximal velocity, which can be addressed by the slower is around $610\,m\,s^{-1}$, which includes in principle about 99.4 % of the longitudinal velocity distribution. The laser frequency ($-746.2\,MHz$ red-detuned) and the magnetic field of the slower are chosen so that the atoms leave the slower with a remaining velocity of about $70\,m\,s^{-1}$, which is far above the capture velocity of the MOT. An additional second laser beam, named **Booster**, which is about 720 MHz less red-detuned and overlapped with the main slower beam, forms an additional longitudinal slowing unit together with the rising slope of the magnetic field at the end of the MOT. By this implementation the divergence of the atom beam at the end of the slower is minimised and the atoms can be refocused in the MOT region again. Thereby, losses due to collision with the vacuum walls are reduced significantly[4].

The Zeeman slower is not equipped with any sideband frequencies, since, as soon as the ^{39}Ar-atoms have reached the stretched state, off-resonant excitation to any other state than the F = 13/2 should be forbidden, if the light is perfectly circularly polarised. No difference in the ^{39}Ar-count rate was experimentally observed using a ZSL equipped with the 1st and 2nd sideband frequencies [43].

[4]For more details concerning the slower it is referred to [3, 73].

Magneto-optical trap (MOT)

The MOT is the centrepiece of any ATTA-apparatus and the essential part for the high isotopic selectivity. The MOT of the ArTTA-apparatus is realised with three laser beams of ∼25 mm in diameter, which are retro-reflected, and with a magnetic field gradient of $6\,\mathrm{G\,cm^{-1}}$ in horizontal directions and with $12\,\mathrm{G\,cm^{-1}}$ in vertical direction along the axis of the magnetic coils, respectively. A maximal capture velocity of around $\sim 10\,\mathrm{m\,s^{-1}}$ [4] can be achieved with the current setup. More details of the exact implementation and simulation can be found in [73, 3, 4]. An extension with two slightly shifted laser frequencies in the MOT-beams was studied in [76]. One laser frequency was chosen near resonant and optimised for a reliable detection of the trapped atoms, while the other one was by about 10 MHz more detuned and optimised for a maximal capture-efficiency. With this double frequency MOT a gain of about 20 % was observed. However, the double frequency MOT was only tested for ^{38}Ar and requires a more detailed investigation. Thus, it is not implemented permanently.

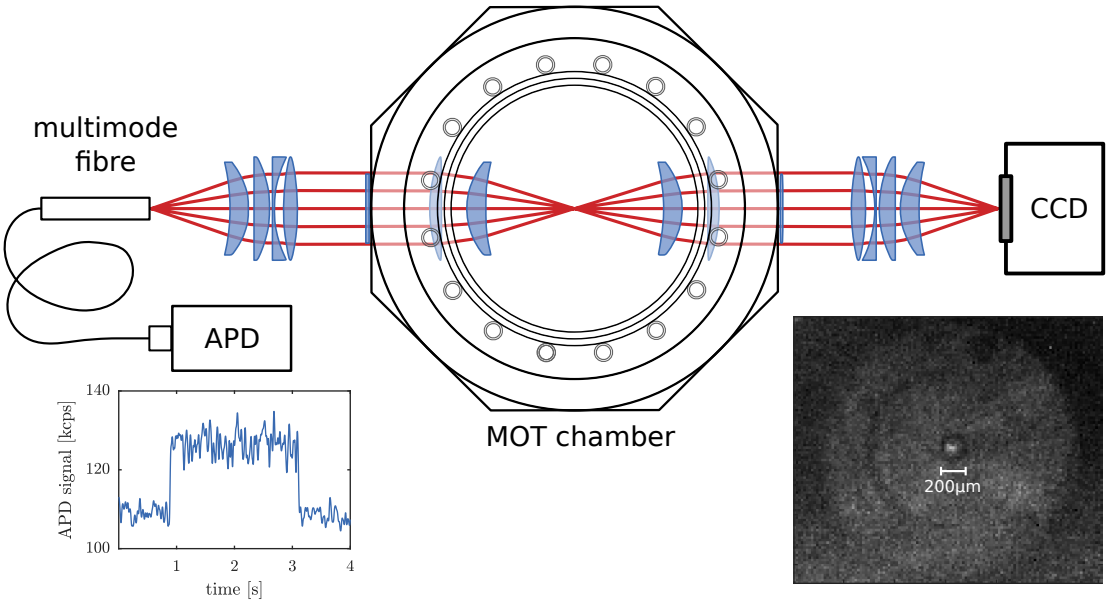

Fig. 2.7.: Imaging system for single atom detection: The fluorescence light can be detected simultaneously by an APD with a high time resolution and from the opposite side by a CCD-camera spatially resolved. The two identical optical 1:1 imaging systems map the head of the fibre core on the CCD-camera. The fibre core, with a width of 200 µm, appears as a dark spot on the image, surrounded by bright region originating from the fibre cladding. (Sketch based on [4].)

Single atom detection

ArTTA relies on a reliable detection of single trapped atoms. The optics of the detection system are depicted in figure 2.7. The emitted fluorescence light of the

single atoms while being trapped in the centre of the MOT is collected with help of a 1:1 imaging either via multimode fibre by an APD with a high time resolution or from the opposite side by a CCD-camera with spacial resolution. The current ArTTA-system uses exclusively the APD signal for the single atom detection. The camera is used for adjusting the fibre and for monitoring the single atom signal. In order to reduce the data volume pictures will be only recorded if the APD-signal triggers. The stray light is suppressed by a coating of the inside of the MOT chamber with a highly absorptive, black paint and the objectives are mounted in black tubes. The single atom signal of the current system is about 16 kcps on top of a background with around 105 kcps. This single atom signal corresponds for an atom with a lifetime of 40 ms to a maximal signal to noise ratio of 10.[5]

For a reliable detection, an exact and stable position of the trapped atoms in the focus of the fibre is crucial. Already relatively small displacements of the atoms due to fluctuation of the magnetic field, the laser power or polarisation reduces the single atom signal dramatically so that a detection of the atoms is not possible anymore. One possible future improvement might be to use the camera instead of the APD for the single atom detection. Therefore the frame rate has to speed up to at least 25 frames per second, otherwise atoms with a short lifetime will be lost. An adaptive algorithm could compensate small drifts of the atom position automatically and choose the camera region with the highest signal to noise ratio.

Quench and atom flux monitor

Off-resonant excitation of the most abundant isotope ^{40}Ar in the MOT is the largest contribution to the APD-signal background. By an isotopic selective quenching of metastable ^{40}Ar-atoms about 98.8 % of all ^{40}Ar-atoms can be removed out of the metastable state and the background is reduced to ∼40 %, which is illustrated in figure 2.8. The signal of single trapped atoms becomes more clearly separable from the background noise. In comparison with previous works the reduction of the background light due to the quench of the current system is about 2.5-times higher, which is most probably due to a higher metastable atom flux reaching the MOT region and leading to a higher background in principle.

The ArTTA-system relies on a stable and at least over one measurement period comparable performance. One major source of fluctuations are changes in the metastable argon flux, which can be monitored simultaneously to the ^{39}Ar-measurements by the atom flux monitor. This tool utilises the fact, that each quenched atom emits one 843 nm-photon on the way to the ground state (figure 2.9a). The 843 nm-fluorescence light is collected and imaged on the active area of a 1 cm^2-photodiode (see sketch 2.9b). A 840 nm to 850 nm-bandpass filter suppresses the 812 nm-cooling light of the ZSL. A half circle beam profile of the quench laser is chosen to have a smaller defined region and thus a higher photon yield of the fluorescence light. Furthermore it is ensured that the interaction is long enough to remove most of the ^{40}Ar atoms from the ground state.

[5] More details concerning the imaging system can be found in [3].

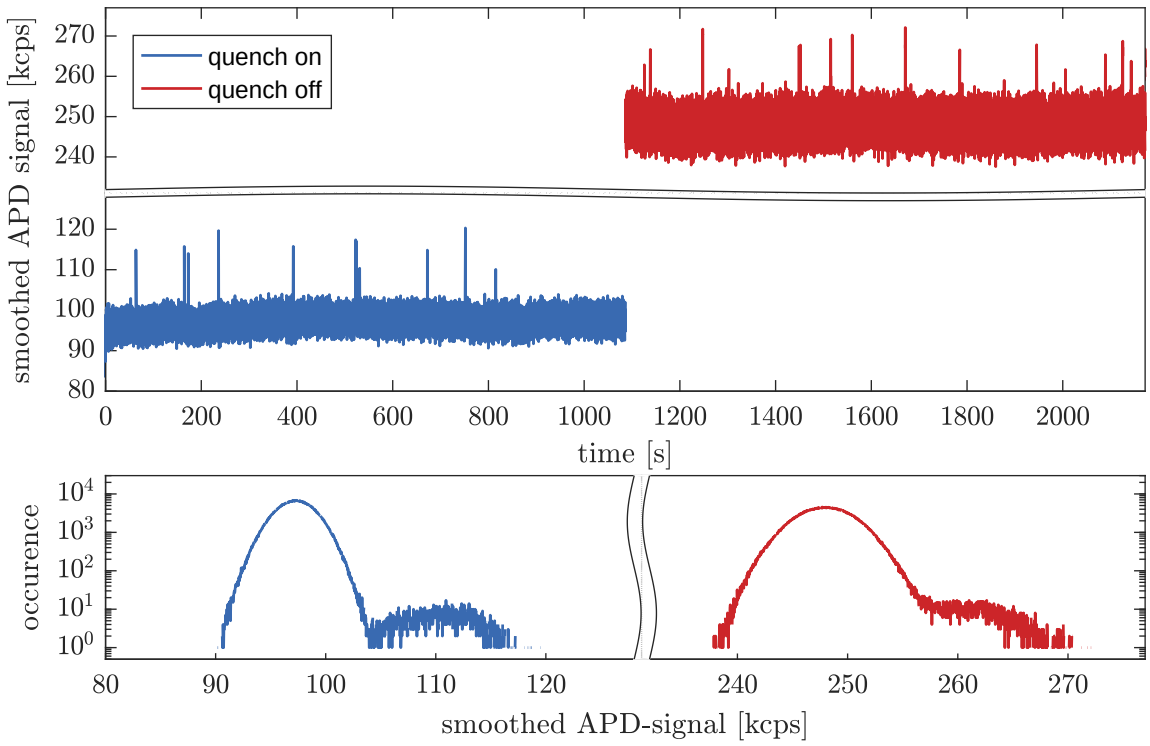

Fig. 2.8.: Reduction of the background light with help of the ^{40}Ar-quench: The upper graph shows the time series of the APD-signal with quench on (blue, first 1100 s) and quench off (red, second 1100 s). Thereby, the background can be suppressed by ∼150 kcps down to 100 kcps. The corresponding histogram (lower graph) illustrates the reduction of the variance of the background noise. The single atom signal is without the ^{40}Ar-quench not clearly separable from the background.

Atom beam profiler

The atom beam profiler gives a cross section and thereby a spatially resolved flux of the metastable ^{40}Ar-atom beam behind the MOT. The optical system and a typical atom beam profile are depicted in figure 2.10. A thin sheet of light tilted by 45°, which is resonant to ^{40}Ar and power-stabilised, illuminates the atom beam. The generated fluorescence light is imaged on a CCD-camera. The optical system maintains the aspect ratio of the beam profile. The beam profiler is very sensitive and changes on the percent-level can be monitored. Additionally it has the big advantage of a spatially resolved real-time signal which can be used to adjust and align the collimator and MOL and to quantify the metastable atom flux precisely. This tool is therefore used to control the source, collimator and MOL before and after each ^{39}Ar-measurement. However, it is not suitable for adjusting or optimising the ZSL or MOT nor can it be used to monitor the metastable flux simultaneously to an ^{39}Ar-measurement, since almost all ^{40}Ar-atoms are quenched. Furthermore it is important to note, that an

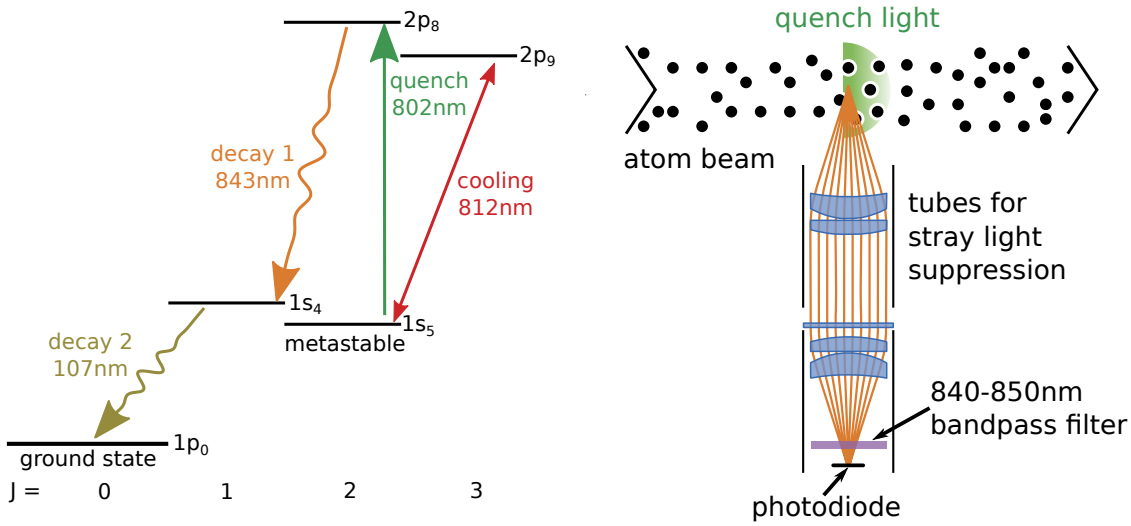

Fig. 2.9.: **a)** Schematic of the quench transition: ^{40}Ar can be isotopic selectively removed from the metastable state $1s_5$ by an excitation to the $2p_8$ level, from where it decays with 71 % to the ground state mainly via the transient level $1s_4$. On the way to ground state each atom emits one photon with 843 nm which can be detected to measure the metastable atom flux.
b) Atom flux monitor: A quench laser beam illuminates the atom beam in a defined small volume. The 843 nm light emitted by the deexciting atoms is imaged on a photodiode. (Sketch based on [4].)

optimised flux on the beam profiler does not necessarily lead to a higher ^{39}Ar-count rate, since another velocity class of atoms is relevant for the beam profile and the capture efficiency of the MOT and the performance of ZSL are not included in the beam profile.

Measuring the MOT loading rate of an abundant isotope might be used to optimise and control MOT and ZSL. However, it is much more difficult to measure the loading rate reliably and comparably over a longer period of time. Different implementations can be found in [43, 4, 76].

2.2. Laser system

The laser system was rearranged using mainly the existing components with the aim of improving the stability and to simplify and speed up the maintenance. The reconstruction of the system is partly described in [76], but is treated in more detail in this thesis. The laser system has to fulfil several requirements: First, generating and mixing of all different cooling and sideband laser frequencies to compensate the different Zeeman and Doppler shifts of the various atom-optical cooling stages. The cooling frequencies should be easily switchable between the different isotopes. Second,

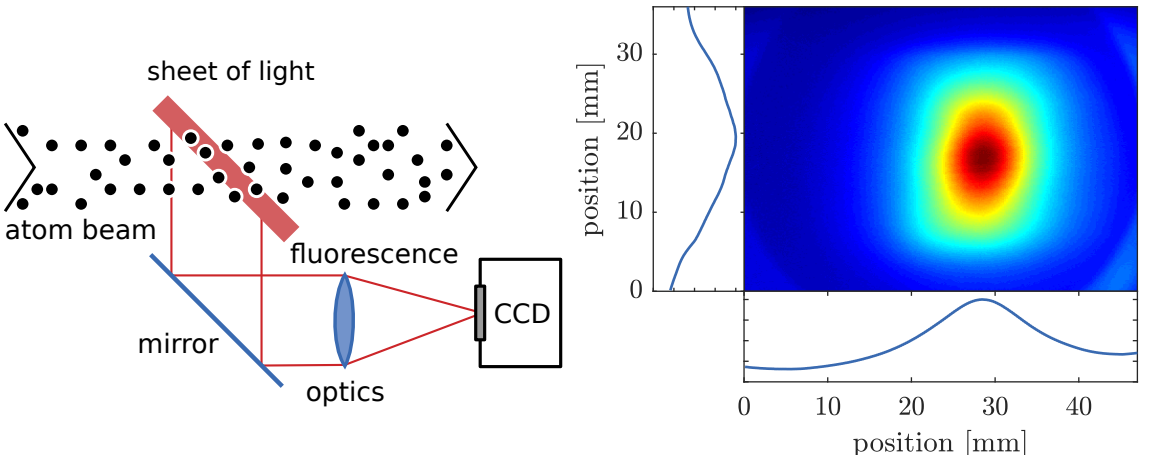

(a) (b)

Fig. 2.10.: **a)** Schematic of the ^{40}Ar-beam profiler: The atom beam crosses a homogeneous and thin sheet of light, which is tilted by 45°. The fluorescence light is observed by a CCD-camera. The geometry of the optics maintains the aspect ratio of the beam profile. (Sketch adapted from [43].)
b) Exemplary profile of the collimated and focused atom beam. (Data are taken from [43].)

sufficient laser power must be provided for an efficient laser cooling. And finally, frequency and power stability is indispensable to guarantee a stable count rate. The previous laser system and the components of the system are described in more detail in [77, 4].

The new laser system was designed to eliminate several main disadvantages of the previous one:

- The previous laser system evolved with the increasing requirements of the atom-optical apparatus and with the implementation of new ideas. Thus, most of the optical path were unnecessary long and complex, which was a source of instabilities.

- The two commercial (Toptica) master oscillator power amplifier (MOPA) systems were not decoupled by optical fibres from the rest of the laser system, so that an adjustment of the amplifiers entailed a readjustment of all subsequent optical components and the maintenance of the system was a time consuming procedure.

- The old system was constructed so that all required laser frequencies of an atom-optical component were mixed at first and amplified afterwards. The non-linearity of the gain medium in the TA-diode led to additional, undesired laser frequencies, which are clearly visible as artefacts in the Fabry–Pérot interferometer signal plotted in figure 2.11a. Due to mode competition between different

laser frequencies amplified in the same TA-diode, small variations of the relative seed power can cause high fluctuations of the relative output power. Thus, it was difficult to adjust and keep the laser power of all frequencies stable.

- The two main lasers of the system, which generate the ^{40}Ar-reference frequency of the cooling and the quench transition, respectively, were self-built ones and mode hops permanently led to losses of measurement time.

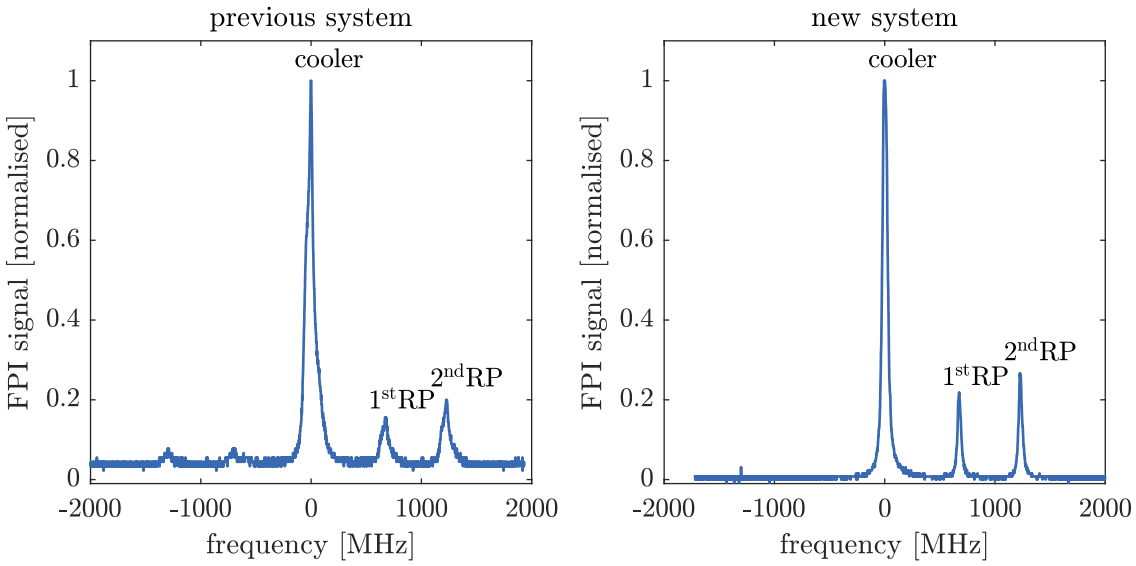

(a) Previous system (b) New system

Fig. 2.11.: Fabry–Pérot interferometer signal of the MOT laser light with the cooler and two RP frequencies: In the previous system two additional peaks are visible on the left side of the cooler. Additional frequencies are generated, if more than one frequency is amplified by a TA at the same time. In comparison the new system does not show any artefacts in the signal.

Sketch 2.12 gives an overview of the frequency generation and summarises the current values of all laser frequencies. The master-laser, which provides the ^{40}Ar-reference was replaced by a stable, commercial Toptica DL pro laser system, which is stabilised with help of a Doppler free saturation spectroscopy of ^{40}Ar onto the cooling $1s_5 \rightarrow 2p_9$ transition of 811.754 nm. This master-laser serves as the frequency reference for two additional master oscillator power amplifier (MOPA) systems, which are offset-locked relative to the master-laser. One provides the laser frequencies for cooling and the other one for the sideband-transitions. The Ar-isotope, which is cooled and trapped, can be switched easily by changing the offset-frequency between the master and the cooling-laser. The exact frequency shifts for collimator, MOT, ZSL and Booster are generated with help of acousto-optic modulators (AOM) in double-pass configuration. The cooling laser of the collimator is amplified by a self-built TA. The 1st-repumper

(RP) as well as the light of the beam imaging is generated directly from the ^{40}Ar-reference of the master-laser, which is amplified by a second self-built TA. The 4$^{\text{th}}$ RP is envisaged but not yet implemented. The theoretically expected gain by providing the 4$^{\text{th}}$ RP in the collimator is 11 % and a gain of 3 % was measured experimentally with the previous system [43]. Collimator and MOT share the same frequencies for the 1$^{\text{st}}$ and 2$^{\text{nd}}$-RP, which thus have to be compromised between both cooler frequencies. Experimentally it turned out, that the exact frequency and power of the repumper laser light is not critical, since only few excitations are required to transfer an atom back into the cooling transition. All corresponding laser frequencies are mixed and guided through polarisation-maintaining single mode fibres to each atom-optical component.

The quench system is independent from the rest of the laser system and the former self-built quench laser was replaced by a commercial Toptica DL pro laser system, too. This laser is stabilised, similarly to the master laser, with help of a Doppler free saturation spectroscopy of ^{40}Ar onto the quench transition $1s_5 \rightarrow 2p_8$ of 801.699 nm. The ^{38}Ar-quench, which can be utilised to measure the ^{38}Ar-loading rate of the MOT, is not in use at the moment.

The complete layout of the new system is depicted in figure 2.13. While redesigning the laser system attention was paid to keeping the optical path short and the system as simple as possible to improve the passive stability. The system is subdivided into four sections, which are decoupled by polarisation-maintaining single mode fibres. Section **A** contains the laser and the spectroscopy of the ^{40}Ar-reference of the cooling transition and the lasers and optics for the two offset-locks. The frequency generation with help of AOMs in double-pass configuration and the frequency mixing is located in section **B**. The two self-built TAs, which amplify the collimator cooling frequency and the ^{40}Ar-reference are located in section **C)**. The quench laser and the corresponding spectroscopy are mounted in section **D**.

Table 2.1.: Laser power used for the atom-optical components measured behind the fibres on the atom-optical apparatus side. The absolute power of the collimator is estimated.

	collimator (per axis)	ZSL	MOL vertical	MOL horizontal	MOT (per axis)
total power [mW]	∼150	∼75	42	51	11
cooler	80 %	80 %	42 %	54 %	76 %
1$^{\text{st}}$RP or booster	5 %	20 %	28 %	25 %	10 %
2$^{\text{nd}}$RP	7 %	-	29 %	21 %	13 %
3$^{\text{rd}}$RP	8 %	-	-	-	-

All frequencies are (if necessary) amplified at first and then mixed, which makes the laser power of each frequency much more stable. Moreover, the additional generation of undesired frequencies during the amplification is prevented, so that no artefacts are visible in the Fabry–Pérot interferometer signal of the new laser system (shown in figure 2.11b). Since the mixed laser frequencies are not amplified at the end, a much

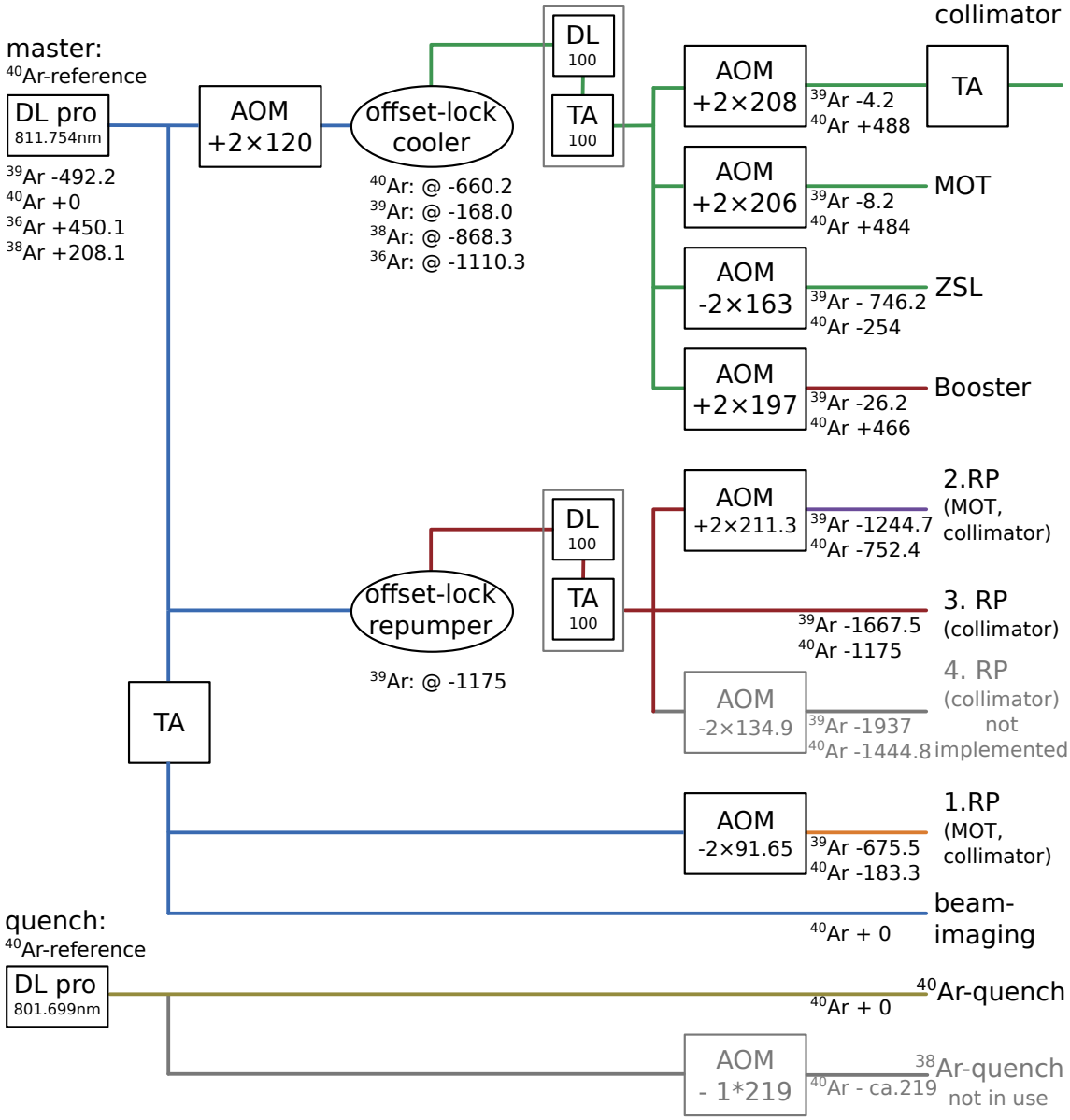

Fig. 2.12.: Overview of the frequencies of the current system: All frequencies are given in MHz relatively to the cooling transition. The isotope, which is cooled and trapped, can be switched easily by changing the frequency offset with help of the offset-lock.The 4^{th} repumper is not implemented and the ^{38}Ar-quench is not in use at the moment (TA: tapered amplifier, AOM: acousto-optic modulator, RP: repumper).

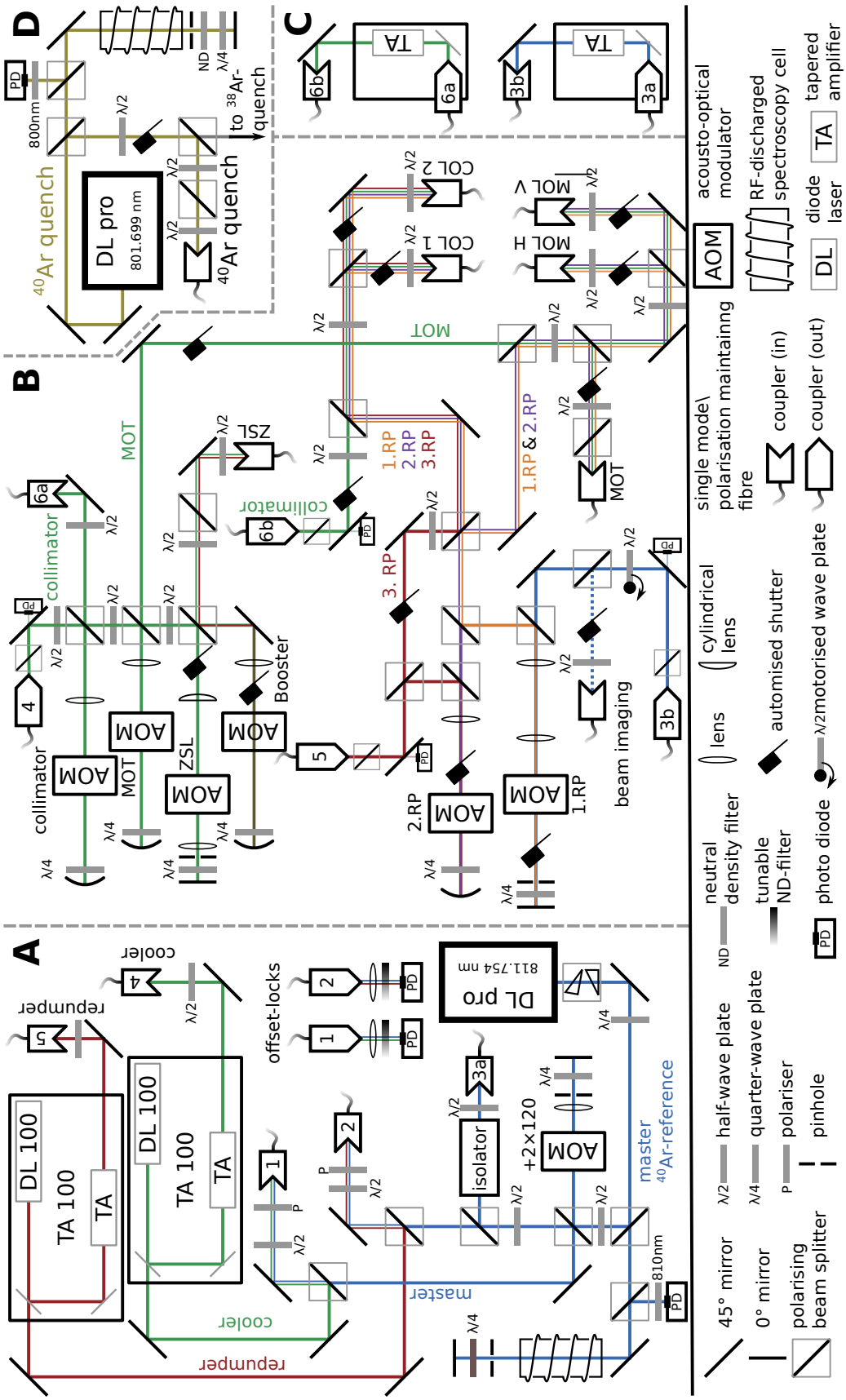

Fig. 2.13.: Sketch of the complete optical setup: For details it is referred to the main text.

more efficient use of the available laser power is needed. Therefore, both polarisations of two combined frequencies are used, whenever it is possible. The output power of all TAs is monitored with photo diodes and the two self-built TAs are stabilised actively. To guarantee a defined polarisation of the light, all fibres are equipped with a polarising beam splitter at their end. The used laser powers of the current system measured behind the fibres are listed in table 2.1. A self-built shutter system was included in the laser system which enables an automatic measurement of all laser powers and together with the help of the beam imaging system an automatic test of the source, collimator and MOL.

Additionally, the old spliced fibre splitter of the three MOT axes was replaced by a new one built from Thorlabs FiberBench System components (see appendix B.1). The power fluctuations of the old and new splitter are compared in figure 2.14. Due to this improvement of polarisation and power fluctuations a much more stable position of the MOT position could be achieved and thus also a much more robust single atom detection.

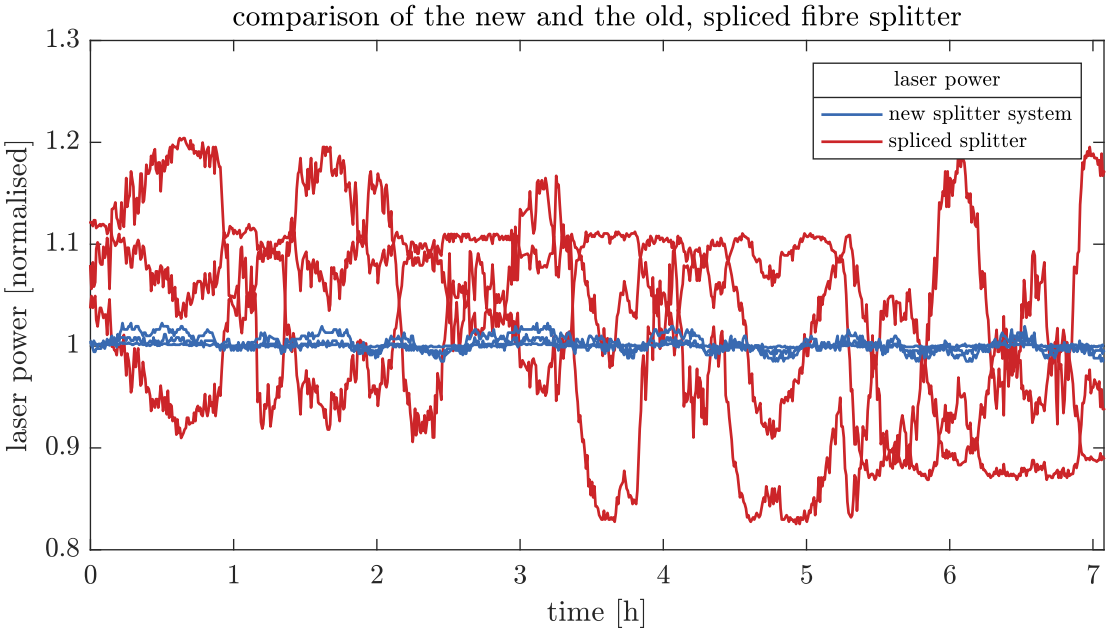

Fig. 2.14.: Comparison of the new fibre splitter (Thorlabs FiberBench System) and the old, spliced fibre splitter: The three lines represent the two horizontal and the vertical axis. The new splitter reduces the power fluctuations of the MOT beams by almost a factor 10 down to 2.5 %.

The decoupling of the different sections of the laser system via fibres was proven to be very helpful for adjusting and maintaining the laser system, although some additional effort is required for a stable polarisation. Thus the laser system of the second ArTTA-apparatus which is under construction, is designed in a complete modular concept.

2.3. Vacuum system

There was a redesign of a large portion of the vacuum system. The fore-vacuum was extended to handle a wide range of sample sizes and optimised for small samples down to 100 μL. A replacement of all high vacuum components, which might be in contact with ions from the source, resulted in a high reduction of the contamination. The main gain of the ^{39}Ar-count rate was achieved by increasing the pumping speed and by optimising the conductance of the differential pumping tubes (DPT). The complete high vacuum was simulated with a Monte Carlo simulation for this purpose.

2.3.1. Fore-vacuum

The fore-vacuum is depicted in sketch 2.15. There are two different basic modes, in which the ArTTA-apparatus can be operated.

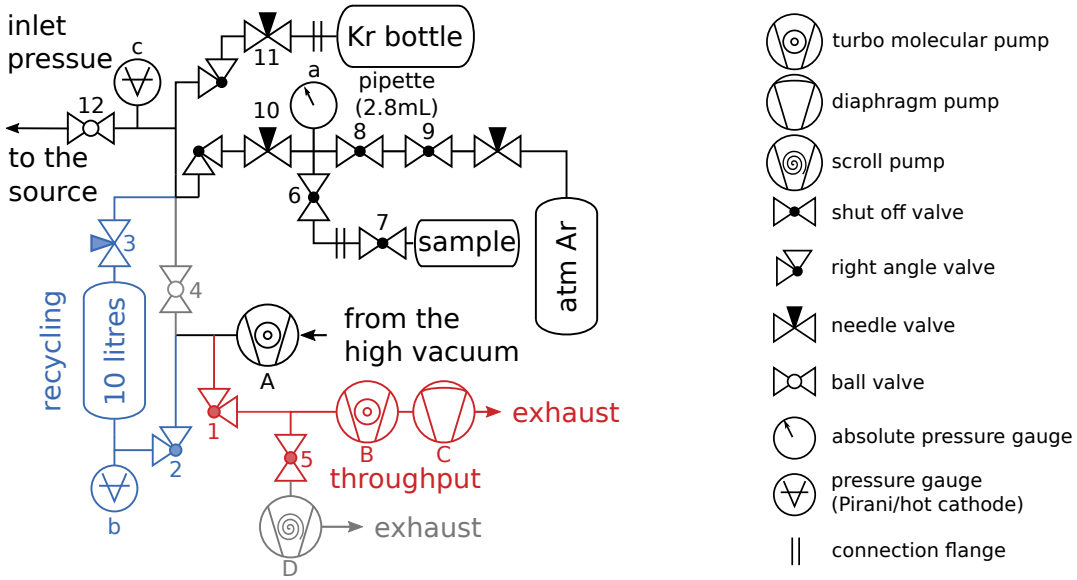

Fig. 2.15.: Sketch of the fore-vacuum system optimised for operation in recycling mode for measuring samples in the range of 0.1 mL to 10 mL. For a detailed explanation see text.

Throughput mode

In the throughput or open mode valve **1** is open and **2**, **3** and **4** are closed. The sample flows in continuously and is pumped out immediately into the environment of the laboratory after one pass through the apparatus. The current consumption in throughput mode is about 51 mL h^{-1} of Ar gas. Since it is the easiest mode of operation and there is no detectable ^{39}Ar background due to the contamination embedded in the system, the first groundwater samples were measured in this configuration [44].

Recycling mode

The recycling or closed mode reduces the needed sample size by more than two orders of magnitude. The basic idea of recycling the sample inside the closed vacuum system (valve **1** closed, valve **2**,**3** and **12** open) follows [78]. To be able to close the system completely, an advantage of the usual disadvantage of getter pumps is used. Reactive outgassing gases such as nitrogen and water are removed by the getter pump, but it can not pump noble gases. The argon sample will remain in the vacuum chamber and stay clean during the measurement process. The efficiency of the metastable argon source is highly dependent on the argon pressure and must always operate at the same optimal pressure to have a reliable reference. To handle sample sizes in the range from 700 μL up to more than 10 mL, an additional 10 L buffer volume is included in the circulation loop. The gas flow of about 51 mL h^{-1} is regulated by the dose valve **3** at its outlet, so that the inlet pressure at gauge **c** is kept constant at all time. Different valves were tested for this task. It is important that it has a high flow coefficient to handle small samples and many turns to regulate the flow precisely. The different sample volumes are compensated by varying the pressure in this buffer volume. The gas buffer container can be bypassed by a ball valve **4**, which is then used to regulate the pressure. With help of this bypass much smaller sample sizes in the range from 100 μL up to 550 μL are possible. On the one hand, the contribution due to contamination is maximised by this very small samples and can thereby be studied more precisely, on the other hand it is difficult to keep the system stable over a longer period of time. The turbomolecular pumps (TMP) of the high vacuum compress the gas into the smaller TMP **A** (50 L s^{-1}), which has a twofold function. It acts as a second compression stage, which allows higher pressures in the buffer volume and thereby a higher variation in the sample sizes. In addition to this task, it reduces the minimal sample size by reducing the pressure in the relatively big fore-vacuum volume of the main TMPs.

To prevent the system from any leaks through the dose valves (which might be under over pressure at the sample ports) each of them is protected by an additional shut off valve. By measuring the pressure at the absolute pressure gauge **a** and knowing the reference volume of the system between valve **10**, **8** and **7**, the amount of gas which is let into the apparatus can be determined. Since valve **7** is part of each sample container, the reference volume might differ slightly from one to another type of sample cylinder. Valve **8** and **9** form an integrated pipette with a known volume of 2.8 mL, which can be used to measure the reference volume easily. Another way to determine the used amount of gas is to measure the pressure inside the buffer volume with help of pressure gauge **b**. This is necessary as soon as the sample container is emptied out. In this case the exact reference volume is unclear due to the charcoal inside the sample cylinders and it is impossible to use the absolute pressure gauge. The atmospheric reference (see chapter 1.4) is connected permanently to the system. The Kr port can be used for flushing the system without disconnecting the sample and subsequent pumping down of the system. While connecting a new sample, about 3 mL of air enters the system. By closing the ball valve **12**, the high vacuum can be separated from the fore-vacuum and the intruded air can leave the system directly.

Otherwise there is the risk that mainly water vapour or oxygen and other components of air freeze on the liquid nitrogen cooled source. If the source is ignited again now, there is burst of gas released, which makes the sample impure and stresses the getter pump. Between two different samples it is important to clean the fore-vacuum by pumping it down below 7×10^{-5} mbar which is at least three orders of magnitude below the normal operation pressure in the buffer volume. Therefore a further TMP **B** ($50\,\mathrm{L\,s^{-1}}$) is necessary, which forms one pumping unit together with a diaphragm pump **C**. For normal operation and sample changing, the pumping speed is sufficient. Additionally a scroll pump **D** is connected to the system, which is only used after venting the complete system.

2.3.2. High vacuum

To reduce the contamination embedded in the vacuum system originating from former characterisation and optimisation measurements of the whole system with highly enriched samples of ^{39}Ar abundances as high as 10^{-9}, the collimator, the main source chamber and some smaller parts were exchanged. In the context of this reconstruction the pumping speed of the system was upgraded by a second main pump connected to the source chamber and by replacing three broken pumps by bigger ones. The upgrade of the pumps allows an about 10 % higher Ar-throughput[6] combined with a reduction of the losses by collision with the background gas. The simulations of the vacuum indicate that the pressure inside the differential pumping tubes (DPT) are problematic. This issue was optimised by a redesign of the 1$^{\mathrm{st}}$ and 3$^{\mathrm{rd}}$ DPT.

Simulation of the high vacuum

The high vacuum was simulated using MolFlow+, a Monte-Carlo simulation package written at CERN [79]. It can be applied for simulating the steady-state pressure under the assumption of ultra-high vacuum, when the free path of the molecules is long compared to the typical size of the system. This condition might be not absolutely fulfilled everywhere, which might lead to some deviations from the real system. A model of the vacuum system is depicted in figure 2.16. It is essential to adapt the velocity distribution of the front facet of the source to emulate the measured velocity distributions. Thereby the assumption is made, that the measured metastable Ar-atoms have the same velocity distribution as the rest of all atoms leaving the source. The Ar-input is set to the measured throughput of $51\,\mathrm{ml\,h^{-1}}$ for the current system and $46\,\mathrm{ml\,h^{-1}}$ for the previous one. An outgassing of the rest of the vacuum system is neglected. More information about importing a model into MolFlow and how to calculate the parameter to emulate the measured velocity distributions are compiled in appendix B.3.

[6] The increase of 10 % refers to a measurement direct before the upgrade of the vacuum system. The gas throughput is about ∼50 % higher compared to [44].

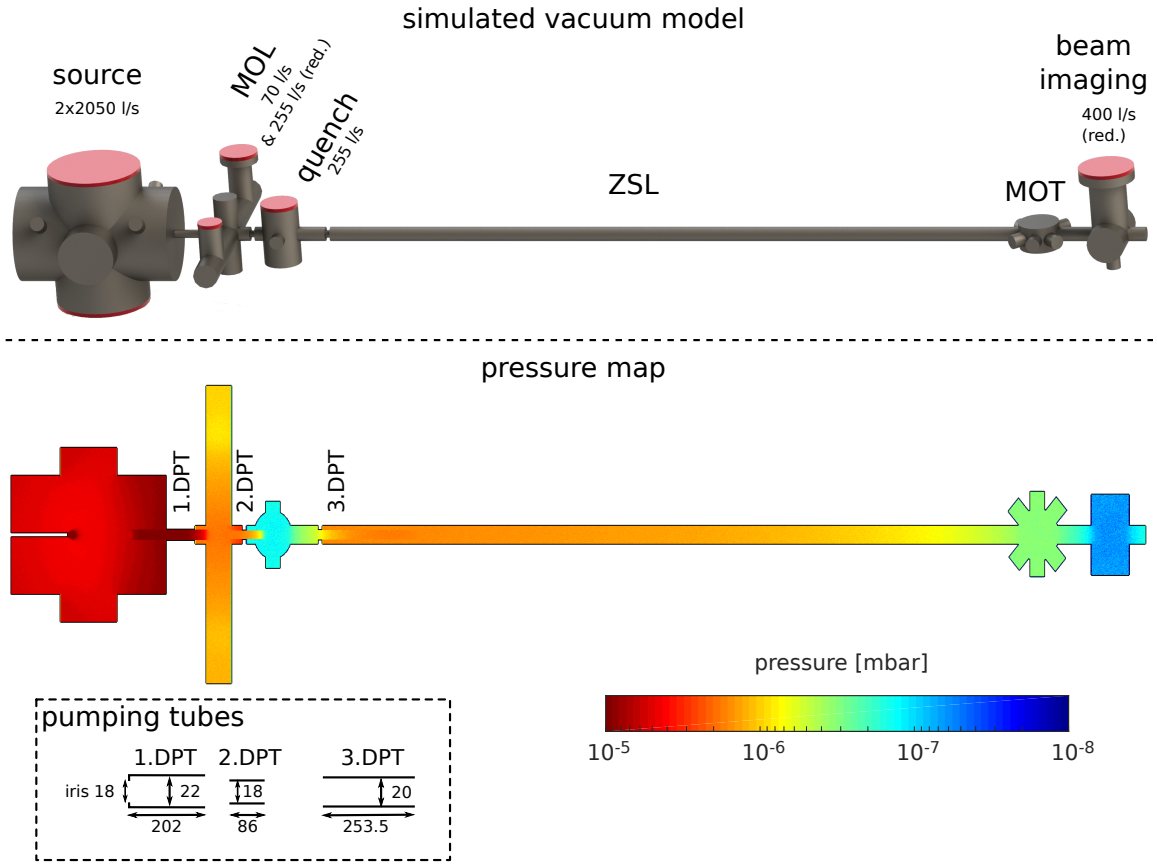

Fig. 2.16.: Model of the ArTTA high vacuum system (upper figure): The red faces indicate the flanges to which the vacuum pumps are connected. The pumping speeds marked with *red.* are reduced significantly, since these pumps are connected with reducing flanges. Horizontal cross section of the simulated pressure (lower figure): The areas, which are well pumped, are clearly visible. The pressure increases inside the ZSL again, since it is not directly connected to any pump. The small inset shows the dimensions of the DPTs in mm.

Figure 2.16 shows the pressure map of a horizontal cross section of the current system and figure 2.17 compares the pressure profile of the current system to the previous one with less pumping power. Additionally the pressure profile without the optimised DPTs was simulated, as well as the one of a diffuse undirected source. The pressure profile with a diffuse source decreases rapidly and is inside the MOT chamber about 2 orders of magnitude below the measured pressure. This shows clearly that the pressure profiles are dominated by the diverging atom beam of the directed source and that the velocity and the direction of the atoms leaving the source are crucial for the calculation of the vacuum. Thus, the effect of DPTs can not be estimated by the standard equations describing the conductance of a molecular flow through a pipe.

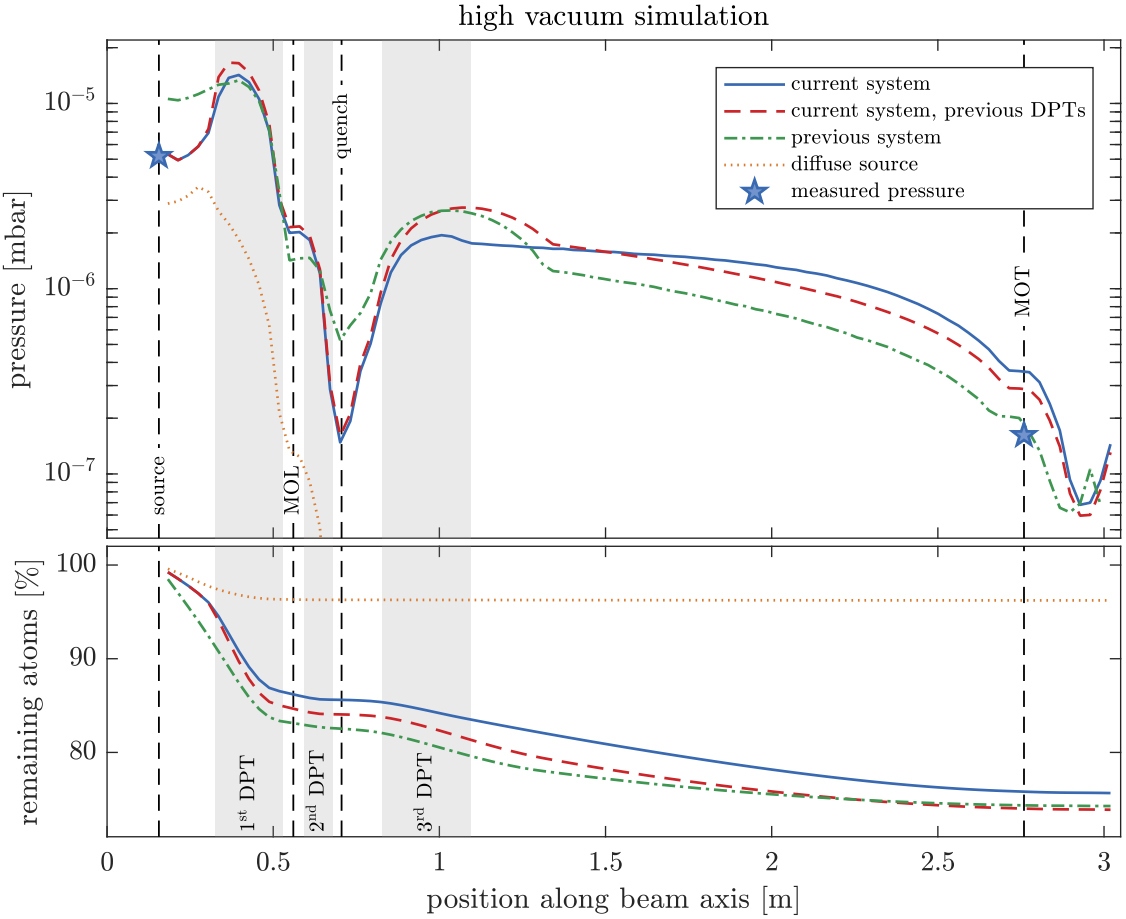

Fig. 2.17.: **Upper plot:** Simulated pressure profiles along the beam axis of the current system, of the current system with the previous geometry of the differential pumping tubes (DPT) (1st DPT without iris and 3rd DPT doubled length), of the previous system and of the current system with a diffuse source. **Lower plot:** Losses due to collisions of metastable atoms with the background gas: The remaining fraction of metastable atoms is calculated with help of equation 2.1.

The pressure profile of the previous system shows a huge increase of the pressure in the 1st and 3rd DPT. The divergent atom beam collides inside the tubes with the tube wall. Due to the small diameter of 18 mm to 20 mm of the tubes, they are not well pumped and the collided atoms remain inside the tube for a while. Thus, the 1st DPT was optimised by increasing the diameter from 18 mm to 22 mm to improve the conductance of the tube and additionally a faceplate with 18 mm is mounted at the front side. All atoms leaving the source and passing the faceplate are restricted geometrically, so that they can not collide inside the tube with the wall. The geometry of the 2nd DPT was not changed. The length of the 3rd DPT was halved, which leads to a slightly higher pressure inside the MOT but reduces the losses due to collisions of metastable atoms with the background gas inside the 3rd DPT significantly. The dimensions of all pumping tubes are sketched in figure 2.16. Since the long vacuum tube of the ZSL with a diameter of 40 mm is not directly pumped, the pressure increases inside the ZSL by one order of magnitude compared to the quench chamber.

The measured pressure in the source chamber is around 5.2×10^{-6} mbar and in the MOT chamber around 1.6×10^{-7} mbar, which agrees well with the simulated pressure in the source chamber and is about a factor two below the simulated pressure in the MOT chamber. This might be due to a slightly different velocity distribution of the metastable atoms, which is used for the simulation, compared to the majority of atoms in the ground state, which determine the measured pressure. Additionally, the used velocity data belong to the previous system [74], since no measurements for the current system are available. Another explanation of the differences is the fact, that in the source chamber and inside the pumping tubes the assumption of ultra-high vacuum conditions is not fulfilled absolutely.

The losses of metastable atoms due to collisions with the background gas can be calculated by integrating over the mean free path λ of the atoms. The remaining fraction of metastable atoms at position z along the beam axis is given by:

$$\frac{I(z)}{I_0} = \exp\left(-\int_0^z \frac{1}{\lambda(z')}\mathrm{d}z'\right) \tag{2.1}$$

where $\lambda(z) = {}^1/_{\sigma n(z)}$ is the mean free path, $n(z) = {}^{p(z)}/_{k_B T_{bg}}$ the particle density, $p(z)$ the pressure profile, $T_{bg} = \sim 300\,\mathrm{K}$ the temperature of the background gas and $\sigma \approx 229\,\text{Å}^2$ the total collision cross section of metastable Ar-atoms with the neutral background, which can be calculated from the pressure dependent lifetime of trapped atoms (see equation 2.3).

The resulting graphs are plotted in figure 2.17. Only 72 % of all metastable atoms, which would reach the MOT without any background gas, are remaining at the position of the MOT. Already 15 % are lost between source and the 1st DPT. The estimated gain due to the optimisation of the pumping tubes is about 3 %, however the uncertainty of the assumed cross section is high.

The biggest potential for further improvements of the vacuum system lies in rapid pressure decrease directly behind the source, for example with help of an iris, and in an improved pumping of the ZSL and MOT, which are not pumped directly, but only via the beam imaging chamber. One possibility is to split the ZSL and to

install an additional pump in between and to connect one pump directly to the MOT chamber. The ZSL was designed for a source without liquid nitrogen cooling and is thus unnecessarily long. A shorter ZSL would also improve the vacuum conditions.

Pressure dependency of the metastable atom flux

The flux of metastable atoms depends highly on the inlet pressure. A higher pressure leads to a higher Ar-throughput but on the other hand the background pressure increases and losses due to collisions with the background gas become dominant. Thus, the different fluorescence signals measured with the flux monitor and the beam imaging, which are plotted in 2.18a, show slightly different pressure optima with respect to the inlet pressure measured at pressure gauge **c** (compare figure 2.15). The fluorescence signal of the beam imaging decreases above a pressure of $\sim 3 \times 10^{-2}$ mbar again, since it is located behind the MOT at the end of the beam line, which makes it more sensitive to collisions with the background gas. As opposed to this, the signal of the flux monitor which is much closer to the source is still rising with higher pressures. Pressures above the typical operation pressure of 3.3×10^{-2} mbar (corresponding to a pressure in the source champer of 5.2×10^{-6} mbar) lead to a slightly higher single ^{38}Ar-atom count rate, but the mean lifetime of the atoms decreases rapidly with higher pressures and a reliable detection of single atoms becomes more difficult.

Pressure dependency of the MOT lifetime

The measured mean lifetime τ of single ^{38}Ar-atoms trapped inside the MOT is plotted in figure 2.18b as a function of the measured background pressure inside the MOT. The pressure dependency of the MOT-lifetime τ can be calculated similarly to equation 2.1 from the mean velocity of the background gas $< v_{bg} >$ and the mean free path λ. If there are only a few atoms trapped, two-body collisions are suppressed and for the stable Ar-isotopes the only loss mechanism[7] is collisions with the background gas. The loss rate $\gamma = 1/\tau$ is given by

$$\gamma = \frac{1}{\tau} = \frac{< v_{bg} >}{\lambda} = \frac{\sigma p}{k_B T_{bg}} < v_{bg} > \tag{2.2}$$

with the mean velocity of the background gas $< v_{bg} >= 3\sqrt{\pi/8}\sqrt{k_B T_{bg}/m}$ and the mass m. The total collision cross section σ of metastable Ar-atoms with the neutral background can be calculated from the measured pressure dependency of the MOT lifetime:

$$\sigma = \frac{k_B T_{bg}}{\tau p < v_{bg} >} = 195(9)\,\text{Å}^2 \tag{2.3}$$

The measured total cross section σ is about a factor 6 smaller compared to the measured value of $1198(211)\,\text{Å}^2$ and comparable to the cross section of $\sim 300\,\text{Å}^2$ calculated from diffusion coefficients, which are both reported in [3].

[7] For ^{39}Ar there is a second loss channel due to the hyperfine structure, which reduces the lifetime.

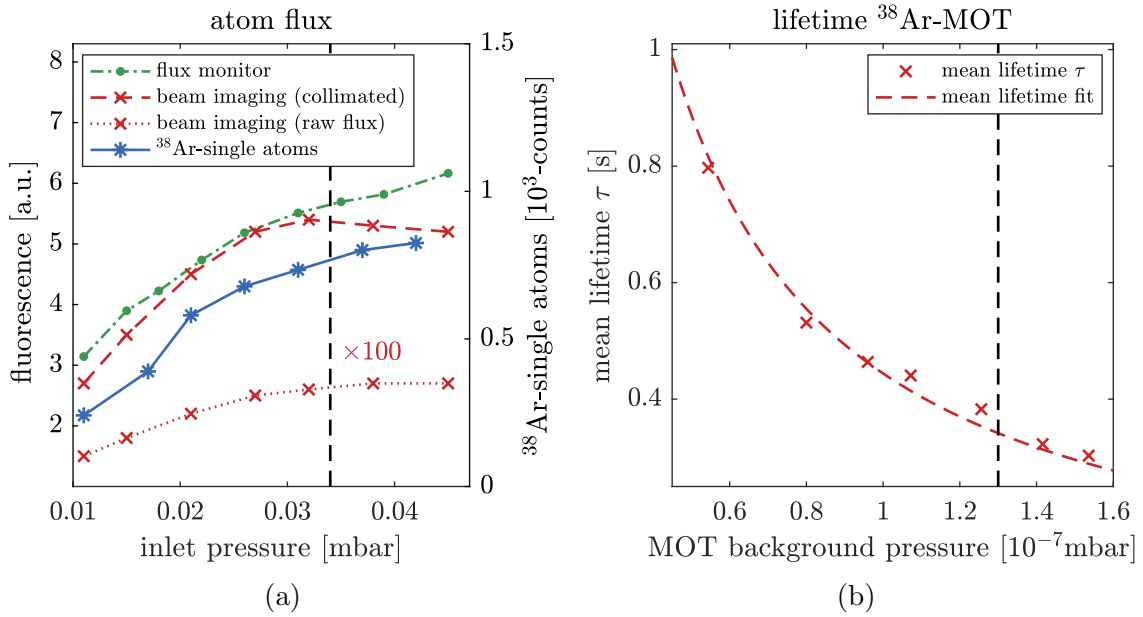

Fig. 2.18.: Pressure dependencies: The vertical dashed lines indicate the typical pressure during ^{39}Ar-measurements. Pressure above 4.5×10^{-2} mbar might lead to damages of the source and were not tested. To get a single atom signal, the ^{38}Ar trapping efficiency is reduced artificially.
a) Metastable atom flux measured with the flux monitor 0.71 m and with the beam imaging 2.96 m behind the source as a function of the Ar-inlet pressure. Additionally the single ^{38}Ar-atom count rate is plotted. Due to collisions with the background gas the different signals along the beam axes have different pressure optima.
b)Mean lifetime as a function of the MOT background pressure measured with single ^{38}Ar-atoms: The mean lifetime τ shows the expected $1/p-$dependency of equation 2.3.

3. Analysis

This chapter describes the way from the raw signal of counted photons on the APD to a final result of an ^{39}Ar-concentration together with its estimated uncertainties. This procedure is divided into two main parts: Firstly, atoms have to be identified in the APD-signal and counted. This step was fully automatised and optimised to handle the huge amount of data from the ocean measurements more efficiently. In the second step, the total number of atoms is combined with the other parameters, such as measurement time and Ar-volume to infer the ^{39}Ar-concentration of natural or unknown samples. Reference and contamination measurements quantify the reference count rate and a potential contamination. Similar or identical samples or measurements might be combined to a more precise result. The statistics during the analysis of all these steps are elaborated in detail. The APD-signal analysis is treated in a frequency probability context, the rest in a Bayesian one [80]. But first of all the basic properties of the statistics of the Poisson distribution as the fundamental description of counting photon and atoms are summarised.

3.1. Poisson process and distribution

The Poisson distribution and its underlying Poisson point process describe the probability of a given number of events N occurring in a fixed interval of time Δt or space under the assumption of a known constant rate μ and that the occurrence of the next event is independent from the time since the last one. It can be derived from the limit of an infinite number of Bernoulli experiments and thus from the Binomial distribution [81] or from the following three axioms of a stochastic point process [81, 82]:

1. **Stationarity**: The probability that in the interval $(t, t + \delta t)$ one event occurs is $p_1(\delta t) = \mu \cdot \delta t + o(\delta t)$, δt sufficiently small and independent from the number of points in the interval $(0, t)$.

2. **Memoryless**: The occurrence of an event in $(t, t + \delta t)$ does not effect the probability of later events.

3. **Orderliness and simplicity**[1]: The probability that more than one event occurs in the interval $(t, t + \delta t)$ is $p_{>1} = o(\delta t)$

[1] As a consequence of axiom 3 the Poisson distribution is sometimes called the *distribution of rare events*.

As soon as a (physical) process fulfils these three axioms it follows a Poisson distribution and the probability of N events in time Δt can be expressed by the following probability mass function with the average number of events $\lambda = \mu\Delta t$ as parameter[2]:

$$\phi\,(N, \lambda) = \frac{\lambda^N \cdot e^{-\lambda}}{N!}\ . \tag{3.1}$$

The Poisson distribution is characterised by only one parameter λ which defines the mean $< N >= \lambda$ and the variance $\sigma^2 = \lambda$ at the same time. For sufficiently large λ it can be approximated by a normal distribution. However, for small λ the skewness of the Poisson distribution is not reflected correctly, which is critical for very low concentrations and can lead for instance to unrealistic confidence intervals of negative concentrations.

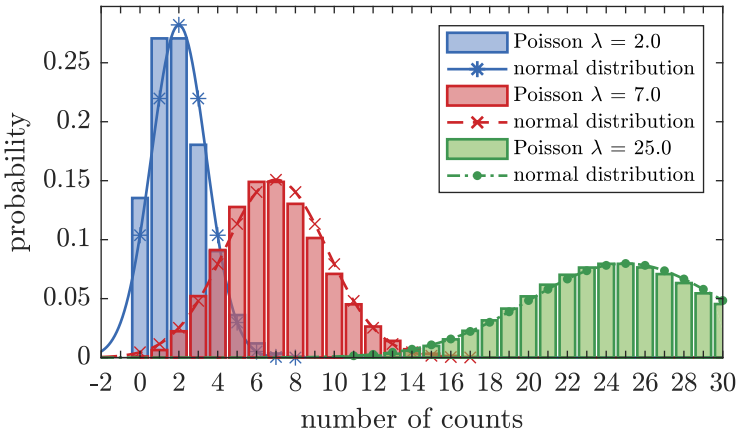

Fig. 3.1.: Poisson distribution for $\lambda = 2$, 7 and 25 and its corresponding approximation by a normal distribution with a mean and variance of λ.

There are four main topics in the context of ArTTA were the Poisson distribution plays a major role:

Counting atoms: The counting of the trapped ^{39}Ar atoms is a classical Poisson process, as soon as the system is stable so that the stationarity is fulfilled.

Photon detection: The detection of the photons scattered by the trapped atoms with help of the APD can be described by a Poisson distribution. With ∼100 counts in the considered time interval of 1 ms the count rate is high enough to approximate the Poisson distribution by a normal distribution.

Radioactive decay: The number of decays of a radioactive substance in a given time interval follows a Poisson process as well, if the time interval is short compared to the half-life and the number of atoms can be assumed as constant.

[2]Mathematically strictly speaking it must be distinguished between the discrete probability mass function $p_\lambda(N)$, if the average rate λ is given, and the continuous probability density function $p_N(\lambda)$, for example if the number N of events was measured and the average rate is estimated.

Sampling of small samples: The number of ^{39}Ar-atoms in a small sample can be approximated by a Poisson distribution, too. The typical amount of ^{39}Ar in modern water is ∼9000 atoms/L, which gives a natural limit on the sample sizes, if the initial variation in the sample should not exceed 1 %. For a sample at the current detection limit of ∼10 pmAr and with 1 mL STP argon this intrinsic error is already ∼2 %.[3]

3.2. Single atom detection

The aim of this section is to discuss the analysis of the APD-data to identify the atoms with a high fidelity. All parameters determined in this chapter are based on the APD-data from the ocean measurement presented in chapter 6. The starting point is a model to describe the APD signal, which is used to infer a decision rule and thresholds above which an atom is excepted. This decision process is structured in a preselection and a postselection. The probability to detect and accept a trapped atom should be maximised under the condition that the rate of erroneously counted atoms generated by the background noise is below a given limit. Since an analytic calculation based on the atom model is only possible for a few properties, a Monte Carlo simulation of the atom signal and the background noise is used to deduce the optimal detection parameters.[4]

From the experimental side the accumulated photon counts on the APD are read out with a 1 ms time resolution and stored in 10 min frames which makes the system more insusceptible to data losses due to computer failures. All data and simulations are based on this minimal time resolution of 1 ms.

3.2.1. Model of the atom signal

The most simple model of the APD signal of an atom is sketched in figure 3.2a. Each time step t_i of 1 ms is considered as an independent random experiment based on a time-dependent normal distribution with a mean $\mu_n(t_i)$ and a standard deviation $\sigma_n(t_i)$. The background noise has a mean n_0 and a standard deviation σ_{n_0} of detected photons per time step[5]. During the lifetime t of an atom the single atom signal δ_n is added to the background and the mean number of counted photons and its standard

[3] If a small sample is enclosed (for example stored or included in the ice matrix) for a longer period of time, the statistics of the initial sample selection process, i.e. before decaying, as well as of the radioactive decay play a role.

[4] A similar chapter can be found in [4], where the probabilities of counting real atoms or counting atoms from the background noise are normalised to the total number of counted atoms. Due to this fact, most of the results depend on the specific ^{39}Ar-count rate. Furthermore the minimum and not the total probability that a counted atom is really an atom is optimised erroneously and finally the implementation as a running average lead to correlations which are not treated at all in the mathematical descriptions. Consequently it wasn't possible to reproduce the results and a higher background atom rate must be expected.

[5] To be more precise all photon numbers should be technically treated as rates, since they depend on the length of the time steps. This is not written explicitly in all steps for simplicity and clarity.

deviation become $n_1 = n_0 + \delta_n$ and σ_{n_1}, respectively. The lifetime t itself follows an exponential distribution with a mean lifetime of τ. Under ideal conditions the deviations should be that of a Poisson process and only dependent on the mean photon number:

$$\sigma_n(t_i) = \sqrt{\mu_n(t_i)} \tag{3.2}$$

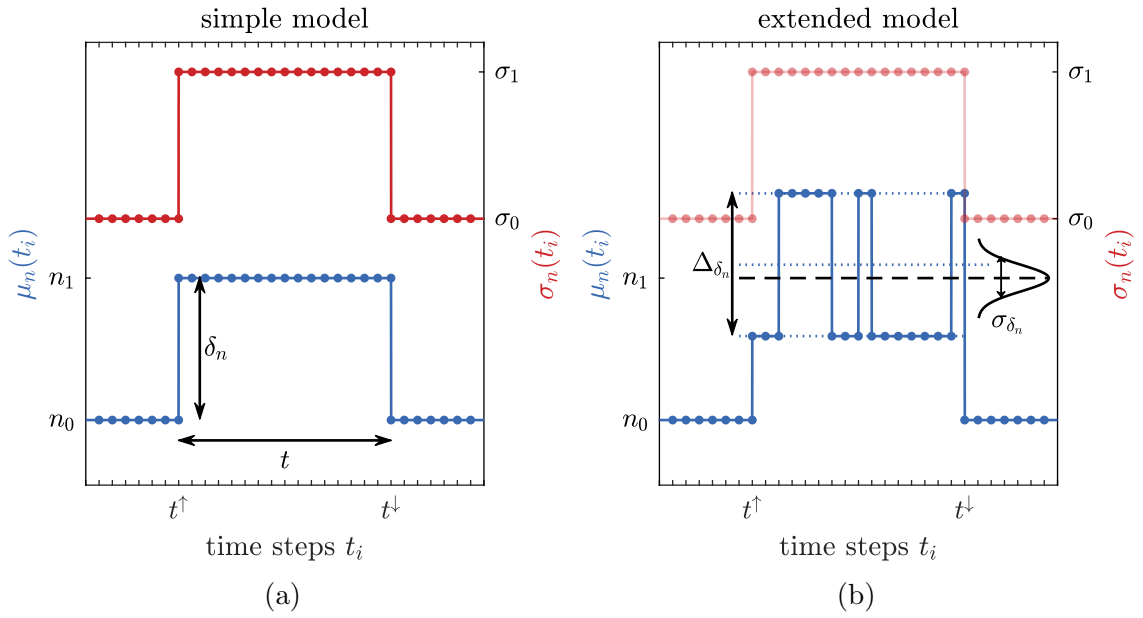

Fig. 3.2.: **a)** Illustration of the main parameters of the simple model to describe the APD signal of a single trapped atom.
b) Extended model to treat correlations between the single random processes and the additional noise on the single atom signal δ_n. For details it is referred to the text.

In practice it turns out that this model is too idealised. The single random processes are correlated as soon as an atom is trapped as it is shown in figure 3.3b. The standard derivation σ_{n_1} is higher than the pure Poisson process would predict and an additional variation of the single atom signal δ_n is observed. Therefore the model is extended by the following consideration: On the CCD-camera one can observe that trapped atoms are not fixed at one position but they jitter a little bit. In the most simple case they hop with a probability p_h per time step between two positions, whose single atom signals differ by Δ_{δ_n}, since one of them is not perfectly in the focus of the detection system and has a lower photon yield. Beyond that a variation σ_{δ_n},which is normally distributed, is added to the mean single atom signal δ_n. The σ_{δ_n} contains also small fluctuation in the background, which is measured for each atom individually and subtracted from the signal in order to obtain δ_n. The standard deviation $\sigma_n(t_i)$ remains unchanged and is the same top hat function as in the simple model. A sketch of the adjusted model of the atom signal is depicted in figure 3.2b.

To make all equations and considerations independent from the background, all parameters are expressed in terms of relative deviation from the background according to the following transformation:

$$n \mapsto x = \frac{n - n_0}{\sigma_{n_0}} \,. \tag{3.3}$$

The mean number of background photons n_0 and its standard deviation σ_{n_0} become in the transformed frame:

$$x_0 = 0 \quad \text{and} \quad \sigma_{x_0} = 1 \,. \tag{3.4}$$

The mean parameters of trapped atoms are mapped as follows:

$$\delta_n \mapsto \delta_x = \frac{\delta_n}{\sigma_{n_0}}, \quad n_1 \mapsto x_1 = \frac{n_1 - n_0}{\sigma_{n_0}} = \delta_x \quad \text{and} \quad \sigma_{n_1} \mapsto \sigma_{x_1} = \frac{\sigma_{n_1}}{\sigma_{n_0}} \tag{3.5}$$

and the additional parameters of the extended model are

$$\Delta_{\delta_n} \mapsto \Delta_{\delta_x} = \frac{\Delta_{\delta_n}}{\sigma_{n_0}} \quad \text{and} \quad \sigma_{\delta_n} \mapsto \sigma_{\delta_x} = \frac{\sigma_{\delta_n}}{\sigma_{n_0}} \,. \tag{3.6}$$

All parameters are determined from the ocean sample data set which is described in all details in chapter 6. Only measurements are regarded during which the quench was working properly, since there is a big difference in the background and its noise, which would distort the inferred parameters disproportionately. In total $T = 1302.8\,\text{h}$ of measurement time are analysed. For all mean parameters only detected atoms with a lifetime of $t > 100\,\text{ms}$ are taken into account, because the precise detection of shorter atoms might be dependent on the exact thresholds which are determined thereafter using in turn the inferred parameters of the model. The single atom signal parameters δ_n, n_1 and σ_{n_1} are calculated for each atom separately and afterwards the average over all 11 782 atoms is taken. All parameters are summarised in table 3.1. The background noise conforms to that of an ideal Poisson distribution with mean n_0 and $\sigma_{n_0} = \sqrt{n_0}$. In contrast the variance of the photon counts, when an atom is trapped, can not be explained by a pure Poisson process for counting photons, because $\sigma_{n_1} = 13.57 \geq \sqrt{n_1} = 11.0$.

An exponential decay with the mean lifetime τ

$$p(t) = \frac{1}{\tau} e^{-t/\tau} \tag{3.7}$$

is fitted to the histogram of the lifetimes of all detected atoms, which is plotted in figure 3.3a. The obtained mean lifetime of $\tau = 290\,\text{ms}$ is much shorter compared to the previous result in [4] of $\tau = 520\,\text{ms}$, which might be a consequence of the higher gas input and the reduction of the differential pumping tubes. Both facts increase the background pressure in the MOT and collisions with the background gas are more likely.

Table 3.1.: Compilation of all parameters describing the model of the APD signal.

	n [kcps] [6]	x
background:		
background mean photon number	$n_0 = 104.1$	$x_0 = 0$
background noise	$\sigma_{n_0} = 10.20$	$\sigma_{x_0} = 1$
one atom:		
single atom signal	$\delta_n = 15.9$	$\delta_x = 1.56$
mean photon number	$n_1 = 120.4$	$x_1 = 1.56$
standard deviation	$\sigma_{n_1} = 13.57$	$\sigma_{x_1} = 1.33$
mean lifetime	$\tau = 290\,\mathrm{s}$	
extended parameters:		
single atom signal difference	$\Delta_{\delta_n} = 16.0$	$\Delta_{\delta_x} = 1.57$
deviation of single atom signal	$\sigma_{\delta_n} = 0.094 \cdot \delta_n$	$\sigma_{\delta_x} = 0.094 \cdot \delta_x$
hopping probability	$p_h = 0.1625\,\mathrm{ms}^{-1}$	

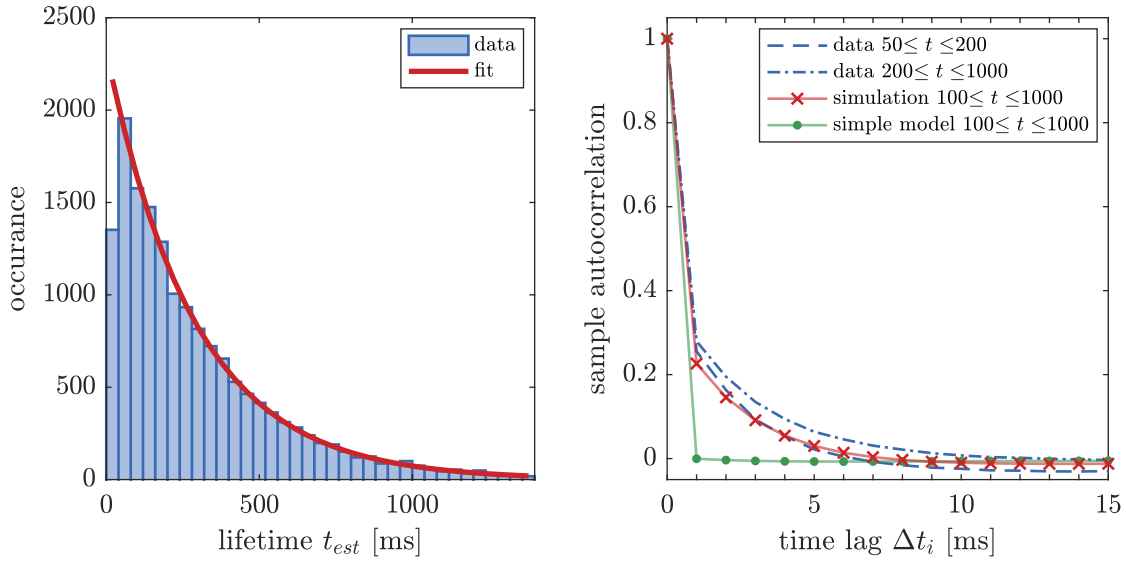

Fig. 3.3.: **a)** Histogram with a binning of 40 ms of the measured lifetimes t_{est}: The fitted curve follows an exponential decay described by equation 3.7 and yields to a mean lifetime of $\tau = 290\,\mathrm{ms}$. Atoms with a lifetime below 40 ms are underrepresented, since the detection fidelity decreases rapidly for shorter lifetimes (see also 3.7b).
b) Sample autocorrelation for the APD signal while an atom is trapped as a function of the time lag Δt_i: The autocorrelation of the data is slightly dependent on the range of lifetimes over which the average is taken. The simple model has no correlations included at all.

It is more difficult to find proper values for the extended model. The difference in the single atom signal of the two trap positions Δ_{δ_n} can be calculated directly, since it is the only parameter which accounts for the additional noise on the photon count rate beyond that of a Poisson distribution with mean n_1. From the discrepancy between the two variances $\sigma^2_{n_1}$ and $\sigma^2_{\text{Poisson}} = n_1$ one obtains:

$$\Delta_{\delta_n} = 2 \cdot \sqrt{\left(\sigma^2_{n_1} - n_1\right)} = 16.0 \tag{3.8}$$

The variation in the single atom signal Δ_{δ_n} and the hopping probability p_h are determined by minimising the residuals between the measured and simulated data in figure 3.6a. Figure 3.3b compares the resulting sample autocorrelation of the simulated photon signal of an atom to the data. Again, the autocorrelation is calculated for each individual atom separately and is averaged afterwards. The result of the measured data depends slightly on the range of lifetimes of the atoms, over which the average is taken and is in agreement to the simulation. The simple model shows no correlation at all.

Simulation

All simulated data are based on 10^6 simulated atoms using the parameters in 3.1. To consider erroneously detected atoms due to background noise, in total 10^4 h of background have been simulated. Both, the simulated atoms and the simulated background, are analysed identically to the real data as described in the following.

3.2.2. APD data analysis

The analysis of the APD data is structured in preselection with a much less strict acceptance threshold and a postselection during which every potential atom candidate is examined in all details. This procedure has the advantage that an adjustment of the final acceptance thresholds is possible without analysing the complete raw data again. Furthermore the separation between true atoms and background noise becomes clearly visible (see figure 3.6) and can be studied systematically.

Preselection

The preselection combines the 10 min APD-data frames together, links the metadata and logdata from the monitoring system and starts with an automatic error detection to identify the valid measurement times, where the system was able to detect atoms under comparable and stable conditions.

In the raw APD-data with 1 ms integration time most of the atoms disappear in the high background noise and are not clearly visible as it can be seen for the two short atoms in figure 3.4. The data are therefore filtered with a Gaussian filter, discretised by a binomial filter, which is defined as a cascade of the elementary smoothing mask $\mathcal{B} = [\mathbf{1}\,\mathbf{1}]/2$ [83]:

$$\mathbf{h} := \mathcal{B}^R = \underbrace{\mathcal{B}\mathcal{B}\ldots\mathcal{B}}_{\text{R times}} . \tag{3.9}$$

In practice a filter width of $R = 400$ turned out to be suitable, which corresponds to an effective width[7] of $\sigma_{bin} = 10$, which is shorter than 96.6 % of the atoms[8]. The filtered data are not longer uncorrelated and the noise suppression β is given by the convolution of the filter mask $\mathbf{h}$ with itself [83]:

$$\beta := \sqrt{\frac{\widetilde{\sigma}^2}{\sigma^2}} = \sqrt{(\mathbf{h} \circledast \mathbf{h})_0} = 0.168 \tag{3.10}$$

All parameters characterising the smoothed data are marked with $\sim$ and defined identically to the unfiltered ones. To make the parameters independent from the background again, they are transformed analogously to equation 3.3:

$$\widetilde{n} \mapsto \widetilde{x} = \frac{\widetilde{n} - \widetilde{n}_0}{\widetilde{\sigma}_{n_0}} \tag{3.11}$$

As soon as the lifetime of an atom is at least in the order of the effective filter width $\sigma_{bin} = 10$, the signal to noise ratio is enhanced by a factor of β^{-1} by this smoothing process:

$$\widetilde{\delta}_x = \beta^{-1}\delta_x = 5.95 \cdot \delta_x \tag{3.12}$$

The background photon number is calculated adaptively with a running average of size 10 000 $\widehat{=}$ 10 s everywhere where there are no atoms. Long-term drifts due to slow variations in the laser power are compensated by this adaptive background. As soon as the signal exceeds a preselection threshold $\widetilde{x} \geq \hat{\widetilde{x}}_{\text{pre}\uparrow}$, the averaging of the background is interrupted until the signal falls below a second threshold $\widetilde{x} < \hat{\widetilde{x}}_{\text{pre}\downarrow}$. Such an event is stored for further analysis as an preselected atom candidate. A dead time of 100 ms prevents the algorithm to trigger more than once per atom, even if the noisy signal undershoots the threshold while an atom is trapped. The preselection threshold $\hat{\widetilde{x}}_{\text{pre}\uparrow}$ must be compromised between the risk, that an atom is missed and an unnecessarily huge number of preselected atom candidates, which are generated by the background noise (compare figure 3.6a). In practice it turned out that $\hat{\widetilde{x}}_{\text{pre}\uparrow} = 4.5$ and $\hat{\widetilde{x}}_{\text{pre}\downarrow} = 1$ are suitable values.

[7] For comparison: A box filter integrating over 40 ms has an effective width of $\sigma_{\text{box}} = 11.5$ [83].

[8] To speed up the calculation the filter mask $\mathbf{h} = [\ldots, h_{-2}, h_{-1}, h_0, h_1, h_2, \ldots]$ is reduced to its central part, where for the coefficients h_i applies $h_i \geq 0.001 \cdot h_0$, which is only about 18 % of the original filter.

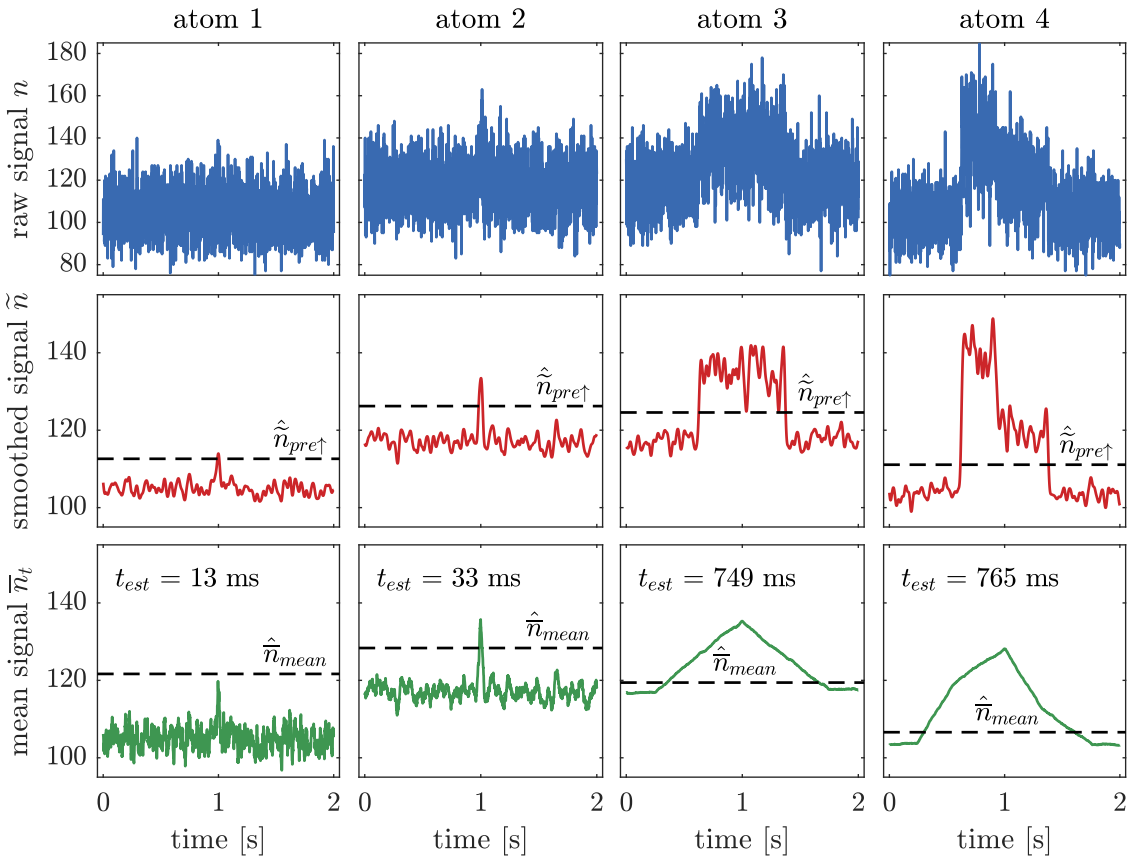

Fig. 3.4.: The raw and the smoothed APD signal for four representative (preselected) atoms:

1. row: In the raw data, with 1 ms integration time, especially short atoms are not clearly visible.
2. row: By smoothing the data with the Gaussian filter, the signal to noise ratio is increased. The horizontal lines indicate the preselection thresholds.
3. row: For illustration of the mean criterion, the raw data are filtered with an individual box filter with a width of the estimated lifetime t_{est}. The horizontal lines indicate the corresponding postselection threshold. For longer atoms the noise of the background is suppressed much more and a lower absolute threshold is set. Atom **1** is too short to be identified, since it does not fulfil the mean criterion and is deselected during the postselection process.

For this illustration all data and thresholds are plotted in or transformed into the unnormalised frame. Atom **4** shows the typical signal of two atoms trapped in the MOT at the same time, which is discussed in detail in section 3.2.3.

Postselection

In a second step all atom candidates are examined in more detail. Therefore a more precise estimation of the exact atom position in time is necessary. In the simplified atom picture only half of the filter overlaps with the atom at time $t_\uparrow$ and the filtered signal is 50 % of the single atom signal $\widetilde{\delta}_x$, which is depicted in figure 3.5a. The beginning $t_\uparrow$ and the end $t_\downarrow$ of a trapped atom can thus be estimated by the point in time when the smooth signal rises above the threshold $\widetilde{x} \geq \hat{\widetilde{x}}_{t_{\text{est}}} = 0.5 \cdot \widetilde{\delta}_x$ for the first time or falls below the threshold $\widetilde{x} < \hat{\widetilde{x}}_{t_{\text{est}}}$, respectively.

Figure 3.5b shows the discrepancy between the initially simulated lifetime t_{sim} and the estimated one t_{est}. Atoms which are not detected at all are not considered in this plot. There is a good agreement for the simple model and lifetimes above $t = 40\,\text{ms}$. Shorter atoms are not covered by the complete core of the filter mask at any time and therefore not detected (see figure 3.7b), but if they are, their lifetime is overestimated[9]. In the extended atom model the lifetimes of the atoms are slightly underestimated by about 3 ms due to the jumps in the atom signal which can also lead to a reduced signal at the edges of the atoms. This effect is difficult to quantify because of the randomness of the jumps and is therefore not considered.

Atom acceptance

Two different criteria for a decision rule to accept a preselected atom as a real atom are considered and compared:

Maximum criterion One simple method is to use the maximum of the smoothed data $\max_t(\widetilde{x})$ between $t_\uparrow$ and $t_\downarrow$. If this maximum exceeds the threshold $\hat{\widetilde{x}}_{\max}$ an atom is accepted:

$$\max_t (\widetilde{x}) \geq \hat{\widetilde{x}}_{\max} \tag{3.13}$$

This criterion is simple to implement and robust if the position in time is not estimated correctly, but might not take all photons from the atom into account. Since it is based on the smoothed data, the signal of shorter atoms is reduced, because the smoothing mask has in this case only a small overlap with short atoms.

Mean criterion To overcome this disadvantages the mean $\overline{x}_t$ of the raw, unfiltered APD signal between $t_\uparrow$ and $t_\downarrow$ is considered and compared with the background noise. Taking the mean over the lifetime t is equivalent to a box filter of length t, which suppresses the noise by a factor of $1/\sqrt{t}$. Thus for threshold relative to the background noise the mean $\overline{x}_t$ is scaled by $\sqrt{t}$. The average signal of longer atoms must not be as high as the one of shorter atoms to have the same

[9] Reference [4] proposes therefore a smoothing with a set of box filters with a broad range of time constants. This approach needs a lot of extra computational power and as soon as the correlations of the filtered data are treated correctly no improvements compared to the method described in this theses have been observed.

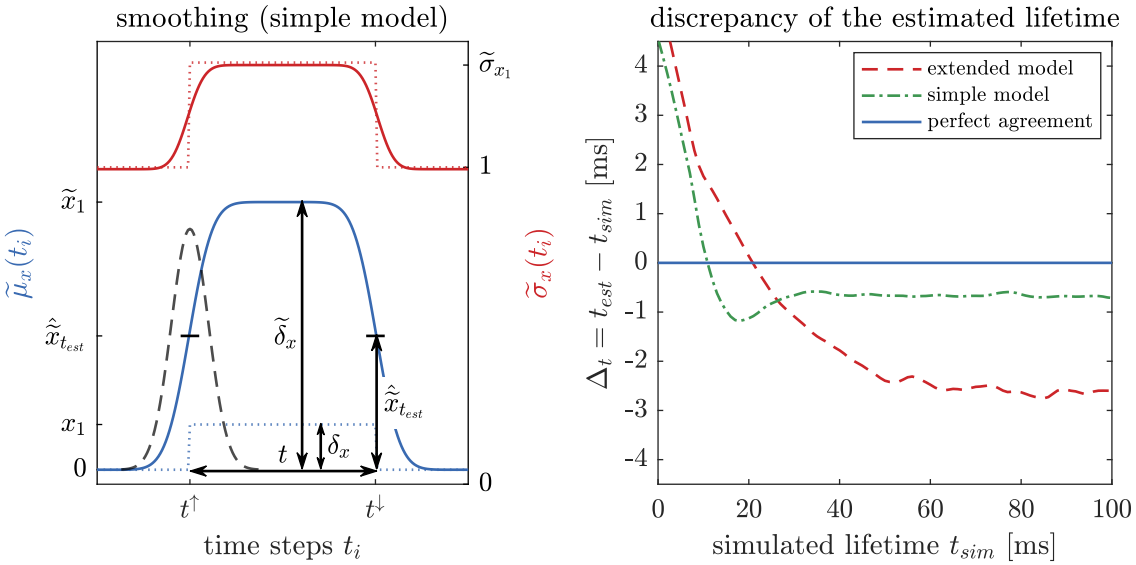

Fig. 3.5.: **a)** Smoothing the APD signal in the scope of the simple model. The unfiltered data are plotted with a dotted line. In contrast to figure 3.2, this figure is given in the normalised coordinates x and $\widetilde{x}$, respectively. In this frame the noise stays constant, but the single atom signal is amplified by β^{-1}. The exact atom position in time can be estimated when the smoothed signal reaches half of the single atom signal $\widetilde{\delta}_x$ (threshold $\hat{\widetilde{x}}_{t_{\mathrm{est}}}$). At that point half of the filter mask (dashed line and enlarged) overlaps with the atom.
b) Difference $\Delta_t = t_{\mathrm{est}} - t_{\mathrm{sim}}$ between the initially simulated lifetime t_{sim} and the estimated one t_{est}. The straight line indicates a perfect agreement. The lifetimes of atoms simulated with the extended model are a little bit underestimated by $\sim$3 ms. Atoms shorter than 40 ms are too short to be localised correctly.

significance, which is illustrated in figure 3.4. An atom is counted as soon as the scaled mean $\overline{x}_t \cdot \sqrt{t}$ is bigger than the threshold $\hat{\overline{x}}_{\text{mean}}$:

$$\overline{x}_t \cdot \sqrt{t} \geq \hat{\overline{x}}_{\text{mean}} \tag{3.14}$$

By this criterion all detected photons from a trapped atom are included and there is no smoothing with the background at the edges of the atom signal. The exact shape of the atom signal doesn't play any role, so that the simple and the extended atom model should behave very similarly.

Figure 3.6 shows the histograms of the maximum $\max_t(\widetilde{x})$ of the smoothed data and the mean $\overline{x}_t$ of the raw data respectively of all atom candidates. The extended model describes both values very well. In contrast to this, the simple model can not explain the maximum of the smoothed data $\max_t(\widetilde{x})$ at all. Since the mean of the atom signal is independent from its exact shape, there is no difference between the two models for the mean $\overline{x}_t$. The signal from atoms generated by the background becomes dominant at the lower bound of the histograms and is clearly separated. The simulation slightly underestimates the background, which might be an indication that there are some rare fast fluctuations which are not included in the simulations. The clear cut at $\overline{x}_t = 4.5$ in the histogram of the maximum criterion is caused by the preselection threshold $\hat{\widetilde{x}}_{\text{pre}\uparrow} = 4.5$, which results in a rate of 1.6 preselected atoms per hour triggered by the background noise. In fact, the preselection is identical to the maximum criterion with the lower threshold $\hat{\widetilde{x}}_{\text{pre}\uparrow}$. In contrast to this, the histogram of the mean criterion is washed out at the lower bound, because for small mean $\overline{x}_t$ values the probability that an atom fails already at the preselection is high.
In order to find the optimum thresholds $\hat{x} \in \{\hat{\widetilde{x}}_{\max}, \hat{\overline{x}}_{\text{mean}}\}$ and to compare the two criteria a compromise has to be found between

- $\lambda_{\text{bg}}(\hat{x})$ the rate of erroneously counted atoms, which are generated by the background noise[10]
- $p(\hat{x})$ the probability that a real ^{39}Ar atom is detected

The chosen approach maximises the probability $p(\hat{x})$ under the constraint that the background atom rate $\lambda_{\text{bg}}(\hat{x})$ does not exceed a given limit $\hat{\lambda}_{bg}$:

$$\lambda_{\text{bg}}(\hat{x}) \leq \hat{\lambda}_{bg} \; . \tag{3.15}$$

The calculation of the rate of erroneously counted atoms $\lambda_{\text{bg}}(\hat{x})$ is based on a simulation of 10^4 h of background noise. The probability to detect an atom $p(\hat{x})$ is plotted in figure 3.7a as a function of the background atom rate $\hat{\lambda}_{bg}$. Since the mean criterion is slightly better and independent from the exact atom model, this criterion is used[11].

[10] The background rate $\lambda_{\text{bg}}(\hat{x})$ can be mathematically treated and corrected identically to the cross sample contamination (see 3.3.1), but this effect is negligibly small for the chosen design parameter $\hat{\lambda}_{bg} = 10^{-2}$.

[11] One might think of a combination of both criteria (for example an and- or an or-combination) or lifetime t dependent thresholds, but for both ideas no improvement could be observed.

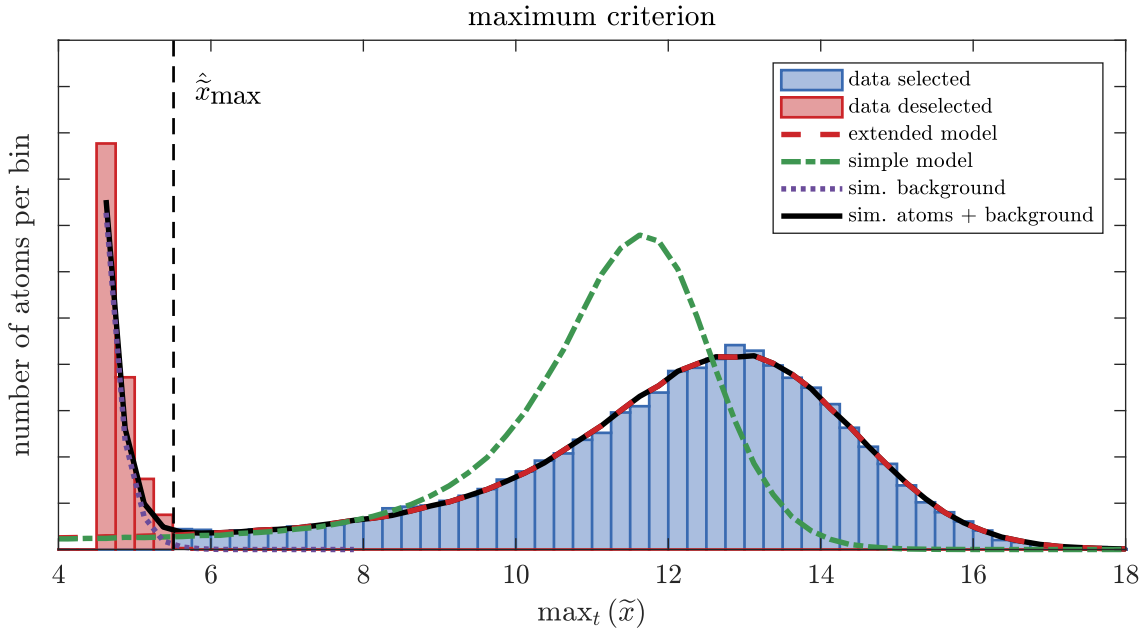

(a) Maximum criterion $\max_t \widetilde{x}$

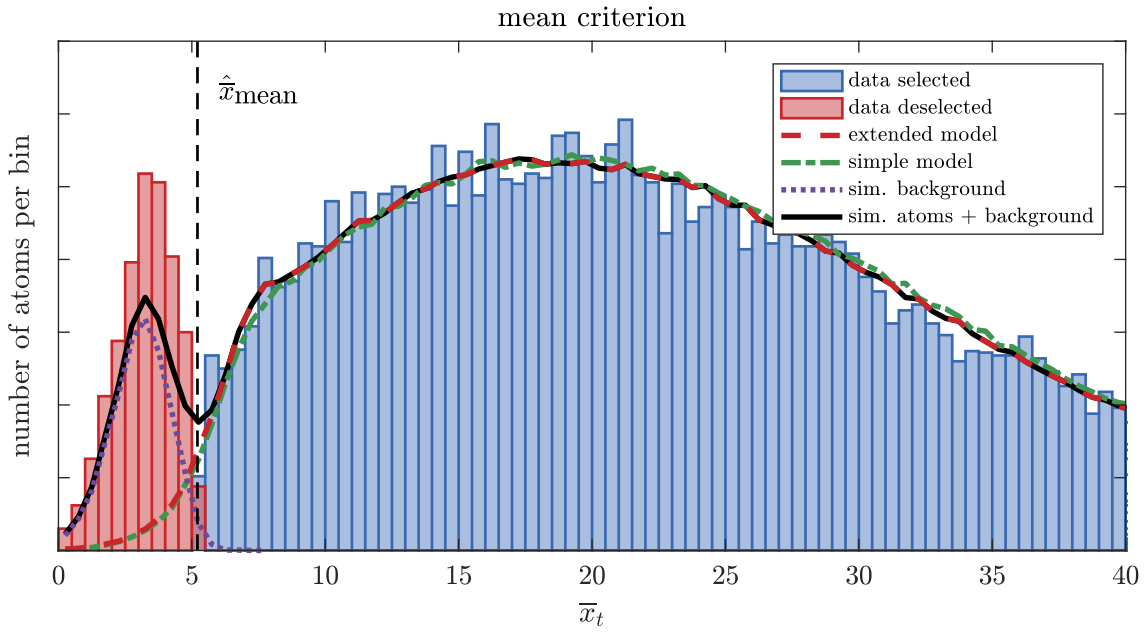

(b) Mean criterion $\overline{x}_t$

Fig. 3.6.: Histogram of all atom candidates compared with the simulated atoms and the background noise. The vertical lines indicate the optimal threshold for a maximal background rate of $\hat{\lambda}_{bg} = 10^{-2}$ atoms/h. Both histograms show a clear separation between atom candidates generated by the background noise (left side of the histogram) and trapped real atoms. For more details it is referred to the main text.

As a design parameter the background rate is limited to $\hat{\lambda}_{bg} = 10^{-2}$. From that a postselection threshold of $\hat{\overline{x}}_{\text{mean}} = 5.21$ is calculated and we get the following final decision rule from the **mean criterion**:

Final decision rule for the identification of an atom:

If the mean $\overline{x}_t \cdot \sqrt{t}$ of the raw, unfiltered APD signal between $t_\uparrow$ and $t_\downarrow$ exceeds the postselection threshold $\hat{\overline{x}}_{\text{mean}} = 5.21$, the preselected atom is accepted as an atom.

$$\overline{x}_t \cdot \sqrt{t} \geq \hat{\overline{x}}_{\text{mean}} = 5.21 \tag{3.16}$$

This means, that the mean atom signal must be higher than 5.21 standard deviation of background noise. The detection probability is 94 % and the rate of falsely detected atoms is 1 atom in 100 h. All other atoms are too short to be reliably detected, which is plotted in figure 3.7b. For atoms with lifetimes below 40 ms the detection probability decreases rapidly. The mean criterion is especially for shorter atoms slightly better, since all detected photons are taken into account.

Table 3.2.: Summary of all thresholds

threshold	value
preselection start: $\widetilde{x} \geq \hat{\widetilde{x}}_{\text{pre}\uparrow}$	4.5
preselection stop: $\widetilde{x} < \hat{\widetilde{x}}_{\text{pre}\downarrow}$	1
time estimation: $\widetilde{x} \geq \hat{\widetilde{x}}_{t_{\text{est}}}$	4.69
dead time:	100 ms
postselection maximum criterion: $\max_t(\widetilde{x}) \geq \hat{\widetilde{x}}_{\text{max}}$	not applied
postselection mean criterion: $\overline{x}_t \cdot \sqrt{t} \geq \hat{\overline{x}}_{\text{mean}}$	5.21
double atom detection: $\max_t(\widetilde{x}) \geq \hat{\widetilde{x}}_{\text{double}}$	19.0

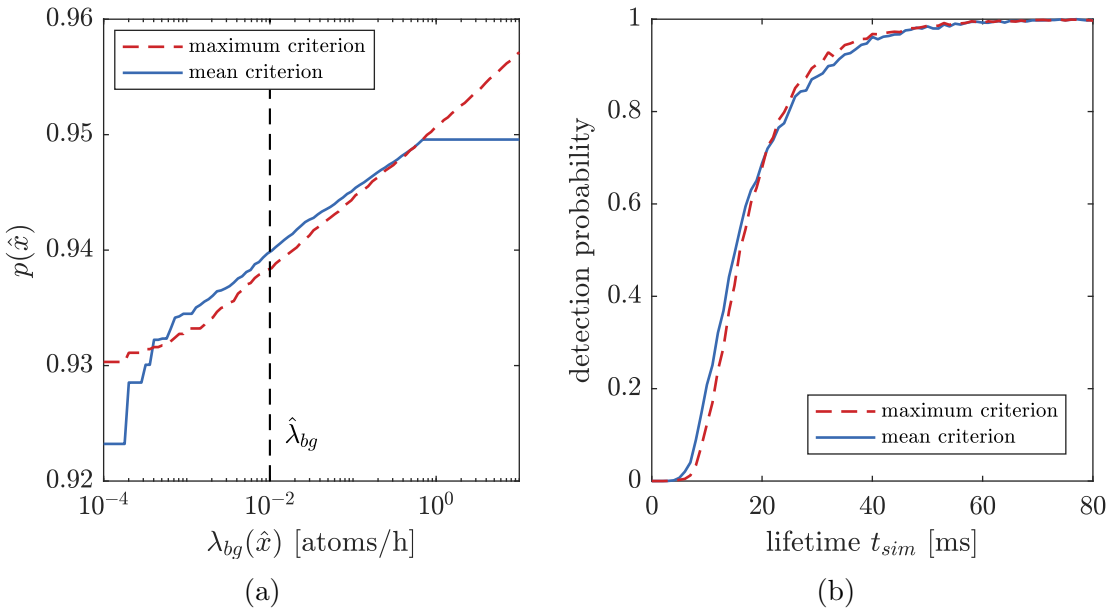

Fig. 3.7.: **a)** Detection probability $p(\hat{x})$ as a function of the background atom rate $\hat{\lambda}_{bg}$: The steps for very low background rates originate from the statistic of rare events, although the data are based on 10^4 h of background simulation. The kink in the mean criterion at a background rate of $\hat{\lambda}_{bg} \approx 0.8\,\text{atom/h}$ originates from the preselection which limits the background rate. The vertical line indicates the limit of the background rate $\hat{\lambda}_{bg} = 10^{-2}$, which is chosen as a design parameter for all measurements in this thesis.
b) Detection probability dependent on the lifetime of the atoms t_{sim} for maximum background rate of $\hat{\lambda}_{bg} = 10^{-2}$: The mean criterion is for shorter atoms slightly better, since all photons are taken into account.

3.2.3. Double atoms detection

The rate of two atoms trapped in the MOT at the same time is given by the atom count rate λ and the mean lifetime τ of the atoms:

$$\lambda_{\text{double}} = \lambda^2 \cdot \tau \tag{3.17}$$

Estimating λ_{double} for the ten-time enriched $60X_{\text{dil}}$ reference sample (see 5.1) results in $\lambda_{\text{double}} \approx 0.3$ double atoms per hour and about 63 double atoms for the complete ocean sample data set. The scatter plot 3.8a shows the estimated lifetime and the maximum criterion[12] of all accepted atoms. A reasonable threshold of $\hat{\tilde{x}}_{\text{double}} = 19.0$ is chosen. The corresponding probability to detect a single atom erroneously as a double one is only in the order of 1.1×10^{-5}. Thus all 32 outliers which fulfil $\max_t(\tilde{x}) \geq \hat{\tilde{x}}_{\text{double}}$ can be clearly identified as double atoms. However, this criterion finds only about 50 % of the expected events with two atoms at the same time. Some atoms with far above-average estimated lifetimes t_{est} might belong to two atoms which are too close together to be separated. But they can not be distinguished from one atom with a very long lifetime.

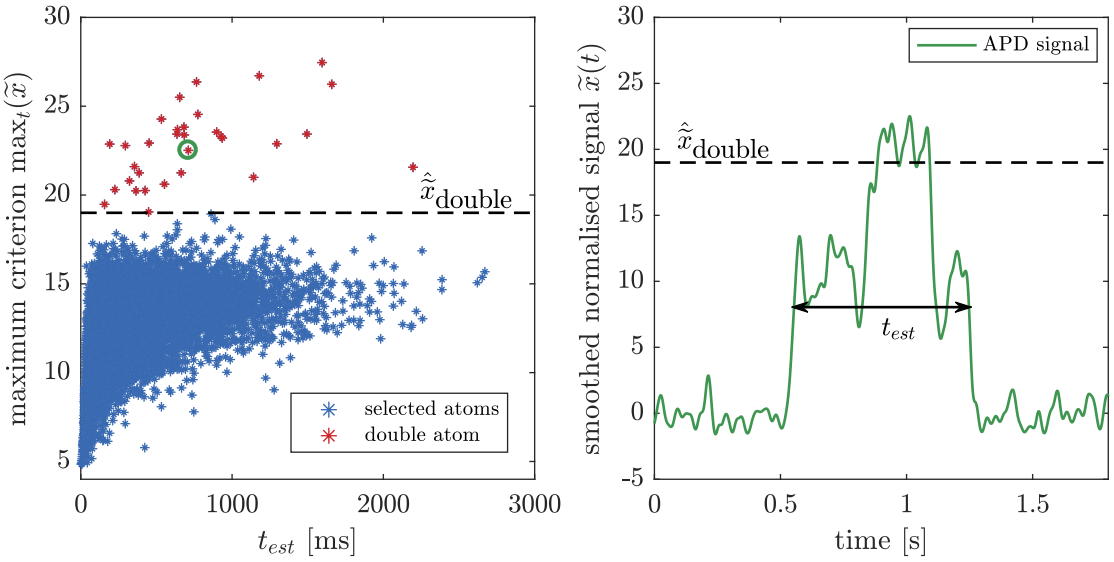

Fig. 3.8.: **a)** Scatter plot of all 16 013 selected atoms of the ocean measurement period: The horizontal line marks the threshold $\hat{\tilde{x}}_{\text{double}}$ above which an atom is counted as a double one. In the ocean data 32 double atoms are identified. **b)** Filtered APD signal of a typical double atom (marked with a circle in the scatter plot). The discrete step of one and two atoms in the trap is clearly visible.

[12] The mean criterion is inappropriate to detect double atoms, since the time in which both atoms are in the MOT can be much shorter compared to the estimated lifetime t_{est}.

3.2.4. Possible improvements

The discussion of the APD signal analysis is finally concluded with the question how an improved atom signal can increase the reliability of the atom detection. The two main parameters are the normalised single atom signal δ_x, which describes the signal to noise ratio, and the mean lifetime τ. Both together give the sum of all photons collected from one single atom compared to the background. In figure 3.9 the simulated detection probability is plotted as a function of the normalised single atom signal δ_x or the mean lifetime τ, respectively. There is a rapid decrease in the detection fidelity below the parameter of the current system. Small variations in the atom signal, e.g. if the position of trapped atoms is moving out of the focus, or in the lifetime might influence the atom count rate. Thus for a constant and comparable detection efficiency it is important to have a stable atom signal. An increase in one or both of these parameters can gain a few percent in the detection probability, or, which might be even more important, bring the atom detection to a more robust regime.

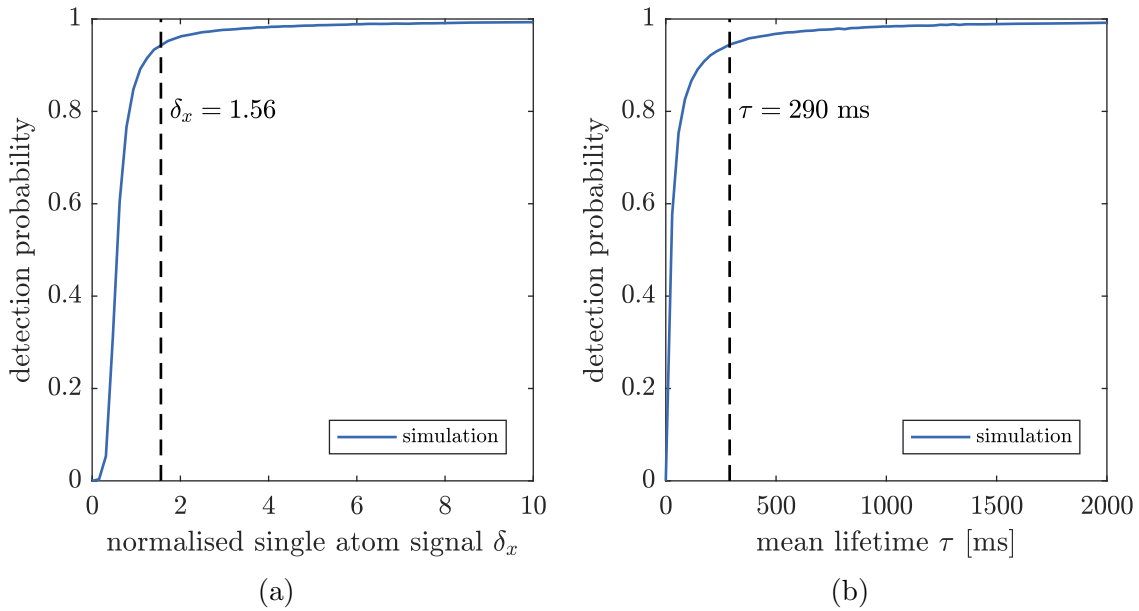

Fig. 3.9.: Simulated detection probability as a function of

a) the normalised single atom signal δ_x: The noise of the atom signal σ_{x_1} is scaled with respect to δ_x. All other parameters are kept fixed, in particular $\tau = 290\,\text{ms}$.

b) the mean lifetime τ: All other parameters are kept fixed.

The vertical lines mark the current parameters of the current system summarised in table 3.1.

3.3. Calculation of the ^{39}Ar concentrations

The analysis of the APD signal of the previous section gives a total number of counted atoms N and the total measuring time T for each measurement which was analysed, together with some additional information from the monitoring system. To proceed with the calculation of the ^{39}Ar concentration, each measurement must now be analysed in a broader context. Important are the reference count rate, which quantifies the current efficiency of the ATTA-apparatus, and the contamination of the system. The reference can change due to instabilities from one to another or even during a measurement. In contrast, the contamination which is embedded in the vacuum system is a characteristic parameter of the ArTTA-apparatus, which changes only significantly if there is a major modification at the vacuum system.[13] This section is subdivided into two subsections. Firstly, a general model including contamination is discussed to describe the measurements, whereby the two main parameters (the contamination rate a and the reference count rate ν_0) are investigated in more detail. Finally a Bayesian approach based on this model is applied for the statistical inference of the measured concentration.

3.3.1. General contamination model

The aim of the following section is to develop a general model describing the counted number of atoms N, which includes cross sample contamination from previous measurements and long-term contamination which is embedded in the vacuum system, without going into the details of the exact contamination mechanism. Therefore the sample volume inside the vacuum and the effective volume implanted in the surface of the apparatus are considered as distinct reservoirs. This situation is depicted in sketch 3.10a.

Additionally to the Ar-gas volume[14] V with an ^{39}Ar concentration c_{sample}, there might be a leftover volume V_{cross} with concentration c_{cross} from previous measurements, which is diluted by the sample volume V. This contamination is referred to as *cross sample contamination* in the following and can give an offset on the measured sample concentration c_{sample}, which is independent from the measurement time. Furthermore, there is an exchange, with rate a, between the surface reservoir and the sample volume[15]. This results in accumulation of ^{39}Ar inside the sample over time and thus in an increasing count rate, which is demonstrated in figure 3.10b. Since the exchange with the surfaces is driven by the discharge of the RF-source, the time t_s since the source has been switched on and not the measurement time must be taken into account. This time dependent component is named *contamination* in the following. Our observations indicate that this part is dominated by the contamination

[13] The contamination might changes for different plasma modes of the source. Since the source was always operated in the same mode, this effect was not investigated.

[14] To be precise, V is a gas amount and given in mL STP , not a volume. However *gas volume* is used synonymously for *gas amount*.

[15] Due to the resulting similarity to the equation of motion, we sometimes call a the *contamination acceleration*.

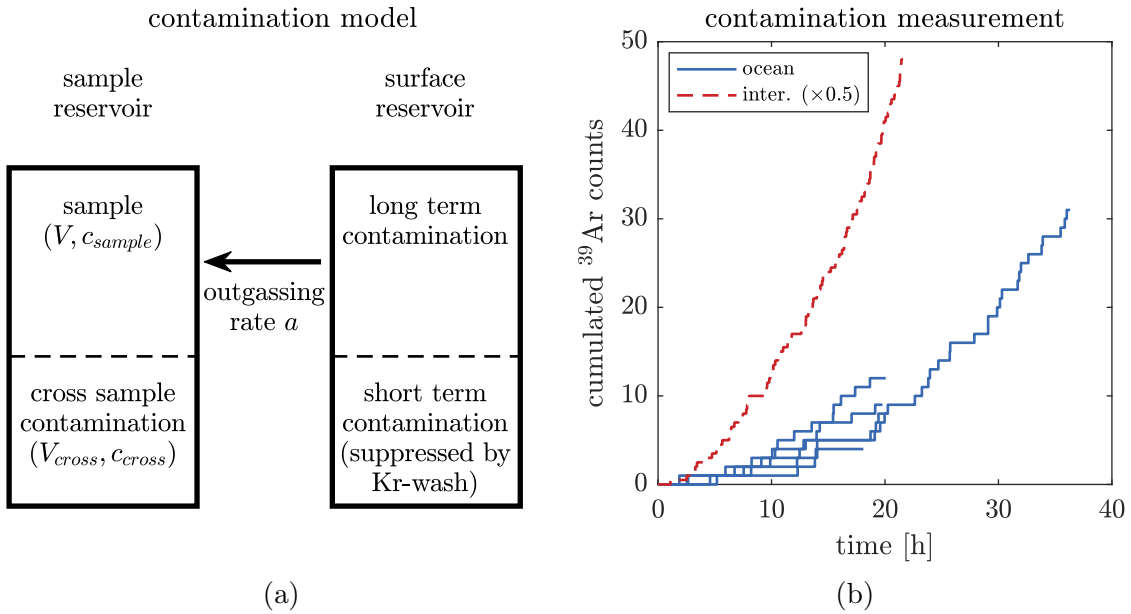

Fig. 3.10.: **a)** General contamination model: The sample volume inside the vacuum and the effective volume of the surfaces are considered as two distinct reservoirs. There is an ^{39}Ar-gas exchange with rate a between the surface and the sample reservoir, which contaminates the sample. Remnant of argon from the previous measurement in the sample is referred to as cross sample contamination. A short term contamination, mainly effected by the cool parts of the source, is suppressed by a Kr-wash. For more details it is referred to the text.

b) Cumulated ^{39}Ar-counts as a function of time during the contamination measurements with an ^{39}Ar-free sample and comparable values of ν_0/V. The measurement from the intercomparison study is scaled by a factor of 0.5 to fit better to the scale of the diagram. Clearly visible is the quadratic behaviour of equation 3.19. Between the ocean and the intercomparison studies a major part of the vacuum system was replaced and the contamination was improved by a factor 5.6 thereby.

as a consequence of optimisation with up to 10^6-times enriched samples at least five years ago. Even if the main parts of the vacuum system have been replaced, there is still a significant contamination left, and as soon as there is no modification of the system, the exchange rate a of this long-term contamination can be treated as constant and is not influenced by the measurement process. The volume of the cross sample contamination V_{cross} as well as the exchanged volume with the surface reservoir is small compared to the sample volume V. Therefore the total amount of argon inside the sample reservoir is assumed to be constant in time and equal to the sample volume V. From this considerations we get the following time dependent ^{39}Ar-concentration:

$$c(t) = \underbrace{c_{\text{sample}}}_{\text{sample}} + \underbrace{c_{\text{cross}} \cdot \frac{V_{\text{cross}}}{V}}_{\text{cross sampling}} + \underbrace{\frac{a}{V} \cdot t_s}_{\text{contamination}} \quad . \tag{3.18}$$

Because of the high ^{39}Ar abundance of the contamination, saturation effects should not be an issue during the typical time range of one day. An integration over time gives the expected total average number of counted atoms λ_N:

$$\lambda_N(t) = \left(\left(c_{\text{sample}} + c_{\text{cross}} \cdot \frac{V_{\text{cross}}}{V} \right) \cdot \underbrace{(t - t_0)}_{=:T} + \frac{a}{V} \cdot \frac{1}{2} \underbrace{\left(t^2 - t_0^2\right)}_{=:T^2} \right) \cdot \nu_0 \, . \tag{3.19}$$

As a consequence of the quadratic term it is principally important to consider the start point of the measurement $t = t_0$ related to the start point of the plasma $t = 0$, particularly if a failure makes an exclusion of part of the measurement time in between necessary. But for simplification this disquisition is not written explicitly in the following and shortened sloppily to the quadratic measurement time T^2. Another consequence of the T^2 dependency is a limit of the maximal measurement time. After a certain time the contribution to the counted atoms due to contamination will exceed the contribution by the sample itself and the uncertainties will increase further with longer measurement times again. This limit can be suppressed by splitting a bigger sample into smaller parts and measure them separately.

The *generalised referenced count rate* ν_0 related to a reference concentration c_0 must not be mandatorily the atmospheric one. The concentrations c_{sample} and c_{cross} and the contamination rate a are then given in units relative to c_0. This means, the unit of the contamination rate a is $[\mu\text{L STP c}_0\ \text{h}^{-1}]$ or in other words, a contamination of $a = 1000\,\mu\text{L STP c}_0\ \text{h}^{-1}$ increases the concentration of a 1 mL STP sample by one reference concentration c_0 per hour. All results presented in this thesis are finally normalised to the atmospheric concentration $c_0 = c_{\text{atm}}$ to give comparable values. The contamination rate a is a parameter particular to the vacuum system and requires a reevaluation, if changes are made to the chamber. Table 3.3 summarises the contamination rates a for the three measurement periods treated in this thesis. By replacing the main chamber and the collimator a reduction by nearly a factor 5.6 could

be achieved. Since the vacuum system was comparable for the ice and intercomparison studies, there should be no significant difference in the contamination rates. The lower rate for the antecedent ice measurement period might be due to systematic effects measuring very small sample sizes in the range of $100\,\mu$L STP , which were mainly used to determine the contamination for the ice measurements.

Table 3.3.: By the atmospheric count rate normalised contamination rates a of the different measurement periods discussed in this thesis

measurement period	contamination a [μL STP c_{atm} h^{-1}]	outgassing $^{39}Ar - atoms/h$
ice samples	$67.0^{+3.3}_{-3.3}$	∼1460
intercomparison study	$93.0^{+6.1}_{-5.8}$	∼2027
ocean samples	$16.5^{+2.2}_{-2.0}$	∼360

3.3.2. Analysis of the contamination

The contamination can be quantified with help of the argon free underground sample, which is presented in chapter 1.4. This sample can be used in a two fold function: On the one hand as a blank sample with $c_{sample} \approx 0$ in equation 3.19, so that all counted ^{39}Ar-atoms can definitely be identified as (cross sample) contamination. The cumulated sum of counted ^{39}Ar atoms as a function of time for typical contamination measurements is plotted in figure 3.10b. The quadratic behaviour of equation 3.19 is clearly visible.

On the other hand the ^{36}Ar-abundance of this very special sample originating from the earth's mantle is depleted by a factor 45 compared to environmental argon (see chapter 1.2.1). This fact can be utilised to quantify the typical volume of the cross sample contamination V_{cross} and the exchanged argon volume with the surface reservoir of the long-term contamination. Measuring the $^{36}Ar/^{40}Ar$-ratio has the advantage of giving a unique direct handle on the Ar-outgassing rate driven by an Ar-plasma and can be observed parallel to the standard measurement process. The time evolution of the $^{36}Ar/^{40}Ar$-ratio, measured with the residual gas analyser during counting the underground sample, is shown in figure 3.11a. From the excess ^{36}Ar the admixture of natural argon can be calculated. The intercept gives a limit on the cross sample volume V_{cross}:

$$V_{cross} \leq 5\,\mu\text{L STP} \quad . \tag{3.20}$$

Since this value is much smaller compared to any practicable sample volumes, the cross sampling term in equation 3.18 and 3.19 is insignificant and neglected in the following.

The flux of outgassing argon $\dot{V}_a$ can be inferred from the slopes of the $^{36}Ar/^{40}Ar$-ratio[16]. The clustering of the data indicates that there are two different modes, one with a high and one with a low outgassing rate, which might be due to different modes of the RF-source. But this observation is not explained satisfactorily and needs further investigations.

$$\dot{V}_a = \frac{\frac{\mathrm{d}\left(^{36}\mathrm{Ar}/^{40}\mathrm{Ar}\right)}{\mathrm{d}t}}{\left(^{36}\mathrm{Ar}/^{40}\mathrm{Ar}\right)_{\mathrm{atm}}} \cdot V = \begin{cases} 2.6\,\mu\mathrm{L\,STP\ /h} & \text{upper three slopes} \\ 1.6\,\mu\mathrm{L\,STP\ /h} & \text{lower two slopes} \end{cases} \tag{3.21}$$

Assuming an average of $\dot{V}_a = 2.2\,\mu\mathrm{L\,STP\ /h}$ gives an ^{39}Ar-concentration of the outgassing argon of 7.5-times the atmospheric one for the present system.

A 40 min to 60 min Kr-wash was included before all measurements of the ocean measurement period. A potential short time ^{39}Ar-contamination is thereby replaced by krypton. The main mechanism for this fast outgassing can be identified to be dominated by adsorbed argon to the liquid nitrogen cooled parts of the source. For more details it is referred to the ocean chapter 6.2.2. Since these processes are not well controlled and strongly influenced by the exact operation of the previous measurements, this type of short term contamination varies widely, which can be seen in the Kr-outgassing during the contamination measurements plotted in figure 3.11b. The Kr-fraction increases rapidly in the first 5 h and saturates then. This uncontrolled fast term contamination is difficult to quantify and, at least for the ocean samples, suppressed by the flushing process and therefore not considered.

A slightly different contamination model for Kr-ATTA is discussed in [84]. As a consequence of the by more than two orders of magnitude smaller Kr-sample sizes compared to ArTTA, a precise quantification of contamination is essential. On the other hand the measurement times are with 1 h for ^{85}Kr much shorter, so that cross sample contamination is dominating. The used model also considers the influence of the current measurement on the ^{85}Kr-concentration of the outgassing isotopic ratio in future. The current outgassing rate is measured prior to each measurement with an active Ar-plasma and is then extrapolated to the Kr. It is found out that flushing a Kr-system by Kr instead of Ar is 2.4-times more efficient.

3.3.3. Reference and stability

The ^{39}Ar count rate of a sample with unknown concentration alone has no significance. Only combined with the reference count rate ν_0 of a well known sample with a defined concentration c_0 allows a determination of the unknown ^{39}Ar concentrations. The reference affects the precision of each measurement essentially and it is therefore necessary to have a precise reference count rate and to ensure that all reference measurements are comparable to the measurements of the unknown concentrations. The latter is in general very difficult to test at a high statistical significance and can

[16]Since these results are performed after a Kr-wash, they can not be transferred directly to the ice and intercomparison measurements. There are no data with sufficient quality without a previous Kr-flushing available, due to a degenerating of the RGA.

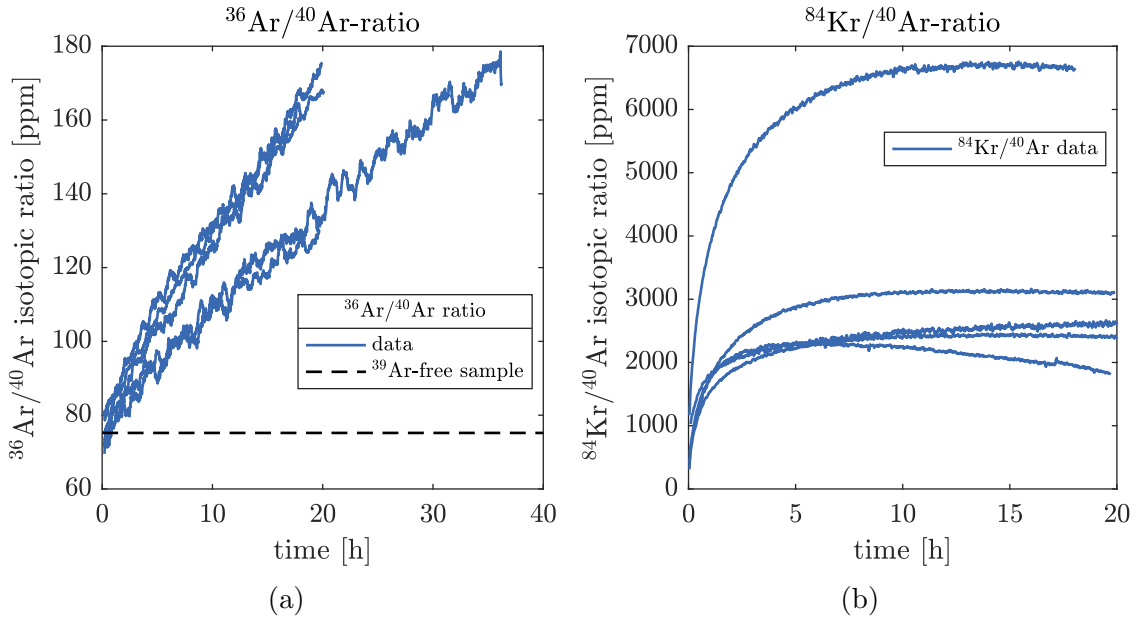

Fig. 3.11.: Time evolution of ^{36}Ar **(a)**) and ^{84}Kr (**b**)) during the five contamination measurements of the ocean sample measurement period using an ^{36}Ar-depleted underground sample. The stable isotope ratios are measured with the residual gas analyser (RGA). The intercept and the slope can be used to study cross sampling or the long-term contamination, respectively. It should be noted that these measurements were performed after a 40 min to 60 min Kr-wash and might not represent the situation of the ice and intercomparison measurements. The ^{36}Ar-signal indicates that there are two different modes of the system, one with a high and one with a low outgassing rate. The exact reason for these two discrete modes is unclear. The leveling of the ^{84}Kr-curves indicates a more uncontrolled fast contamination component as well, which is suppressed by cleaning the system with Kr-discharge. All ratios are not corrected for the slightly different sample volumes of about 2 mL STP .

only be assumed from the stability of additional monitoring data in most cases. It must be compromised between the statistic uncertainty mainly given by the number of reference measurements and its integrated counting time and the time gap between the reference and the unknown sample, which makes fluctuations or drifts more likely. Two different strategies are used in the context of ArTTA so far:

Global atmospheric reference: Easily available atmospheric bottle argon is used as reference sample and the analysis of unknown concentrations is embedded in a huge set of atmospheric measurements. Due to the relatively low count rate, most of the time is needed for referencing, and averaging of several atmospheric measurements is necessary. This approach was used for the first groundwater studies in [43, 4, 44], which were run in the throughput mode, as well as for the ice and intercomparison measurements discussed in chapter 4 and 5 respectively. A long-term stability is indispensable for this strategy. Since there is up to 10 % discrepancy between the less efficient throughput mode compared to operation in recycling configuration, additional uncertainties are introduced by normalising recycling measurements with a throughput reference, which would decouple the problem of contamination from the references in principle. This fact was disregarded for the ice samples reported in chapter 4.

Local or global reference with an enriched sample: The statistics of the reference can be enhanced by using slightly enriched ^{39}Ar samples, which was tested with a ten-times enrichment in the context of the ocean samples presented in chapter 6. Due to the higher statistics it is possible to consider only a few references in the neighbourhood of the unknown sample or even reference on a daily basis might be possible in the future. Long-term drifts and fluctuations in the counting efficiency can be compensated thereby. However, this strategy has the disadvantage compared to an atmospheric reference, that the uncertainty of the enrichment, which must be measured with a very high precision once, enters into the over-all uncertainties of the ArTTA method. Furthermore, a cross sample contamination between the enriched reference and the natural sample with a much lower ^{39}Ar abundance might be the consequence. An additional flushing process in between the reference and the natural samples included into the measurement routine, as presented in section 6.2.2, can reduce this risk.

State of the art ATTA-devices for the two rare Krypton isotopes ^{85}Kr and ^{81}Kr pursue a third strategy and utilize the stable ^{83}Kr isotope with a relative natural abundance of 11.5 % as a reference. A switching between the rare isotope and ^{83}Kr on a minute time scale can enable a very precise reference [85]. However, a Kr-reference sample is measured after each unknown sample to ensure stable operation and to calibrate the ^{83}Kr-reference. A possible adaptation of this strategy to argon is discussed in the outlook 7.1.2.

Stability and uncertainty of the reference count rate

The stability of the counting efficiency is closely linked to the reference count rate. In order to deduce the current efficiency of the ArTTA-apparatus for a measurement of an unknown sample, it must be ensured that all reference count rates are obtained only from measurements under identical conditions. Already small changes in the system can entail the requirement of a new reference. Therefore analysing a measurement period starts with an examination of the stability addressing the question over which time periods a constant reference count rate can be assumed and when relevant changes have been made to the system so that the reference has to be split. Due to the Poissonian character of counting atoms and the poor statistical base of each single measurement, it is difficult to find a suitable statistical method to identify and quantify variations in the reference count rate during a measurement period. Here are some basic ideas presented, which were applied in the past to address this problem.

The Allan-Variance (two-sample variance) was used to characterise the stability of the system, but this approach needs a high count rate and was therefore tested with a 1000-times enriched sample [43]. It can be applied for a singular test, but not for the day-to-day stability.

Subdividing the reference measurements into smaller frames and considering the Poissonian shape of the histogram of counted atoms per frame is used as an argument for stability in [43, 44]. This is not a sensitive test as it is demonstrated in figure 3.12 exemplary with the reference data of the ocean measurements. In the time series domains are clearly visible with a reference count rate significantly below and above average and the data points do not scatter consistently around the mean. Taking the global mean $\overline{\nu_0}$ would ignore this fact and introduce a high systematic uncertainty. On the contrary, the histogram of the same data identifies no clear discrepancy from the pure Poisson distribution at all. It is unfavorable to illustrate variations, since it ignores any time information.

Another classical statistical approach is to compare the weighted variance σ^2_{int} (*internal variance*) and the weighted sample variance σ^2_{ext} (*external variance*) of the weighted mean $\bar{\nu}$. One natural choice of weights can be the measurement time T_j:

$$\bar{\nu} = \frac{\sum_{j=1}^{m} w_j \cdot \nu_j}{\sum_{j=1}^{m} \cdot w_j} \qquad \text{with weights } w_j = T_j \tag{3.22}$$

$$\sigma^2_{int} = \frac{\sum_{j=1}^{m} w_j^2 \cdot \sigma^2_{\nu_j}}{\left(\sum_{j=1}^{m} \cdot w_j\right)^2} \tag{3.23}$$

$$\sigma^2_{ext} = \frac{1}{m-1} \cdot \frac{\sum_{j=1}^{m} w_j \cdot (\nu_j - \bar{\nu})^2}{\sum_{j=1}^{m} \cdot w_j} \tag{3.24}$$

The sample variance σ^2_{ext} is sensitive to instabilities and changes of the performance between different measurements. In the ideal case of no instabilities of the system we would expect $\sigma^2_{int} \approx \sigma^2_{ext}$, whereas we obtain for the 60 reference measurements

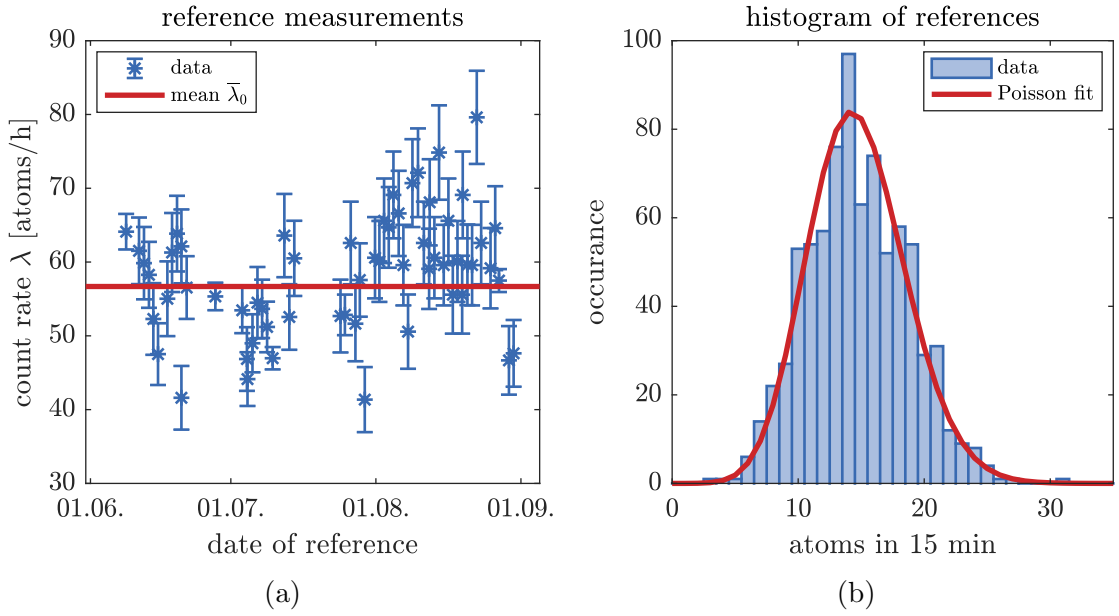

Fig. 3.12.: Compilation of the reference measurements from the ocean samples using a ten-times enriched sample. In total $N = 11\,725$ atoms in $T = 206.8\,\mathrm{h}$ were counted for referencing. The statistical uncertainty of the over-all mean count rate $\overline{\nu} = 56.7(5)\,\mathrm{atoms/h}$ is negligibly small.

a) The time series of the references shows time domains with a reference count rate significantly below and above average. A more detailed plot can be found in the context of the ocean samples in chapter 6.4. Consequently a non global reference was applied and each unknown sample was only normalised with the reference measured directly before and directly afterwards.

b) Histogram of counts in 15 min subdivisions of the reference data. There is no clear discrepancy from the pure Poisson distribution.

during the ocean measurement period an internal variance of $\sigma^2_{int} = 0.52\,\mathrm{atoms/h}$ and an external variance of $\sigma^2_{ext} = 0.94\,\mathrm{atoms/h}$, which is a clear signal of instabilities. Consequently the reference during the ocean measurements was split at the cost of statistical uncertainties of each single reference and each unknown sample was normalised separately with the reference count rate measured directly before and directly afterwards. But comparing the internal and external variance is only significant for sufficiently large data sets.

If there is an idea for a model describing the variations it can be included in the Bayesian analysis, so that the variations are included in the statistical analysis. Since no clear drifts or correlations to the monitoring data have been found, this approach is not considered in this thesis.

3.3.4. Statistical analysis – a Bayesian approach

The previously discussed contamination model is finally applied for the statistical interference of the second step, the calculation of the concentrations in the global context of a measurement period. A Bayesian approach is implemented, in that sense, that the complete probability distributions are considered and that a prior probability distribution and a statistical model are assumed explicitly. The different concepts of interpretation of probabilities, particularly the differences between a frequency interpretation and an interpretation as reasonable expectation [86], is let out deliberately at this point. The consideration of the complete probability distributions takes the skewness of the Poissonian distribution into account and has the big advantage that unrealistic results, such as negative concentrations, can be easily excluded in the calculation by the choice of the range of the prior distribution. Bayes' rule is the central theorem, on which Bayesian inference is based. The probability distribution[17] $P(\theta|D)$ for a model parameter θ, which is not directly accessible and has to be estimated, is updated with the new information of the measured data D [87]:

$$P(\theta|D) = \frac{P(D|\theta) \cdot P(\theta)}{P(D)} \quad \propto P(D|\theta) \cdot P(\theta) \tag{3.25}$$

Prior $P(\theta)$**:** In the following the start point is always a uniform prior ($P(\theta) =$ constant) distribution, which expresses maximum uncertainness. But already with the choice of appropriate bounds for the prior, θ is limited to a reasonable range.

Posterior $P(\theta|D)$**:** New updated probability given the evidence of data D. As soon as more data are available, the posterior distribution becomes the new prior distribution.

Likelihood $P(D|\theta)$**:** The likelihood is the crucial part, which contains all information about the statistical model and describes how plausible the observation of the data D under the assumption of parameter θ is.

Model evidence $P(D)$**:** Since this factor is independent from θ, it is basically a normalisation factor and can easily be calculated by integrating $P(\theta|D)$. For a better clarity it is therefore not written explicitly in all equations.

The probability distribution can be updated sequential, as soon as the single data of a data set $\boldsymbol{D} = (D_1, D_2 \dots D_m)$ are statistically independent:

$$P(\theta|\boldsymbol{D}) = \frac{P(D_1|\theta) \cdot P(D_2|\theta) \cdots P(D_m|\theta) \cdot P(\theta)}{P(D_1) \cdot P(D_2) \cdots P(D_m)} \tag{3.26}$$

$$= \frac{P(D_1|\theta) \cdot P(\theta)}{P(D_1)} \cdots \frac{P(D_m|\theta) \cdot P(\theta)}{P(D_m)} \cdot \frac{P(\theta)}{P(\theta)^m} \tag{3.27}$$

$$\underset{\text{uniform prior}}{\propto} P(\theta|D_1) \cdot P(\theta|D_2) \cdots P(\theta|D_m) \cdot P(\theta) \tag{3.28}$$

[17] The expression $P(A|B)$ denotes the *conditional probability* of A under the condition of B.

In the case of a uniform prior, different independent measurements can be averaged to a common distribution by a pointwise multiplication[18] of the single posterior distributions, which is illustrated in figure 3.13a. It should be noted that correlations, for example trough an underlying common reference or contamination measurement, are not treated correctly by this simple multiplication and have to be included in the likelihood via a multivariate distribution.

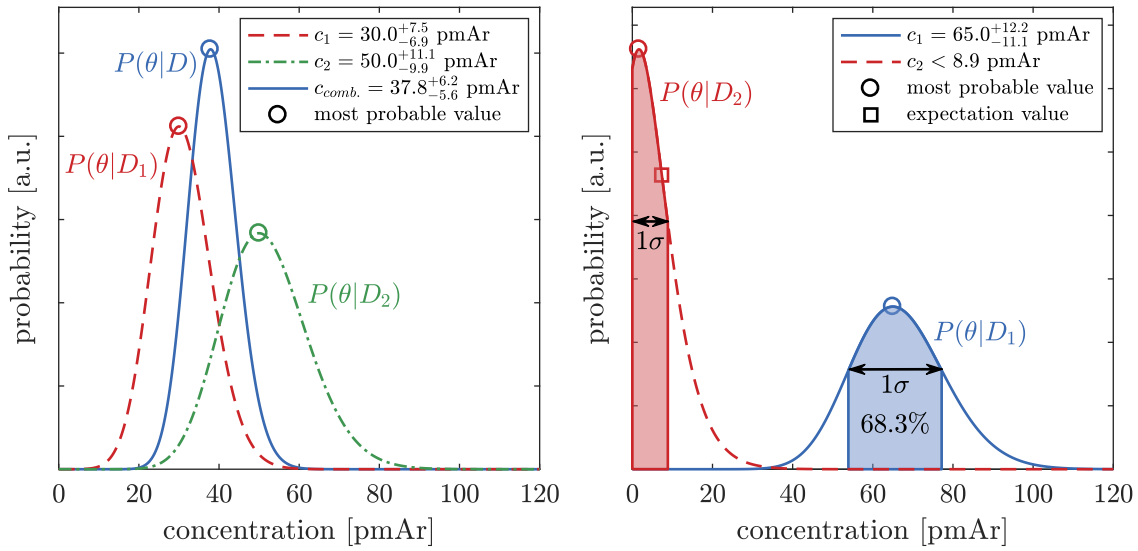

Fig. 3.13.: **a)**Pointwise multiplication of two posterior distributions $P(\theta|D_1)$ and $P(\theta|D_1)$ to calculate a common averaged distribution $P(\theta|\boldsymbol{D})$.
b)In the context of this thesis the most probable value and the maximum likelihood credible interval of 1σ corresponding to 68.3 % are always reported. As soon as the lower bound of the credible interval is zero, the present detection limit is reached and the upper bound of the confidence interval is reported as an upper limit. The expectation value is not suitable, since it is shifted the results to higher values for low concentrations.
For illustration all shown distributions are broader than typically measured ones.

[18]For reason of numerical stability it is preferable to add the logarithms of the likelihoods or probability densities, respectively.

The statistical model

The statistical model describes the likelihood $P(D|\theta)$ and is based on the expected total number of counted atoms λ_N from equation 3.19, which can be simplified due to the discussed assumptions:

$$\lambda_{N,\mathrm{exp}}(T, V, \nu_0, a, c) = \left(c \cdot T + \frac{a}{V} \cdot \frac{T^2}{2}\right) \cdot \nu_0 \tag{3.29}$$

The observed number of counted atoms N is modelled by a Poisson process with parameter $\lambda_{N,\mathrm{exp}}$. The general likelihood for the i^{th} measurement of a measurement period is given by

$$p(\underbrace{N_i, T_i, V_i}_{D_i} \,|\, \underbrace{\nu_{0,i}, a, c_i}_{\theta_i}) = \phi\left(N_i, \lambda_{N,\mathrm{exp}}(T_i, V_i, \nu_{0,i}, a, c_i)\right) \tag{3.30}$$

$$= \frac{\lambda_{N,\mathrm{exp}}^{N_i} \cdot e^{-\lambda_{N,\mathrm{exp}}}}{N_i!} \tag{3.31}$$

with the probability mass function of the Poisson process ϕ defined in equation 3.1. The contamination rate a is considered as constant during one measurement period. With help of Bayes' theorem 3.25 the likelihood can be inverted principally to the general multivariate distribution $p(\nu_{0,i}, a, c_i|N_i, T_i, V_i)$. To indicate that the volume V_i, and the parameters $\nu_{0,i}$, a and c_i are defined by a complete distribution $p(V_i)$, $P(\nu_{0,i})$, $p(a)$ and $p(c_i)$, respectively, they are written in the following as $\widetilde{V}_i$, $\widetilde{\nu}_{0,i}$, $\widetilde{a}$ and $\widetilde{c}_i$, if the distribution and not only one specific value is considered. The sample volume $\widetilde{V}_i$ is determined before each measurement via the pressure inside the prevacuum and therefore belongs, like the measurement time T_i, to the data and is not a model parameter, which has to be inferred with help of the statistical model. If the contribution from contamination is significant, uncertainties in the volume are included in the form of a Gaussian distribution.

To treat all correlations in a very strict sense, it would be even necessary to consider the complete multivariable distribution of the entire measurement period, which might be computationally possible with Markov chain Monte Carlo methods. Here, a different approach is chosen and each measurement is either used to update the knowledge about the reference $\widetilde{\nu_0}$ or the contamination $\widetilde{a}$ or an unknown concentration $\widetilde{c}$. The contamination $\widetilde{a}$ and the reference $\widetilde{\nu_0}$ are determined with samples of known concentration. Therefore, it is only essential for applying this approach that the calculation of the contamination $\widetilde{a}$ and the reference $\widetilde{\nu_0}$ can be separated, which is possible for a global common reference or under the assumption, that the reference measurements are not effected by any contamination.

The calculation is implemented in the following five steps. Thereby, all known parameters from the previous steps are mathematically treated as data and not as parameters anymore. If they are defined by a probability distribution, they are reduced by considering the expectation value and integrating over the probability distribution. The occurring integrals are solved using a Monte Carlo algorithm, which calculates

the sum over 10 000 random values drawn from each parameter distribution.

1.) Reference count rate $\widetilde{\nu_0}$: For the calculation of the reference count rate three cases have to be distinguished:

a) **Global reference:** If a uniform, over all measurements constant reference is assumed, the best way to avoid any conflicts with correlations is to set the reference count rate $\widetilde{\nu_0}$ to constant 1 initially, which is equivalent to consider count rates instead of concentrations, and transform all count rates at the end:

$$p(\nu_0) = \delta\left(1 - \nu_0\right)$$

In this case reference measurements are not exceptional and can be treated just like normal measurements.

b) **Reference measurement without contamination:** If variations of the efficiency have to be taken into account, a simple calculation is only possible, if the contamination can be neglected ($a = 0$). This is the case for the throughput mode or an enriched reference sample and relatively short measurement times, like it was realised during the ocean measurement period. Under this assumption equation 3.29 simplifies to

$$\lambda_{N,\mathrm{exp}}\left(T, \nu_0, c_0\right) = c_0 \cdot T \cdot \nu_0$$

and the reference $\widetilde{\nu}_{0,j}$ determined from the data of the j^{th} reference measurement is given by:

$$p\left(\nu_{0,j} | N_j, T_j\right) \propto \phi\left(N_j, \lambda_{N,\mathrm{exp}}\left(T_j, \nu_{0,j}, c_0\right)\right) \cdot p_{\mathrm{prior}}\left(\nu_{0,j}\right)$$

The reference concentration c_0 is included in the reference count rate ν_0, so that it is normalised to c_0. For a better statistic, some reference measurements, for example the reference before and after each measurement, might be combined utilising equation 3.27. After this potential averaging the individual reference $\widetilde{\nu}_{0,i}$ for each measurement is known. At this point one might get some weak correlation, if some measurements have a joint reference measurement.

c) **Reference and contamination not separable:** As soon as the reference and contamination measurements are not separable a joint distribution $p\left(\nu, a\right)$ has to be considered, which should not be discussed in detail, since it is not relevant in the context of this thesis.

2.) Contamination $\widetilde{a}$: The contamination measurements are performed with help of an ^{39}Ar-free sample, so that all counted atoms originate clearly from contamination. Equation 3.29 simplifies with $c = 0$ to:

$$\lambda_{N,\mathrm{exp}}\left(T, V, \nu_0, a\right) = \frac{a}{V} \cdot \frac{T^2}{2} \cdot \nu_0$$

The contamination rate $\widetilde{a}_k$ resulting from the k^{th} contamination measurement is given by:

$$p\left(a_k|N_k,T_k,\widetilde{V}_k,\widetilde{\nu}_{0,k}\right) \propto \iint p\left(V_k\right)p\left(\nu_{0,k}\right)\phi\left(N_k,\lambda_{N,\text{exp}}\left(T_k,a,V_k,\nu_{0,k}\right)\right)\mathrm{d}\nu_{0,k}\mathrm{d}V_k \cdot p_{\text{prior}}\left(a_k\right)$$

All contamination measurements of one measurement period are combined by equation 3.27 to one common contamination rate $\widetilde{a}$.

3.) Concentration $\widetilde{\mathfrak{c}}$: To symbolise that the concentrations are not yet normalised to the atmospheric one, they are temporally written as $\widetilde{\mathfrak{c}}$. If the same sample was measured in various measurements and if they should be combined, it is necessary to consider all m measurements of the same sample at once, since they are all correlated by the common contamination rate $\widetilde{a}$. At first a joint likelihood of all measurements is determined analogously to equation 3.27 and finally it is integrated over $\widetilde{a}$. In this case equation 3.29 can not be simplified and $\widetilde{\mathfrak{c}}$ is calculated by:

$$p\left(\mathfrak{c}|\boldsymbol{N},\boldsymbol{T},\widetilde{\boldsymbol{V}},\widetilde{\boldsymbol{\nu}}_{\boldsymbol{0}},\widetilde{\boldsymbol{a}}\right) \propto \int p\left(a\right)\left(\prod_{i=1}^{m}\left(p\left(\mathfrak{c}|N_i,T_i,\widetilde{V}_i,\widetilde{\nu}_{0,i},a\right)\right)\mathrm{d}a\right)\cdot p_{\text{prior}}\left(\mathfrak{c}\right)$$

with

$$p\left(\mathfrak{c}|N_i,T_i,\widetilde{V}_i,\widetilde{\nu}_{0,i},a\right) \propto \iint p\left(V_i\right)p\left(\nu_{0,i}\right)\phi\left(N_i,\lambda_{N,\text{exp}}\left(T_i,a,V_i,\nu_{0,i},\mathfrak{c}\right)\right)\mathrm{d}\nu_{0,i}\mathrm{d}V_i$$

4.) Final normalisation: Finally the normalisation to the atmospheric count rate is carried out. Two possible cases have to be considered:

a) **Global reference:** The concentrations $\widetilde{\mathfrak{c}}$ calculated in the previous step are given up to now as count rates and have to be normalised by the count rate $\widetilde{\mathfrak{c}}_0$ of all measurements performed with the reference sample c_0.

$$\widetilde{c} = \frac{\widetilde{\mathfrak{c}}}{\widetilde{\mathfrak{c}}_0}$$

Thereby the quotient distribution of two random variables is given by [88]:

$$p\left(c\right) = \int p_{\mathfrak{c}}\left(c\cdot\mathfrak{c}_0\right)p_{\mathfrak{c}_0}\left(\mathfrak{c}_0\right)\left|\mathfrak{c}_0\right|\mathrm{d}\mathfrak{c}_0$$

b) **Not atmospheric reference:** If a not atmospheric reference is used, all concentrations have to be scaled finally by the known concentration of the reference sample $\widetilde{c}_0$:

$$\widetilde{c} = \widetilde{\mathfrak{c}}\cdot\widetilde{c}_0$$

The resulting product distribution is defined by [88]:

$$p(c) = \int p_{\mathfrak{c}}\left(c/c_0\right) p_{c_0}(c_0) \frac{1}{|c_0|} \mathrm{d}c_0$$

It must be kept in mind, that one might have correlations which are not treated in a mathematically strict way during the normalisation process, especially if measurements influence both, the concentration $\widetilde{\mathfrak{c}}$ calculated in step 4 and the reference count rate $\widetilde{\mathfrak{c}}_0$ or the reference concentration $\widetilde{c}_0$.

5.) Summarising the posterior: The final posterior distributions $\widetilde{c}$ are summarised for a simple representation. In the context of this thesis the most probable value of the distribution is always reported, since the expectation value yields, particularly for small concentration, too high and misleading values, which is depicted in figure 3.13b. The uncertainties are presented by the 1σ (68.3 %) maximum likelihood confidence interval. If the lower bound is identical with $c = 0$ only an upper limit is given by the upper bound of the confidence interval. In this case the measured concentration is within the achievable precision not distinguishable from an argon free sample.

This chapter closes with one last comment on the Bayesian statistic. Compared to a frequentist approach all assumptions are explicitly contained in the statistical model or in the prior. The simple model developed in this chapter includes no drifts or fluctuations of the efficiency, beside a splitting of the reference by hand. To analyse or deal with variations in the efficiency the model must be extended by some more parameters describing these variations.

4. First ArTTA Ice Samples

This chapter records the first ArTTA-measurements of ice samples. About 4 kg to 8 kg ice was extracted, which was collected at the tongue of the Gorner Glacier in the Swiss Alps. Since these samples were the first small natural samples, which were prepared and analysed in recycling mode, the obtained ^{39}Ar-concentrations are likely less accurate and not as reliable as the later intercomparison and ocean measurements. Furthermore, the determined ^{39}Ar-concentrations are not conclusive and disagree with the prediction from ice-flow models, air content and ^{210}Pb, tritium and δ^{18}O measurements. Possible explanations, such as ice fracturing or contamination during sampling, are discussed in the last section of this chapter.

4.1. Samples

The ice samples discussed in this chapter were collected in the lower ablation zone at the tongue of the Gorner Glacier system with the Grenzgletscher as its by far main tributary located at the border of Switzerland and Italy (map 4.1a) in July 2014. This glacier system is polythermal with a non-temperated catchment area at high altitudes which reemerges to the surface in the lower ablation zone with temperatures significantly below the melting point, which should in principle ensure the integrity of the ice. In the mid altitudes the cold basal ice is covered by a tempered section [89]. This situation, which is depicted in figure 4.1b, enables easily accessible preindustrial ice in the lower section of the ablation zone. The ice was collected at two main sample sites at an altitude of ∼2300 m and ∼2440 m above sea, respectively. Assuming an ice flow velocity of $\sim 10\,\mathrm{m\,a^{-1}}$ [89], the horizontal separation of about 2 km along the flowing direction of the glacier should guarantee an age difference of more than 150 years between the upper site, which is expected to be younger, and the lower one, which is expected to be older. At five points along the connecting line additional smaller ice blocks for measurements of stable isotopes were taken. Before digging out the ice samples with help of a chainsaw, the covering 30 cm of wet, warm and milky ice had been removed. The quality of the ice from the upper site is described as very good, with many bubbles and no visible blue ice layers. On the contrary the sampling at the lower site could not be conducted with the same carefulness due to bad weather conditions [90]. In total 16 ice blocks from the upper and 11 from the lower site were collected, which were mainly used for particulate organic carbon (POC) extraction for radiocarbon dating and only three ice blocks became available for ^{39}Ar-analysis. The layout of the exact positions of the two sample sites can be found in appendix C.

The time of the formation of the ice and the time, when the gas bubbles are finally included in the ice and isolated from the contact with the atmosphere must not be

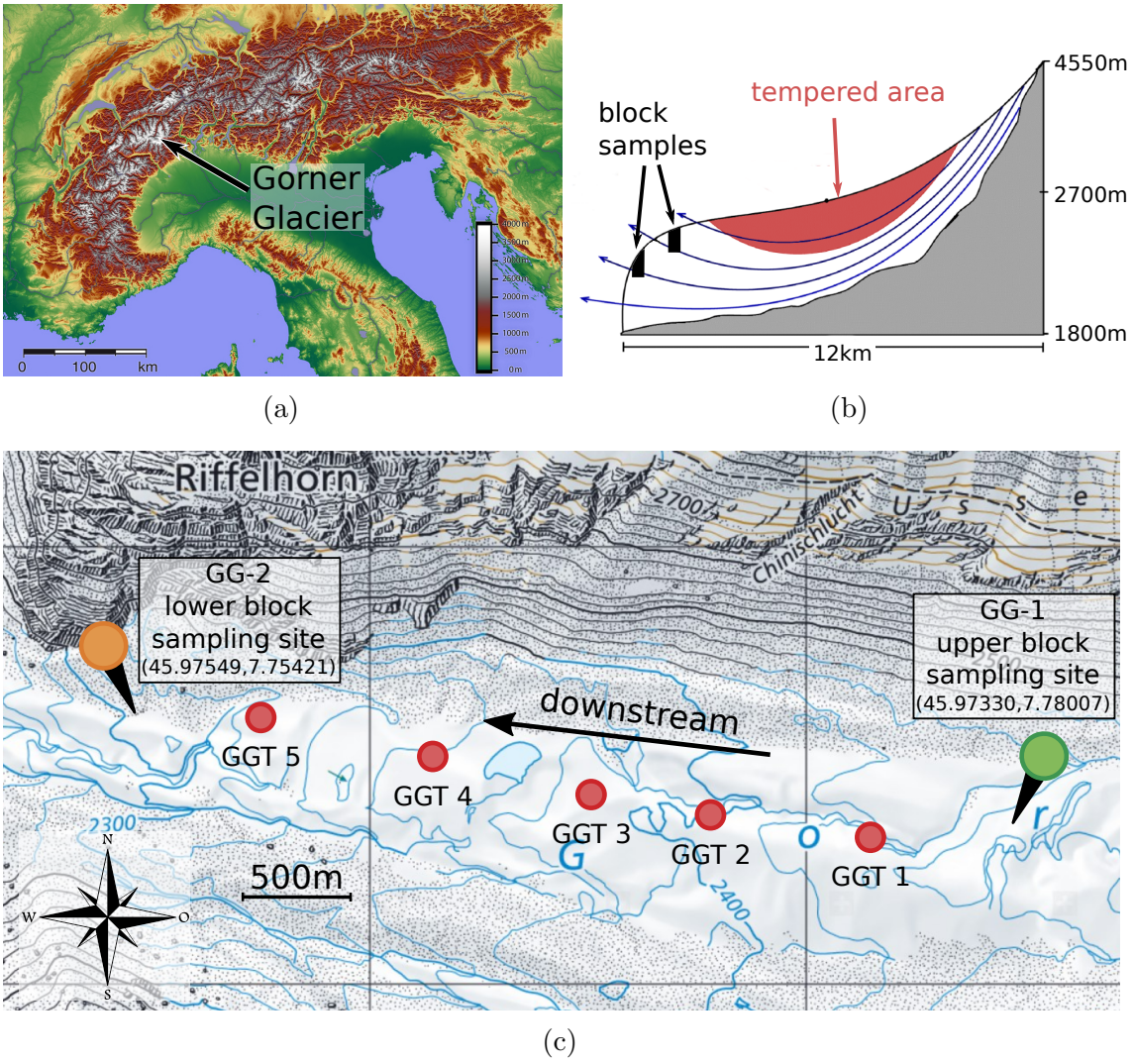

Fig. 4.1.: Sample site of the first ice samples measured with ArTTA:
a) Location of the alpine Gorner Glacier in the Monte Rosa massif close to Zermatt (map taken from [91]).
b) The polythermal Gorner Glacier has a cold ice base with a temperated zone on top of it. The samples were taken from the lower ablation zone, where cold ice from the very high accumulation zone reemerges at the surface [89] and is quite easily accessible by cutting blocks with a chainsaw (graphic adapted from [92]).
c) The ice for ^{39}Ar and radiocarbon analysis were sampled at two main sites separated by ∼2 km in flow direction from each other, expecting an age difference of several hundred years. Following the connecting line several smaller samples addressing altitude effects in stable isotopes were taken (map from [93] (National Map 1:25'000), the positioning of the blocks can be found in appendix C and details of the sampling in [90]).

necessarily the same. The latter is addressed by ^{39}Ar-dating. For the former, the age of the ice mass, there is some additional information available. No tritium was found, which is an indication of a formation before 1950. Additionally, in a former study at the sample site the tracer ^{210}Pb was at the detection limit, which is a clear hint for preindustrial ice older than ∼150 a [89]. The POC extracted from ice blocks collected at both sample sites shows the typical signature of old Saharan dust, which shifts the ^{14}C-ages to much higher values than expected. Only three samples at all yielded enough POC for radiocarbon analysis. The determined ^{14}C-ages are in the range of 1000 a to 4000 a and with high uncertainties due to the small carbon amounts. No significant difference compared to ice blocks, which were obviously biased by Saharan dust, were found [92].

The stable isotope data δ^{18}O, plotted in figure 4.2, show a clear difference between both sample sites with a continuous transition along the connecting line. One possible interpretation might be, that ice from the lower site consists of more summer snow, which is less depleted in ^{18}O compared to winter snow. Due to strong winds at the Colle Cniffeti, the summit region, which is the origin of this glacier, a substantial fraction of winter precipitation is lost and ice formation takes place mainly during summer, when fresh snow consolidation is enhanced and supported by refreezing at the surface melt [94]. Following this argumentation the ice at the lower sampling site comes from higher altitudes, most probably from the summit region and should thus be much older compared to the ice from the upper site due to the longer travelled distance.

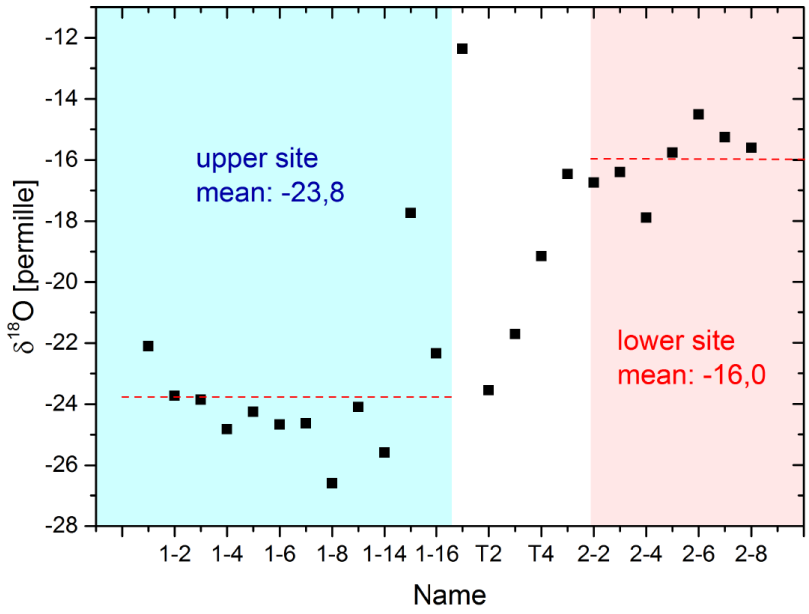

Fig. 4.2.: δ^{18}O-values of all ice samples from the Gorner Glacier: There is a clear difference between both sampling sites with a continuous transition along the connecting line (graphic taken from [50]).

The ice blocks for radiocarbon and ^{39}Ar-analysis were transported in frozen state to the Institute of Environmental Physics in Heidelberg and were stored in the ice storage room. The preparation, degassing and the purification of the argon for measurements with ArTTA has been developed and conducted in [50]. The ice was cleaned from ice powder and whenever signs of melting during transport were visible, a thin layer of ice was cut off and discarded. Subsequently the ice was evacuated down to $\sim 10^{-3}$ mbar in a big stainless steel container cooled with dry ice. Approximately after one hour the pressure stabilised and the dry ice was removed, so that the ice started to melt and the thereby released gases were transformed to a charcoal trap and processed in the same way as the ocean sample [50]. The general process of preparing small samples for ArTTA is described in chapter 1.3. Two ice blocks with masses around 4 kg and one with 7.5 kg were prepared for analysis with ArTTA. The air content and the argon yield are listed in table 4.1.

Table 4.1.: Ice samples: Sample sizes and gas content [50]

sample	mass [kg]	air content [mL STP]	air content/mass [mL STP kg^{-1}]	argon content [mL STP]
GG1-5	7.5(1)	590.8(34)	78.8(11)	5.5(2)
GG2-4 [1]	4.3(1)	200.6(9)	46.7(11)	1.8(2)
GG2-5	3.7(1)	157.6(9)	42.6(11)	1.5(2)

The huge difference in the relative air content per mass between the both sampling sites is a further indication that the ice at the lower site (sample GG2-4 and GG2-5) was mainly formed out of more compact summer snow, whereas ice from the upper sampling site (sample GG1-5) originates also from dry and light, loose structured[50] winter snow, which leads to many air inclusions.

4.2. Measurements

The described ice samples represent the first ArTTA measurements of small natural samples in recycling mode and were performed between April and May 2016. The main parameters of the ice sample measurement period are summarised in table 4.2.

The atmospheric reference was measured in throughput configuration, which makes it insensitive to any contamination, but might introduce additional uncertainties, by normalising recycling measurements with a throughput reference. The ^{40}Ar-flux measured with the beam imaging indicates that the throughput mode is 5 % to 10 % less efficient. Since it is difficult to quantify this effect for the ^{39}Ar-count rate, the determined concentrations are not corrected for this systematic effect. The reported ^{39}Ar-concentrations and ^{39}Ar-ages might thus be shifted to higher concentrations or

[1] For some unexplainable reasons, the sample GG2-4 is listed under the different name GG2-2 in [50]. Since the Ar-sample container was labelled with GG2-4, this name is used in this thesis exclusively.

Table 4.2.: Overview of the main parameters from the ice measurement period.

date of period	25 Apr to 24 May, 5 to 18 Jun 2016
total measurement time	382.9 h
total number of counted atoms thereof estimated background atoms and atoms during cont. meas.	1575 45 718
mean atmospheric count rate ν_{atm}	2.55(17) atoms h^{-1}, 2.92(16) atoms h^{-1}
contamination rate a	$67.3^{+3.3}_{-3.3}$ μL STP $\mathrm{c_{atm}}$ h^{-1}
mean Ar-amount per ice measurement	1.9 mL STP
mean lifetime τ	382 ms
mean single atom signal δ_n (δ_x)	15.6 kcps (1.26)

younger ages, respectively. This potential systematic uncertainty is also not included in the confidence intervals. Since there were some major problems and repair works during the measurement period, which affected the counting efficiency, the measurement period was split into two parts, which were considered independently with respect to the reference. A time overview of all reference and contamination measurements is shown in figure 4.3. The ^{39}Ar-free underground sample was measured six times to quantify the contamination, thereof three times with a substantially reduced volume down to 74 μL STP to enhance the signal of the contamination and the number of counted ^{39}Ar-atoms. The other three measurements are comparable in sample volume with the ice samples. Also the atmospheric argon was measured four times in recycling mode with similar sample sizes. These measurements can be used as a test, due to the known ^{39}Ar-concentration. Even if the main parameters of this measurement period are comparable to the intercomparison measurement period, there were several measurements with significant problems of the single atom detection, which could be traced back later to drifts in the MOT position due to power fluctuations and changes in the polarisation as a consequence of an unfixed quarter-wave plate. Due to the significance of the high contamination rate and the relatively small amount of Ar-gas, an additional uncertainty of the gas volumes of 15 % for the ice samples and 10 % for all other measurements was considered in the analysis, which bundles changes in the gas temperature, uncertainties in the reference volume and of the absolute pressure.

4.3. Results

Table 4.3 summarises the concentrations of the ice samples from the Gorner Glaciers measured with ArTTA and figure 4.4 additionally shows the complete determined posterior distributions. The high uncertainties of all natural samples originate from the small samples and the consequent limitation of the measurement time of maximally

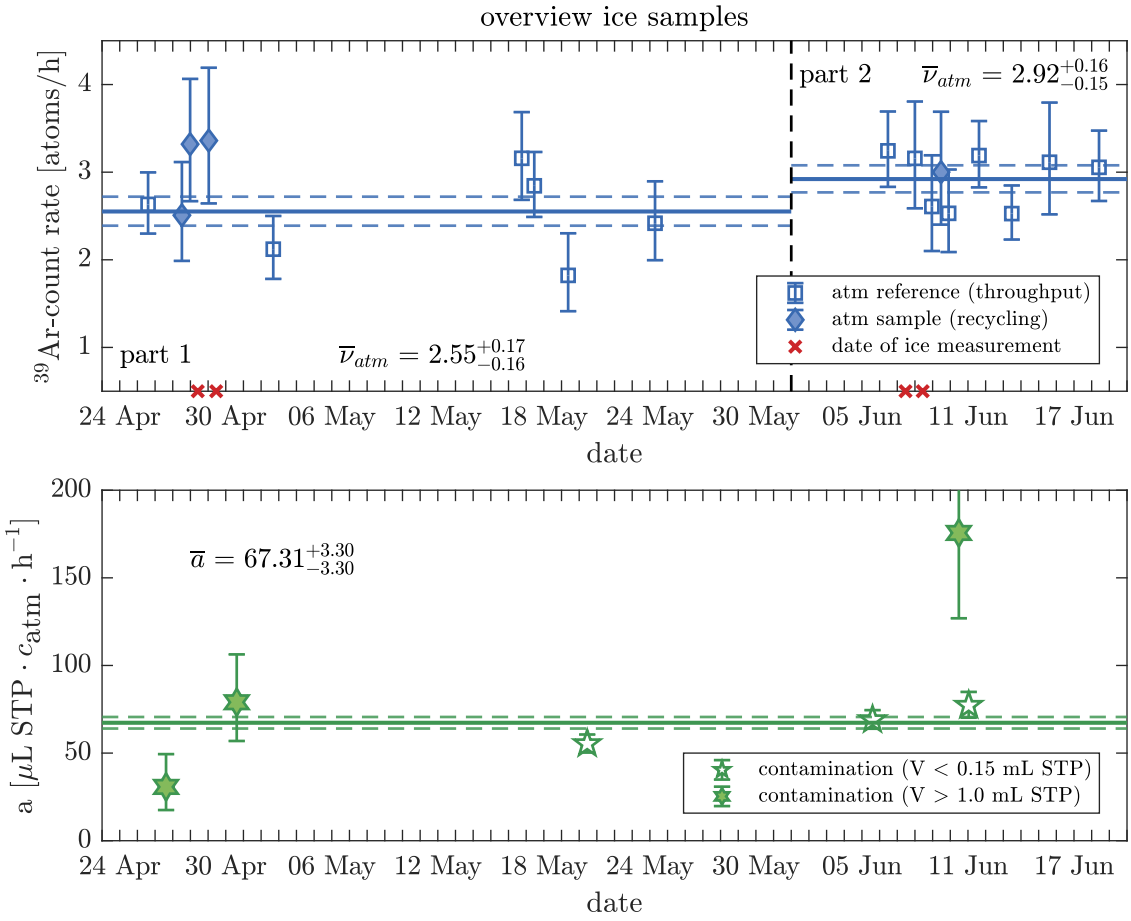

Fig. 4.3.: Overview of the ice sample period: The upper plot shows the atmospheric reference count rate, which was split into two parts, since there were major repair works in between. The measurements in recycling mode are used as test samples and do not enter the mean atmospheric reference. The red stars mark the dates of the ice measurements. The lower plot gives an overview of the six contamination measurements, three of them with very small argon volumes to enhance the signal. The contamination is normalised to a reference volume of 1 μL STP and to the atmospheric concentration. The horizontal lines indicate the means and the 1σ maximum likelihood confidence interval of the Bayesian analysis (see chapter 3.3.4).

∼12 h due to contamination. The result of the sample GG2-5 from the lower sampling site is about 1.6σ above the atmospheric concentration of 100 pmAr. The second sample (GG2-4) from the lower sampling site does not differ significantly from a modern sample. Since these both samples originate from different ice blocks and show significantly distinct ^{39}Ar-concentrations, they are not combined to one result. The two independent measurements of the sample from the upper site (GG1-5) are consistent and show with ∼70 pmAr a combined ^{39}Ar-concentration clearly below modern argon. This corresponds to an ^{39}Ar-age of around 150 a.

The averaged result of the atmospheric test measurements with comparable sample volumes is a little bit above the expected concentration of 100 pmAr, which might be a hint of a systematic difference between the more efficient recycling mode and the throughput configuration, in which the reference was measured. Thus, all concentrations might be shifted to higher concentrations. The combined result of the contamination measurements using the dead, ^{39}Ar-free sample with volumes higher than 1.0 mL STP are in agreement with 0 pmAr.

Table 4.3.: Summary of the ^{39}Ar-measurements of ice samples from the Gorner Glacier: The sample volumes differ slightly from the one in table 4.1, since the exact amount of argon filled in the ArTTA vacuum system was measured directly before the ^{39}Ar-counting. The ice sample GG1-5 from the upper sampling site was big enough to be split for two independent measurements. Only results measured in recycling configuration with more than 1 mL STP are considered for the test with known concentrations (# indicates the number of individual measurements).

sample	site	volume [ml]	time [h]	counted atoms	estimated contam.	^{39}Ar [pmAr]	^{39}Ar-age a
measurement series 1							
GG2-5	lower	1.30(20)	13.8	63	13.7	$139.9^{+27.4}_{-24.9}$	$-130.3^{+76.1}_{-69.4}$
GG1-5 (mes 1)	upper	1.50(23)	10.5	24	7.0	$63.8^{+21.3}_{-18.4}$	$174.4^{+132.0}_{-111.8}$
measurement series 2							
GG2-4	lower	1.89(28)	8.1	27	6.8	$85.7^{+24.9}_{-21.9}$	$59.8^{+114.5}_{-99.0}$
GG1-5 (mes 2)	upper	3.08(46)	12.2	30	5.0	$70.4^{+17.4}_{-15.2}$	$136.2^{+94.4}_{-85.7}$
combined							
GG1-5	upper	4.58(54)	22.6	54	12.0	$67.8^{+13.1}_{-11.9}$	$150.8^{+74.9}_{-68.6}$
samples with known concentration							
atm sample (#4)		1.3 to 4.0	35.0	120	13.7	$113.7^{+12.9}_{-12.0}$	
^{39}Ar-free sample (#3)		1.5 to 4.0	42.6	26	22.7	$4.0^{+4.0}_{-3.6}$	

4.4. Discussion

The measured ^{39}Ar-concentrations of the lower sampling site are much younger than one would expect from the absence of tritium and ^{210}Pb. However, tritium was only

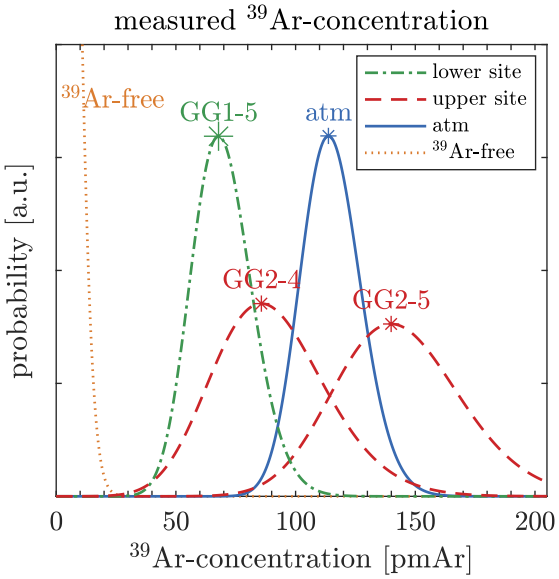

Fig. 4.4.: Posterior probability distribution of the ^{39}Ar-concentrations from the ice samples collected at the Gorner Glacier: For comparison the atmospheric and ^{39}Ar-free sample are included. The two ice samples GG2-4 and GG2-5 from the lower sampling site do not differ significantly from the atmospheric concentration, whereas the sample from the upper site has with an ^{39}Ar-concentration of 67.8 pmAr a clear sub-atmospheric ^{39}Ar-signature. Due to the low count rate and the small sample sizes in combination with a high contamination, the distributions are much broader than typically measured with the present system.

measured in neighbouring samples and ^{210}Pb in a former study. These two tracer address the ice mass directly and not the embedded gas. Furthermore, the expected age gradient between the upper and the lower sampling site is not reflected by the measured ^{39}Ar-concentration at all, on the contrary the samples from the lower site show even higher, modern ^{39}Ar-values. The most probable explanation is, that there was an exchange of the gas enclosed in the ice matrix with the atmosphere, so that the age of the enclosed air gives no information about the time of the ice formation. A possible reason can either be in the history of the ice by partial melting or during the sampling with the chainsaw. Both effects could be enhanced for the lower sampling site, since the selection and the sampling of the ice blocks were not conducted with the same carefulness due to lack of time as a consequence of bad weather conditions.

A contamination using a chainsaw for extraction of ice samples and an impairment of the ice quality due extensive fracturing is cited in the context of the first successful krypton ice dating[41]. Thus, for this first successful study a 24 cm-diameter ice drill was used in the Antarctica to collect 350 kg of ice per sample from a depth between 5 m and 15 m to avoid any gas loss and contact with the atmosphere via near-surface fractures. A similar idea to the one described above to exploit the flow structure of the glacier was used to get easy access to old ice, which was dated with ATTA to

^{81}Kr-ages as old as 120 000 a. The intactness of the ice was proofed with the absence of ^{85}Kr and also ^{39}Ar analysed with LLC, however the sample sizes were too small for precise ^{39}Ar-measurements via radioactive decay counting[41].

For ^{39}Ar-studies of ice samples further investigations are needed addressing especially the sampling process. Promising ice samples can be collected in artificial glacier caves e.g. at the Stubai or Titlis Glacier. Due to the touristic infrastructure they are easily reachable via cable cars and give access to basal ice along the bedrock[92]. Ice samples from the Stubai Glacier cave were radiocarbon dated more reliably with help of a lucky finding of biological remnants. The resulting ^{14}C-ages lie in a range of 325 a to 484 a. Ice blocks sampled in the Titlis Glacier contained sufficient POC for radio carbon analysis and for the ^{14}C-age an upper limit of $\sim$5000 a is given [92]. These sample sites will be studied in a planned ice campaign, which will focus on ^{39}Ar-analysis of ice samples.

5. Intercomparison Study

This chapter summarises the results of the intercomparison studies between the two Low-Level Counting (LLC) laboratories at the Pacific Northwest National Laboratory (PNNL) and the University of Bern on the one hand and the atom-optical technique ArTTA in Heidelberg on the other hand. The measurement period for the intercomparison was at the end of 2016. This intercomparison was initiated by PNNL, where a new low-background proportional ^{39}Ar-counter was established [95]. It was designed as a blind study in that sense, that neither at the time of the measurements nor at the time of the first analysis any results from LLC were known. The results presented here are analysed with the improved statistical methods discussed in chapter 3.

5.1. Samples

In contrast to a previous intercomparison, which addressed the range below the atmospheric concentration [44], this intercomparison was performed with two enriched standards, which were provided by PNNL. One of them with a concentration of approximately three-times the atmospheric abundance (in the following referred to as **3X**) and the other with approximately 60-times the atmospheric concentration (in the following referred to as **60X**). These two samples were generated via reactor neutron irradiation of potassium carbonate and diluted to the desired activity with atmospheric argon. The production of the samples and the results from PNNL are reported in [96]. LLC requires a mixture, which is called *P10*, containing 90 % argon and 10 % methane as quench gas. To compare the LLC results the concentrations of the pure argon samples, which were analysed by ArTTA, are inferred from the LLC results of the P10 samples.

No preparation was necessary for the ArTTA measurements of the 3X sample. However, to reduce the risk of cross sample contamination and of an afresh permanent contamination of the ArTTA apparatus, the 60X sample was diluted by blending with atmospheric argon. For this purpose two sample cylinders with an identical volume ($\sim$500 mL) were filled to $p_{60X} = 457$ mbar of the 60X sample and to $p_{\mathrm{atm}} = 2574$ mbar of atmospheric argon, respectively, and were mixed afterwards (compare section 1.4). This ratio was chosen to reduce the ^{39}Ar-concentration by a factor of about six down to about ten-times the atmospheric concentration. The diluted sample is referred to as $\mathbf{60X_{dil}}$. The measured count rates or concentrations can be translated by the following equation:

$$c_{60X_{dil}} = \frac{p_{60X}}{p_{60x} + p_{atm}} \cdot c_{60X} + \frac{p_{atm}}{p_{60x} + p_{atm}} \cdot c_{atm} \tag{5.1}$$

Applying the measured pressures gives the following relations:

$$c_{60X_{dil}} = 0.1508 \cdot c_{60X} + 0.8492 \cdot c_{\mathrm{atm}} \quad (5.2)$$

$$c_{60X} = 6.632 \cdot c_{60X_{dil}} - 5.632 \cdot c_{\mathrm{atm}} \quad (5.3)$$

Compared to the statistical uncertainty, the uncertainty of this mixing process is small and will be neglected in the following.

5.2. Measurements

The intercomparison measurement period was between 11 Nov and 16 Dec 2016. The apparatus was operating in recycling mode with sample volumes of ∼5 mL STP per measurement. The mean measurement time was about 10 h, so that up to two data points could be taken per day. The contamination was quantified in four measurements of the ^{39}Ar-free underground sample with a substantially reduced volume [1] down to 100 µL STP to enhance the signal and thus 1036 atoms were counted during these four measurements. This might be at the expense of the stability of the contamination measurements, because it is more difficult to keep the pressure conditions inside the system constant. Atmospheric argon, also measured in recycling mode (thus directly comparable to the samples) was chosen for reference. Table 5.1 summarises the main parameters of this measurement period.

Table 5.1.: Overview of the main parameters from the intercomparison measurement period.

date of period	11 Nov to 16 Dec 2016
total measurement time	327.6 h
total number of counted atoms	4386
thereof estimated background atoms	98
and atoms during contamination measurements	1036
mean atmospheric count rate ν_{atm}	3.23(18) atoms h^{-1}
contamination rate a	$93.0^{+6.1}_{-5.8}$ µL STP c_{atm} h^{-1}
mean sample volume	5.1 mL STP
mean lifetime τ	386 ms
mean single atom signal δ_n (δ_x)	13.9 kcps (1.12)

After the intercomparison campaign the vacuum system was upgraded and partly rebuilt, thus compared to the ocean sample period (see chapter6), the contamination

[1] Since the contamination measurements are conducted with an ^{39}Ar-free sample, no intrinsic statistical uncertainty due to the small sample volume must be considered (compare 3.1).

was still high and the count rate with 3.23(18) atoms h^{-1} only half as high. The relative long mean lifetime of the trapped atoms is because of the lower argon throughput. There were some abrupt instabilities in the efficiency of the metastable argon source, but they can be identified clearly in the signal of the flux meter. In total 20.5 h of measurement time are affected by this problem and have been discarded.

5.3. Results

The data are analysed with the method presented in chapter 3. Figure 5.1 shows a time overview over the complete measurement period. Since the internal variance $\sigma_{int} = 0.186$ atoms h^{-1} and the external variance $\sigma_{ext} = 0.175$ atoms h^{-1} of the atmospheric reference measurements are very similar (compare chapter 3.3.3) and since there are no clear drifts nor fluctuations identifiable, a global, over all atmospheric measurements averaged, count rate was used for referencing. Due to the significance of the high contamination rate, an additional uncertainty of the sample volumes of 10 % was considered in the analysis, which bundles changes in the gas temperature, uncertainties in the reference volume and of the absolute pressure measurement. The total error might be slightly overestimated since the uncertainties of the contamination enter in the calculation of all samples as well as in the reference. This leads to a small correlation between these two values, which are not considered during the analysis. The results are summarised in table 5.2.

Table 5.2.: Summary of all measurements

	atm	**3X**	**60X$_{\mathbf{dil}}$**
number of measurements	11	7	6
total time [h]	118.7	74.2	60.4
number of atoms	425	945	1947
consumed volume [mL STP]	55.4	35.3	31.3
concentration [pmAr]	100^{+8}_{-7}	380^{+25}_{-23}	983^{+60}_{-56}

5.4. Discussion

Table 5.3 contextualises the concentration measured with ArTTA with the results from the LLC laboratories. PNNL reports an absolute activity, which can be normalised by the natural ^{39}Ar-activity of $1.80(15) \times 10^{-6}$ Bq/cm$^3_{\mathrm{Ar(STP)}}$ published in [97]. The laboratory in Bern and ArTTA measured relative to an atmospheric reference sample. Since the two intercomparison samples were enriched in ^{39}Ar, the major uncertainties come from the uncertain atmospheric reference: In the case of the PNNL the uncertainty results from the uncertainty of the absolute natural ^{39}Ar-activity and in case of ArTTA from the low statistics of the reference measurements. The effective consumption of the sample gas for ArTTA was only ∼35 mL STP of the 3X and

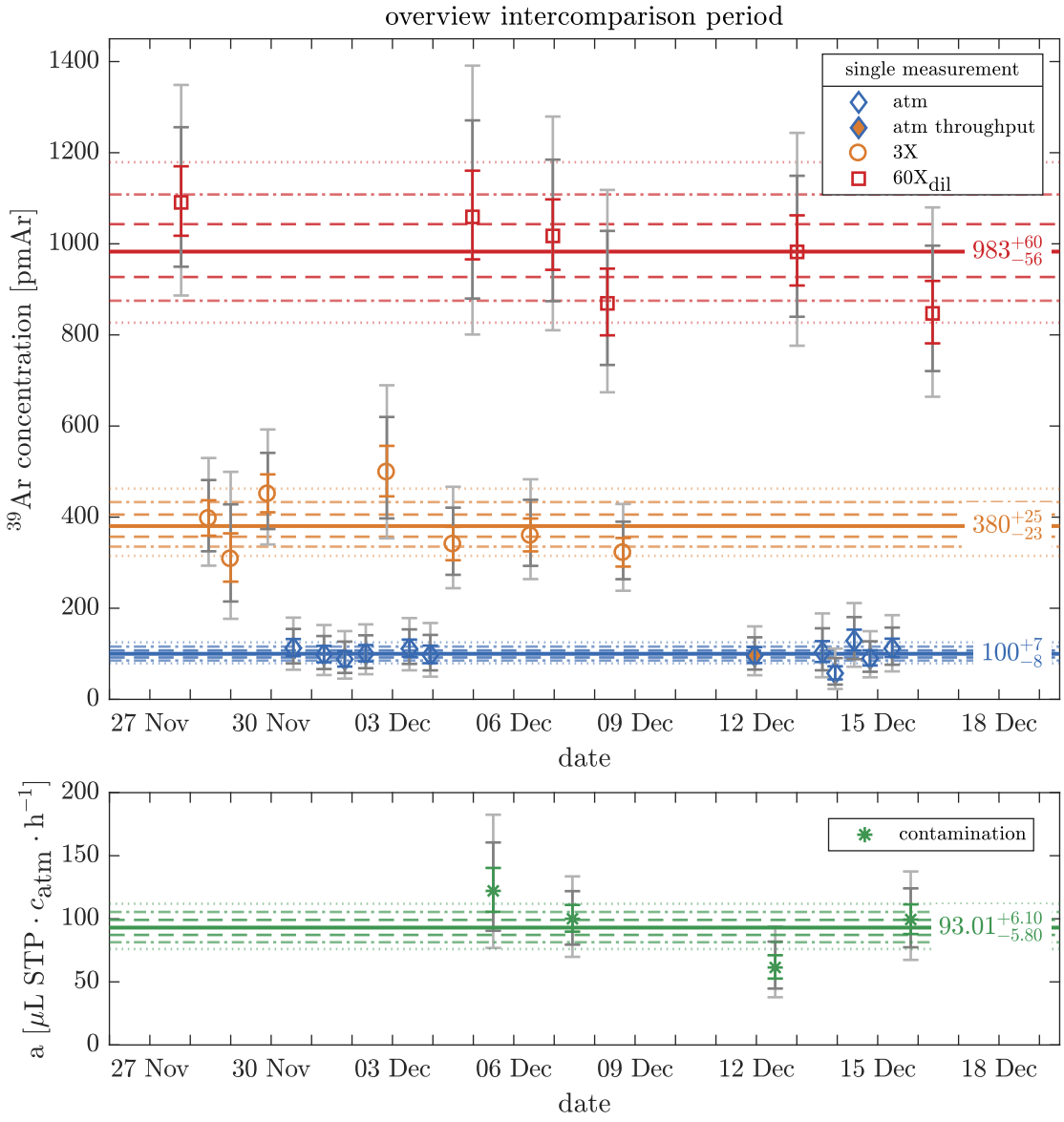

Fig. 5.1.: Overview over the intercomparison measurement period:
Upper: Concentration for each single measurement of the atmospheric reference and of the two enriched intercomparison samples (3X and 60X$_{dil}$). For normalisation the global atmospheric count rate was used. The single atmospheric result, which was measured in throughput configuration, was thereby excluded.
Lower: Overview of the four contamination measurements: The contamination is normalised to a reference volume of 1 μL STP and to the atmospheric concentration.
The vertical lines indicate the means and with decreasing intensity the maximum likelihood confidence interval of 1σ, 2σ and 3σ calculated with the Bayesian analysis described in chapter 3.3.4.

$\sim$5 mL STP of the 60X sample. There were some additional losses due to the high pressure and the large volume of the provided gas cylinders. In comparison around 1000 mL STP per sample have been analysed by LLC at PNNL.

The $60X_{dil}$ sample can be used as a reference sample, without a major risk of re-contamination of the vacuum system. Due to the ten-times enrichment the count rate is high enough for a daily reference with only two hours of measurement time. Thereby it might be possible to detect drifts and fluctuation in the performance of the apparatus and compensate for it. Since a huge amount of the $60X_{dil}$ is available, this method of referencing with an enriched sample was tested in the context of the ocean studies presented in chapter 6. As a side effect of this referencing, the results from the intercomparison studies can be updated with the much higher precision of the current, improved system. The absolute value of the concentration of the $60X_{dil}$ sample changes only marginally due to the new data, but by combining all information measured with ArTTA, the uncertainties can be halved.

Table 5.3.: Compilation of the results measured in the different laboratories. The values measured at PNNL are taken from [96] and normalised by the atmospheric activity of $1.80(15) \times 10^{-6}\,\mathrm{Bq/cm^3_{Ar(STP)}}$ reported in [97]. The results from Bern are preliminary and the uncertainty might change slightly in a more elaborated analysis [98].

laboratory	3X	$60X_{dil}$	60X	60X : 3X
PNNL				
activity [$10^{-6}\,\mathrm{Bq/cm^3_{(STP)}}$]	6.22(12)	-	97.2(18)	15.6(4)
concentration [pmAr]	346(29)	-	5400(450)	
Bern	not			
concentration [pmAr]	measured	-	5810(580)	-
ArTTA				
intercomparison period [pmAr]	380^{+025}_{-023}	983^{+60}_{-56}	5960^{+400}_{-370}	15.7(6)
ocean period [pmAr]	-	949^{+40}_{-37}	5730^{+260}_{-250}	15.1(12)
combined [pmAr]	-	960^{+33}_{-31}	5800^{+220}_{-210}	15.3(12)

The results from LLC in Bern and ArTTA are nearly exactly the same and confirm a good agreement between the two laboratories again. The concentrations reported by PNNL are lower and at the edge of the 1σ interval. The good agreement of the ratio 60X : 3X between both intercomparison samples might allow the conclusion of a systematic discrepancy either in the calibration of the absolute efficiency of the counter at PNNL or in the natural activity for normalisation. However, an intercomparison via enriched samples might reveal systematic deviation in the normalisation but gives no evidence of the more challenging subatmospheric ^{39}Ar-concentration range, which is essential for dating natural samples.

A better constrain on the specific ^{39}Ar activity in natural argon

This chapter concludes by demonstrating the potential of the combination of LLC and ArTTA to infer a better constrain on the specific ^{39}Ar activity in natural argon. LLC suffers from a huge background signal which is in the order of the natural count rate [31]. For enriched samples the activity can be measured much more precisely, but then the exact ^{39}Ar concentration is unknown. This is exactly the point were ArTTA comes into play, to give the absolute concentration of the enriched sample. By combining the activity measured at PNNL and the concentration of the 60X sample analysed by ArTTA a much more precise natural activity can be derived:

$$A_{\text{atm Ar}} = 1.68(7) \times 10^{-6}\,\text{Bq/cm}^3_{\text{Ar(STP)}} \tag{5.4}$$

With a relative uncertainty of 4 %, this result is much more precise compared to the result of $1.80(15) \times 10^{-6}\,\text{Bq/}^3\text{cm}_{\text{Ar(STP)}}$ measured with a 2.3 L two-phase (liquid and gas) argon drift chamber in [97] and comparable with the older result of $1.78(7) \times 10^{-6}\,\text{Bq/cm}^3_{\text{Ar(STP)}}$ published in [27].

6. Ocean Samples

The ^{39}Ar-analysis of three depth profiles, taken in the eastern tropical North Atlantic oxygen minimum zone (ETNA-OMZ) in 2015, represents the main result of this thesis. It demonstrates the full potential of the current ArTTA-system, which enables the quantification of ^{39}Ar with a required sample size of 5 L water and a measurement time of one day. This reduction in the sample size enabled the first ^{39}Ar-study, in which a complete oceanic depth profile of ^{39}Ar was sampled from one cast equipped with standard 10 L Niskin bottles. For a systematic study of the ArTTA-apparatus, 17 measurements of artificial samples with five different well known concentrations between 0 pmAr and 100 pmAr were analysed at different points of time during the measurement period. It is shown that the current detection limit is below 10 pmAr.

The ^{39}Ar results are combined with CFC-12 concentrations to constrain the transit time distributions (TTD). A maximal mean age of about 800 years is reached in a depth of around 3000 m. Below the OMZ, in a depth between 900 m and 2000 m, the obtained TTDs indicate a significant more advective transport than previously assumed and thus these water masses are much more influenced by younger water.

6.1. Samples

This chapter starts with an introduction of all measured samples during the ocean measurement period. Besides the natural ocean samples, some artificial samples with a defined ^{39}Ar-concentration were analysed to ensure consistency.

6.1.1. Ocean samples

The three analysed ocean depth profiles were taken during the M116 research cruise of an east-west transect following mainly the line of latitude at 11 °N, investigating the eastern tropical North Atlantic (ETNA) oxygen minimum zone (OMZ). The route of the cruise is depicted on map 6.1. The expedition started at Pointe-à-Pitre in Guadeloupe on 1 May 2015 and the research vessel METEOR arrived in Mindelo in Cape Verde on 2 June 2015 [99].

The cruise was in the context of the DFG-project "Climate-Biogeochemistry Interactions in the Tropical Ocean" with the main investigation of the circulation and ventilation of the OMZ of the Tropical Atlantic. In December 2012 the "Oxygen Supply Tracer Release Experiment" started by a deliberate injection of about 88.5 kg of halocarbon trifluoromethyl sulfur pentafluoride CF_3SF_5 at a depth of ∼500 m and near the centre of the OMZ. One main task of the cruise M116 was the third mapping of the tracer CF_3SF_5 after the tracer had been released. Additionally, at three stations

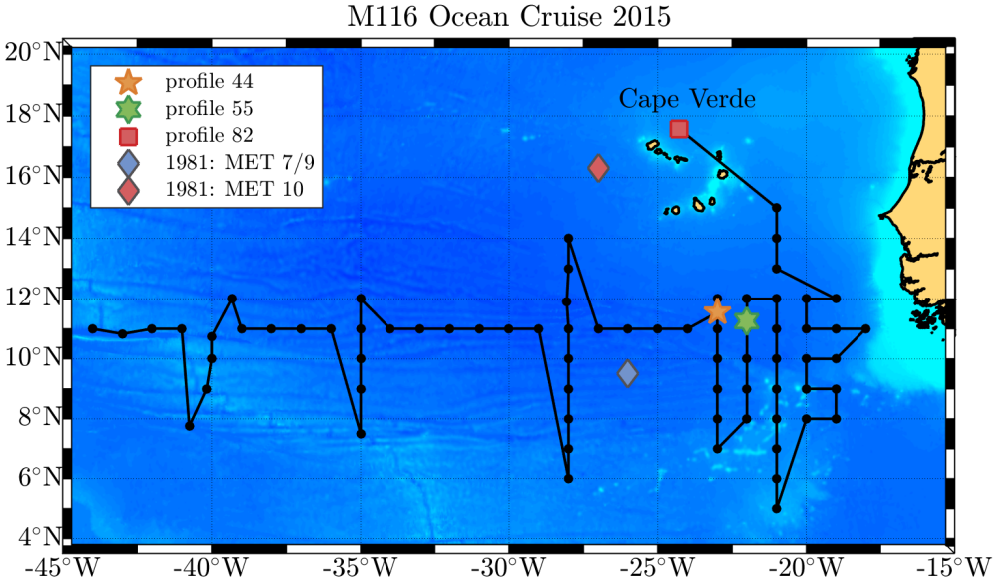

Fig. 6.1.: Route of the M116 research cruise of an east-west transect investigating the eastern tropical North Atlantic oxygen minimum zone (OMZ): At three points depth profiles for ^{39}Ar-analysis were taken, two in the centre of the OMZ and one at Cape Verde Ocean Observatory. The two historical sample sites are included, where in total three samples for LLC were taken in 1981.

water for ^{39}Ar-analysis was sampled. Profile 44 and 55 originate from the centre of the OMZ and are close to each other. Therefore similar properties of the water samples are expected. The profile 82 was taken at the Cape Verde Ocean Observatory north of the islands of Cape Verde.

The samples were taken with a cast equipped with 24 standard 10 L-Niskin bottles. In 2015, when the sampling took place, the requirements for ArTTA were slightly higher, so that always three different 10 L-Niskin bottles, closed at the same depth, were pooled together to one single sample of 21 L to 24 L of ocean water. Thus, each profile consists of 8 samples, originating from depths between 10 m and 4000 m. 20 brand-new, commercial 27 L propane gas bottles were used as sample containers. Since this was the first time using propane gas bottles for ocean water samples, four samples of profile 82 were additionally filled into stainless steel cylinders with a volume of 10 L. The propane gas bottles as well as the stainless steel containers were prepared in advance by flushing three times with nitrogen and refilling with 1100 mbar for shipping to the research vessel. They were evacuated to ∼1 mbar immediately before sampling. To prevent any contamination by partial equilibration of the top water layer in the Niskin bottle with the inflowing air while filling the propane gas bottles, only the lower 8 L of each bottle were maximally taken. The total sampling process of one sample took about 10 min. More detailed information about the sampling during the cruise can be found in [99, 50].

Subsequently, all samples were shipped to the Institute for Environmental Physics in Heidelberg, where up to three samples per day were degassed and purified with the system developed in [50], which is described in section 1.3. The typical achieved purity of the final argon sample was >98 %, which is sufficient, since ArTTA is not sensitive to contaminants. Particularly, the time consuming separation of Kr from Ar, which is necessary for LLC, can be left out. About 5.0 mL STP to 7.8 mL STP of pure Ar was extracted out of the samples in the bigger propane gas bottles and 2.3 mL STP to 2.7 mL STP out of the water stored in the smaller stainless steel cylinders. Detailed information about each sample is itemised in table 6.3. One of the stainless steel containers was broken during transport, one sample of profile 44 was lost during preparation due to an accidental misuse and two samples of profile 82 were excluded, since they might be contaminated. The remaining 20 samples were analysed by ArTTA.

6.1.2. Artificial samples with defined concentrations

For a systematic study also 17 measurements with well defined ^{39}Ar-concentrations between 0 pmAr and 100 pmAr were included in the ocean measurement period. Samples of 10 pmAr, 33 pmAr and 66 pmAr were generated by mixing the Ar-free underground sample and atmospheric bottle argon as described in section 1.4. The pure Ar-free sample and the pure atmospheric reference function as samples with a concentration of 0 pmAr and 100 pmAr, respectively. So five different samples with a well known concentration were analysed in total. The measurements of the Ar-free sample are also used to quantify the contamination.

6.2. ^{39}Ar-Measurements

The ocean measurement period took place, about two years after the cruise, between 7 June and 30 Aug 2017, and is with 1324.07 h of effective counting time by far the most extensive ArTTA-study to date. The measurements were performed with the final system as described in chapter 2. Especially the vacuum system had been partly rebuilt, the pumping speed upgraded and the differential pumping tubes optimised. Due to that, the mean atmospheric count rate was with $\overline{\nu}_{\mathrm{atm}} = 5.9\,\mathrm{atoms/h}$[1] almost doubled and the contamination reduced by factor five compared to the two previous measurement periods for the ice and intercomparison samples. Because of these improvements the amount of extracted argon would be enough to measure each ocean sample up to four times. In practice, each sample was measured at least twice, two samples three times, to improve the statistics. All measurements, including the contamination and the reference measurements, were conducted in recycling mode with sample sizes in the range of 1.3 mL STP to 5.8 mL STP. In total 41 measurements of the ocean samples and 15 of the defined samples were performed applying a one-day

[1] No uncertainties are given, since the reference measurements differ significantly from a Poisson distribution and each measurement is referenced individually.

measurement cycle with 20 h of counting time. With the about 10-times enriched $60X_{dil}$ sample of the intercomparison studies discussed in chapter 5, a non-atmospheric reference sample was used for the first time. Thus, a daily reference within 2 h of measurement was possible and long-term-drifts of the reference count rate thus can be compensated better. The ^{39}Ar-concentration of the $60X_{dil}$-reference is well known and was updated with all atmospheric and ocean samples taken at the ocean surface:

$$960^{+33}_{-31}\ \text{pmAr}$$

The main parameters of the ocean sample measurement period are summarised in table 6.1.

Table 6.1.: Overview of the main parameters from the ocean measurement period. Measurement time which was discarded due to failures of the system is not included in the values.

date of period	7 Jun to 30 Aug 2017
total measurement time	1324.07 h
total number of counted atoms	16 166
thereof estimated background atoms	649
atmospheric count rate ν_{atm}	4.3 atoms h^{-1} to 8.3 atoms h^{-1}
contamination rate a	$16.5^{+2.2}_{-2.0}$ μL STP c_{atm} h^{-1}
mean sample volume per ocean measurement	2.6 mL STP
mean lifetime τ	290 ms
mean single atom signal δ_n (δ_x)	15.9 kcps (1.26)

By far most breakdowns during the ocean measurement period were due to failures of the source, which happens only during igniting the plasma. The source tube and the coil had to be replaced seven times. A Kapton layer protecting the wire was used in the second part of the measurement period to extend the durability of the source coil. The system must be warmed up and the vacuum must be opened each time the source is repaired. After cooling down again, it takes at least one day for the system to stabilise again, which led to some measurements which had to be discarded. But no ocean samples were affected, since they can be stored temporarily in the buffer volume, if there is a break-down. As soon as the system is ready again the measurement can be continued.

6.2.1. Measurement cycle

A fix standard measurement cycle of one day was applied during the ocean measurement period, which is sketched in figure 6.2. The $60X_{dil}$-sample is measured for 2 h as a reference and the natural sample is counted for 20 h. Due to the enrichment of the reference sample, about 120 ^{39}Ar-atoms are counted for both, the reference and a modern natural sample.

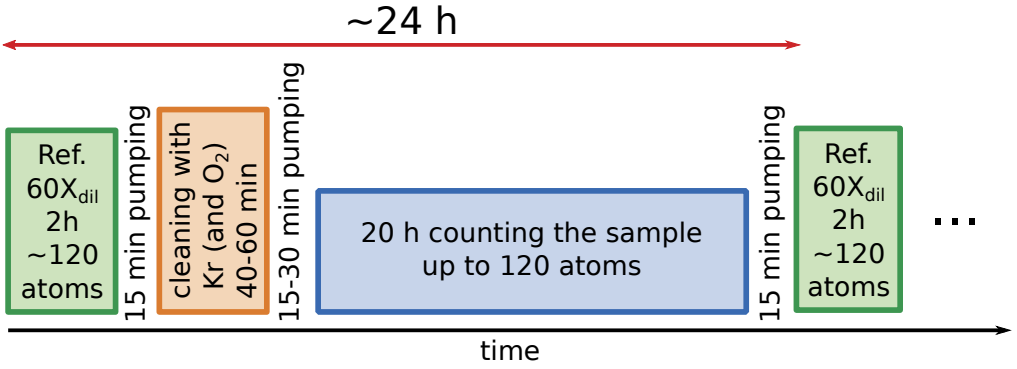

Fig. 6.2.: Measurement cycle of one day: 20 h of counting the sample, followed by 2 h referencing and a 40 min to 60 min wash with a Kr-discharge. About 120 ^{39}Ar-atoms are counted for both, the 10-times enriched reference and a sample with modern ^{39}Ar-concentration.

A 40 min to 60 min Kr-wash is included in between, to avoid any cross sample contamination between the enriched reference or a previous ocean sample and the next one.

The system is pumped between the different samples for at least 15 min and before the natural samples the pumping time is slightly extended to guarantee that the remaining gases do not exceed a pressure of 7×10^{-8} mbar in the source chamber and 7×10^{-5} mbar in the 10 L-buffer volume. This is 2 orders of magnitude below the pressure in the main chamber during operation and at least 4 orders of magnitude below the typical pressure in the buffer volume. The measurement cycle has a repetition rate of about 24 h, so that the sample throughput of the current ArTTA-system is up to one sample per day.

The 10-times enriched reference sample leads to an average ^{39}Ar-concentration inside the vacuum system during the measurement cycle of about ~170 pmAr, which is about 23 % of the ^{39}Ar-concentration of the current outgassing contamination, which is around 7.5-times the atmospheric abundance (compare chapter 3.3.2). Thus, one must be careful using enriched reference samples because of the risk of a recontamination of the exchanged vacuum parts.

6.2.2. Krypton wash

To avoid any cross sample contamination between the enriched reference and the natural sample and to generate a defined, identical initial status of the vacuum system, a standardised 40 min to 60 min Kr-wash was applied before each measurement. During the washing-procedure the apparatus is operating in throughput configuration while the plasma discharge is running. The Kr gas flows continuously and is discarded to clean the vacuum system and to remove the remaining Ar. The getter pump is closed during the wash. The system can be monitored with the RGA and the remaining Ar can be measured by detecting the fluorescence of an ^{38}Ar-MOT. Both signals are plotted in graph 6.3.

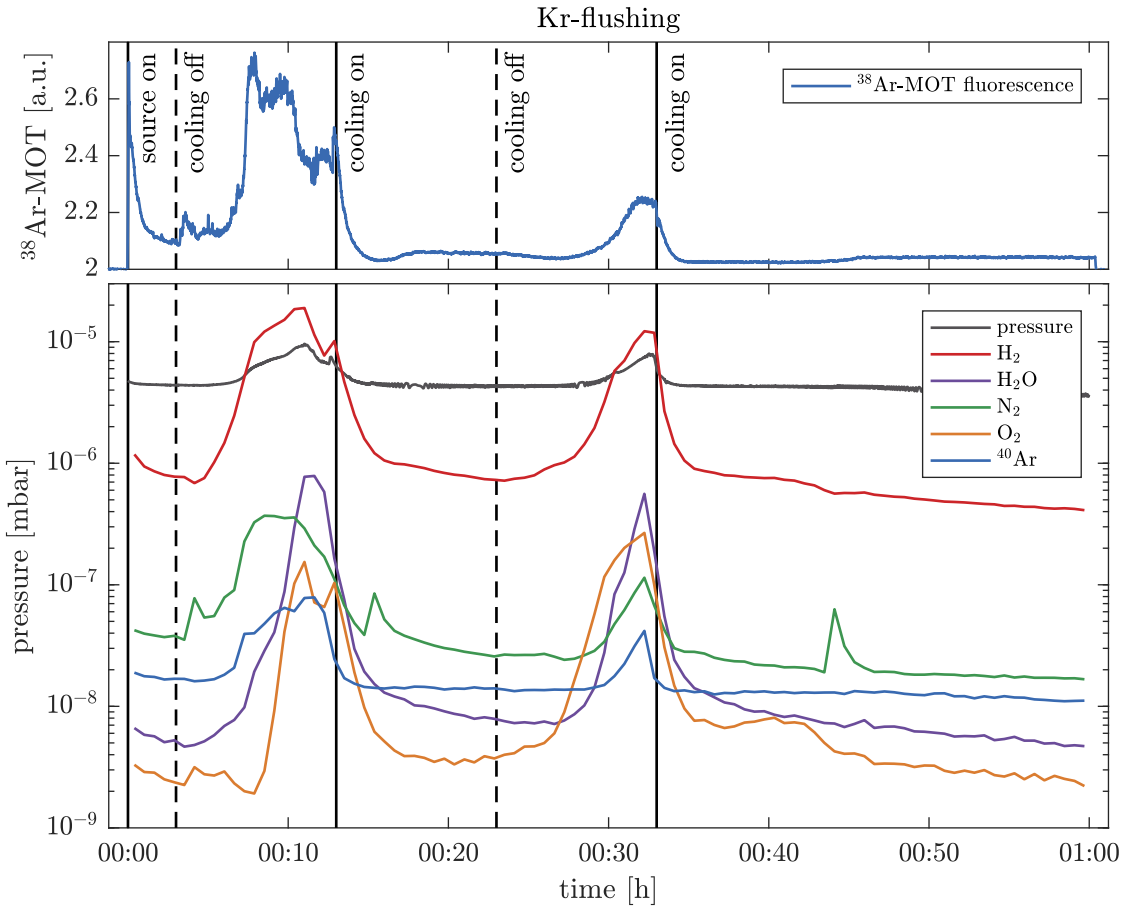

Fig. 6.3.: ^{38}Ar-MOT fluorescence, total pressure and partial pressure measured with the RGA during a Kr-wash: The source is switched on at $t = 0$. To remove remaining gas frozen to the cooled source, the cooling is switched off two times for 10 min each. The main part of gases is released directly after the ignition of the source and when the cooling is switched off for the first time. The H_2-partial pressure exceeds the total pressure due to a miscalibration of the RGA.

A huge part of gases is released directly after the ignition of the source. But the main part is still frozen to the cooled components of the source. Therefore the liquid nitrogen cooling of the source is switched off two times for 10 min each during the Kr-wash. The system is cooled for 10 min in between to avoid any damage to the source. About 5 min after the cooling was switched off there is a strong increase of the ^{38}Ar-signal and of the partial pressures. Mainly hydrogen and nitrogen are released. As soon as the cooling is switched on again all pressures decrease immediately. The peak in the ^{38}Ar-signal during the second time of interrupting the cooling is significantly suppressed compared to the first one. Thus, the mechanism for a fast contamination component as discussed in chapter 3.3.2 is identified to be dominated by adsorbed argon to the cooled parts of the source. This component can be suppressed by a short controlled defrost of the source and is replaced by Kr during flushing the system. Now, Kr, which does not contaminate the Ar-sample, is released instead of Ar during the subsequent measurement (compare also figure 3.11b).

The time of the Kr-wash is meanwhile used to refill the liquid nitrogen storage tank for cooling the source, which has to be done at least every 40 h and takes about 30 min to 45 min. This has the advantage that the refill is not done during the measurements itself, since it entails the risk, that the pressure in the nitrogen tank drops and the source heats slightly up. This can lead to an uncontrolled release of gas frozen to the source, which then contaminates and pollutes the sample. Besides that, it is necessary for a stable operation of the system to keep the temperature conditions constant and therefore to switch the source off as briefly as possible. The Kr-wash bridges the time span of the nitrogen refill.

In the second part of the ocean measurement period an admixture of a small fraction of oxygen during the Kr-wash was tested to rejuvenate the discharge source and to improve its durability, as it is successfully done for Kr-ATTA [100]. The idea behind this procedure is to oxidise the accumulated, conducting carbon layer on the source tube(compare picture 2.3b). An increase of CO_2 while adding O_2 could be observed with the RGA, and the lifetime of the last source, the only one which was treated with O_2, was much longer compared to the others, but it is difficult to quantify these effects yet.

6.2.3. Reference and contamination

Since a reference measurement was included in the daily measurement cycle, there are 60 reference measurements of the 10-times enriched $60X_{dil}$ sample during the ocean measurement period. The time courses of the reference and of the five contamination measurements are plotted in the overview 6.4. The contamination is quantified with help of the ^{39}Ar-free underground sample.

In total $N = 11\,725$ atoms in $T = 206.8$ h were counted during the reference measurements, which would give, considering a perfect Poisson distribution, a statistical uncertainty of the over-all averaged reference count rate $\overline{\nu} = 56.7$ atoms/h of less than 1 %. However, the external variance $\sigma_{ext} = 0.94$ atoms/h of the reference measurements is much higher than the internal variance $\sigma_{int} = 0.52$ atoms/h (compare chapter

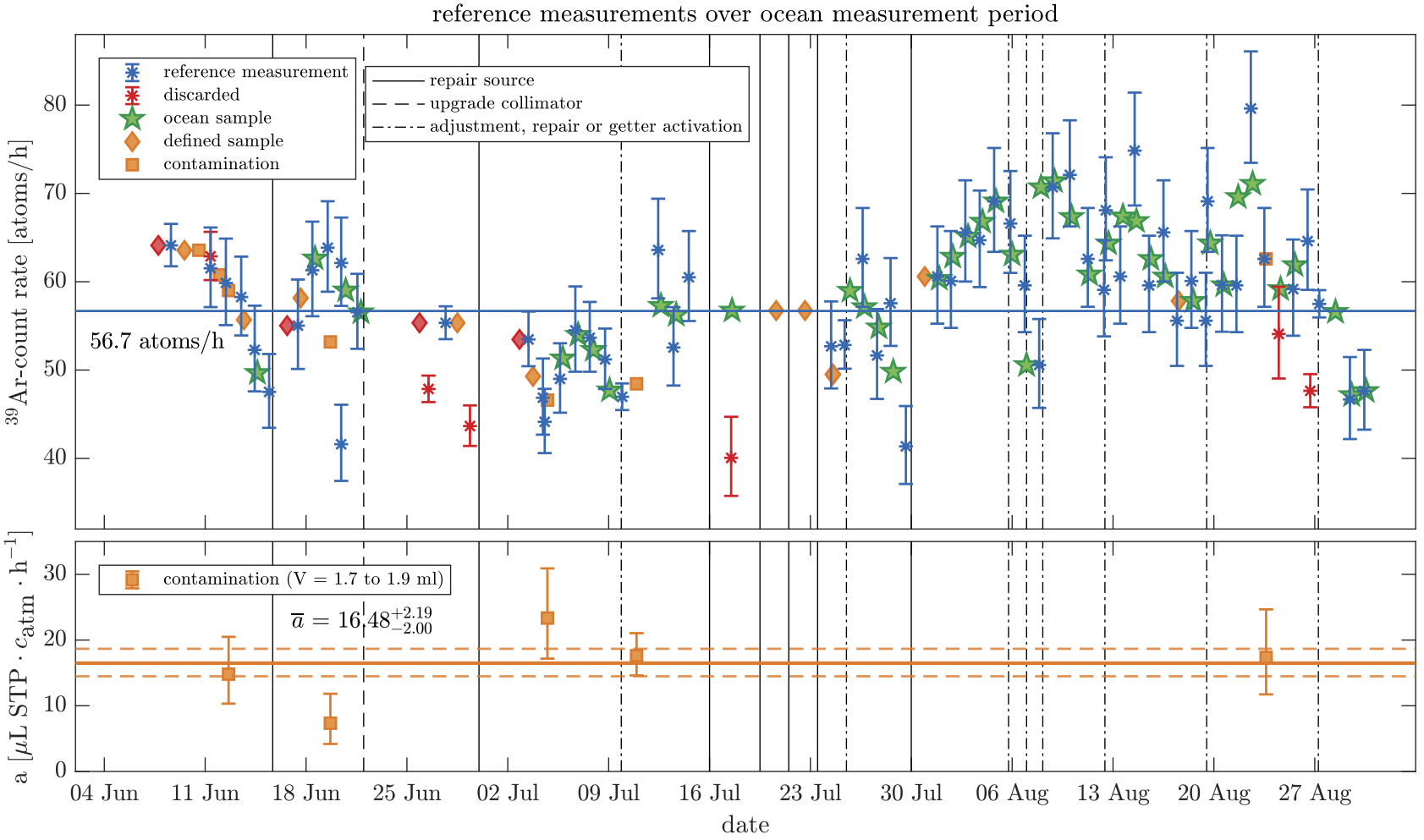

Fig. 6.4.: Overview of all references (top): As the time series show domains with count rates significantly above and below average, only the two references directly before and after each measurement are used. The markers for the samples show the individual reference determined for this measurement. The contamination is quantified with five measurements of the ^{39}Ar-free sample (bottom). The horizontal lines indicate the mean and the bounds of the maximum likelihood confidence interval of 1σ (68.3 %). The vertical lines mark dates of (major) interventions to the system. The system was treated with O_2 during all Kr-washes after 30 July.

100

3.3.3) and the time series shows time domains with count rates clearly above and below average. No conclusive correlations to any monitoring signal, e.g. the signal of the flux monitor or the beam profiler, were found. Instead of a global reference thus, only the two references in the direct neighbourhood of each measurement are considered for referencing the measured count rate of the sample, as already discussed in chapter 3.3.3. By taking an individual reference count rate for each analysis, it is possible to compensate the long-term drifts of the efficiency of the system, but on the expense of the statistical uncertainties. During two reference measurements on average 225 atoms were counted, which gives an uncertainty in the reference of 6.5 %.

The corresponding atmospheric count rate can be calculated by scaling with the concentration of the $60X_{dil}$ reference sample. During the ocean sample measurement period the over-all averaged atmospheric count rate was $\overline{\nu}_{atm} = 5.9\,\text{atoms/h}$ and the maximally achieved one $\nu_{atm,\,max} = 8.29(66)\,\text{atoms/h}$ (one singe measurement).

Contamination

A replacement of the main vacuum chamber and the collimator had reduced the contamination by about a factor five compared to the two previous measurement periods. Thus, the exact quantification of the contamination embedded in the vacuum system is not so significant any more. The contamination rate is inferred from the analysis of five measurements of the ^{39}Ar-free blank sample. A sample size between 1.7 mL STP and 1.9 mL STP was chosen to have identical conditions compared to the ocean samples. The average contamination rate is:

$$\overline{a} = 16.5^{+2.2}_{-2.0}\ \mu\text{L STP}\ c_{atm}\ h^{-1}$$

This corresponds to about ∼360 ^{39}Ar-atoms, which accumulate in the sample per hour, or on average to 9.7 counts due to contamination during a typical 20 h measurement of a 2 ml sample. For an atmospheric measurement this is about 7.5 % of all counted atoms.

6.3. Results

The artificial samples were measured in the exact same way as the ocean samples distributed over the complete measurement period. All data were analysed with the methods presented in chapter 3, which were developed to handle the large data set of this measurement period. If the same sample was measured several times, all measurements are combined to one result. All individual measurements are listed in appendix D.

6.3.1. Mixed samples

The measured ^{39}Ar-concentrations of the well defined samples are summarised in figure 6.5 and table 6.2. The five defined samples were analysed in 15 independent

measurements in total. The results of the ^{39}Ar-free sample were used both, for determination of the contamination and as sample with a defined concentration of 0 pmAr.

Except for one measurement of the 66 pmAr-sample, all measurements are in good agreement with the defined concentration of the sample. Some of the measurements might not have been conducted under perfect conditions. Since the artificial samples are available in a nearly unlimited amount, a complete loss of a measurement is not that critical and some of the measurements were conducted as a test after a repair or an adjustment of the system.

The 10 pmAr sample was included in the measurement period to test and demonstrate the detection limit of the current ArTTA-apparatus. The lower bound of the measured 1σ-confidence interval is clearly distinguishable from an ^{39}Ar-free sample and the 10 pmAr is thus clearly above the detection limit, which is theoretically around 5 pmAr (see figure 7.1).

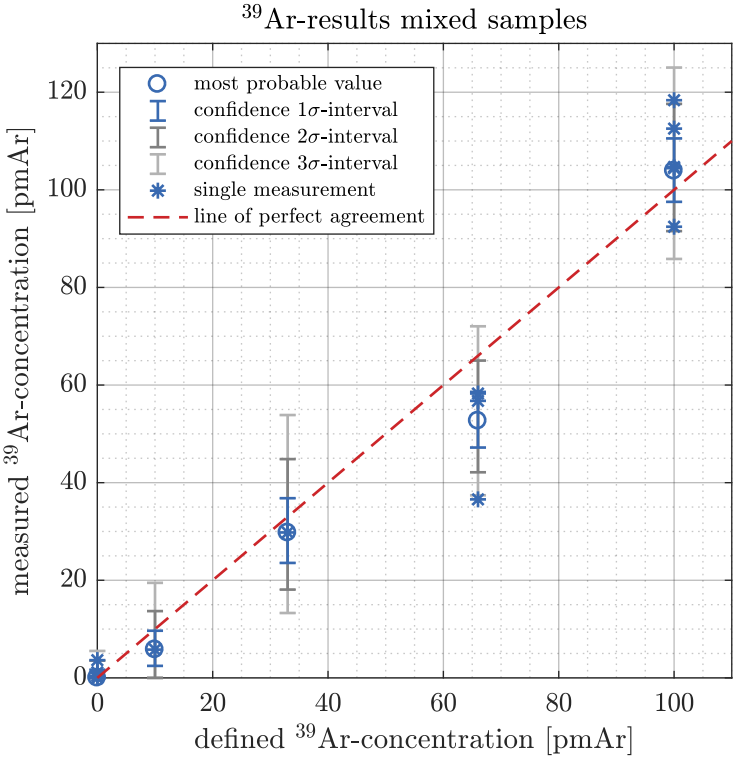

Fig. 6.5.: Measured concentration of the artificial samples as a function of the well defined concentration: The dashed line is a guide to the eye and indicates a perfect agreement between the given and measured concentrations. The 1σ-confidence interval of the 10 pmAr-sample is clearly distinguishable from the background and thus above the detection limit of the current system.

Table 6.2.: Measured ^{39}Ar-concentrations of the artificial samples with defined concentrations

sample	number of measurements	total time [h]	counted atoms	estimated contam. atom	^{39}Ar [pmAr]
dead (0 pmAr)	5	107.2	64	65.1	≤ 1.7
10-pmAr	1	20.7	18	10.9	$5.8^{+3.9}_{-3.3}$
33-pmAr	1	18.0	40	8.8	$29.7^{+7.1}_{-6.2}$
66-pmAr	3	51.9	195	29.5	$52.7^{+5.9}_{-5.5}$
atm (100 pmAr)	5	77.1	510	35.0	$103.9^{+6.7}_{-6.3}$

6.3.2. Ocean samples

Due to the reduced contamination and the improved count rate, the extracted argon of the 20 L ocean water allows in principle three or, for some samples, even four independent measurements. All ocean samples were measured at least in two independent measurements, to have a handle on outlier as well as on the scattering of the measurements and to improve the statistical uncertainties. For the first measurement of each sample ∼1.8 ml of argon were used, which corresponds to about 5 L of ocean water. The two samples of profile 44, for which no samples at the corresponding depth in profile 55 are available, were measured three times to reduce the statistical uncertainties.

The ^{39}Ar-concentrations of the three depth profiles are compiled in figure 6.6 and listed in table 6.7. All profiles show a rapid decrease of the ^{39}Ar-concentrations in the upper 1500 m [2] followed by a more homogeneous concentration down to 4000 m. The lowest ^{39}Ar-concentrations are measured around 3000 m. Below this depth the ^{39}Ar-concentrations rise slightly again. No single measurement shows a very implausible result, so that there would be a reason to exclude it. However, it is difficult to make a statistically reliable statement based on only two or three independent measurements.

6.4. Comparison with previous measurements

In total about 125 ocean samples were analysed by LLC between 1979 and 1991, which are tabulated in [60]. Only three of these Ar-samples were taken at stations close to the ones visited in the current study – each about 200 km southwest of station 44/55 and 82, respectively (see map 6.1). For the analysis with LLC about 300 mL of pure argon gas and a counting time of 6 weeks were required. The corresponding 1000 L of ocean water were obtained by combining the water from four Gerhard-Ewing samplers each with a volume of 250 L. The water was directly degassed on-board on

[2] The pressure in dbar corresponds approximately to the depth in m. Since the pressure is measured while sampling and the exact conversion depends on salinity and temperature of the water column, the pressure is normally used as a measure of the depth in the oceanography.

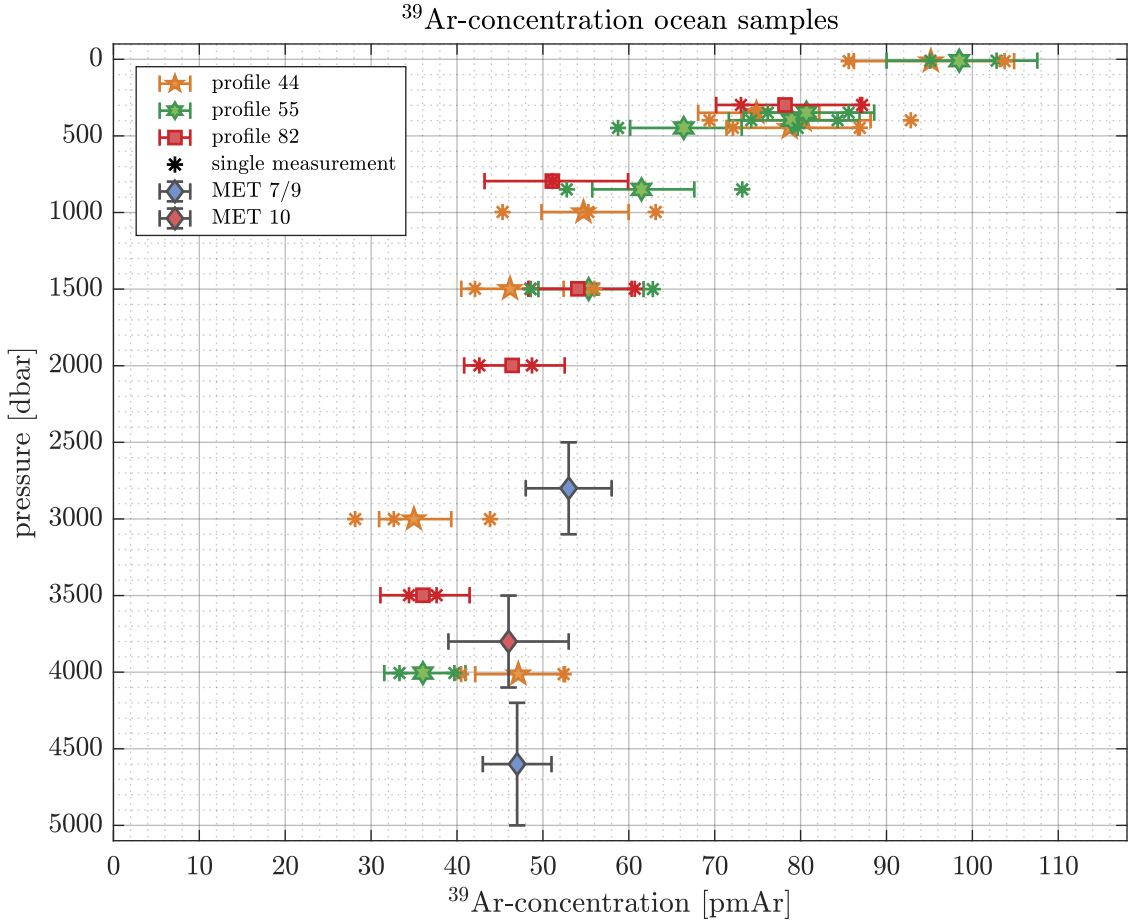

Fig. 6.6.: ^{39}Ar-concentration of the three depth profiles sampled in the east-tropical North Atlantic oxygen minimum zone during cruise M116. Each sample was measured at least twice. The shown error bars indicate the uncertainty of the averaged values. The three historical samples, which were taken nearby in 1981 and analysed by LLC, have similar concentrations [101]. The slightly higher ^{39}Ar-concentration of the upper historical data point might be explained by observed meridional gradients in freons concentrations in this region [102]. The pressure in dbar corresponds approximately to the depth in m.

Table 6.3.: ^{39}Ar-results of the three depth profiles taken during cruise M116

profile	**longitude** [°W]	**latitude** [°N]	**pressure** [dbar]	S_P [‰]	T [°C]	**bottle** #	**weight** [kg]	**extracted Ar amount** [mL STP]	**number of meas.**	**total time** [h]	**counted atoms**	**estimated contam.**	^{39}**Ar** [pmAr]
44	-22.99	11.55	4013	34.889	2.38	10	22.1	7.5	2	39.7	147	17.6	$47.1^{+5.4}_{-5.0}$
44	-22.99	11.55	3001	34.923	2.74	13	22.2	6.6	3	59.8	162	34.9	$35.0^{+4.4}_{-4.1}$
44	-22.99	11.55	1498	34.954	4.34	4	24.1	6.1	2	30.0	103	11.0	$46.2^{+6.2}_{-5.7}$
44	-22.99	11.55	997	34.807	5.62	9	22.0	6.8	3	60.1	231	30.3	$54.7^{+5.3}_{-4.9}$
44	-22.99	11.55	447	35.061	9.93	20	22.5	5.3	2	42.3	216	20.5	$78.7^{+8.0}_{-7.4}$
44	-22.99	11.55	398	35.100	10.41	17	23.1	5.7	2	40.0	217	18.0	$80.3^{+7.8}_{-7.2}$
44	-22.99	11.55	348	35.191	11.21	19	22.0	6.5	2	40.1	212	17.4	$74.9^{+7.3}_{-6.8}$
44	-22.99	11.55	12	35.909	24.95	14	20.7	5.2	2	34.9	241	22.1	$95.2^{+9.7}_{-9.0}$
55	-22.00	11.25	4006	34.888	2.38	5	22.5	7.2	2	40.8	104	13.7	$36.0^{+5.0}_{-4.5}$
55	-22.00	11.25	3000	34.922	2.73	18	24.0	lost during preparation					
55	-22.00	11.25	1500	34.962	4.30	8	24.0	6.4	2	40.0	147	14.4	$55.3^{+6.4}_{-5.9}$
55	-22.00	11.25	849	34.758	5.99	16	22.0	6.4	2	43.1	181	19.2	$61.5^{+6.2}_{-5.7}$
55	-22.00	11.25	448	35.096	9.79	7	22.0	6.0	2	47.2	215	19.5	$66.4^{+6.8}_{-6.2}$
55	-22.00	11.25	398	35.155	10.47	11	24.0	5.9	2	40.0	210	16.2	$78.9^{+7.9}_{-7.3}$
55	-22.00	11.25	348	35.190	10.99	15	22.0	5.5	2	40.0	220	15.1	$80.7^{+7.9}_{-7.3}$
55	-22.00	11.25	9	35.877	26.52	6	21.2	5.0	2	40.0	265	19.9	$98.5^{+9.1}_{-8.5}$
82	-24.28	17.58	3498	34.907	2.51	2	25.0	5.4	2	40.0	108	19.8	$36.0^{+5.4}_{-5.0}$
82	-24.28	17.58	2998	34.929	2.77	5HD	10.5	2.7	might be contaminated				
82	-24.28	17.58	2998	34.929	2.77	3HD	10.0	3.1	might be contaminated				
82	-24.28	17.58	1998	34.978	3.66	3	25.5	5.2	2	39.8	131	18.3	$46.4^{+6.1}_{-5.6}$
82	-24.28	17.58	1498	35.012	4.66	1	25.0	7.8	2	40.0	153	12.3	$54.1^{+6.3}_{-5.8}$
82	-24.28	17.58	796	34.918	7.07	4HD	9.0	lost during transport					
82	-24.28	17.58	796	34.918	7.07	1HD	10.0	2.3	1	15.7	71	11.2	$51.1^{+8.8}_{-7.9}$
82	-24.28	17.58	298	35.437	12.15	12	26.3	7.3	2	40.3	210	25.3	$78.2^{+8.7}_{-8.0}$

the research vessel with a rate of 8 L/ min. Due to the mixing of samples the historical samples represent a concentration integrated over a depth of 600 m to 800 m [101]. The reported ^{39}Ar-concentrations are included in plot 6.6.

The two deeper historical samples are in good agreement with the current results. The upper one, taken at a depth of 2800 m, has a slightly higher concentration. This discrepancy might be explained by observed meridional gradients in freon concentrations in this region [102].

LLC of ^{39}Ar extracted from 1000 L of ocean water was only feasible as long as large samples for ^{14}C analysis were routinely collected. However, with the progress of AMS technology, nowadays only sample sizes below 1 L of water are required and no big amounts of water are routinely available. As a consequence LLC of ^{39}Ar dissolved in ocean water was discontinued for the last 25 years [32].

The ^{39}Ar-analysis using Accelerator Mass Spectrometry was demonstrated with three ocean samples from the Southern Atlantic in a proof of principle experiment in 2004. With a measurement time of 6 h to 10 h and a sampling size of 20 L, the requirements were comparable with the current ones for ArTTA. However, due to the needed costly accelerator facility and further required research reducing the ^{39}K-background, no routine ^{39}Ar-measurements were performed [32].

6.5. Transit time distribution constrained by ^{39}Ar

This section should demonstrate the potential of ^{39}Ar in combination with other tracers, here CFC-12, to constrain the transit time distributions (TTD) of the analysed ocean water masses. An exact knowledge about the TTD opens the possibility to calculate the concentration of a tracer, which can not be measured directly or was not measured. The general principle of TTDs and the use of inverse Gaussian distributions are introduced in chapter 1.6. This section is strongly influenced by ideas which came up during discussions with Tim Stöven and Toste Tanhua from the GEOMAR in Kiel while writing the publication concerning the ^{39}Ar-measurements reported here and their impact on TTDs, which was in preparation at the time of handing in this thesis.

Profile 44 and 55 were sampled near to each other and in similar depths. Thus, the ocean samples have very similar properties and these two profiles are combined to one in order to reduce the uncertainties of the ^{39}Ar-concentrations.

CFC-12 concentrations

As a second tracer CFC-12 is used[3], which was measured routinely during the cruise but not directly in the same water samples for the ^{39}Ar-analysis. Therefore the CFC-12 concentrations of the combined profile are extrapolated values along constant density lines from the neighbouring station 54 located at 11.00 °N and 22.00 °W. The CFC-12 concentrations of profile 82 are taken from profile 81, which was sampled ∼3 h before

[3] SF_6 data are also available, however here it is focused on the tracer couple CFC-12 and ^{39}Ar, since SF_6 only has advantages in the time ranges of the last 25 years.

at the same position [103]. The resulting ^{39}Ar and CFC-12 concentrations used for the TTD-calculations are plotted in figure 6.7 and are itemised in table 6.4.

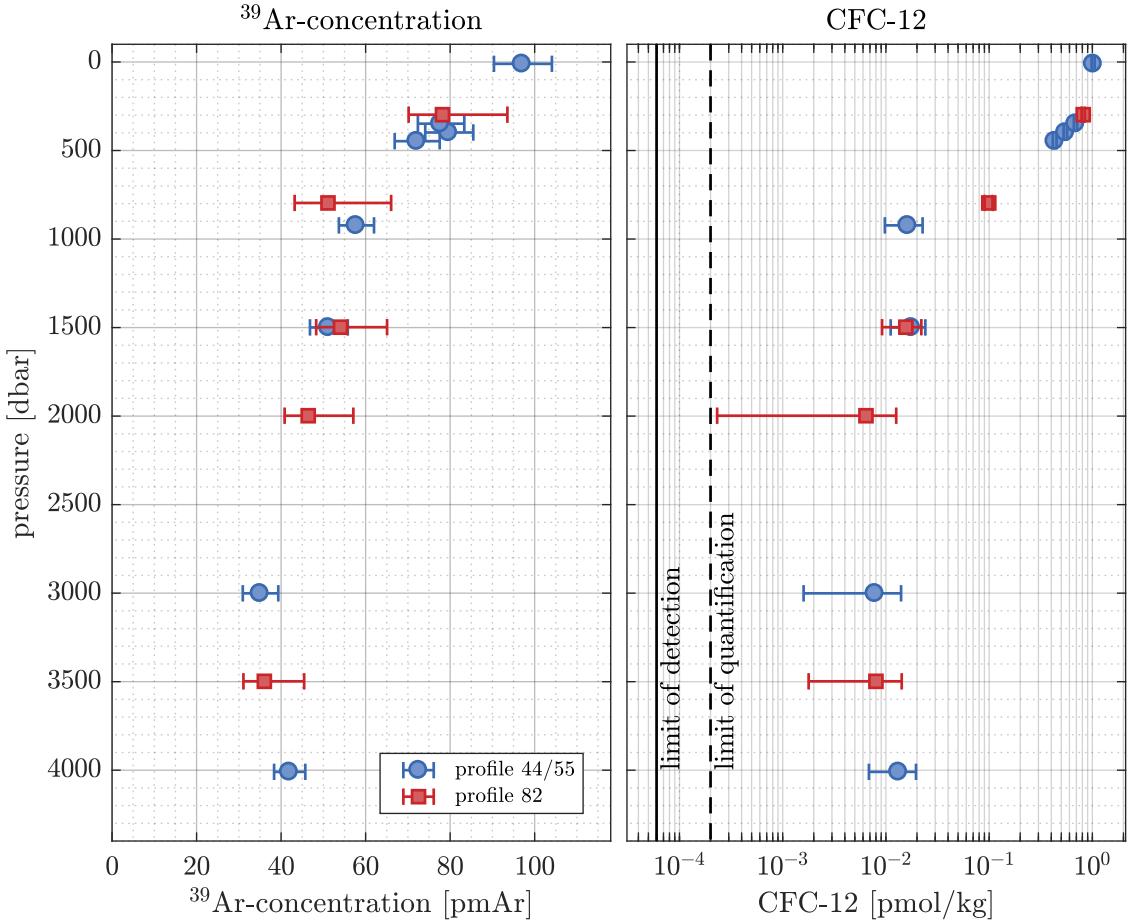

Fig. 6.7.: ^{39}Ar and CFC-12 concentrations used for constraining the transit time distributions: The two neighbouring profiles 44 and 55 are combined to one profile. The two vertical lines indicate the limit of detection ($0.06\,\mathrm{fmol\,kg^{-1}}$) and the limit of quantification ($0.2\,\mathrm{fmol\,kg^{-1}}$), which are defined 3σ and 10σ, respectively above the background noise.

The tracer CFC-12 is based on the absolute concentration and not like ^{39}Ar only on a relative abundance. However, the solubility of CFC-12 is highly dependent on temperature and salinity [104], which is plotted in figure 6.8a, and thus the temperature and the salinity of the water masses at the time of the last contact with the atmosphere have to be estimated. One common approximation is to consider temperature and salinity as conservative properties which only change at the water surface. This can introduce some uncertainties, since these properties can erode slowly as the water properties are transported to different parts of the ocean or if water masses blend.[4]

[4]The noble gas tracer ^{85}Kr is only based on the relative concentration and thus not on temperature and salinity and covers a similar time window as CFC-12. ^{39}Ar and ^{85}Kr might be an ideal tracer couple for future studies.

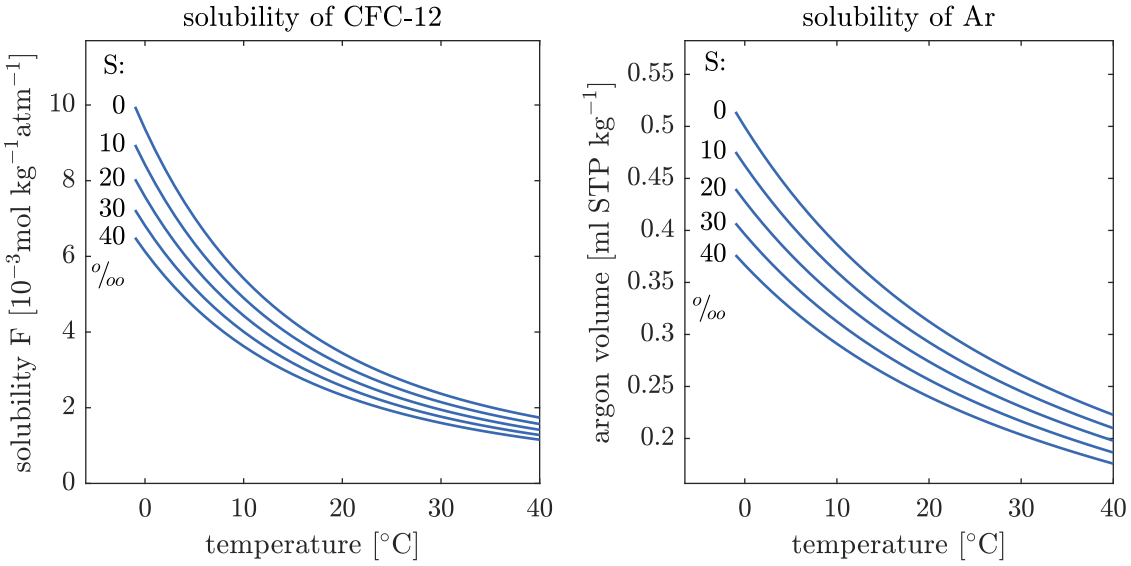

(a) Solubility CFC-12 [104] (b) Solubility of Ar [17]

Fig. 6.8.: Solubility of CFC-12 and argon: The solubility of CFC-12 is given as solubility function F, the solubility of Ar directly as ^{39}Ar-concentration. All values are related to moist air. The CFC-12 solubility is required for the calculation of the partial pressures (equation 6.1). The solubility of Ar gives an estimation of the expected Ar-yield. Saline warm water samples contain much less Ar than cold freshwater.

In a first step the measured salinities, which are given as practical salinities S_P (a measure of the conductivity of seawater), have to be converted to absolute salinity S_A (mass fraction of salt in seawater). In a second step the measured in situ temperatures T of each sample are transformed to potential temperatures θ referenced to the ocean surface [105]. This is the temperature, which a water parcel would have when it moved adiabatically to the surface, and corresponds to the temperature which the water parcel had at the last contact with the atmosphere assuming the temperature as a conserved property.

Finally the partial pressure p_{CFC12} of CFC-12 is calculated for each sample from the expression[65]:

$$p_{\mathrm{CFC12}} = \frac{c_{\mathrm{CFC12}}}{F_{\mathrm{CFC12}}(\theta, S_A)} \,. \tag{6.1}$$

Where c_{CFC12} is the measured concentration of dissolved CFC-12 in the water sample and $F_{\mathrm{CFC12}}(\theta, S_A)$ the solubility of CFC-12 as a function of potential temperature θ and salinity S_A. The solubility of CFC-12 is reported in [104] and plotted in figure 6.8a. The partial pressure is independent of the salinity and the temperature, thus it is possible to compare the levels of dissolved CFC-12 directly with the corresponding atmospheric partial pressure.

Calculation of the TTDs

An inverse Gaussian distribution, given by equation 1.13, is used to describe the TTDs of the ocean samples. For a grid of different pairs of the two parameters, mean age Γ and width Δ/Γ, the expected concentrations of ^{39}Ar and CFC-12 are calculated applying equation 1.12. Thereby a constant input function of ^{39}Ar is assumed and the CFC-12 concentration of the northern hemisphere as reported in [8] and plotted in 1.7.

By comparing the measured tracer concentrations (or partial pressures[5]) with the calculated concentrations, each tracer constrains the TTD to one curve in the parameter space (see figure 6.9). The curves of two different tracers, covering different time ranges, intersect in one point in the parameter space. This intersection point determines the mean age Γ and the width Δ/Γ of the TTD of the water sample.

The uncertainties of the measured tracer concentrations are mapped into the parameter space of the TTD, which is illustrated in figure 6.9. Considering the uncertainties, each tracer does not only give one curve, but allows an area of possible parameters. The TTD is constrained by the area which is covered by both tracers. The area of the most probable values of the tracer concentrations is given by the ellipse, defined by the sum of the quadratic difference Δ from the mean values normalised to the standard deviation σ

$$\sqrt{\left(\frac{\Delta_{^{39}Ar}}{\sigma_{^{39}Ar}}\right)^2 + \left(\frac{\Delta_{\mathrm{CFC12}}}{\sigma_{\mathrm{CFC12}}}\right)^2} \leq \xi \; . \tag{6.2}$$

In principle $\xi = 1.515$ would lead to common 1σ-confidence intervals (68.3 % of all values are inside the ellipse). However, the uncertainties of the CFC-12 concentrations are highly asymmetric because the sensor operates in a non-linear regime at higher concentrations [103]. For the lower CFC12-limits the larger uncertainties of the upper limits are reported in the cruise report. A simple scaling of the CFC12-confidence intervals is thus not possible and would lead to negative concentrations, so that $\xi = 1$ was chosen to estimate the uncertainties of the TTDs in this thesis. It should be noted that as a consequence of this the reported confidence intervals of the mean age Γ and of the width Δ/Γ only correspond to 39 %. However, the uncertainties of the CFC-12 concentrations are estimated conservatively, so that this value can be seen as a lower bound. Since the ^{39}Ar-confidence intervals are asymmetric, different values of the standard deviations are used for each quadrant. This ellipse is transformed into the parameter space of the TTD, where it has an elongated shape. The deduced mean age Γ and width Δ/Γ are highly correlated. The reported uncertainties of the mean age Γ and the width Δ/Γ are the minimal and maximal values of this transformed ellipse, which is again a conservative estimation due to the correlations.

[5] In the following it is not distinguished between concentration and partial pressure, and the expression concentration is used imprecisely for both.

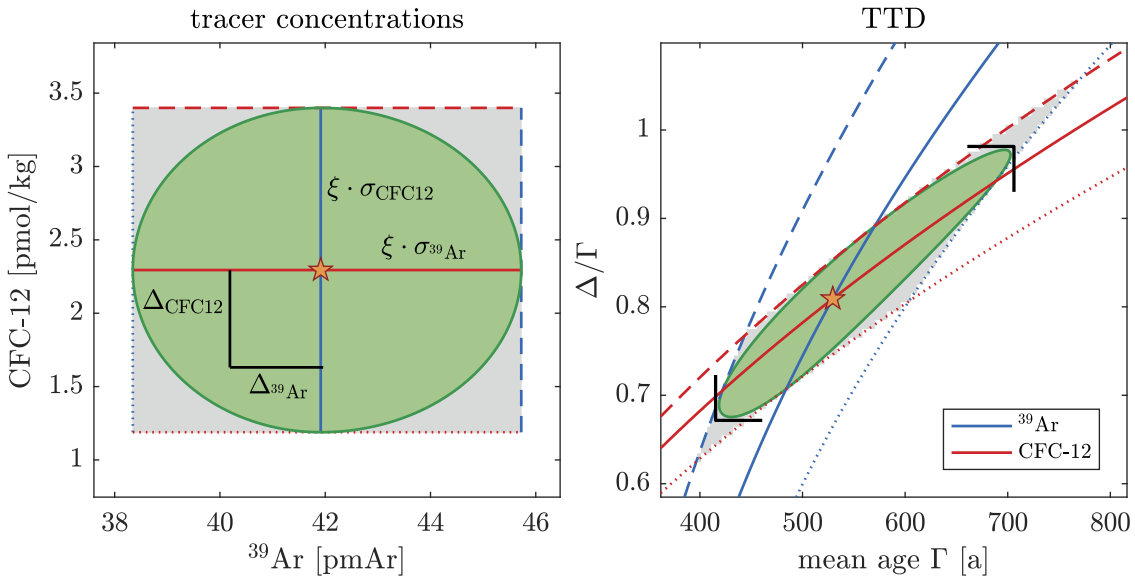

Fig. 6.9.: Calculation of the parameters of the TTD using the tracer couple ^{39}Ar and CFC-12: The measured tracer concentrations (left side) are mapped into the parameter space of the TTD (right side). Each tracer constrains the TTD to one curve in the parameter space. The mean age Γ and the width Δ/Γ are given by the intersection point of both curves (marked with the pentagram). Due to the uncertainties of the measured concentrations (grey area) each tracer does not only give one possible line in the parameter space but an area. This area is bounded by the dashed and dotted lines. The area of the most probable concentrations is given by the (green) ellipse, defined by equation 6.2. Here $\xi = 1$ (corresponding only to a 39 %-confidence interval) is used, since a scaling of the CFC-12 uncertainties is not possible. This ellipse is mapped into the parameter space of the TTD, where it has an elongated shape. The minimal and maximal values of this transformed ellipse (illustrated by the two black triangles) are reported as the uncertainties of Γ and Δ/Γ. By this error propagation two extreme values of both concentrations (grey corners) do not lead to disproportionately high uncertainties of the parameters describing the TTD.

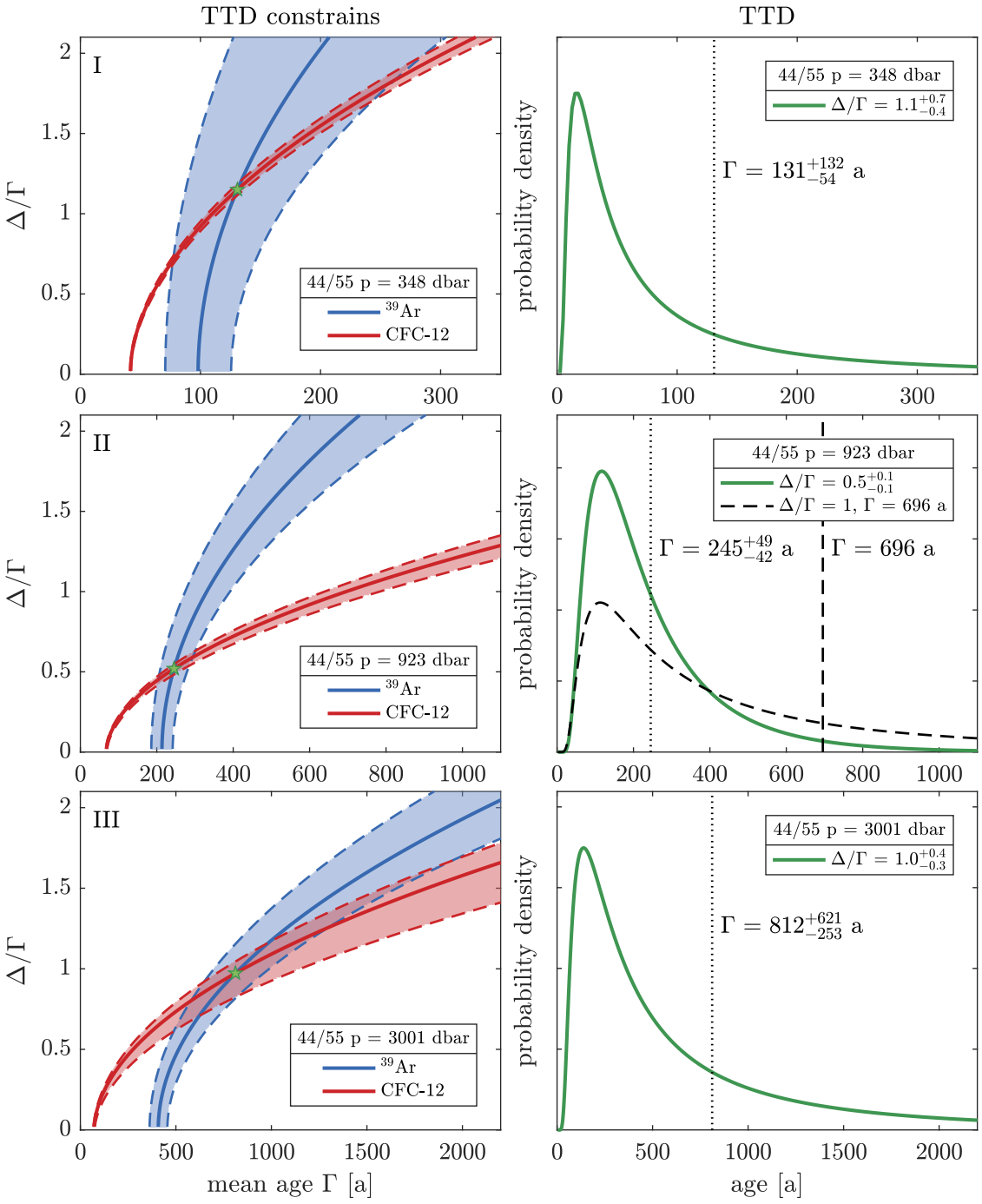

Fig. 6.10.: Three typical TTDs constrained by the ^{39}Ar and CFC-12 concentrations of the combined profile 44/55 sample at depths of 348 dbar (upper), 923 dbar (middle) and 3001 dbar (lower). The TTD in the second row, plotted as dashed line, shows the TTD, which was previously assumed with the fix standard parametrisation of $^{\Delta}/_{\Gamma} = 1$, as long as no ^{39}Ar-data were available. For more details it is referred to the main text.

Three typical TTDs (348 dbar, 923 dbar and 3001 dbar) constrained by the ^{39}Ar and CFC-12 concentrations of the combined profile 44/55 are shown in figure 6.10.

For the well ventilated upper sample the currently obtainable precision of ^{39}Ar-concentration is not sufficient for a precise determination of the TTD. While the CFC-12 value constrains the parameters to a small area, the measured ^{39}Ar-concentration allows a huge range of parameters. Thus, the uncertainties of the obtained TTD are huge.

For the water sampled in a depth of around 1000 m the constrains of both, ^{39}Ar and CFC-12, give nearly orthogonal curves, which only have a small overlap. The time range of this tracer couple fits perfectly for this water mass and the TTD is very well constrained. The obtained mean age Γ is $245^{+49}_{-42}\,a$ and the width $\Delta/\Gamma = 0.5(1)$ are much lower than the standard parametrisation of $\Delta/\Gamma = 1$, which is used, if not enough or no appropriate tracer data are available [71, 72]. Thus, the water mass is much more dominated by an advective flux than by diffusion. Using only the CFC-12 data and a fix ratio of $\Delta/\Gamma = 1$ would give a much higher mean age of 696 a and a TTD which has only a small contribution of young water. For this sample there is a high benefit using ^{39}Ar as a tracer.

The third sample was taken in a depth of around 3000 m and has the lowest CFC-12 concentration. Thus, it becomes more difficult again to constrain the TTD. The curves of both parameters are more parallel and the area to which CFC-12 constrains the TTD is relatively large compared to the other samples. Consequently, there is a large overlap of both tracers and the uncertainties of the TTD are huge. With a mean age of $\geq$559 a this sample is the oldest sample measured in this study and this calculated mean age is much older than the simple ^{39}Ar-tracer age of 400 a, corresponding to 35 pmAr.

The inferred TTD of these three typical water samples are compared to the relative tracer concentrations of SF_6, CFC-12, ^{39}Ar and ^{14}C in figure 6.11. It demonstrates the overlap and thus the applicability of these tracers for the different time ranges of the TTDs. The two anthropogenic tracers SF_6 and CFC-12 have a perfect overlap with the young TTD and might be a better choice for the upper water masses. For the TTD of the second example (923 dbar) the time range of the tracer couple CFC-12 and ^{39}Ar fits perfectly. However, the TTD of the third example (3001 dbar) has only a small overlap with the CFC-12 input function. Hence, the CFC-12 concentrations are low and not very sensitive to variations of the TTD. The tracer couple ^{39}Ar and ^{14}C, with a half life of 5730 a, might be a better choice for such less ventilated water masses in the deep ocean. The depletion of ^{14}C does not look very sensitive, but on the other hand, the analysis of ^{14}C-concentration can be done very precisely with help of accelerator mass spectrometry. However, there are major corrections required counting for reservoir effects and a non-complete equilibration at the surface.

In principle it would be possible to use three or even more tracers at the same time to validate the chosen transit time distribution and its parametrisation, and to get a possibility to cross check this method. However, since TTDs are not the focus of this thesis, this is not treated in more detail here.

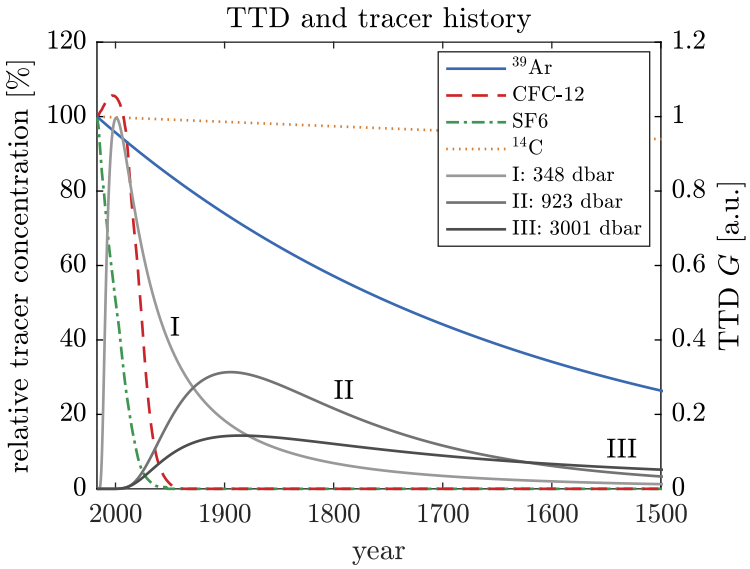

Fig. 6.11.: The TTD of the three typical water samples discussed in figure 6.10 compared with the different relative tracer concentrations of the tracers SF_6, CFC-12, ^{39}Ar and ^{14}C. The tracer history of the two chemical tracers SF_6 and CFC-12 are taken from [8] (northern hemisphere). For ^{39}Ar and ^{14}C only a decay and no variations in the input function are considered.

The mean age Γ and the width Δ/Γ of the TTD are plotted for all samples of the combined profile 44/55 and of profile 82 in figure 6.12. The three regions, which are discussed above, are clearly visible. Down to a pressure of 850 dbar (section **I**), which is the lower bound of the ETNA-OMZ [106], the currently achievable precision of ArTTA is not sufficient for a precise determination of the TTDs. This upper section **I** belongs to the central and intermediate water masses of the Atlantic (compare figure 6.13). In section **II** between a pressure of 850 dbar and ∼2500 dbar, which consists of the North Atlantic Deep Water masses, the tracer couple CFC-12 and ^{39}Ar is perfectly suitable and TTD can be well constrained. A clear deviation from the standard parametrisation of $\Delta/\Gamma = 1$ is visible. With a Δ/Γ-ratio of around 0.5 the transport of the water masses in this region is much more advective than previously assumed. Below a pressure of 2500 dbar (section **III**), with the transition to the Antarctic Bottom Water, it becomes difficult again to constrain the TTDs with the tracer couple CFC-12 and ^{39}Ar, since the history of CFC-12 does not go back far enough to the past. Nevertheless, the obtained Δ/Γ-ratios in section **I** and **III** are consistent with $\Delta/\Gamma = 1$. The mean age Γ shows a more or less linear increase, with an "aging"-gradient of about $\sim 0.27\,\mathrm{a\,dbar^{-1}}$, down to a pressure of 3000 dbar. In the deepest region there might be slightly younger water masses again.

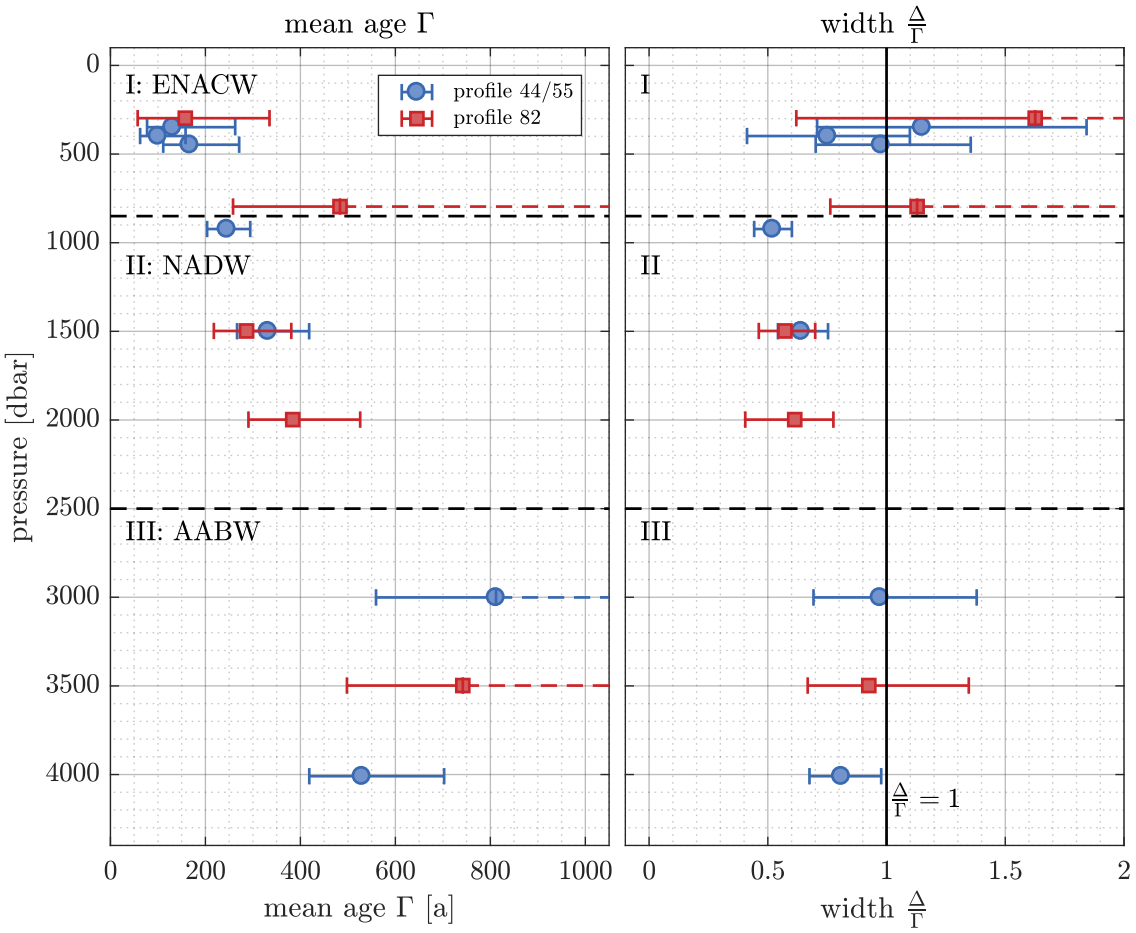

Fig. 6.12.: Mean age Γ and Δ/Γ of the TTD obtained by the tracer couple CFC-12 and ^{39}Ar: An example of each section is depicted in figure 6.10 in more detail. The vertical line indicates the standard parametrisation of $\Delta/\Gamma = 1$, which is used as a fixed ratio, if not enough or no sufficient tracer data are available. In section **II**, which consists of the North Atlantic Deep Water, the TTDs can be well constrained by the additional information given by ^{39}Ar. The transport of this water masses with a $\Delta/\Gamma \approx 0.5$ is much more advective than with $\Delta/\Gamma = 1$ as previously assumed. (Water masses: Eastern North Atlantic Central Water (ENACW), North Atlantic Deep Water (NADW), Antarctic Bottom Water (AABW).)

Table 6.4.: Summary of all parameters and results of the combined profile 44/55 and profile 82: The CFC-12 concentrations are extrapolated values from neighbouring profiles. For the sample at 3001 dbar only ^{39}Ar data from profile 44 are available. If the upper bound of the mean age Γ exceeds 1000 a or the upper bound of Δ/Γ is higher than 2, only a lower bound is given.

profile	**longitude** [°W]	**latitude** [°N]	**pressure** [dbar]	S_P [‰]	T [°C]	**^{39}Ar** [pmAr]	**CFC-12** [fmol kg^{-1}]	**mean age Γ** [a]	Δ/Γ
44/55	-22.50	11.40	4009	34.888	2.38	$41.9^{+3.8}_{-3.6}$	13.2(64)	529^{+173}_{-111}	$0.8^{+0.2}_{-0.1}$
44	-22.99	11.55	3001	34.923	2.74	$35.0^{+4.4}_{-4.1}$	7.8(62)	812_{-253}	$1.0^{+0.4}_{-0.3}$
44/55	-22.50	11.40	1499	34.958	4.32	$51.2^{+4.6}_{-4.3}$	17.6(65)	332^{+87}_{-65}	$0.6^{+0.1}_{-0.1}$
44/55	-22.50	11.40	923	34.783	5.80	$57.7^{+4.3}_{-4.0}$	16.2(64)	245^{+49}_{-42}	$0.5^{+0.1}_{-0.1}$
44/55	-22.50	11.40	447	35.078	9.86	$72.1^{+5.5}_{-5.2}$	431.6(179)	167^{+104}_{-56}	$1.0^{+0.4}_{-0.3}$
44/55	-22.50	11.40	398	35.127	10.44	$79.6^{+5.9}_{-5.5}$	547.6(211)	100^{+58}_{-37}	$0.8^{+0.3}_{-0.3}$
44/55	-22.50	11.40	348	35.191	11.10	$77.7^{+5.7}_{-5.3}$	686.6(249)	131^{+132}_{-54}	$1.1^{+0.7}_{-0.4}$
44/55	-22.50	11.40	10	35.893	25.74	$97.0^{+7.1}_{-6.6}$	1017.6(340)	-	-
82	-24.28	17.58	3498	34.907	2.51	$36.0^{+-9.4}_{-5.0}$	8.0(62)	742_{-244}	$0.9^{+0.4}_{-0.3}$
82	-24.28	17.58	1998	34.978	3.66	$46.4^{+-10.7}_{-5.6}$	6.4(62)	384^{+142}_{-93}	$0.6^{+0.2}_{-0.2}$
82	-24.28	17.58	1498	35.012	4.66	$54.1^{+-11.0}_{-5.8}$	15.6(64)	287^{+94}_{-69}	$0.6^{+0.1}_{-0.1}$
82	-24.28	17.58	796	34.918	7.07	$51.1^{+-14.9}_{-7.9}$	99.2(87)	483_{-225}	$1.1_{-0.4}$
82	-24.28	17.58	298	35.437	12.15	$78.2^{+-15.4}_{-8.0}$	815.5(284)	158^{+177}_{-100}	$1.6_{-1.0}$

S-T-diagram

The two parameters salinity and temperature are assumed to be conserved parameters, which do not change significantly as soon as the water masses have no contact to the atmosphere anymore. Therefore, these two parameters can be used to identify different water masses [107], which have a unique salinity and temperature signature. This is typically done with help of a $S-T$-diagram, which is plotted in figure 6.13.

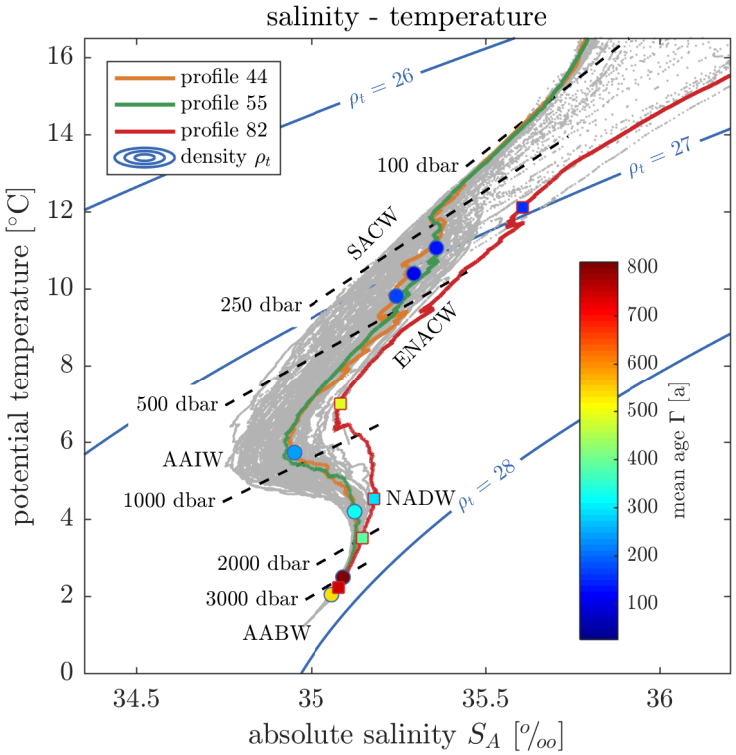

Fig. 6.13.: S-T-diagramm of the cruise M116 with the determined mean ages Γ of the water samples analysed with ArTTA: The contours indicate lines of constant density (ρ_t is defined as $\rho(S,T) - 1000\,\mathrm{kg\,m^{-3}}$). The different water masses can be identified by their specific salinity and temperature values [107]: SACW South Atlantic Central Water, ENACW Eastern North Atlantic Central Water, AAIW Antarctic Intermediate Water, NADW North Atlantic Deep Water, AABW Antarctic Bottom Water. The dashed lines mark data taken at the same pressure. The determined mean ages increase with depth down to a pressure of 3000 dbar.

The salinity and the temperature determine the density of the water, and mixing is only possible along lines of constant density. Salinity and temperature are measured continuously with a resolution of 1 dbar with the CTD-sensor[6], which is incorporated into the rosette of Niskin bottles for water sampling. The grey spots in the background

[6]CTD: **C**urrent as a measure for the salinity, **T**emperature and pressure (**D**epth).

are the data of all profiles taken during the cruise M116. The salinity and temperature curves of the two neighbouring profiles 44 and 55 are very similar, which is another justification that these two profiles can be combined to one in order to reduce the uncertainties. Profile 82 is the last profile of this cruise and was sampled north of Cape Verde and thus differs from the other profiles. Clearly visible is also the transition between the South Atlantic Central Water and the North Atlantic Central Water along the track of the cruise departing in the Caribbean and arriving at Cape Verde off the cost of West Africa. A summary of the different water masses and their origin, flow path and properties can be found in [108].

With this classification of the sampled water masses it might be possible to use the input function either for the northern or the southern hemisphere according to the production region of this particular water mass. Since the difference between the two input functions is maximal 10 %, this effect is not considered.

Estimation of the dissolved anthropogenic CO_2

As soon as the TTD of a water mass is known, the concentration of an arbitrary tracer or property which can not be measured or which was not measured can be calculated applying equation 1.12, if its input function and interaction at the water surface are known. Two possible examples in the context of the anthropogenic climate change and the global warming are the uptake of anthropogenic carbon dioxide and excess heat. To conclude this chapter this estimation is exemplarily done in a very simplified way for the uptake of the anthropogenic CO_2 dissolved in the ocean.

Figure 6.14 shows the development of the CO_2 concentration of the atmosphere since 1850. All CO_2 above a level of 280 ppm is assumed to have anthropogenic origin. Additionally, the two TTDs of the analysed sample from the combined profile 44/55 taken at a pressure of 923 dbar, which is discussed in figure 6.10, are plotted. These two TTDs once again show the difference between the standard parametrisation and the TTD, which is constrained by the additional ^{39}Ar-concentrations.

Carbon is involved in a complex chemical system of the ocean and only about 0.5 % of the dissolved inorganic carbon are dissolved in the form of free aqueous $CO_{2(aq)}$. However, most of the anthropogenic CO_2 is stored as bicarbonate HCO_3^- (∼89 %) and carbonate ion CO_3^{2-} (∼10.5 %)[110]. The dissolved carbonate species are related by the equilibria:

$$CO_2 + H_2O \rightleftharpoons HCO_3^- + H^+ \rightleftharpoons CO_3^{2-} + 2\,H^+$$

This chemical carbonate system does not react linearly, so that the amount of dissolved inorganic carbon in the surface layer is not proportional to the fraction of CO_2 in the atmosphere. In principle it is possible to compute the amount of dissolved inorganic carbon in contact with the atmosphere as a function of the atmospheric CO_2 mixing ratio using equilibrium inorganic carbon chemistry [111], the salinity and temperature dependent CO_2-solubility [112] as well as the stoichiometric dissociation constant of carbon acid [113] and an estimation of the alkalinity (e.g. [114]).

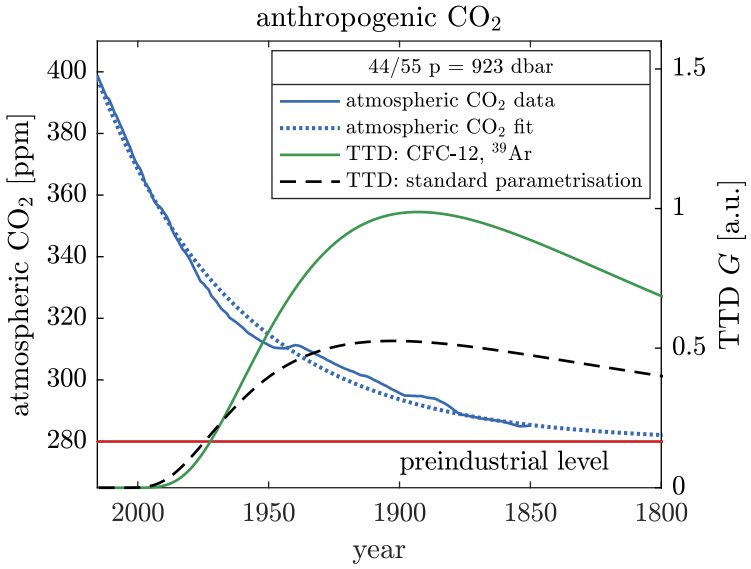

Fig. 6.14.: Development of the atmospheric CO_2 concentration since 1850 [109]. It is assumed that all CO_2 above the level of 280 ppm have anthropogenic origin. Since the amount of anthropogenic CO_2 increased almost exponentially since 1850 (fitted curve), the TTD is important for the amount of stored anthropogenic CO_2 inside the ocean. The two plotted TTDs demonstrate the difference between the TTD deduced from the additional ^{39}Ar-data (green, solid line) and the TTD with standard parametrisation (black, dashed line). The estimated uptake of dissolved anthropogenic CO_2 of the former TTD is about 50 % higher compared to the latter.

Since these calculations are beyond the scope of this rough estimation, here the simplification reported in [66] is chosen and the almost exponential increase (see figure 6.14) of the anthropogenic CO_2 in the atmosphere since 1850

$$c(t) = c_0 \cdot e^{\lambda_{\text{atm}} \cdot t} \,,$$

with a time constant of $\lambda_{\text{atm}} = (53.6\,\text{a})^{-1}$, is exploited. Due to the non-linearity of the chemical carbonate system of the ocean, this increase is slightly attenuated in the ocean mixing layer. For the characteristic properties of the North Atlantic Deep Water (NADW) a time constant of dissolved inorganic anthropogenic carbon in the mixing layer of $\lambda_{NADW} = (59.4\text{a})^{-1}$ can be calculated [66].

Using this exponential increase as an input function, the amount of dissolved anthropogenic CO_2 (C_{ant}) can be calculated for both TTDs with help of equation 1.12. The ratio of these two values only depends on the time constant λ_{NADW} and not on the absolute values of dissolved inorganic anthropogenic carbon in the mixing layer:

$$\frac{C_{\text{ant}}(\Gamma = 245\,\text{a}, \Delta/\Gamma = 0.5)}{C_{\text{ant}}(\Gamma = 696\,\text{a}, \Delta/\Gamma = 1.0)} = 1.54$$

It should be noted, that the CO_2 uptake of this particular water mass, the NADW, is considered here and not the one of the entire water column. According to this simple estimation, the amount of stored dissolved anthropogenic CO_2 in this water mass is ∼50 % higher than previously assumed without the ^{39}Ar-data. This is only a rough estimation and does not include any disequilibrium effects at the ocean surface, but it clearly shows the potential of the additional knowledge about the ocean ventilation which can be deduced from the ^{39}Ar-concentrations.

6.6. Discussion

The ocean measurement period demonstrates the full potential of the current ArTTA-system. The improvements of the system described in chapter 2 and the replacement of contaminated vacuum components were successful and led to a reduction of the contamination by more than a factor 5 and to an ^{39}Ar-count rate of up to 7.0 atoms/h (averaged over the week 8 to 14 August), which is almost twice as high as before. These improvements enable, together with a daily reference utilising a 10-times enriched sample, ^{39}Ar-analyses with 2 mL STP of Ar corresponding to ∼5 L of water in one day.

The measurements of the five artificial samples with well known concentrations show a good agreement and the sample with 10 pmAr is clearly distinguishable from the background and thus above the detection limit of the current system. Concentrations significantly below 10 pmAr are not expected in ocean water.

The reduction in the required sample volume by a factor ∼200 compared to LLC allows sampling with standard 10 L-Niskin bottles, which can be included in a standard sampling routine. However, a potential contamination by partial equilibration of the top water layer in the Niskin bottle with the inflowing air while sampling should be examined in more detail in a future study. A possible tracer in this context might be ^{85}Kr [7]. The reported ^{39}Ar-results of the three depth profiles sampled in the ETNA-OMZ are the first ocean measurements in 25 years and represent 14 % of the over-all available ^{39}Ar-data in the ocean. The achieved uncertainties are comparable with the historical data measured with LLC.

The benefit of a globally gridded ^{39}Ar-data set for reducing the uncertainty in the knowledge of oceanic transport and ventilation was several times shown based on the few historical data points [61, 62]. However, the required manpower and expense for the ^{39}Ar-analyses are still high and the sample throughput is low. Furthermore, the achieved present accuracy is low compared to other tracers and, especially in the upper well ventilated layers not yet sufficient for a precise determination of the TTDs. Thus, further developments considering the ^{39}Ar-count rate, the operationality and the stability of the ArTTA-systems are required, before the full potential of ^{39}Ar for oceanography can be used.

[7] Concentrations of ^{85}Kr below 5 % were measured in a Chinese ocean study. However, it is not clear whether the sampling procedure is comparable [36].

However, the ^{39}Ar-concentrations can be used in combination with other tracers (e.g. CFC-12) to constrain the TTD of different water masses already now. Especially for the North Atlantic Deep Water (NADW), for which the time windows of the tracer couple CFC-12 and ^{39}Ar match perfectly, it is found that the water transport is much more advective ($\Delta/\Gamma \approx 0.5$) than previously assumed with the standard parametrisation $\Delta/\Gamma = 1$. This implies an about 50 % higher amount of anthropogenic carbon stored in this water mass.

7. Conclusion and Outlook

The goal of this thesis, to enable ^{39}Ar-measurements with a sample size of less than 10 L of water, could be achieved. In order to reach this goal, the laser system was completely rearranged and the vacuum system renewed and optimised. The contamination embedded in the vacuum system as a consequence of using highly enriched samples in the early days of the ArTTA-project could be reduced by more than a factor five and the atmospheric count rate, which is the key parameter quantifying the performance of the ArTTA-apparatus, could almost be doubled up to 7.0 atoms/h. This is about four-times more efficient than state of the art ATTA-systems for krypton, if only the difference in the isotopic abundance of argon and krypton is taken into account.

The achieved performance of the current ArTTA-system is summarised in figure 7.1, which shows the simulated accuracy of the current system applying the one-day measurement cycle as introduced for the ocean measurements (see chapter 6.2.1) and assuming the typical parameters of the final system (contamination $a = 16.5^{+2.2}_{-2.0}$ μL STP c_{atm} h^{-1}, atmospheric count rate $\nu_{atm} = 6.5$ atoms/h, sample size 2 mL STP).

The expected uncertainty is around 10 pmAr for a modern sample and around 5 pmAr for a 20 pmAr-sample. The current theoretical detection limit is around 5 pmAr, which corresponds to ∼4.3 half-lives or ∼1150 years ago and is mainly limited by the remaining contamination. For a sample of 5 pmAr only 6.5 counts are due to the concentration of the sample, whereas the major part of 10.7 counts is attributable to the contamination. Below 5 pmAr it thus becomes difficult do distinguish the concentration of the samples from the background. This limit can be easily pushed further down by replacing the remaining contaminated parts of the vacuum system systematically. This should be no limitation for the new system, which is under construction. The contamination can be further suppressed by splitting the sample into several smaller parts and analysing them separately, since the contribution due to contamination increases quadratically with the measurement time.

The three ice blocks taken at the tongue of the Gorner Glacier were the first ice samples analysed with ArTTA. The inferred ^{39}Ar-concentrations are much younger than expected from flow models and further investigations are necessary. The full potential of the current ArTTA-system and of ^{39}Ar as a tracer in general was finally demonstrated in an ocean study consisting of three depth profiles originating from the North Atlantic. All three profiles show a rapid depletion of ^{39}Ar with depth in the upper 1000 m followed by a more homogeneous ^{39}Ar-concentration down to 4000 m with a slight absolute minimum of around 40 pmAr in 3000 m. This ^{39}Ar-behaviour represents the transition of the Antarctic Intermediate Water to the North Atlantic

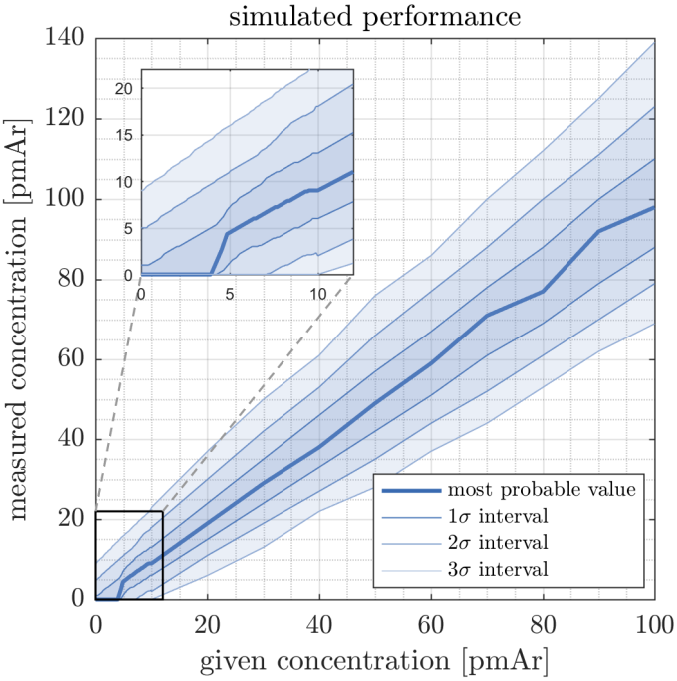

Fig. 7.1.: Simulated uncertainties of the current system as a function of the ^{39}Ar-concentration of the sample: In total $\sim 10^6$ measurements with the one-day measurement cycle (see chapter 6.2.1) and a sample size of 2 mL STP were simulated employing a Monte Carlo method and analysed, as all measurements in this thesis, by the Bayesian approach discussed in chapter 3.3.4. The simulation is based on the current status of the ArTTA-system: Contamination $a = 16.5^{+2.2}_{-2.0}$ μL STP c_{atm} h^{-1} and atmospheric count rate $\nu_{atm} = 6.5$ atoms/h. For each concentration 10^4 measurements were simulated to infer the probability distribution of the resulting, hypothetically measured concentration. The three different transparencies indicate the confidence interval of 1σ, 2σ and 3σ, respectively. The small fluctuations are due to the limited number of simulated measurements. The theoretical detection limit is around 5 pmAr (see inset). Below this limit the remaining contamination in the vacuum system becomes dominant and it is difficult to distinguish the concentration of the sample from the background.

Deep Water and finally to the Antarctic Bottom Water. The achieved precision of the ^{39}Ar-concentrations is not sufficient for an accurate determination of the transit time distribution (TTD) in the younger upper layer. However, the TTD of the North Atlantic Deep Water could be constrained very well by the tracer couple CFC-12 and ^{39}Ar and a much stronger influence by younger water masses was found than previously assumed.

In general all these investigations of TTDs would highly benefit from ^{85}Kr as an additional tracer to test the basic methods. On one hand ^{85}Kr would be a direct indicator for any contamination while sampling or during preparation and on the other hand ^{85}Kr is based on a relative measurement and not on an absolute concentration. It is, like ^{39}Ar, independent of the solubility and thus independent of the assumption that salinity and temperature are conservative properties of the ocean, which only change at the ocean surface during the interaction with the atmosphere. The time range which is covered by ^{85}Kr is similar to the one of CFC-12. ^{85}Kr has the advantage that it has a particular high sensitivity for very young water due to its radioactive decay. By measuring both tracers the basic principle of dating with Freons, which can be measured with less effort, thus could be benchmarked. For an analysis of ^{85}Kr it is necessary to separate the krypton fraction from the argon in an additional preparation step. The amount of krypton in a 5 L water sample is sufficient for analysing ^{85}Kr with ATTA. The general method of TTDs and especially the commonly used inverse Gaussian distribution could be tested in a multi tracer study. If this approach describes the water masses correctly, all water tracers should intersect in one point in the parameter space. A precise ^{39}Ar-measurement has a key part in such a study, since it is the only tracer sensitive to the intermediate time range between 50 and 1000 years ago.

7.1. Possible future improvements

For a routine application of ArTTA with a high sample throughput, which is essential for a comprehensive grid of ^{39}Ar-data in the ocean, three major issues will be crucial in the future:

1. A stable and durable metastable argon source since the source is the weak point of the system.

2. A high atmospheric count rate which primarily determines the precision of the inferred ^{39}Ar-concentrations and the required counting time.

3. A reliable tool to ensure the stability of the system, which can be used to normalise the ^{39}Ar-count rate as well as to optimise the system and especially the MOT with help of the stable isotopes.

During the ocean measurements the source had to be replaced seven times, which interrupts the measurements for at least one day. The durability of the source can be extended apparently by an admixture of oxygen during the krypton wash, which

was tested during the second part of the ocean measurements (see 6.2.2). Further developments of the source require an independent testing facility with comparable parameters to the main system.

7.1.1. New atom-optical developments

Several atom-optical ideas were tested by the ArTTA-group addressing the second point, an increase of the ^{39}Ar-count rate, during the last years. Bichromatic forces, which are only limited by the available laser power and thus can exceed the standard radiative force, might be one "candidate" to improve the efficiency of the collimator by pushing fast atoms below the capture velocity of the collimator in a relatively short interaction zone directly behind the source. The basic principle was proven for the stable isotope ^{40}Ar [115, 116], and a factor of more than two by implementing a bichromatic pre-collimator was predicted in [4].

An enhancement of the metastable density in the source by optical pumping with additional laser frequencies was investigated in an ^{40}Ar-spectroscopy cell [117, 118]. Two pumping transitions $1s_2 \rightarrow 2p_6$ at 800.836 nm and $1s_4 \rightarrow 2p_6$ at 922.703 nm (compare A.3) were explored and a maximal measured enhancement of 81 % was observed in a spectroscopy cell by driving both transitions at the same time.

An improvement of the capture efficiency of the MOT by an additional cooling frequency was studied in [76]. One laser frequency was chosen near resonant and optimised for a reliable detection of the trapped atoms, while the other one was optimised for a maximal capture-efficiency. A gain of about 20 % was observed with this double frequency MOT.

All these methods have in common that they were only tested for one of the stable isotopes and not for ^{39}Ar with a much more complex atomic transition spectrum. Beside the double frequency MOT, these techniques are based on an additional complex laser system, which requires further developments.

The third point, an integration of a reliable tool to ensure the stability, to normalise the ^{39}Ar-count rate and to optimise the system, is of similar importance. A high but not stable ^{39}Ar-count rate or one which can not be monitored, is nearly useless since all ^{39}Ar-measurements are based on a normalisation with a reference count rate. The existing atom flux monitor is only sensitive to bare flux of metastable atoms and thus only monitors the source. The atom beam profiler additionally includes the collimator and the magneto-optical lens, however it is insensitive to the ZSL and MOT, too. The atom beam profiler might also prefer faster atoms, which can not be captured by the MOT. Measuring the loading rate of the MOT is indispensable, if all atom-optical components should be considered. Since highly enriched ^{39}Ar-samples can not be used due to a recontamination of the system, other isotopes must be employed, which is discussed in the next section.

7.1.2. Referencing by ^{40}Ar or ^{38}Ar-MOT-loading rate

The strategy of referencing with another (stable) isotope is used for the two rare krypton isotopes ^{85}Kr and ^{81}Kr and enables relative uncertainties in the range of 1 % [119]. This concept should be adaptable to ^{39}Ar-measurements. In the early days of ATTA ^{81}Kr-measurements were normalised by adding a calibrated amount of ^{85}Kr to each krypton sample [37]. The mixing with a control gas complicates the sample preparation and may introduce additional errors. Thus the state of the art ATTA-systems utilise the stable ^{83}Kr isotope with a relative natural abundance of 11.5 %. The critical point is to bridge the at least eleven orders of magnitude in the abundances and thus in the MOT-loading rates between the isotopes of interest and ^{83}Kr. The loading rate of ^{83}Kr is either measured via the ionisation loss mechanism and the ion current on a Faraday cup next to the MOT centre [85], by quenching [2] or through measuring the fluorescence of the trapped atoms on the linear slope of the MOT-loading [120]. The rare ^{x}Kr abundance, $x \in \{81, 85\}$ is derived from the "superratio" [84]:

$$ {}^{x}\mathrm{Kr}_{\mathrm{SR}} = \frac{{}^{x}\mathrm{Kr}_{\mathrm{Sample}}/{}^{83}\mathrm{Kr}_{\mathrm{Sample}}}{{}^{x}\mathrm{Kr}_{\mathrm{Reference}}/{}^{83}\mathrm{Kr}_{\mathrm{Reference}}} \tag{7.1} $$

This method does not supplant all reference measurements, since the single atom counting efficiency for the rare krypton isotopes and the detection of the loading rate of ^{83}Kr might drift differently due to various changes of the experimental conditions. But the ^{83}Kr loading rate can be measured repeatedly every few minutes while counting the rare isotope. This gives a handle on the current efficiency of the apparatus and can compensate instabilities in the system during the measurements up to a very high level.

Unfortunately, there is no abundant argon isotope which has a non-integer nuclear spin and thus an atomic spectrum similar to ^{39}Ar. The only possibility is to employ one of the stable isotopes ^{36}Ar, ^{38}Ar and ^{40}Ar. It should be noted, that the isotopic abundances ^{36}Ar/Ar and ^{38}Ar/Ar might differ in some exotic underground samples, but for all standard applications of dating water and ice this is no issue and the ^{40}Ar/Ar-ratio is constant for all practical purposes. None of the stable isotopes is suitable to investigate the repumper frequencies required for ^{39}Ar, however no critical influence of their exact power or frequencies could be observed.

A measurement of the ion current with help of a Faraday cup should be possible for argon, too. But this method has the disadvantage that the detector is inside the vacuum and thus its development is time-consuming. An optical detection scheme avoids this drawback. Employing a quench-laser and a detection of the 843 nm-photon (similar to the flux monitor 2.9), which is emitted exactly once by each atom on the way to the ground state, gives a measure which is independent of the scattering rate and thus independent of the exact laser powers or frequencies of the cooling lasers and of the magnetic fields. Furthermore, light of 843 nm can be separated by commercial band-pass filter from all other used laser frequencies.

Two possible implementations at the current ArTTA-system are discussed in the following and some of the optical components (e.g. the MOT fibre splitter) were already designed in prospect for this purpose. The first and most simple way is to integrate an ^{40}Ar-quench focused and well-aligned to the centre of the MOT and to detect the 843 nm-light continuously with the CCD camera. The challenge is a stable alignment, the limited optical access of the MOT and possible fluctuations due to the special loading scheme caused by the Booster. Another possibility is to use a discontinuous measurement procedure and to load an ^{38}Ar-MOT for a defined time interval and quench it afterwards. The 843 nm-light can be either detected by the APD or by the CCD. It is preferable to use an ^{38}Ar-quench as a fast atom beam shutter and to wait until all atoms are trapped in the centre of the MOT. During detection all cooling light can be switched off in order to reduce the background. Switching the laser light can be easily done with help of the AOMs.

The current ArTTA-system would benefit strongly from the realisation of a reliable tool to measure the loading rate of the MOT, especially this method can also be used to optimise and understand the system independently from the low ^{39}Ar-count rate.

7.2. Chronology of the ^{39}Ar-count rate

This thesis concludes with a dip into the past to predict the future. Figure 7.2 contains the chronology of the ^{39}Ar-count rate, which is the key parameter of the ArTTA-system. In the early days the count rate could only be predicted. As the knowledge about the ArTTA-apparatus grew and more components were implemented step-by-step, the predicted values decreased rapidly. In autumn 2011 the first atmospheric sample was analysed and 18 atoms were counted within 62 h [3]. The maximal achieved reference ^{39}Ar-count rate during this thesis was in summer 2017 with 7.0(2) atoms/h averaged over one week (8 to 14 August). The increase of the ^{39}Ar-count rate might be another version of Moore's law [121] with a very rough estimated doubling of the count rate every two years, but so far there is a better agreement with a linear increase with an estimated rate of about 1.1 atom/h every year. Generally speaking there is no obvious fundamental limit in the near future.

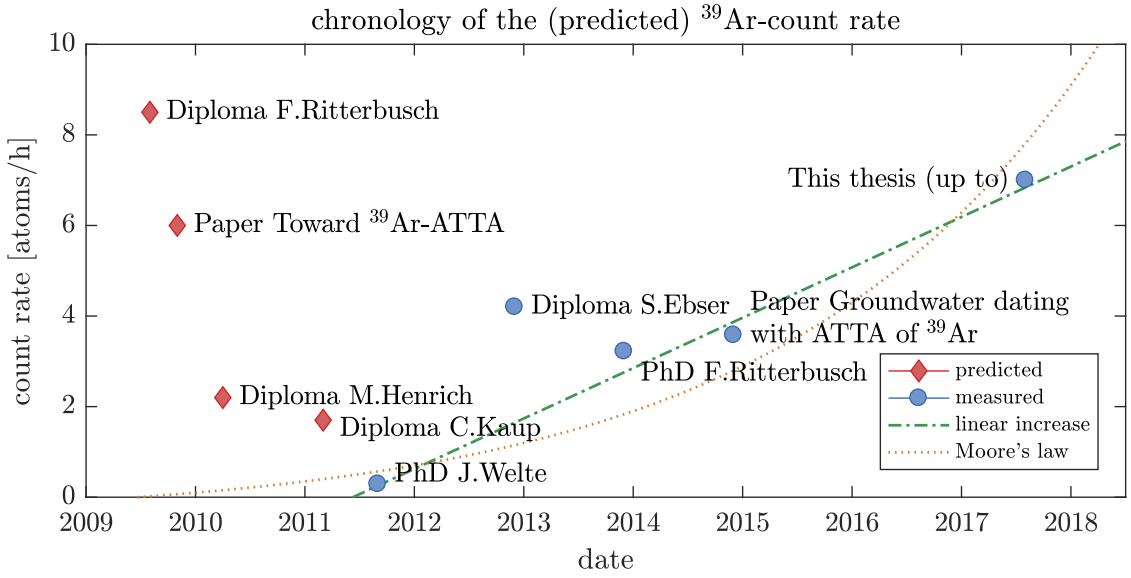

Fig. 7.2.: Chronology of the atmospheric count rate during the ArTTA-project: For the current system the maximal value averaged over one week is plotted (7.0(2) atoms/h). The two lines indicate a linear increase with a rate of about 1.1 atom/h every year or exponential increase (Moore's law) with a doubling of the count rate every two years (previous count rates taken from [45, 122, 77, 73, 3, 43, 4, 44]).

A. Fundamentals

A.1. Argon isotopes

Table A.1.: Compilation of all 24 known Ar-isotopes (data taken from [6]).

isotope	mass $[m_u]$	natural abundance	nuclear spin I	$T_{1/2}$	main decay	discovery
^{30}Ar	30.0225	-	0	10 ps	p to ^{29}Cl	
^{31}Ar	31.0122	-	$^5/_2$	14.4(6) ms	ec, p to ^{30}S	1986
^{32}Ar	31.9976	-	0	98(2) ms	ec to ^{32}Cl	1977
^{33}Ar	32.9899	-	$^1/_2$	173(20) ms	ec, β^+ to ^{33}Cl	1964
^{34}Ar	33.9802	-	0	843.8(4) ms	ec, β^+ to ^{34}Cl	1966
^{35}Ar	34.9752	-	$^3/_2$	1.7756(10) s	ec, β^+ to ^{35}Cl	1940
^{36}Ar	35.9675	0.3336(21) %	0	stable	-	1920
^{37}Ar	36.9968	-	$^3/_2$	35.001(19) d	ec to ^{37}Cl	1941
^{38}Ar	37.9627	0.0629(7) %	0	stable	-	1934
^{39}Ar	38.9643	8.23×10^{-16}	$^7/_2$	269(3) a	β^- to ^{39}K	1950
^{40}Ar	39.9623	99.6035(25) %	0	stable	-	1920
^{41}Ar	40.9645	-	$^7/_2$	109.61(4) min	β^- ^{41}K	1936
^{42}Ar	41.9630	7.4×10^{-21} [123]	0	32.9(11) a	β^- ^{42}K	1952
^{43}Ar	42.9656	-	$^5/_2$	5.37(6) min	β^- ^{43}K	1969
^{44}Ar	43.9649	-	0	11.87(5) min	β^- ^{44}K	1969
^{45}Ar	44.9680	-	$^5/_2$,$^7/_2$	21.48(15) s	β^- ^{45}K	1974
^{46}Ar	45.9680	-	0	8.4(6) s	β^- ^{46}K	1974
^{47}Ar	46.9727	-	$^3/_2$	1.23(3) s	β^- ^{47}K	1985
^{48}Ar	47.9760	-	0	475(40) ms	β^- ^{48}K	2004
^{49}Ar	48.9815	-		170(50) ms	β^- ^{49}K	1989
^{50}Ar	49.9856	-	0	106(6) ms	β^- ^{50}K	1989
^{51}Ar	50.9928	-			β^- ^{51}K	1989
^{52}Ar	51.9986	-	0	620 ns		1989
^{53}Ar	53.0072	-		620 ns		2009

A.2. Noble gas composition of the atmospheric reference standard

Table A.2.: Noble gas isotope composition of the atmospheric reference standard (commercial bottle argon 4.6) measured with a noble gas mass spectrometer. All values are normalised to the literature values of dry atmospheric air. A value of 1.0 would represent an exact atmospheric mixing proportion. The bottle argon contains a relatively high level of Kr and Xe. The noble gas measurements have been performed by Simon Mayer at the Institute of Environmental Physics in Heidelberg.

isotope	abundance normalised to air composition
^{3}He	0.150(11)
^{4}He	0.1445(26)
^{20}Ne	0.0935(17)
^{22}Ne	0.0889(15)
^{36}Ar	101.0(12)
^{40}Ar	102.3(12)
^{84}Kr	13.78(62)
^{132}Xe	2.1(12)

A.3. ^{40}Ar-transition scheme

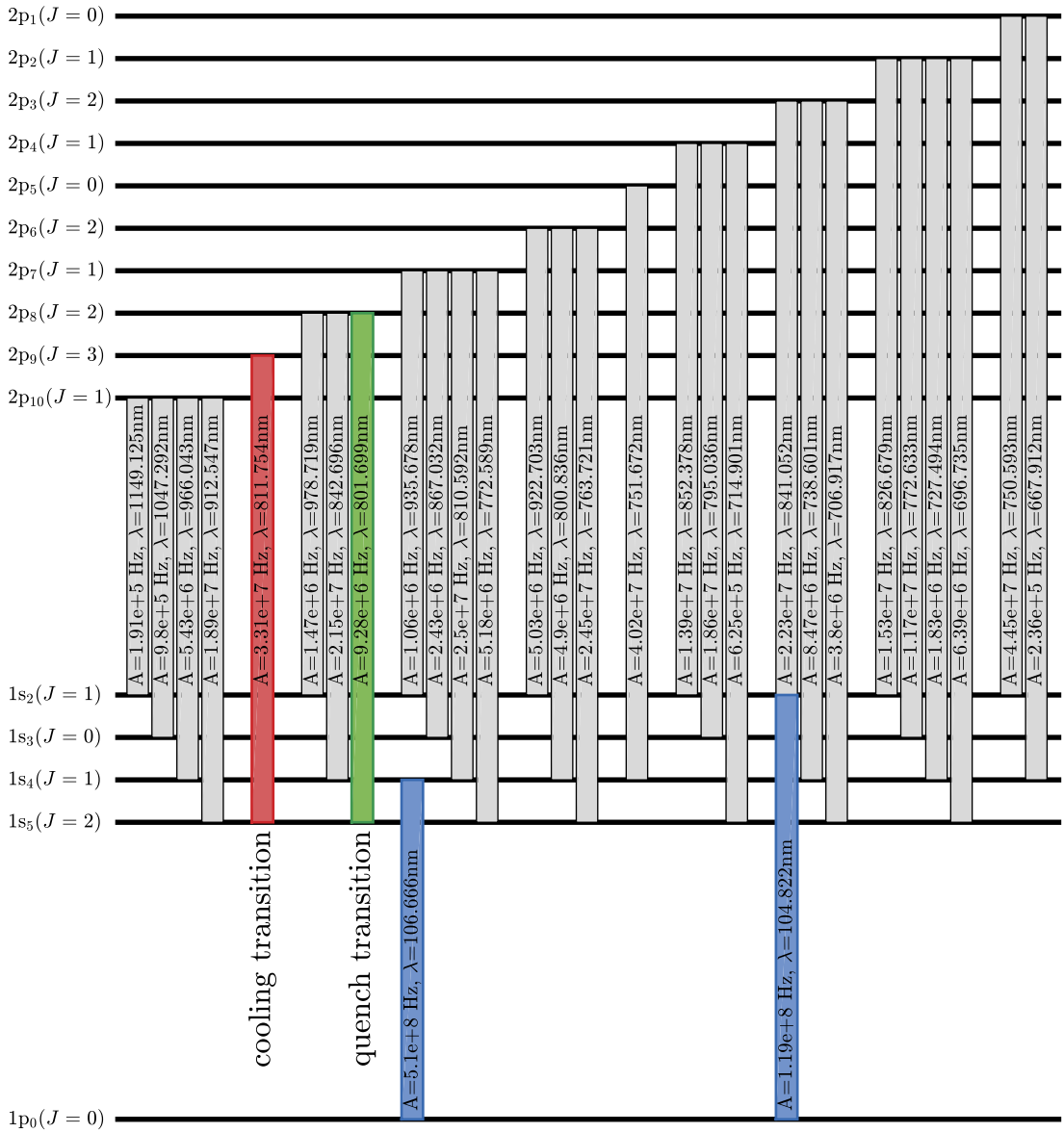

Fig. A.1.: ^{40}Ar-transition scheme of the s- and p- multiplets (adapted from [43, 3], data taken from [124]).

B. Apparatus

B.1. Fibre splitter

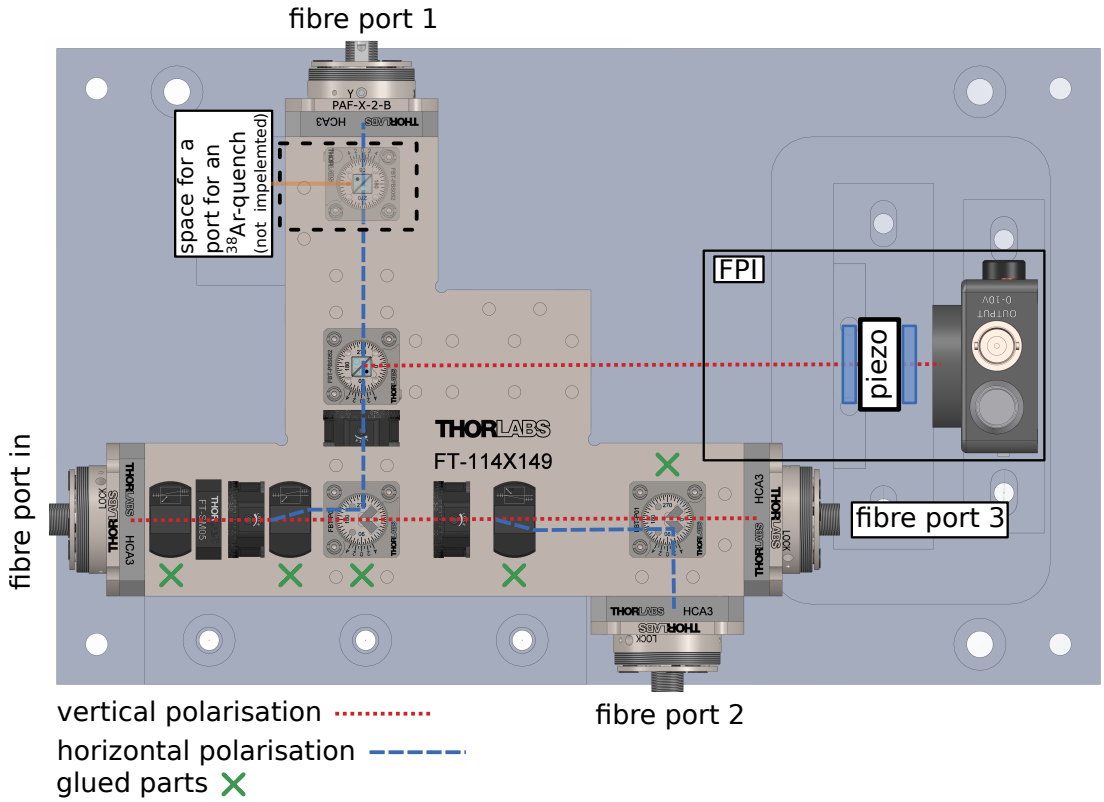

Fig. B.1.: Sketch of the new fibre splitter based on Thorlabs FiberBenches-System: All three optical paths from the input fibre port to the three output ports have the same length, which enables a similar coupling efficiency of about 65 % of all ports. Some optical components are glued to the bench for a higher stability (marked with green crosses). A self-built Fabry-Pérot interferometer (FPI, rough sketch) is included in the fibre splitter and can be used to detect potential mode hops of the cooler as well as of the repumper laser. The system can be easily extended by an additional port for an ^{38}Ar-quench or ^{40}Ar-quench to measure the loading rate of the MOT. The fibre bench and the FPI are mounted on a common aluminium plate, which is enclosed in a PVC-box for protection and stability.

B.2. Temperature stabilisation

This section contains some information about the self-built temperature stabilisation system. The situation of the different heat sources and of the air flow inside the lab is depicted in figure B.2. The strong fluctuations of the heat input from outside through the windows are suppressed by reflecting aluminium foil and by a 10 cm Styrofoam wall directly behind the windows. The ventilation and the air conditioning system lead to an additional varying heat input. The temperature is measured with a digital and factory-calibrated temperature sensor (TSYS01), which is mounted at the end of a tube to be protected from local temperature fluctuations. A small fan generates a slow, constant air flow passing the sensor. The temperature fluctuations are compensated by two regulated fan heaters each of 2.2 kW, which are controlled by a digital PI-loop implemented on an Arduino microcontroller platform. Humidity fluctuations are reduced by a dehumidifier, but still present, since the dehumidifier is only regulated via the inbuilt two-point controller, because the compressor is not designed for a switching on short time scales. The air conditioning, the humidifier and the fan heaters are manipulated, so that their fans are running permanently with constant speed to generate a constant air circulation inside lab. The cold air from the air conditioning system is guided to the back part of the lab, where the different airflows mix.

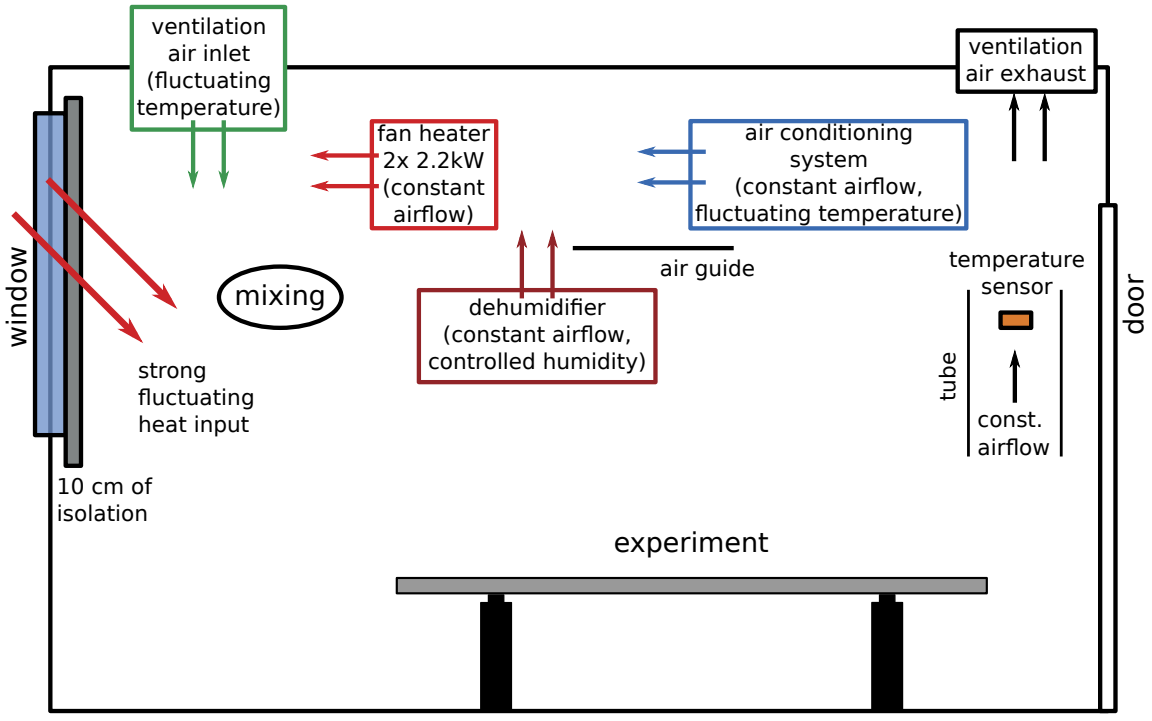

Fig. B.2.: Temperature and humidity stabilisation of the lab environment: For more details see text.

Figure B.3 shows a flow chart of the self-built temperature controller. The digital PI-

controller is implemented on an Arduino microcontroller, which controls zero-crossing switches and regulates the heat of the two fan heaters via pulse width modulation. The data can be displayed and recorded on a PC via RS232-connection. In total six temperature sensors are connected to the microcontroller which measure the temperature at three different points in the lab, the temperature of the airflow of the ventilation and the air conditioning system and additionally the supply temperature of the cooling water feeding the air conditioning unit. At the moment only one out of six measured temperatures is used by the PI-controller. The additional temperature information might be used together with the additional independent controllable channels for heaters to improve the system and to compensate temperature gradients, too.

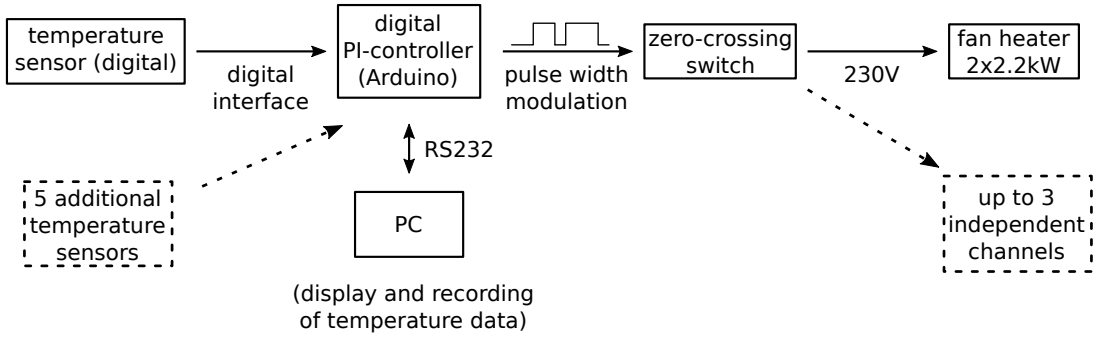

Fig. B.3.: Schematic of the self-built temperature controller: For more details see text.

The measured stabilised room temperature and the temperature of the airflow of the ventilation and the air conditioning system are plotted in figure B.4. The stabilised room temperature only shows small, fast fluctuations, although especially the inflowing air from the air conditioning unit is oscillating with an amplitude of up to 2.5 °C. The alternating time domains of higher and smaller amplitudes are typical for the fluctuations of the air conditioning system. The ventilation system sometimes has temperature jumps, which do not occur during the time span of this data set. The power of the heaters, which compensate the volatile temperature inputs, clearly follows a daily cycle, which is due to the remaining heating through the windows.

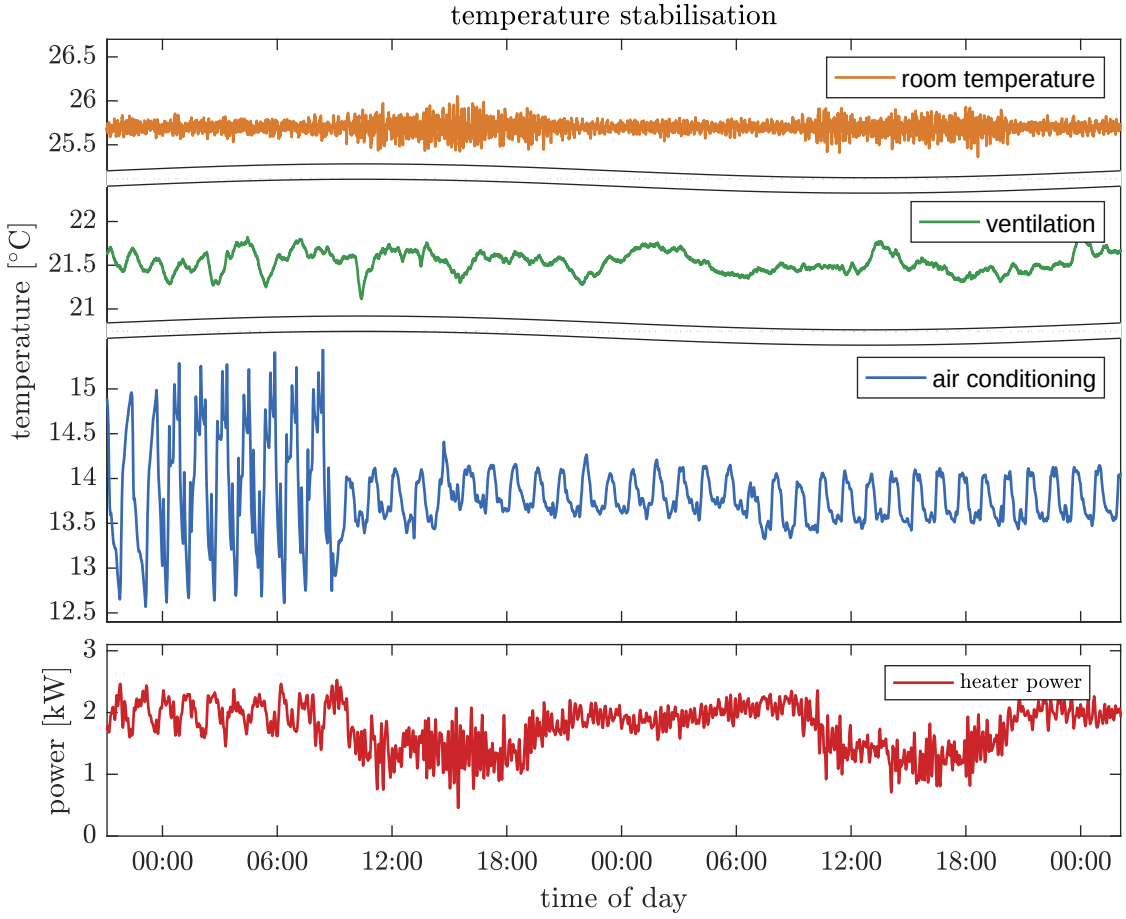

Fig. B.4.: Stabilised room temperature: The air temperature measured at the outlet of the air conditioning system and of the room ventilation are strongly fluctuating, whereas the stabilised room temperature only has small, fast fluctuations. The power of the heaters, which are used to compensate the temperature, fluctuations shows clear differences between day and night.

B.3. MolFlow-Simulations

The vacuum simulations were conducted with MolFlow+, a Monte-Carlo simulation package written at CERN [79], which was developed to simulate the steady-state pressure in arbitrarily complex geometries under the assumption of ultra-high vacuum. The conditions of ultra-high vacuum are fulfilled, if the mean free path of the molecules is long compared to the typical size of the system, so that collisions between two particles can be neglected, which is typically the case below 10^{-7} mbar. For general information about the handling it is referred to the user guide [125] and more details of the algorithm can be found in [126]. In this section some additional information concerning the simulation of the ArTTA vacuum system is documented.

Generating the geometry of the system

The geometry of the system can be imported from CAD programmes (e.g. SolidWorks) supporting the STL file format. The following procedure has proven to be practicable:

1. Starting with a simplified version of the vacuum system with help of the CAD-programme. The time for editing the model in MolFlow can be minimised, if all parts are massive and filled. Pumping tubes and other parts inside the vacuum chambers must be generated by cutting them out, so that there is a surface in the geometry later on. It is advisable to create the drawing from one part and avoid any transitions between different parts, since there might be some leaks due to numerical uncertainties.

2. Saving the model in the STL file format. Ensure that the right units are selected.

3. Importing the model into MolFlow.

4. Verify and, if necessary, swap the normal orientation of all facets. All facets inside the vacuum (e.g. of the pumping tubes) must be changed to two-sided, otherwise they are permeable in one direction. The front side of the pumping tube must be changed to two-sided and permeable (opacity = 0), so that they can be passed in both directions.

5. Set the pumping speed of the facets to which the pumps are connected to the corresponding values.

6. Adapt the molecular mass of the gas to argon.

7. Set the desorption (outgassing rate, temperature and angular distribution) of the front of the source tube to emulate the velocity distributions and gas throughput of the liquid nitrogen cooled source. Since this is the most difficult part, there are some additional calculations listed below.

8. Choose and set the pressure profiles and texture, which should be recorded.

9. Run the simulation.

10. Remark: Small changes of the geometry can be made directly in MolFlow, so that the time consuming adaptation of the Model must not be repeated.

Modelling the velocity distribution of the source

There are two free parameters (temperature T and exponent of the angular distribution n (see equation B.7)), which can be adjusted to adapt the velocity distribution of the metastable argon source. The absolute velocity v of molecules in a given volume of ideal gas at equilibrium can be described by the Maxwell-Boltzmann distribution. Since fast molecules of the gas cross or hit a surface more frequently than slow ones, it is important to distinguish between the probability density function of molecular speeds $f(v)_{gas}$ in a given volume and the probability density function $f(v)_{coll}$ of molecules colliding with a wall during a given time. The collision frequency scales linearly with the speed, so that the velocity distributions can be transformed by the following relation:

$$f(v)_{coll} = f(v)_{gas} \cdot v \cdot C \propto f(v)_{gas} \cdot v \tag{B.1}$$

The normalisation constant C can be calculated by integration, but is mostly left out for simplicity in the following. The probability distribution of the absolute velocity v is given by [126]:

$$f(v)_{gas} = \sqrt{\frac{2}{\pi}} \cdot \frac{v^2}{a^3} \cdot e^{-\frac{v^2}{2a}} \tag{B.2}$$

$$f(v)_{coll} = \frac{v^3}{2a^4} \cdot e^{-\frac{v^2}{2a}} \tag{B.3}$$

$$\text{where} \quad a = \sqrt{\frac{k_B \cdot T}{m}} \tag{B.4}$$

The mean velocity $< v >_{gas}$ and the most probable value $\widehat{v}_{gas}$ of $f(v)_{gas}$ can be written as:

$$< v >_{gas} = \sqrt{\frac{8}{\pi}} a \tag{B.5}$$

$$\widehat{v}_{gas} = \sqrt{2} \cdot a \tag{B.6}$$

The angular distribution is given by the probability $\mathrm{d}s$ that a particle leaves the surface in the solid angle $\mathrm{d}\omega$:

$$\mathrm{d}s \propto \cos(\theta)^n \mathrm{d}\omega \tag{B.7}$$

For $n = 1$ we get the normal Knudsen's cosine law, which is usually used to describe the rebounds at the vacuum surfaces [127, 128].

The solid angle is $\mathrm{d}\omega = \sin(\theta)\mathrm{d}\theta\mathrm{d}\phi$ in spherical polar coordinates, and the general velocity distribution is:

$$f_{coll}(v,\theta,\phi) \propto f(v)_{coll}\cos(\theta)^n \sin(\theta)\mathrm{d}v\mathrm{d}\theta\mathrm{d}\phi\ . \tag{B.8}$$

The distribution of the longitudinal velocity $\vec{v_l}$ and the radial velocity $\vec{v_r}$ can be calculated by a transformation into cylindrical coordinates, which is depicted in figure B.5a. The transformation of the solid angle from spherical to cylindrical coordinates introduces a factor $1/v$ by the Jacobian determinant:

$$f_{coll}(v_l,v_r,\phi) \propto f(v)_{coll}\cdot\cos(\theta)^n\cdot\frac{\sin(\theta)}{v}\mathrm{d}v_l\mathrm{d}v_r\mathrm{d}\phi\ , \tag{B.9}$$

where $v=\sqrt{v_l^2+v_r^2}$ and $\theta=\arctan(v_r/v_l)$.

By integrating over ϕ, which only gives a constant factor, and over v_r or v_l, respectively, we get:

$$f_{coll}(v_l) \propto \int_0^\infty f_{coll}(\sqrt{v_l^2+v_r^2})\cos\left(\arctan(v_r/v_l)\right)^n\frac{\sin(\arctan(v_r/v_l))}{\sqrt{v_r^2+v_l^2}}\,\mathrm{d}v_r \tag{B.10}$$

$$f_{coll}(v_r) \propto \int_0^\infty f_{coll}(\sqrt{v_l^2+v_r^2})\cos\left(\arctan(v_r/v_l)\right)^n\frac{\sin(\arctan(v_r/v_l))}{\sqrt{v_r^2+v_l^2}}\,\mathrm{d}v_l \tag{B.11}$$

The probability distribution of the transversal velocity $\vec{v_t}$ can be calculated by a further coordinate transformation from $\vec{v_r}$ into $\vec{v_t}$, $v_t=\cos(\phi)v_r$, which introduces an additional factor of $1/|\cos(\phi)|$:

$$\begin{aligned} f_{coll}(v_t) \propto \int_0^{2\pi}\int_0^\infty f_{coll}\left(\sqrt{(v_t/\cos(\phi))^2+v_l^2}\right)\cos\left(\arctan(v_t/(\cos(\phi)\cdot v_l))\right)^n \\ \cdot\frac{\sin(\arctan(v_t/(\cos(\phi)\cdot v_l)))}{\sqrt{(v_t/\cos(\phi))^2+v_l^2}}\cdot\frac{1}{|\cos(\phi)|}\,\mathrm{d}v_l\,\mathrm{d}\phi \end{aligned} \tag{B.12}$$

All velocity distributions can be transformed analogously to equation B.1 from collisions per time to particles per volume by dividing with the corresponding velocity. For example:

$$f_{gas}(v_l) \propto \frac{f_{coll}(v_l)}{v_l} \tag{B.13}$$

The geometry depicted in figure B.5b can be used to 'measure' the velocity distributions in a MolFlow simulation. Figure B.6 compares these results to the distributions described by the equations discussed above. There is a perfect agreement between the distributions used by MolFlow and the mathematical descriptions derived above.

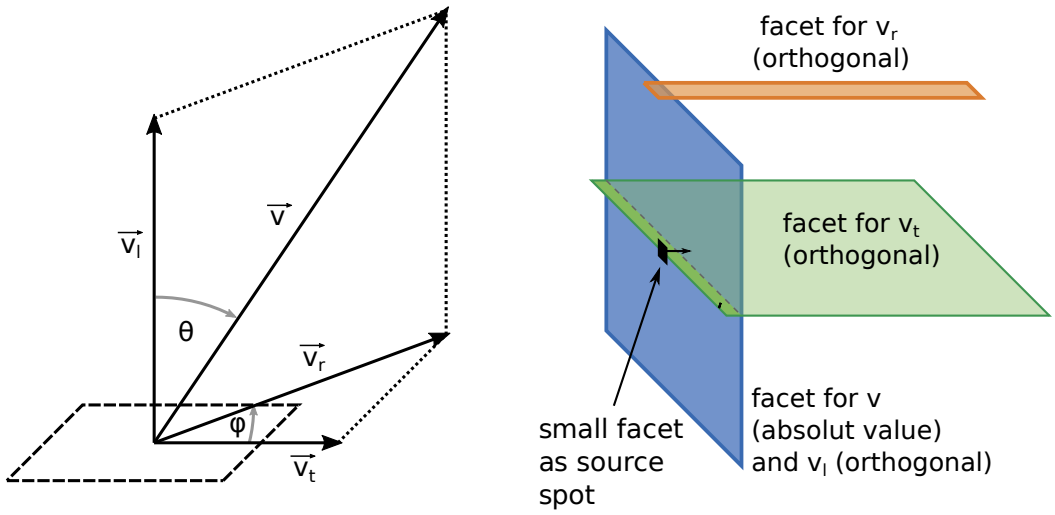

(a) (b)

Fig. B.5.: **a)** Definition of the absolute velocity v, the longitudinal $\vec{v_l}$, the radial $\vec{v_r}$ and the transversal $\vec{v_t}$ velocity components as well as the two angles θ and ϕ.
b) Geometry for 'measuring' the velocity distribution in a MolFlow simulation: The facet of the source is comparably small. MolFlow allows to measure either the velocity distribution of the molecules hitting the surface or the component orthogonal to the surface. The radial component $\vec{v_r}$ is measured in some distance to select only generated particles with approximately $\phi \approx \pi/2$, for which $\vec{v_r} \approx \vec{v_t}$ holds.

The velocity distributions of the metastable atoms have been measured in [74] directly behind the source by a fluorescence and absorption measurement, respectively, which both give the velocity distribution in a given volume. The measured longitudinal velocity can be approximated by a Maxwell-Boltzmann distribution with a most probable velocity of $\widehat{v_l} = 243\,\mathrm{m\,s^{-1}}$ [74]:

$$f_{l,meas}(v_l) = \frac{4}{\sqrt{\pi}} \cdot \frac{v_l^2}{\widehat{v_l}^3} \cdot e^{-\frac{v_l^2}{\widehat{v_l}^2}} \tag{B.14}$$

The absorption measurement with a small laser beam directly behind the source (illustrated in figure B.8a) quantifies, apart from fringe effects, the radial component

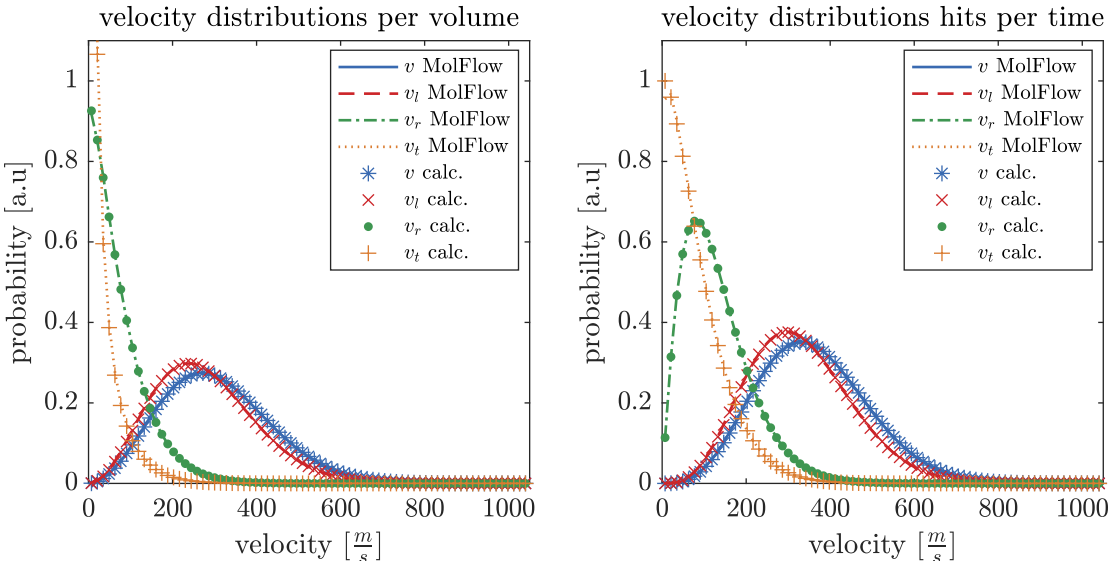

(a) collision per time, $f_{coll}(v)$ (b) per volume, $f_{gas}(v)$

Fig. B.6.: By MolFlow generated velocity distribution compared to the description by equation B.3, B.10, B.11 and B.12.

v_r and not the transversal component v_t of the velocity distribution[1]. The measured radial velocity can be approximated by a normal distribution with $\sigma_r = 85\,\mathrm{m\,s^{-1}}$[74]:

$$f_{r,meas}(v_r) = \frac{1}{2\pi\sigma_r^2} \cdot e^{-\frac{v_r^2}{2\sigma_t^2}} \tag{B.15}$$

The absolute value can be calculated by transforming the measured velocity distribution with respect to equation B.1 from particles per volume to hits on a surface per time. v_l is then expressed as a function of v and v_r, which introduces a factor $v/\sqrt{v^2-v_r^2}$ due to the corresponding transformation. Finally the probability is transformed back to particles per volume. Most of the factors cancel each other and we obtain:

$$f_{v,meas}(v) = \int_0^\infty f_{r,meas}(v_r) \cdot v_r \cdot f_{l,meas}(\sqrt{v^2 - v_r^2})\,\mathrm{d}v_r \tag{B.16}$$

The two free parameters temperature T and the exponent n of the angular distribution in the equations B.3, B.10, B.11 and B.12 can be used to adjust the desorption of the front facet of the source tube to emulate the measured velocity distributions in MolFlow. It should be noted, that at this point the assumption is made, that the

[1]This fact was simulated with a small facet directly behind the source and orthogonally to the front plane of the source. It can be calculated by introducing a factor v_t/v_l in equation B.12, which accounts for the fact, that transversally fast and longitudinally slow particles have a higher probability to hit the test area **A** (compare figure B.8a). It was shown numerically (by integrating over ϕ), that the resulting equation is identical to equation B.11. However, the formal proof is left to the interested reader.

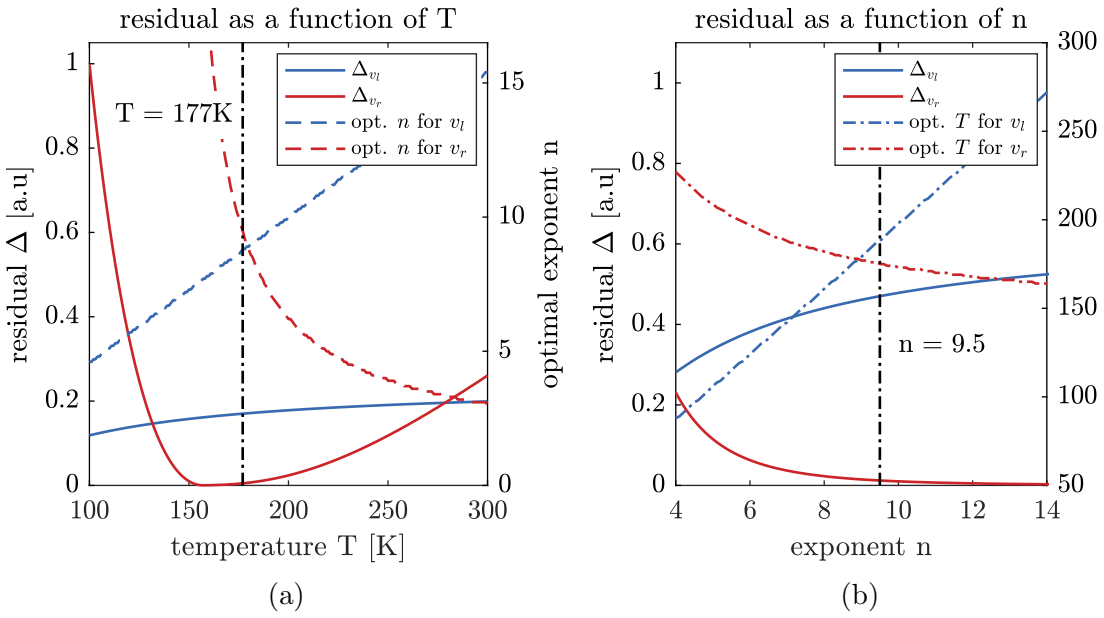

Fig. B.7.: Quadratic residual Δ (equation B.17) between the approximated velocity distributions used by MolFlow and the measured one. The residual is minimised with respect to the other parameter:

a) Residual Δ as a function of the temperature T and corresponding optimal exponent n of the angular distribution.
b) Residual Δ as a function of the exponent n and corresponding optimal temperature T.

The vertical lines show the compromised parameter of $T = 177\,\mathrm{K}$ and $n = 9.5$ used for the simulations in chapter 2.3.2.

metastable atoms have the same velocity distribution as the rest of the atoms[2], which are in the ground state and responsible for the background pressure. Figure B.7 shows the quadratic residual

$$\Delta_{v_x} = \int_0^\infty \left(f_{gas}(v_x) - f_{meas}(v_x)\right)^2 \,\mathrm{d}v_x, \qquad x \in \{l, r\} \tag{B.17}$$

between the approximated velocity distribution used by MolFlow and the measured one as a function of T and n, respectively. The residual is minimised with respect to the other parameter.

The temperature T must be compromised between an optimal approximation of the longitudinal and the radial velocity distribution at the same time. Additionally, the corresponding optimal exponent n should be similar for both distributions. The same consideration applies, if n is compromised. For the high vacuum simulation in

[2]This is not obvious since the metastable atoms are generated by energetic collisions with electrons and there might be a velocity dependency of the excitation efficiency inside the source.

chapter 2.3.2 a temperature of $T = 177\,\mathrm{K}$ and an exponent of the angular distribution of $n = 9.5$ were chosen. The resulting distributions are plotted in figure B.8b. The measured longitudinal velocity distribution is very well approximated. However there is a discrepancy for smaller radial velocities v_r and over the complete range of the total velocity v.

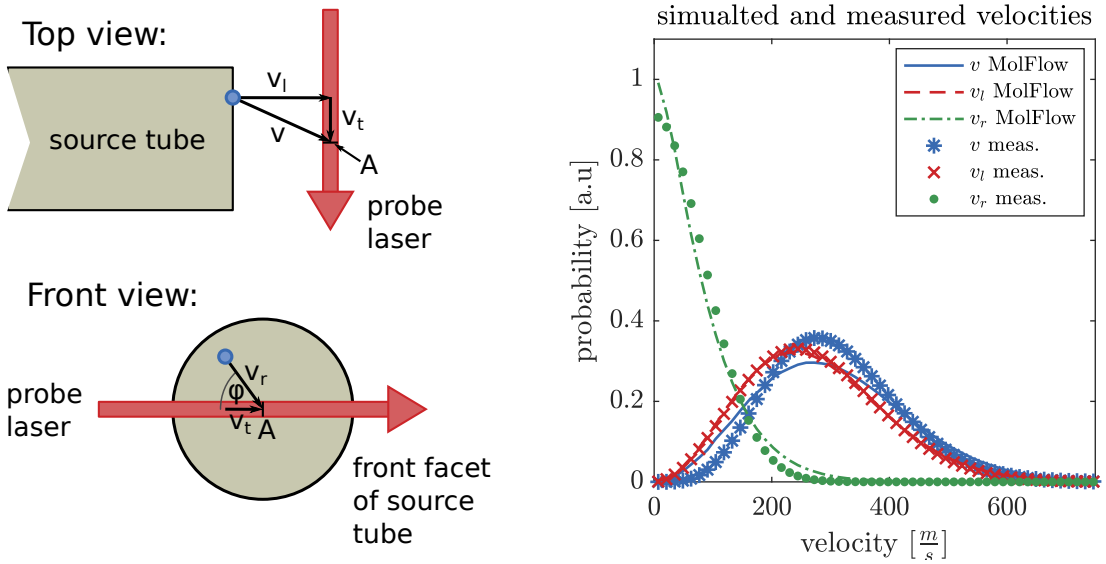

(a) (b)

Fig. B.8.: **a)** Geometry of the transversal absorption measurement directly behind the source: The probe laser probes, which is counterintuitive, the radial velocity component v_r and not the transversal one v_t.
b) Comparison of the measured and by MolFlow approximated ($T = 177\,\mathrm{K}$, $n = 9.5$) velocity distributions.

C. Ice Samples

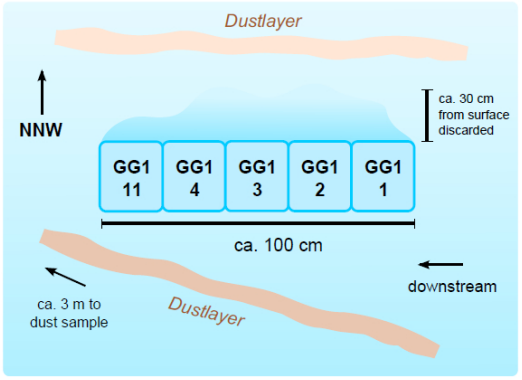

(a) Upper sampling side: View from surface of slope

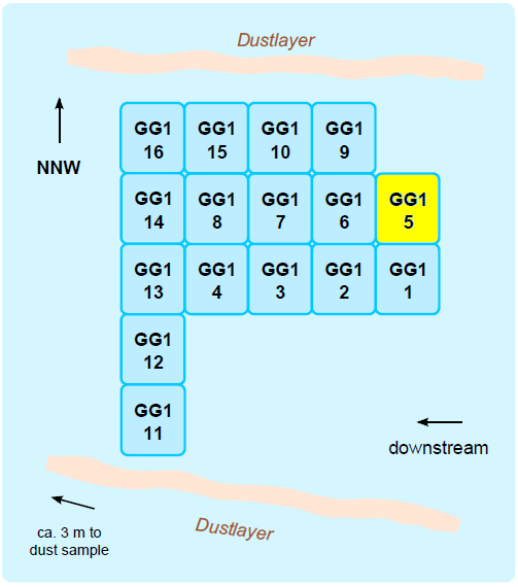

(b) Upper sampling side: Top view

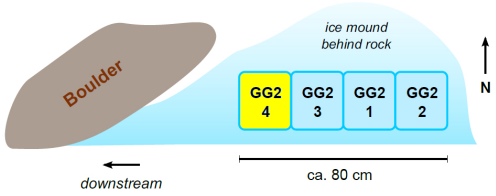

(c) Lower sampling side: View from the side

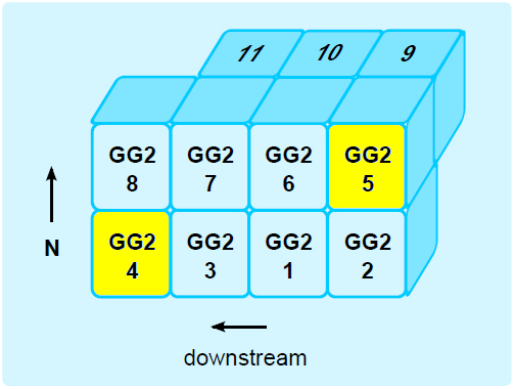

(d) Lower sampling side: Top view (bright sides of the blocks)

Fig. C.1.: Scheme of block extraction: The blocks which were analysed with ArTTA in the scope of this thesis are marked with yellow. The sketches are copied from [90].

D. Ocean Measurements

Table D.1.: List of all measurements during the ocean measurement period. For the reference measurement the raw count rate is listed.

date	**type**	**sample/ bottle**	**volume** [mL STP]	**time** [h]	**counted atoms**	**estim. contam.**	**^{39}Ar [pmAr]**	**count rate [atoms/h]**
06/07/17	defined	100 pmAr	4.0	17.5	discarded			
06/08/17	reference	$60X_{dil}$	4.1	11.0	708			$64.1^{+2.4}_{-2.4}$
06/09/17	defined	100 pmAr	4.0	20.3	131	6.6	$92.4^{+10.0}_{-9.3}$	
06/10/17	contam.	0 pmAr	0.2	18.3	34	discarded		
06/11/17	test	$60X_{dil}$	2.0	8.4	discarded			
06/11/17	reference	$60X_{dil}$	2.0	3.0	186			$61.5^{+4.6}_{-4.4}$
06/11/17	contam.	0 pmAr	0.2	10.3	36	discarded		
06/12/17	reference	$60X_{dil}$	1.3	2.5	149			$59.9^{+5.0}_{-4.8}$
06/12/17	defined	0 pmAr	1.9	19.3	9	10.2	≤ 3.0	
06/13/17	reference	$60X_{dil}$	1.5	2.9	170			$58.3^{+4.6}_{-4.4}$
06/13/17	defined	33 pmAr	1.8	18.0	40	8.8	$29.8^{+7.1}_{-6.2}$	
06/14/17	reference	$60X_{dil}$	1.6	2.2	116			$52.3^{+5.0}_{-4.7}$
06/14/17	ocean	#6	1.7	20.0	117	10.1	$102.8^{+14.0}_{-12.5}$	
06/15/17	reference	$60X_{dil}$	1.7	2.7	129			$47.5^{+4.3}_{-4.1}$
06/15/17	repair	new source						
06/16/17	defined	100 pmAr	2.0	14.5	discarded			
06/17/17	reference	$60X_{dil}$	2.0	2.1	118			$55.0^{+5.2}_{-4.9}$
06/17/17	defined	66 pmAr	1.9	20.0	80	11.0	$56.8^{+9.3}_{-8.3}$	
06/18/17	reference	$60X_{dil}$	2.0	2.1	131			$61.3^{+5.5}_{-5.2}$
06/18/17	ocean	#10	1.9	20.3	66	12.4	$40.5^{+7.4}_{-6.7}$	
06/19/17	reference	$60X_{dil}$	1.6	2.4	155			$63.8^{+5.3}_{-5.0}$
06/19/17	defined	0 pmAr	1.7	18.0	4	9.1	≤ 1.9	
06/20/17	reference	$60X_{dil}$	1.9	4.7	247			$52.4^{+3.4}_{-3.3}$
06/20/17	ocean	#19	1.9	20.0	103	11.0	$74.8^{+10.4}_{-9.4}$	
06/21/17	reference	$60X_{dil}$	1.6	3.1	177			$56.5^{+4.4}_{-4.1}$
06/21/17	ocean	#4	1.8	10.0	38	4.8	$56.0^{+12.7}_{-11.0}$	
06/22/17	repair	upgrade collimator						
06/25/17	defined	100 pmAr	1.9	12.0	discarded			
06/26/17	reference	$60X_{dil}$	1.6	21.0	discarded			
06/27/17	reference	$60X_{dil}$	2.3	15.9	878			$55.3^{+1.9}_{-1.8}$
06/28/17	defined	100 pmAr	2.1	19.1	125	9.6	$104.7^{+11.9}_{-11.0}$	
06/29/17	test	$60X_{dil}$	1.3	8.2	discarded			
06/30/17	repair	new source						
07/02/17	defined	100 pmAr	2.1	11.8	discarded			
07/03/17	reference	$60X_{dil}$	1.7	5.6	298			$53.5^{+3.2}_{-3.0}$
07/03/17	defined	100 pmAr	2.0	15.8	97	5.4	$112.5^{+14.3}_{-13.1}$	
07/04/17	reference	$60X_{dil}$	1.8	2.5	118			$46.9^{+4.4}_{-4.2}$
07/04/17	reference	$60X_{dil}$	2.8	3.3	147			$44.1^{+3.7}_{-3.5}$
07/04/17	defined	0 pmAr	1.9	19.9	12	8.6	$3.6^{+3.5}_{-3.0}$	
07/05/17	reference	$60X_{dil}$	1.9	3.2	155			$49.0^{+4.0}_{-3.8}$

Table D.2.: Continuation of table D.1.

date	**type**	**sample/ bottle**	**volume** [mL STP]	**time** [h]	**counted atoms**	**estim. contam.**	**^{39}Ar [pmAr]**	**count rate [atoms/h]**
07/05/17	ocean	#20	1.7	20.0	104	10.7	$86.9^{+12.2}_{-11.0}$	
07/06/17	reference	$60X_{dil}$	1.9	2.3	127			$54.5^{+5.0}_{-4.7}$
07/06/17	ocean	#13	2.0	19.9	41	9.5	$28.1^{+6.7}_{-5.9}$	
07/07/17	reference	$60X_{dil}$	1.9	3.4	184			$53.7^{+4.1}_{-3.9}$
07/07/17	ocean	#17	1.9	20.0	111	9.7	$92.8^{+11.9}_{-10.9}$	
07/08/17	reference	$60X_{dil}$	1.9	4.4	223			$51.2^{+3.5}_{-3.3}$
07/09/17	repair	adjustment collimator						
07/09/17	ocean	#9	1.9	20.0	54	9.0	$45.3^{+8.2}_{-7.4}$	
07/09/17	reference	$60X_{dil}$	2.0	20.5	962			$47.0^{+1.5}_{-1.5}$
07/10/17	defined	0 pmAr	1.8	35.2	31	29.4	≤ 4.6	
07/12/17	reference	$60X_{dil}$	1.8	2.0	127			$63.6^{+5.8}_{-5.5}$
07/12/17	ocean	#14	1.5	18.4	127	12.9	$103.8^{+13.8}_{-12.5}$	
07/13/17	reference	$60X_{dil}$	1.9	2.7	140			$52.6^{+4.6}_{-4.3}$
07/13/17	ocean	#8	2.0	20.0	84	10.1	$62.8^{+9.8}_{-8.8}$	
07/14/17	reference	$60X_{dil}$	1.6	2.3	141			$60.5^{+5.2}_{-5.0}$
07/16/17	repair	new source						
07/17/17	reference	$60X_{dil}$	0.2	2.0	discarded			
07/17/17	ocean	#11	1.9	20.0	111	11.3	$84.3^{+11.8}_{-10.6}$	
07/19/17	repair	new source						
07/20/17	defined	100 pmAr	2.1	10.3	79	6.5	$118.4^{+18.3}_{-16.3}$	
07/21/17	repair	new source						
07/22/17	defined	100 pmAr	2.3	11.5	78	6.8	$104.4^{+16.2}_{-14.5}$	
07/23/17	repair	new source						
07/24/17	reference	$60X_{dil}$	2.0	2.2	114			$52.7^{+5.1}_{-4.8}$
07/24/17	defined	66 pmAr	2.1	6.3	discarded			
07/24/17	defined	66 pmAr	2.1	11.9	29	6.5	$36.6^{+10.3}_{-8.9}$	
07/25/17	repair	adjustment MOT						
07/25/17	reference	$60X_{dil}$	1.7	7.0	369			$52.8^{+2.8}_{-2.7}$
07/25/17	ocean	#16	2.0	19.9	100	10.2	$73.2^{+10.1}_{-9.2}$	
07/26/17	reference	$60X_{dil}$	1.8	2.0	125			$62.6^{+5.8}_{-5.4}$
07/26/17	ocean	#15	2.6	20.0	110	7.7	$85.6^{+11.8}_{-10.5}$	
07/27/17	reference	$60X_{dil}$	1.8	2.0	103			$51.7^{+5.3}_{-4.9}$
07/27/17	ocean	#5	2.0	20.0	55	9.6	$39.7^{+7.9}_{-7.0}$	
07/28/17	reference	$60X_{dil}$	1.6	2.3	134			$57.6^{+5.1}_{-4.8}$
07/28/17	ocean	#7	1.9	20.0	92	9.1	$79.7^{+12.0}_{-10.8}$	
07/29/17	reference	$60X_{dil}$	1.6	2.1	88			$41.4^{+4.6}_{-4.3}$
07/30/17	repair	new source						
07/30/17	defined	66 pmAr	1.8	20.0	86	12.0	$58.3^{+10.5}_{-9.2}$	
07/31/17	reference	$60X_{dil}$	1.8	2.0	121			$60.6^{+5.7}_{-5.3}$
07/31/17	ocean	#13	1.8	20.0	67	11.9	$43.8^{+8.1}_{-7.2}$	
08/01/17	reference	$60X_{dil}$	1.7	2.0	120			$60.1^{+5.7}_{-5.3}$
08/01/17	ocean	#9	1.9	20.1	95	11.8	$63.1^{+9.5}_{-8.6}$	
08/02/17	reference	$60X_{dil}$	2.1	2.0	131			$65.6^{+5.9}_{-5.6}$
08/02/17	ocean	#19	3.7	20.2	109	6.3	$74.9^{+9.9}_{-8.9}$	
08/03/17	reference	$60X_{dil}$	1.5	2.2	140			$64.7^{+5.6}_{-5.3}$
08/03/17	ocean	#4	3.8	20.0	65	6.2	$42.1^{+7.0}_{-6.2}$	
08/04/17	reference	$60X_{dil}$	1.6	2.0	138			$69.1^{+6.0}_{-5.7}$
08/04/17	ocean	#2	1.9	20.0	67	12.6	$37.6^{+7.6}_{-6.7}$	
08/05/17	repair	cleaning getter, adjustment collimator						
08/05/17	reference	$60X_{dil}$	1.8	2.0	133			$66.6^{+5.9}_{-5.6}$
08/06/17	ocean	#12	1.9	19.6	106	11.4	$73.1^{+10.4}_{-9.4}$	
08/06/17	reference	$60X_{dil}$	1.7	2.0	119			$59.6^{+5.6}_{-5.3}$
08/06/17	repair	failure quench						
08/06/17	ocean	#3	2.1	19.8	53	8.3	$42.6^{+9.5}_{-8.2}$	

Table D.3.: Continuation of table D.1.

date	**type**	**sample/ bottle**	**volume** [mL STP]	**time** [h]	**counted atoms**	**estim. contam.**	**^{39}Ar [pmAr]**	**count rate [atoms/h]**
08/07/17	reference	$60X_{dil}$	1.6	2.0	101			$50.6^{+5.2}_{-4.9}$
08/08/17	repair	failure quench						
08/07/17	ocean	#14	2.6	16.5	114	9.2	$85.6^{+13.0}_{-11.4}$	
08/08/17	reference	$60X_{dil}$	1.7	2.0	141			$70.7^{+6.1}_{-5.8}$
08/08/17	ocean	#1HD	2.5	15.7	71	11.2	$51.1^{+8.9}_{-7.9}$	
08/09/17	reference	$60X_{dil}$	1.7	2.0	144			$72.1^{+6.2}_{-5.8}$
08/10/17	ocean	#7	4.2	27.2	123	10.5	$58.7^{+7.7}_{-7.0}$	
08/11/17	reference	$60X_{dil}$	1.6	2.0	125			$62.6^{+5.8}_{-5.4}$
08/11/17	ocean	#20	2.7	22.3	112	9.8	$72.1^{+9.9}_{-8.9}$	
08/12/17	reference	$60X_{dil}$	1.5	2.0	118			$59.1^{+5.6}_{-5.3}$
08/12/17	repair	cleaning getter, adjustment collimator						
08/12/17	reference	$60X_{dil}$	1.5	2.0	136			$68.1^{+6.0}_{-5.7}$
08/12/17	ocean	#1	2.6	20.0	74	8.7	$48.5^{+8.0}_{-7.1}$	
08/13/17	reference	$60X_{dil}$	1.7	2.0	121			$60.6^{+5.7}_{-5.3}$
08/13/17	ocean	#17	2.8	20.0	106	8.3	$69.4^{+9.5}_{-8.6}$	
08/14/17	reference	$60X_{dil}$	1.6	1.8	137			$74.8^{+6.6}_{-6.2}$
08/14/17	ocean	#3	2.4	20.0	78	10.0	$48.7^{+7.9}_{-7.1}$	
08/15/17	reference	$60X_{dil}$	1.8	2.0	119			$59.6^{+5.6}_{-5.3}$
08/15/17	ocean	#9	2.4	20.1	82	9.4	$55.3^{+8.7}_{-7.8}$	
08/16/17	reference	$60X_{dil}$	2.0	2.0	131			$65.6^{+5.9}_{-5.6}$
08/16/17	ocean	#11	4.3	20.0	99	5.0	$74.3^{+10.3}_{-9.2}$	
08/17/17	reference	$60X_{dil}$	1.6	2.0	111			$55.6^{+5.4}_{-5.1}$
08/17/17	defined	10 pmAr	2.0	20.7	18	10.9	$5.8^{+3.9}_{-3.3}$	
08/18/17	reference	$60X_{dil}$	1.6	2.0	120			$60.1^{+5.7}_{-5.3}$
08/18/17	ocean	#8	4.7	20.0	63	4.3	$48.6^{+8.1}_{-7.2}$	
08/19/17	reference	$60X_{dil}$	1.9	2.0	111			$55.6^{+5.4}_{-5.1}$
08/19/17	repair	cleaning getter, adjustment laser system						
08/19/17	reference	$60X_{dil}$	1.8	2.0	138			$69.1^{+6.0}_{-5.7}$
08/19/17	ocean	#15	3.1	20.0	110	7.4	$76.2^{+10.3}_{-9.2}$	
08/20/17	reference	$60X_{dil}$	1.7	2.0	119			$59.6^{+5.6}_{-5.3}$
08/20/17	ocean	#13	1.6	19.9	54	13.5	$32.6^{+7.3}_{-6.4}$	
08/21/17	reference	$60X_{dil}$	1.6	2.0	119			$59.6^{+5.6}_{-5.3}$
08/21/17	ocean	#6	2.5	20.0	148	9.8	$95.1^{+11.5}_{-10.4}$	
08/22/17	reference	$60X_{dil}$	1.7	2.0	159			$79.6^{+6.5}_{-6.2}$
08/22/17	ocean	#10	4.5	19.4	81	5.3	$52.4^{+7.7}_{-6.9}$	
08/23/17	reference	$60X_{dil}$	1.6	2.0	125			$62.6^{+5.8}_{-5.4}$
08/23/17	defined	0 pmAr	1.8	14.9	8	7.7	≤ 4.1	
08/24/17	reference	$60X_{dil}$	1.9	2.0	discarded			
08/24/17	ocean	#1	5.8	20.0	79	3.6	$60.7^{+10.2}_{-8.9}$	
08/25/17	reference	$60X_{dil}$	1.7	2.0	118			$59.2^{+5.6}_{-5.3}$
08/25/17	ocean	#5	5.7	20.8	49	4.1	$33.3^{+6.2}_{-5.5}$	
08/26/17	reference	$60X_{dil}$	2.1	2.0	129			$64.6^{+5.9}_{-5.5}$
08/26/17	reference	$60X_{dil}$	2.2	13.5	discarded			
08/27/17	repair	cleaning getter, adjustment collimator						
08/27/17	reference	$60X_{dil}$	1.5	23.8	1370			$57.5^{+1.6}_{-1.5}$
08/28/17	ocean	#16	3.1	23.2	81	9.0	$52.8^{+7.4}_{-6.8}$	
08/29/17	reference	$60X_{dil}$	1.9	2.2	101			$46.7^{+4.8}_{-4.5}$
08/29/17	ocean	#2	2.3	20.0	41	7.0	$34.4^{+7.8}_{-6.8}$	
08/30/17	reference	$60X_{dil}$	1.7	2.3	111			$47.6^{+4.7}_{-4.4}$
08/30/17	ocean	#12	1.3	20.7	104	13.9	$87.2^{+15.3}_{-13.3}$	

Bibliography

[1] B. Eakins and G. Sharman. Volumes of the World's Oceans from ETOPO1, NOAA. *National Geophysical Data Center, Boulder, CO*, 2010.

[2] W. Jiang, K. Bailey, Z.-T. Lu, et al. An atom counter for measuring ^{81}Kr and ^{85}Kr in environmental samples. *Geochimica et Cosmochimica Acta*, 91:1 – 6, 2012.

[3] J. Welte. *Atom Trap Trace Analysis of ^{39}Ar*. PhD thesis, Faculty of Physics and Astronomy, University of Heidelberg, www.matterwave.de, 2011.

[4] F. Ritterbusch. *Dating of groundwater with Atom Trap Trace Analysis of ^{39}Ar*. PhD thesis, Faculty of Physics and Astronomy, University of Heidelberg, 2013.

[5] A. Kersting. *Dating of groundwater and ocean samples with noble gas radioisotopes – Sample preparation and field applications*. PhD thesis, Faculty of Physics and Astronomy, University of Heidelberg, 2018.

[6] IAEA. Live Chart of Nuclides [online]. 2018. URL: `https://www-nds.iaea.org/relnsd/vcharthtml/VChartHTML.html`.

[7] D. W. Waugh, T. M. Hall, and T. W. N. Haine. Relationships among tracer ages. *Journal of Geophysical Research: Oceans*, 108(C5), 2003. 3138.

[8] J. L. Bullister. Atmospheric histories (1765-2015) for CFC-11, CFC-12, CFC-113, CCl_4, SF_6 and N_2O. *NOAA National Centers for Environmental Information. Unpublished Dataset*, 2015.

[9] S. F. Jean Margat and A. Droubi. *Non Renewable Groundwater Resources – A guidebook on socially-sustainable management for water-policy makers*, chapter Concept and importance of non-renewable resources, pages 13–24. UNESCO United Nations Educational, 2006.

[10] International Atomic Energy Agency. *Isotope Methods for Dating Old Groundwater*. International Atomic Energy Agency, Vienna, 2013.

[11] M. Geyh. An overview of ^{14}C analysis in the study of groundwater. *Radiocarbon*, 42:99–114, 2000.

[12] B. Philippsen. The freshwater reservoir effect in radiocarbon dating. *Heritage Science*, 1(1):24, Aug 2013.

[13] G. Gebbie and P. Huybers. The mean age of ocean waters inferred from radiocarbon observations: Sensitivity to surface sources and accounting for mixing histories. *Journal of Physical Oceanography*, 42(2):291–305, 2012.

[14] L. Rayleigh and W. Ramsay. Argon, a new constituent of the atmosphere. *Proc. R. Soc. Lond.*, 57(6):265–287, 1894.

[15] N. Media. nobelprize.org [online]. 2018. URL: `https://www.nobelprize.org/`.

[16] A. Liquide. Gas Encyclopedia [online]. 2018. URL: `https://encyclopedia.airliquide.com/argon`.

[17] R. C. Hamme and S. R. Emerson. The solubility of neon, nitrogen and argon in distilled water and seawater. *Deep Sea Research Part I: Oceanographic Research Papers*, 51(11):1517 – 1528, 2004.

[18] S. M. Gilfillan, C. J. Ballentine, G. Holland, et al. The noble gas geochemistry of natural CO_2 gas reservoirs from the Colorado Plateau and Rocky Mountain provinces, USA. *Geochimica et Cosmochimica Acta*, 72(4):1174 – 1198, 2008.

[19] S. K. Atreya, M. G. Trainer, H. B. Franz, et al. Primordial argon isotope fractionation in the atmosphere of Mars measured by the SAM instrument on Curiosity and implications for atmospheric loss. *Geophysical Research Letters*, 40(21):5605–5609, 2013. 2013GL057763.

[20] J.-Y. Lee, K. Marti, J. P. Severinghaus, et al. A redetermination of the isotopic abundances of atmospheric Ar. *Geochimica et Cosmochimica Acta*, 70(17):4507 – 4512, 2006.

[21] K. Gopalan. *Principle of Radiometric Dating*. Cambridge University Press, 2017.

[22] A. R. Brosi, H. Zeldes, and B. H. Ketelle. ^{39}Ar beta-spectrum. *Phys. Rev.*, 79:902–902, Sep 1950.

[23] H. Oeschger, A. Gugelmann, H. Lossli, et al. ^{39}Ar dating of groundwater. *Proc. Conf. Isotope Techniques in Groundwater Hydrology , Vienna, IAEA*, pages 179–90, 1974.

[24] D.-M. Mei, Z.-B. Yin, J. Spaans, et al. Prediction of underground argon content for dark matter experiments. *Phys. Rev. C*, 81:055802, May 2010.

[25] J. Xu, F. Calaprice, C. Galbiati, et al. A study of the trace ^{39}Ar content in argon from deep underground sources. *Astroparticle Physics*, 66:53 – 60, 2015.

[26] O. A. S. R. W. Stoenner and S. Katcoff. Half-lives of ^{37}Ar, ^{39}Ar, and ^{42}Ar. *Science*, 148:1325–1328, 1965.

[27] H. Loosli. A dating method with ^{39}Ar. *Earth and Planetary Science Letters*, 63(1):51 – 62, 1983.

[28] P. Collon, W. Kutschera, and Z.-T. Lu. Tracing noble gas radionuclides in the environment. *Annual Review of Nuclear and Particle Science*, 54(1):39–67, 2004.

[29] Z.-T. Lu and P. Mueller. Chapter 4 - Atom Trap Trace Analysis of rare noble gas isotopes. In P. Berman, E. Arimondo, and C. Lin, editors, *Advances In Atomic, Molecular, and Optical Physics*, volume 58 of *Advances In Atomic, Molecular, and Optical Physics*, pages 173 – 205. Academic Press, 2010.

[30] H. Loosli, M. Heimann, and H. Oeschger. Low-Level gas proportional counting in an underground laboratory. *Radiocarbon*, 22(2):461–469, 1980.

[31] H. Loosli. ^{39}Ar: A tool to investigate ocean water circulation and mixing. *Handbook Environ. Isot. Chem.*, 3:385–392, 1989.

[32] P. Collon, M. Bichler, J. Caggiano, et al. Development of an AMS method to study oceanic circulation characteristics using cosmogenic ^{39}Ar. *Nuclear Instruments and Methods in Physics Research Section B: Beam Interactions with Materials and Atoms*, 223-224:428–434, 2004. Proceedings of the Ninth International Conference on Accelerator Mass Spectrometry.

[33] P. Collon, M. Bowers, F. Calaprice, et al. Reducing potassium contamination for AMS detection of ^{39}Ar with an electron-cyclotron-resonance ion source. *Nuclear Instruments and Methods in Physics Research Section B: Beam Interactions with Materials and Atoms*, 283(0):77 – 83, 2012.

[34] H. J. Metcalf and P. v. d. Straten. *Laser cooling and trapping*. Springer, New York; Berlin; Heidelberg [u.a.], 1999.

[35] C. Y. Chen, Y. M. Li, K. Bailey, et al. Ultrasensitive isotope trace analyses with a magneto-optical trap. *Science*, 286(5442):1139–1141, 1999.

[36] F. Ritterbusch. Personal communication. Private.

[37] N. C. Sturchio, X. Du, R. Purtschert, et al. One million year old groundwater in the Sahara revealed by ^{81}Kr and ^{36}Cl. *Geophys. Res. Lett.*, 31:L05503, 2004.

[38] R. Yokochi, N. Sturchio, R. Purtschert, et al. Noble gas radionuclides in Yellowstone geothermal gas emissions: A reconnaissance. *Chemical Geology*, 339(0):43 – 51, 2013.

[39] P. K. Aggarwal, T. Matsumoto, N. C. Sturchio, et al. Continental degassing of ^{4}He by surficial discharge of deep groundwater. *Nature Geoscience*, 2014.

[40] N. C. Sturchio, K. L. Kuhlman, R. Yokochi, et al. ^{81}Kr in groundwater of the Culebra Dolomite near the waste isolation pilot plant, New Mexico. *Journal of Contaminant Hydrology*, 160:12 – 20, 2014.

[41] C. Buizert, D. Baggenstos, W. Jiang, et al. Radiometric ^{81}Kr dating identifies 120,000-year-old ice at Taylor Glacier, Antarctica. *PNAS*, 111(19):6876–6881, 2014.

[42] W. Jiang, W. Williams, K. Bailey, et al. ^{39}Ar detection at the 10^{-16} isotopic abundance level with Atom Trap Trace Analysis. *Physical Review Letters*, 106(10), March 2011.

[43] S. Ebser. Optimierung und Stabilisierung von ^{39}Ar-ATTA bis hin zur erstmaligen Anwendung auf die Datierung natürlicher Wasserproben. Master's thesis, Faculty of Physics and Astronomy, University of Heidelberg, 2012.

[44] F. Ritterbusch, S. Ebser, J. Welte, et al. Groundwater dating with Atom Trap Trace Analysis of ^{39}Ar. *Geophysical Research Letters*, 41(19):6758–6764, oct 2014.

[45] F. Ritterbusch. Realization of a collimated beam of metastable atoms for ATTA of ^{39}Ar. Master's thesis, Faculty of Physics and Astronomy, University of Heidelberg, 2009.

[46] H. Katori and F. Shimizu. Lifetime measurement of the $1s_5$ metastable state of argon and krypton with a magneto-optical trap. *Phys. Rev. Lett.*, 70:3545–3548, Jun 1993.

[47] J. Welte, I. Steinke, M. Henrich, et al. Hyperfine spectroscopy of the $1s_5 - 2p_9$ transition of ^{39}Ar. *Review of Scientific Instruments*, 80(11):113109, 2009.

[48] W. Williams, Z.-T. Lu, K. Rudinger, et al. Spectroscopic study of the cycling transition $4s[3/2]_2 - 4p[5/2]_3$ at 811.8 nm in ^{39}Ar: Hyperfine structure and isotope shift. *Phys. Rev. A*, 83:012512, 2011.

[49] T. Reichelt. *Groundwater Degassing and Separation of Argon from Air for ^{39}Ar Dating with ATTA*. PhD thesis, University of Heidelberg, 2013.

[50] S. Beyersdorfer. Argon extraction from glacier ice and ocean water for dating with ^{39}Ar-ATTA. Master's thesis, Heidelberg University, 2016.

[51] R. Rausch. Das Periodensystem der Elemente online [online]. 2017. URL: `www.periodensystem-online.de`.

[52] U. Beyerle, W. Aeschbach-Hertig, D. M. Imboden, et al. A mass spectrometric system for the analysis of noble gases and tritium from water samples. *Environmental Science & Technology*, 34(10):2042–2050, 2000.

[53] K. J. R. Rosman and P. D. P. Taylor. Isotopic compositions of the elements 1997. *Pure and Applied Chemistry*, 1998.

[54] H. O. Back, F. Calaprice, C. Condon, et al. First large scale production of low radioactivity argon from underground sources. *ArXiv e-prints*, April 2012.

[55] H. O. Back, T. Alexander, A. Alton, et al. First commissioning of a cryogenic distillation column for low radioactivity underground argon. *ArXiv e-prints*, April 2012.

[56] J. A. Corcho Alvarado, Barbecot, R. Purtschert, et al. European climate variations over the past half-millennium reconstructed from groundwater. *Geophys. Res. Lett.*, in press, 2009.

[57] H. Loosli, B. Lehmann, and W. Balderer. ^{39}Ar, ^{37}Ar and ^{85}Kr isotopes in Stripa groundwaters. *Geochimica et Cosmochimica Acta*, 53(8):1825 – 1829, 1989.

[58] R. Yokochi, N. C. Sturchio, and R. Purtschert. Determination of crustal fluid residence times using nucleogenic ^{39}Ar. *Geochimica et Cosmochimica Acta*, 88:19 – 26, 2012.

[59] H. Oeschger, P. Stauffer, P. Bucher, and M. Moell. Extraction of trace components from large quantities of ice in boreholes. *Journal of Glaciology*, 17(75):117–128, 1976.

[60] J. Rodriguez. *Beiträge zur Verteilung von ^{39}Ar im Atlantik.* PhD thesis, Universität Bern, 1993.

[61] M. Holzer and F. W. Primeau. Improved constraints on transit time distributions from ^{39}Ar: A maximum entropy approach. *Journal of Geophysical Research: Oceans*, 115(C12), 2010. C12021.

[62] W. Broecker and T.-H. Peng. Comparison of ^{39}Ar and ^{14}C ages for waters in the deep ocean. *Nuclear Instruments and Methods in Physics Research Section B: Beam Interactions with Materials and Atoms*, 172(1):473 – 478, 2000. 8th International Conference on Accelerator Mass Spectrometry.

[63] E. Nolte, W. Rühm, H. Loosli, et al. Measurements of fast neutrons in Hiroshima by use of ^{39}Ar. *Radiat. Environ. Biophys.*, 44:261, 2006.

[64] T. M. Hall and R. A. Plumb. Age as a diagnostic of stratospheric transport. *Journal of Geophysical Research: Atmospheres*, 99(D1):1059–1070, 1994.

[65] T. Tanhua, D. W. Waugh, and D. W. R. Wallace. Use of SF_6 to estimate anthropogenic CO_2 in the upper ocean. *Journal of Geophysical Research: Oceans*, 113(C4), 2008. C04037.

[66] R. Steinfeldt, M. Rhein, J. L. Bullister, and T. Tanhua. Inventory changes in anthropogenic carbon from 1997–2003 in the Atlantic Ocean between 20°S and 65°N. *Global Biogeochemical Cycles*, 23(3), 2009. GB3010.

[67] T. Stöven and T. Tanhua. Ventilation of the Mediterranean Sea constrained by multiple transient tracer measurements. *Ocean Science*, 10(3):439–457, 2014.

[68] D. W. Waugh, M. K. Vollmer, R. F. Weiss, T. W. N. Haine, and T. M. Hall. Transit time distributions in Lake Issyk-Kul. *Geophysical Research Letters*, 29(24):84–1–84–4, 2002. 2231.

[69] N. B. Engdahl, T. R. Ginn, and G. E. Fogg. Using groundwater age distributions to estimate the effective parameters of Fickian and non-Fickian models of solute transport. *Advances in Water Resources*, 54:11 – 21, 2013.

[70] D. Waugh and T. Hall. Age of stratospheric air: Theory, observations, and models. *Reviews of Geophysics*, 40(4):1–1–1–26, 2002.

[71] A. Schneider, T. Tanhua, W. Roether, and R. Steinfeldt. Changes in ventilation of the Mediterranean Sea during the past 25 years. *Ocean Science*, 10(1):1–16, 2014.

[72] D. W. Waugh, T. W. Haine, and T. M. Hall. Transport times and anthropogenic carbon in the subpolar North Atlantic ocean. *Deep Sea Research Part I: Oceanographic Research Papers*, 51(11):1475 – 1491, 2004.

[73] C. Kaup. Single-atom detection of ^{39}Ar. Master's thesis, Faculty of Physics and Astronomy, University of Heidelberg, 2011.

[74] Z. Feng. Implementierung einer Atomflussüberwachung für ^{39}Ar ATTA. Bachelor's thesis, Faculty of Physics and Astronomy, University of Heidelberg, 2012, www.matterwave.de, 2012.

[75] M. Kohler, H. Daerr, P. Sahling, et al. All-optical production and trapping of metastable noble-gas atoms down to the single-atom regime. *EPL (Europhysics Letters)*, 108(1):13001, 2014.

[76] L. Ringena. Optimization of ^{39}Ar-ATTA with new laser system and a double-frequency magneto-optical trap. Master's thesis, Faculty of Physics and Astronomy, University of Heidelberg, 2016.

[77] M. Henrich. Design and realization of a laser system for ATTA of ^{39}Ar. Master's thesis, Faculty of Physics and Astronomy, University of Heidelberg, www.matterwave.de, 2010.

[78] X. Du, R. Purtschert, K. Bailey, et al. A new method of measuring ^{81}Kr and ^{85}Kr abundances in environmental samples. *Geophysical Research Letters*, 30(20), oct 2003.

[79] CERN. MolFlow+ [online]. 2018. URL: `https://molflow.web.cern.ch/`.

[80] J. Vallverdú. The false dilemma: Bayesian vs. Frequentist. *ArXiv e-prints*, April 2008.

[81] F. A. Haight. *Handbook of the Poisson Distribution*. Wiley, 1967.

[82] G. R. Grimmett and D. R. Stirzaker. *Probability and Random Processes*. Oxford, 2009.

[83] B. Jähne. *Practical Handbook on Image Processing for Scientific and Technical Applications, Second Edition*. CRC Press, Inc., Boca Raton, FL, USA, 2004.

[84] J. C. Zappala, K. Bailey, P. Mueller, T. P. O'Connor, and R. Purtschert. Rapid processing of ^{85}Kr/Kr ratios using Atom Trap Trace Analysis. *Water Resources Research*, 53(3):2553–2558, 2017.

[85] W. Jiang, K. Bailey, Z.-T. Lu, et al. Ion current as a precise measure of the loading rate of a magneto-optical trap. *Optics Letters*, 39(2):409, January 2014.

[86] R. T. Cox. Probability, frequency and reasonable expectation. *American Journal of Physics*, 14(1):1–13, 1946.

[87] A. B. Downey. *Think Bayes*. Green Tea Press, 2012.

[88] M. D. Springer. *The Algebra of Random Variables*. Wiley, 1979.

[89] P. Steier, R. Drosg, M. Fedi, et al. Radiocarbon determination of particulate organic carbon in non-temperated, alpine glacier ice. *Radiocarbon*, 48(1):69–82, 2006.

[90] H. M. Hoffmann and et al. Ice block sampling at Gorner Glacier 22.-25.7.2014. sampling protocol, June 2014.

[91] Wikipedia. Digital relief of the Alps [online]. 2017. URL: `https://en.wikipedia.org/wiki/Alps#/media/File:Alpenrelief_01.jpg`.

[92] H. M. Hoffmann. *Micro radiocarbon dating of the particulate organic carbon fraction in Alpine glacier ice: Method refinement, critical evaluation and dating applications*. PhD thesis, Ruperto-Carola University of Heidelberg, Germany, 2016.

[93] Bundesamt für Landestopografie swisstopo. geo.admin.ch - das Geoportal des Bundes [online]. 2017. URL: `https://map.geo.admin.ch`.

[94] P. Bohleber, D. Wagenbach, W. Schöner, and R. Böhm. To what extent do water isotope records from low accumulation alpine ice cores reproduce instrumental temperature series? *Tellus B: Chemical and Physical Meteorology*, 65(1):20148, 2013.

[95] C. E. Aalseth, R. M. Bonicalzi, M. G. Cantaloub, et al. A shallow underground laboratory for low-background radiation measurements and materials development. *Review of Scientific Instruments*, 83(11):113503, 2012.

[96] R. Williams, C. Aalseth, J. Brandenberger, et al. Development of a low-level ^{39}Ar calibration standard – Analysis by absolute gas counting measurements augmented with simulation. *Applied Radiation and Isotopes*, 126:243 – 248, 2017.

[97] P. Benetti, F. Calaprice, E. Calligarich, et al. Measurement of the specific activity of ^{39}Ar in natural argon. *Nuclear Instruments and Methods in Physics Research Section A: Accelerators, Spectrometers, Detectors and Associated Equipment*, 574(1):83 – 88, 2007.

[98] W. Aeschbach. Intercomparison with Bern. Personal communication, November 2017.

[99] M. Visbeck. Oxygen in the Tropical Atlantic OSTRE Third Tracer Survey - Cruise No. M116/1 – May 1 – June 3, 2015 – Pointe-a-Pitre (Guadeloupe) – Mindelo (Cape Verde). *METEOR-Berichte, M116/1, 43 pp., DFG-Senatskommission für Ozeanographie*, 2016.

[100] Z.-T. Lu. Personal communication. Private.

[101] R. Schlitzer, W. Roether, U. Weidmann, P. Kalt, and H. H. Loosli. A meridional ^{14}C and ^{39}Ar section in northeast Atlantic deep water. *Journal of Geophysical Research: Oceans*, 90(C4):6945–6952, 1985.

[102] T. Tanhua. Personal communication. Private.

[103] T. Stöven. Personal communication. Private.

[104] M. Warner and R. Weiss. Solubilities of chlorofluorocarbons 11 and 12 in water and seawater. *Deep Sea Research Part A. Oceanographic Research Papers*, 32(12):1485 – 1497, 1985.

[105] S. IOC and IAPSO. The international thermodynamic equation of seawater – 2010: Calculation and use of thermodynamic properties. *Intergovernmental Oceanographic Commission, Manuals and Guides No. 56, UNESCO*, 2010.

[106] J. Hahn, P. Brandt, S. Schmidtko, and G. Krahmann. Decadal oxygen change in the eastern tropical North Atlantic. *Ocean Science*, 13(4):551–576, 2017.

[107] W. Emery. Water types and water masses. In *Encyclopedia of Ocean Sciences*, pages 3179 – 3187. Academic Press, Oxford, 2001.

[108] E. Morozov, A. Demidov, R. Tarakanov, and W. Zenk. *Abyssal Channels in the Atlantic Ocean*, chapter Deep Water Masses of the South and North Atlantic, pages 25–50. Springer, Dordrecht, 2010.

[109] N. Aeronautics and G. I. f. S. S. Space Administration. Forcings in GISS climate model [online]. 2018. URL: `https://data.giss.nasa.gov/modelforce/ghgases/`.

[110] R. Zeebe and D. Wolf-Gladrow. *Encyclopedia of paleoclimatology and ancient environments*, chapter Carbon dioxide, dissolved (Ocean), pages 123–127. Dordrecht: Springer, 2009.

[111] A. G. Dickson and C. Goye, editors. *Handbook of Methods for the Analysis of the Various Parameters of the Carbon Dioxide System in Sea Water.* DOE, 1994.

[112] R. Weiss. Carbon dioxide in water and seawater: The solubility of a non-ideal gas. *Marine Chemistry*, 2(3):203 – 215, 1974.

[113] A. Dickson and F. Millero. A comparison of the equilibrium constants for the dissociation of carbonic acid in seawater media. *Deep Sea Research Part A. Oceanographic Research Papers*, 34(10):1733 – 1743, 1987.

[114] P. G. Brewer, A. L. Bradshaw, and R. Williams. *The Changing Carbon Cycle – A Global Analysis*, chapter Measurement of Total Carbon Dioxide and Alkalinity in the Noth Atlantic Ocean in 1981, pages 348–370. Springer, 1986.

[115] Z. Feng, S. Ebser, L. Ringena, F. Ritterbusch, and M. K. Oberthaler. Bichromatic force on metastable argon for Atom Trap Trace Analysis. *Phys. Rev. A*, 96:013424, Jul 2017.

[116] Z. Feng. Observation and characterization of the bichromatic force on metastable ^{40}Ar. Master's thesis, Faculty of Physics and Astronomy, University of Heidelberg, 2014.

[117] M. Hans. Optisches Pumpen zur Erhöhung der Dichte von metastabilem Argon in einer RF-Gasentladung. Bachelor's thesis, Faculty of Physics and Astronomy, University of Heidelberg, www.matterwave.de, 2014.

[118] A. Frölian. Optisches Pumpen über das transiente $2p_6$-Niveau zur Erhöhung der Dichte von metastabilem Argon in einer RF-Gasentladung. Bachelor's thesis, Faculty of Physics and Astronomy, University of Heidelberg, www.matterwave.de, 2015.

[119] J. Zappala, K. Bailey, W. Jiang, et al. Setting a limit on anthropogenic sources of atmospheric ^{81}Kr through Atom Trap Trace Analysis. *Chemical Geology*, 453:66 – 71, 2017.

[120] C. F. Cheng, G. M. Yang, W. Jiang, et al. Normalization of the single atom counting rate in an atom trap. *Opt. Lett.*, 38(1):31–33, Jan 2013.

[121] G. E. Moore. Cramming more components onto integrated circuits, Reprinted from Electronics, volume 38, number 8, April 19, 1965, pp.114 ff. *IEEE Solid-State Circuits Society Newsletter*, 11(3):33–35, Sept 2006.

[122] J. Welte, F. Ritterbusch, I. Steinke, et al. Towards the realization of Atom Trap Trace Analysis for ^{39}Ar. *New Journal of Physics*, 12(6):065031, 2010.

[123] P. Cennini, S. Cittolin, D. D. Giudice, et al. On atmospheric ^{39}Ar and ^{42}Ar abundance. *Nuclear Instruments and Methods in Physics Research Section A: Accelerators, Spectrometers, Detectors and Associated Equipment*, 356(2):526 – 529, 1995.

[124] A. Kramida, Yu. Ralchenko, J. Reader, and and NIST ASD Team. NIST Atomic Spectra Database (ver. 5.5.2) [online]. 2018. URL: `https://physics.nist.gov/asd`.

[125] M. Ady and R. Kersevan. MolFlow+ user guide. *https://molflow.web.cern.ch/*, 2014.

[126] M. Ady. Molfow 2.6 algorithm. *https://molflow.web.cern.ch/*, 2016.

[127] M. Knudsen. Das Cosinusgesetz in der kinetischen Gastheorie. *Annalen der Physik*, 353(24):1113–1121, 1916.

[128] J. Greenwood. The correct and incorrect generation of a cosine distribution of scattered particles for Monte-Carlo modelling of vacuum systems. *Vacuum*, 67(2):217 – 222, 2002.

Acknowledgements

As always in experimental physics this thesis is not the result of one individual person, but more the yield of many people who were and are directly or indirectly involved in the ArTTA-project. Furthermore, there are many people and friends who supported me throughout the past years and particularly during the final phase of this thesis. I would like to say a very warm thank you to all of you!

This wonderful and forward-looking project was initialised by Professor Markus Oberthaler and Professor Werner Aeschbach and would not have come into being without their commitment.

Markus was my direct supervisor and provided me with a lot of input. He gave me the unique opportunity to work at the ArTTA-experiment in this outstanding group. Furthermore, he gave me many chances to share our results at international conferences, where I met and discussed with many interesting people and got new ideas. Vielen Dank Dir, Markus!

Werner, who manages the environmental part in the ArTTA-collaboration, provided me with plenty of hydrological background. He always has a sympathetic ear for everything. Unfortunately, I did not have enough time to take his offer to work at Lake Kivu. Auch Dir vielen Dank, Werner!

Professor Norbert Frank kindly agreed to grade this thesis as a second referee and supports this project at the Institute of Environmental Physics. Danke!

Toste Tanhua and Tim Stöven from the GEOMAR in Kiel enabled the ocean sampling, contributed to a high extent to the results of the ocean samples, especially to the discussion of transit time distributions, and gave me private coaching in oceanography. Weest bedankt und tack så mycket!

A special thanks to all my colleagues in the ArTTA-laboratories who contributed essentially to the success of this thesis.

Zhongyi Feng set up the major parts of the laser system and adjusted all fibres in nearly countless hours. Furthermore, he was an inspiring discussion partner for physical questions but also while talking about anything and everything. Dir ein ganz herzliches Dankeschön!

Lisa also contributed significantly to the new laser-system, particularly by improving the self-built TAs and Max supported the ocean measurements last year. Euch beiden vielen Dank!

Florian introduced me to the project during my diploma thesis, taught me the spirit of a real Argonaut, and I learned a lot from him in my first two years in the ArTTA-group.

He still supports me, even if eight hours of time difference separate us. Especially during the past few months he struggled through the entire manuscript and gave me innumerable very helpful and constructive feedback, so that this thesis benefited largely from his expertise. Dir, Florian, einen ganz besonderen Dank!

There were many students who invested their time to develop new ideas and to further the ArTTA-project. Euch, Alex, Anke, Maurus, Annika und Andreas vielen Dank für die gemeinsame Zeit im Labor!

Ben from Israel first shared his expertise about moody RF-sources in Heidelberg and then hosted me and gave me an unforgettable time in Jerusalem. תודה (Hopefully these are capital letters again and mean thank you!)

On the other side of the collaboration, Stefan, Florian again, Philip and Arne did a great job constructing a new degassing system for small samples and prepared all samples analysed in this thesis. Euch allen ganz herzlichen Dank!

Furthermore I would like to thank all other Matterwavers, particularly my two office colleagues Simon and Andrea, who sometimes had to share my frustration about Matlab involuntarily, but who also gave the one or other helpful advice for fighting the PCs. Danke und grazie!

There are many people in the background who are essential for the scientific operation at the institute: Dagmar Hufnagel and Christiane Jäger work in the office and the whole group would fall into chaos without them. Euch einen besonderen Dank!

Furthermore I would like to thank Jürgen Schölles and Knud Azeroth, who supported me and the project in all electronic and electrical questions, and finally the complete team of the mechanical workshop, who tried to realise all my ideas – especially Werner Lamade, who always finds a suitable solution, Siegfried Spiegel, who taught me in metal processing and Julia Bing and Christian Herdt, who solved many problems directly and informally. Vielen Dank!

I further gratefully acknowledge the uncomplicated financial and ideational support of the *Studienstiftung des Deutschen Volkes* and the unforgettable and inspiring time at the summer school in Neubeuern.

Last but not least I would like to thank all proofreaders, Conrad from Australia, Gisela and Helena for your linguistic and orthographic corrections, as well as Max, Jan, Zhongyi and Florian.

Finally I would like to thank all my friends for not taking it too badly that the lab-work sometimes seemed to be more important than staying in touch with you. I hope that this will change for the better in future.

Dear Parents, Hanjo and Gisela, dear Siblings, Jan, Nicole with Matteo, Saskia and dear Grandmother Irmgard, thank you for always supporting me. It is great to have such a unique family!

Dear Helena, thank you for your tireless support in English questions, taking me as I am and for always being there for me. I am glad that you are there!